Tailored-Potential Semiconductor Quantum Nanostructures Grown in Inverted Pyramids

Thèse N° 9461

Présentée le 5 avril 2019

à la Faculté des sciences de base
Laboratoire de physique des nanostructures
Programme doctoral en physique

pour l'obtention du grade de Docteur ès Sciences

par

Mikhail LAZAREV

Acceptée sur proposition du jury

Prof. C. Hébert, présidente du jury
Prof. E. Kapon, directeur de thèse
Prof. S. Sanguinetti, rapporteur
Prof. A. Madhukar, rapporteur
Prof. C. Galland, rapporteur

2019

ÉCOLE POLYTECHNIQUE
FÉDÉRALE DE LAUSANNE

Acknowledgements

First of all, my sincere gratitude goes to my thesis supervisor Prof. Eli Kapon for taking me as a Ph.D. student and providing me fascinating opportunities at EPFL. I'm also grateful to Eli for his patience and time that he invested in me, with his help I have learned a lot. Thanks to his attention to the details in each step of my research, valuable feedbacks and inputs during paper writing and especially my thesis writing.

Thanks to Dr. Alok Rudra without whom my work would not have been possible, he was able to realize the quality and reproducibility of the growth sequence and gave me insight of MOVPE growth techniques.

My acknowledgments go to our cleanroom staff Nicolas Leiser, Damien Trolliet and Yoan Trolliet who have trained me and taught all the tricks related to cleanroom usage. They do an excellent job, taking care of all cleanroom equipment. Essential help especially with Schottky diode fabrication technique and experimental setup was available from Dr. Andrei Caliman and Dr. Benjamin Dwir.

I am deeply grateful to Prof. Fredrick Karlsson who helped me with theoretical background providing beneficial material. I was lucky to have an opportunity to collaborate with our colleagues from the Lebedev Institute in Moscow, Russia, and parts of this thesis would not have been possible without their help. I especially thank Prof. N. N. Sibeldin, Dr. M. Skorikov and Dr. V. Tsvetkov for the high-quality data of the streak camera measurements and the great work that they have done.

I would also like to thank all present and past LPN lab members for their support, scientific discussions, advises and for the time that we have spent together: Dr. Irina Kulkova, Dr. Clément Jarlov, Dr. Zlatko Mickovic, Dr. Alessio Miranda, Dr. Alexey Lyasota, Dr. Bruno Rigal, Antoine Delgoffe, Dr. Justina Szeszko, Dr. Vladimir Yakovlev, Dr. Alexei Sirbu, Dr. Andrei Caliman, Dr. Alexandru Mereuta, Dr. Pascal Gallo and my office mate Dr. Moshe Judelewicz. It was a great pleasure to have you all around.

Separately I wish to thank members of the LPN secretariat Nadia Gauljaux and Gabriella Fuchs, who found me a place to live in Lausanne at the beginning of my Ph.D period. Thank you for your kindness and for all administrative work that you did every day.

Finally, I would like to thank my parents and friends for the constant support and inspiration during all this time.

Lausanne, 15 of January 2019

Abstract

Semiconductor nanostructures are a beautiful research field due to a variety of possible and already usable applications. Today, the use of nanostructures is greatly expanded starting from science laboratories to telecommunication, modern computers, biosensors and other technological applications. For example, random number generators based on quantum effects in semiconductor nanostructures are already available on the market. Soon chips that contain integrated nanophotonic circuits and devices will be available, offering higher processing speed than traditional semiconductor electronic devices. This thesis is related to the materials science and nanophotonics aspects of such nanostructures. More particularly, it deals with low dimensional nanostructures such as Quantum Wires (QWRs) and Quantum Dots (QDs), which represent part of the nanostructure family that has great importance for future applications in this field. However, despite substantial recent progress in the area, reproducible fabrication technologies of QDs and QWRs are still challenging, and this thesis addresses some of the issues involved.

We use the metalorganic vapor phase epitaxy (MOVPE) growth process on substrates patterned by inverted pyramids to prepare site controlled GaAs/AlGaAs QD/QWR nanostructures. Our fabrication technique has a significant advantage compared to others in controlling with high accuracy the position, size and composition of the nanostructure along the growth direction, which provides control of heterostructure potential and the properties of the emitted light. Thus, we can realize a whole family of 1D and 0D nanostructures. Our nanostructures are embedded inside the GaAs substrate, which gives an opportunity to integrate such nanostructures in semiconductor photonic circuits.

We have focused on the ability to tune the aluminum (Al) content of the AlGaAs alloy along the growth direction, thus tailoring the potential along a QWR nanostructure. Three parabolic-potential QDs (PQDs) of different potential gradients have thus been realized. The parabolic profiles were changed systematically by fixing the minimum and maximum Al content and varying the total length (120 nm, 240 nm, 480 nm) of the resulting parabolic QDs. The impact of the different effects of quantum confinement was investigated using polarization-resolved and time-resolved photoluminescence spectroscopy. The results indicate that such PQDs can be used as a model structure for investigating the transition in optical properties from QWR-like to QD-like structures. Two extreme cases in terms of confinement strength were also realized: a thin, lens shaped GaAs QD, and a long (480 nm) AlGaAs QWR as a model structure of infinitely long QWRs. Polarization-resolved measurements show that the QD and the QWR emit in different polarization, aligned perpendicular and mostly parallel to the growth direction, respectively. This is because the low energy states in the valence band (VB) of the QWR are dominated by light hole (LH) components whereas for the QD, the VB states are more heavy hole (HH) -like.

Using the PQDs as a model structure with intermediate confinement between QWRs and thin QDs, we have investigated the impact of the quantum confinement on the optical polarization properties. Using polarization resolved spectroscopy we have analyzed and compared the degree of linear polarization (DOLP) of PQDs of different confinement strength. Whereas these PQDs emit light mostly polarized along the growth direction, like the corresponding QWRs, the characteristics of their DOLP spectra are more complex. Supplementing the experimental results with detailed numerical modelling, we show that the features of the DOLP spectra depend on valence band mixing, broadening of individual transitions and state filling effects. We have also demonstrated a method for extracting the occupation numbers, the exciton effective temperature and the Fermi levels in these structures, and observed multiexcitonic states in the emission spectra.

MOVPE in inverted pyramids provides nanostructure engineering possibilities with fine control of the confinement geometry and thus the polarization of the emitted photons. We identified several geometries in which fine tuning of the geometry can yield switching from HH-like and LH-like transitions. In particular, single QDs of different aspect ratios, QD molecules of different barrier structures, and several QD superlattice systems were investigated numerically. In addition, the impact of an external electric field on the VB states of such system structurally tuned near the switching point was studied theoretically. The results demonstrate that dynamic switching of polarization can be achieved with electric fields, and first step towards experimental implementation using Schottky diodes are presented.

In conclusion, in this work we show that MOVPE in inverted pyramids provides possibilities to grow a large variety of quantum nanostructures with high structural accuracy. Control of the confinement geometry was used as a basis for controlling the polarization state of the emitted light. The knowledge obtained in this work should be useful for the fabrication of future polarization-controlled single photon devices.

Keywords

Nanophotonics, nanostructure, semiconductor, AlGaAs, GaAs, MOVPE, quantum wire, quantum dot, exciton, heterostructure, bandgap engineering, photoluminescence, effective mass approximation, valance band, conduction band, Luttinger Hamiltonian, heavy hole, light hole, quantum confinement, photoluminescence, time-resolved photoluminescence, localization, carrier relaxation, radiative recombination, site control, quantum dot molecule, polarization-resolved photoluminescence, state hybridization, Stark effect.

Résumé

Les nanostructures semi-conductrices constituent un formidable domaine de recherche par la variété des applications possibles et déjà utilisables. Aujourd'hui, l'utilisation de ces nanostructures couvre un très large domaine allant de la recherche fondamentale jusqu'à une multitude d'applications technologiques, par exemple dans les domaines des télécommunications, des ordinateurs quantiques et des biosenseurs. Ainsi, des générateurs de nombres aléatoires, basés sur les propriétés quantiques des nanostructures semiconductrices sont déjà disponibles sur le marché. Bientôt, des puces contenant des dispositifs intégrants des circuits nanophotoniques seront disponibles, offrant une vitesse d'opération supérieure à celle des dispositifs électroniques semiconducteurs traditionnels.

Cette thèse couvre les aspects de sciences des matériaux et de photoniques de ce chapitre de la nanophysique. Elle traite plus particulièrement des fils et des boîtes quantiques (QWRs et QDs), qui constituent une famille de nanostructures ayant une grande importance pour les applications futures dans ce domaine. Bien que de substantiels progrès aient été faits dans ce domaine, la fabrication reproductible de ces nanostructures reste difficile, et cette thèse s'intéresse à certains des problèmes qu'elle soulève.

Nous réalisons l'Epitaxie en Phase Vapeur à partir d'Organométalliques (MOVPE) sur des substrats dont la surface est gravée de réseaux de pyramides inversées, conçus pour créer des boîtes et des fils quantiques GaAs/AlGaAs. Comparée à d'autres méthodes de fabrication, notre technique présente un avantage significatif par le contrôle très précis de la position, de la taille et de la composition des matériaux le long de la direction de croissance, permettant ainsi le contrôle du potentiel et de la longueur d'onde d'émission de la nanostructure. Nous pouvons ainsi fabriquer une gamme entière de nanostructures à une ou zéro dimension (1D ou 0D, respectivement). Comme elles sont incluses dans la matrice GaAs du substrat, nos nanostructures peuvent peuvent être intégrées dans des circuits photoniques semiconducteurs.

Nous avons concentré nos efforts sur la modulation du taux d'aluminium (Al) le long de la direction de croissance, modifiant de ce fait le potentiel le long d'un fil quantique vertical. Nous avons ainsi réalisé des boîtes quantiques confinées dans des profils de potentiel paraboliques avec trois différents gradients. Nous avons fait varier les valeurs minimales et maximales d'Al et la longueur totale des boîtes quantiques paraboliques résultantes (120 nm, 240 nm et 480 nm). L'impact des différents confinements quantiques a été étudié en utilisant la spectroscopie de photoluminescence résolue en polarisation et en temps. Les résultats obtenus montrent que de telles boîtes quantiques paraboliques peuvent par leur structure servir de modèles pour l'étude des propriétés optiques de la transition nanostructure de type « fil » à nanostructure de type « boîte ».

Deux cas extrêmes en termes d'amplitude de confinement ont été réalisés : une boîte « mince » en forme de croissant et un fil « long » (480nm) en $Al_{0.2}Ga_{0.8}As$ servant de modèle pour un fil infiniment long. Les mesures résolues en polarisation montrent que la boîte et le fil émettent selon des polarisations différentes - perpendiculairement et parallèlement à la direction de croissance, respectivement. En effet, dans la bande de valence du fil quantique, les états de basse énergie sont dominés par des composantes de type « trous légers » (LH) alors que dans la bande de valence de la boîte quantique, les états d'énergie sont plutôt de type « trous lourds » (HH).

En utilisant les boites quantiques paraboliques comme modèles de confinement intermédiaire entre les boîtes « minces » et les fils, nous avons étudié l'impact du confinement quantique sur les propriétés de la polarisation optique. Grâce à la spectroscopie résolue en polarisation, nous avons analysé et comparé les degrés de polarisation linéaire (DOLP) de boites quantiques paraboliques avec des confinements d'amplitudes différentes.

Alors que les boites quantiques paraboliques émettent de la lumière principalement polarisée suivant la direction de croissance, comme les fils correspondants, leur DOLP présente des caractéristiques plus complexes.

Une modélisation numérique détaillée des résultats expérimentaux montre que les caractéristiques spectrales de la DOLP dépendent du mélange de la bande de valence, de l'élargissement des transitions individuelles et d'effets de remplissage d'états d'énergie.

Nous avons aussi mis au point une méthode pour extraire les degrés d'occupation, la température effective de l'exciton et les niveaux de Fermi dans ces structures, et avons observé des états multi-excitoniques dans les spectres d'émission.

La croissance par MOVPE sur des réseaux de pyramides inversées offre des possibilités d'ingénierie de nanostructures et un contrôle fin sur la géometrie de confinement et donc sur la polarisation des photons émis.

Nous avons identifié plusieurs géométries dans lesquelles un fin ajustement des dimensions provoquait une commutation entre transitions de type HH et de type LH. En particulier, des boîtes quantiques uniques avec différents rapports hauteur/largeur, des molécule*s* faites d'assemblage de boîtes quantiques avec des barrières de structures différentes et plusieurs systèmes de super-réseaux ont été étudiés numériquement.

De plus, nous avons simulé l'impact d'un champ électrique externe sur les états de bande de valence d'un tel système dont la structure a été ajustée pour que la polarisation de la lumière se trouve près du point de commutation. Les résultats démontrent que cette commutation peut effectivement être obtenue avec des champs électriques, et des premières mises en oeuvre expérimentales utilisant des diodes Schottky on été présentées.

En conclusion, nous montrons dans ce travail que la MOVPE sur des réseaux de pyramides inversées offre des possibilités de croître une grande variété de nanostructures quantiques avec une haute précision structurale. Nous contrôlons l'état de polarisation de la lumière émise grâce à notre maîtrise de la géometrie de confinement. La connaissance acquise dans ce travail devrait être utile pour la fabrication de composants à photons uniques à polarisation contrôlée.

Mots-clés

Nanophotonique, nanostructure, semi-conducteur, AlGaAs, GaAs, MOVPE, fil quantique, boîte quantique, exciton, hétérostructure, ingénierie de la bande interdite, photoluminescence, approximation de la masse effective, bande de valence, bande de conduction, Hamiltonien de Luttinger, trou lourd, trou léger, confinement quantique, photoluminescence, photoluminescence résolue en temps, localisation, relaxation de porteurs, recombinaison radiative, contrôle spatial, molécule à boîtes quantiques, pholuminescence résolue en polarisation, hybridation d'état, Effet Stark.

List of abbreviations

QD : Quantum Dot
QW : Quantum Well
QWR : Quantum Wire
HH : Heavy Hole
LH : Light Hole
MOVPE : Metal-Organic Vapor Phase Epitaxy
VB : Valence Band
CB : Conduction Band
CCD : Charge-Coupled Device
PL : Photoluminecense
PQD : Parabolic Quantum Dot
Al : Aluminium
In : Indium
Ga : Galium
As : Arsenic
EBL : Electron Beam Lithography
DOS : Density Of State
AFM : Atomic Force Microscopy
RIE : Reacting Ion Etching
APD : avalanche photodiode
HBT : Hanbury Brown and Twiss
DOLP : degree of linear polarization
μ-PL : micro-photoluminescence
FWHM : full width at half maximum
MBE : molecular beam epitaxy
PECVD : plasma-enhanced chemical vapor deposition
X : neutral exciton
2X : biexciton
TMGa : trimethylgallium
TEGa : triethylgallium

Contents

Acknowledgments...i

Abstract...ii

Résumé...iv

List of abbreviations...vii

Chapter 1. Introduction to semiconductor nanostructures 1

1.1 Light-matter interaction and nanotechnology 1
1.2 III-V semiconductors...3

1.2.1 III-V semiconductors bulk properties 4
1.2.2 Low-dimensional semiconductor nanostructures...............................6

1.3 Specific low-dimensional III-V nanostructures 9

1.3.1 Quantum wires 9
1.3.2 Quantum dots...11

1.4 Tailored-potential quantum nanostructures 14

1.4.1 Mixed-geometry nanostructures 14
1.4.2 Quantum nanostructures formed in inverted pyramids.........................15

1.5 Thesis goal and outline...19

Chapter 2. Band Structure and Optical Transitions in Pyramidal Quantum Nanostructures 22

2.1 Hamiltonian formulation 22

2.1.1 From general Hamiltonian to k.p approximation.................................22
2.1.2 Lowdin's Perturbation: beyond simple k.p.......................................24
2.1.3 Effect of low dimensionality on conduction band structure.....................29
2.1.4 Effect of low dimensionality on valence band structure 30

2.2 Optical transitions...34

2.2.1 Charge carrier-photon interaction 34
2.2.2 Valence band mixing and light polarization.....................................35

2.3 Excitons..........36

2.3.1 General concept of excitons 36
2.3.2 Excitons in low-dimensional structures..........38

2.4 Numerical simulation 40

2.4.1 Modelling of pyramidal nanostructures 40
2.4.2 Example of simulation results..........44

2.5 Summary 46

Chapter 3. Fabrication and characterization of pyramidal quantum nanostructures..........47

3.1 Fabrication of pyramidal heterostructures 47

3.1.1 Substrate patterning 47
3.1.2 MOVPE growth..........49
3.1.3 Post-growth processing..........51

3.2 Fabrication tools and techniques..........54

3.2.1 Fabrication tools..........54
3.2.2 Polarization-resolved photoluminescence spectroscopy..........56
3.2.3 Time-resolved photoluminescence 58

3.3 Summary 60

Chapter 4. Transition from 2D to 3D Quantum Confinement Studied in Pyramidal Nanostructures..........61

4.1 Fabricated structures..........61

4.1.1 Design and fabrication..........61
4.1.2 Structural features 62
4.1.3 Spectral analysis of the pyramidal nanostructures 63

4.2 Finite-length quantum wire 65

4.2.1 Modeling of QWR system 65

4.2.1.1 Band structure..........65
4.2.1.2 Optical spectra 66

4.2.2 QWR structure – Experimental results 67

4.2.2.1 Power-dependent PL spectra..........67
4.2.2.2 Time-resolved PL measurements..........68

4.2.3 QWR structure: summary 69

4.3 "Thin" quantum dot 70

4.3.1 Modelling of the quantum dot system 70

4.3.1.1 Band structure and wavefunctions 71
4.3.1.2 Optical spectra 72

4.3.2 Experimental results – "thin" QD structure..73

4.3.2.1 Power-dependent PL spectra..73
4.3.2.2 Time-resolved PL measurements..74

4.3.3 Summary: comparison of QD and QWR systems 74

4.4 Parabolically-shaped quantum dot..75

4.4.1 Parabolic potential modeling: evolution with confinement..75

4.4.1.1 Band structure and optical spectra..76

120 nm parabolically shaped QD 76
240 nm parabolically shaped QD 79
480 nm parabolically shaped QD 82

4.4.2 Experimental results 84

4.4.2.1 Power-dependent PL spectra..85
4.4.2.2 Carrier relaxation dynamics..86

4.4.3 Discussion..90

4.5 Summary..92

Chapter 5. Valence band mixing and emission polarization of tailored-potential quantum dots 93

5.1 Measurement of emission polarization in pyramidal nanostructures..93

5.2 Emission polarization of 480nm-QWR 97

5.3 Emission polarization of thin QDs 98

5.4 Emission polarization of parabolic QDs 99

5.4.1 120 nm-PQD..100
5.4.2 240 nm-PQD 102
5.4.3 480 nm-PQD 105

5.5 Effective carriers temperature and Fermi level……………………..........................106
5.6 Effects of VB mixing, broadening and state occupation ……………………………108
5.7 Summary ..…………………………………………………………………….…114

Chapter 6. Control of emission polarization of quantum nanostructures…………….....115

6.1 Dynamic control of QD optical properties….…………………………………..……115

6.2 Single QD polarization control ……………………………………………..……116

6.2.1 Polarization control via structural parameters……………………………..116
6.2.2 Polarization control via external electric field……………………………..118

6.3 QD molecule ………………..…………………………………..………………..120

6.3.1 Formulation of QD coupling ……………………………………………..120
6.3.2 Polarization control by barrier adjustment ………………………………..121
6.3.3 Polarization control via external electric field……………………….………123

6.4 QD superlattices in inverted pyramids ……………………………………………..124

6.4.1 Miniband formation in pyramidal QD superlatticces ……………………..125
6.4.2 Effect of electric field on QD superlattice properties …………………..……128

6.5 Summary ………………………………………………………………………133

Chapter 7. Conclusions and outlook…………………………………….……………..134

7.1 Conclusion ………….……………………………………….…..……………134

7.2 Future directions ……………………………………………..….……………137

Appendix A. Fabrication process flow ………………………………………..…………138

Appendix B. MOVPE growth parameters ……………………………………….…………141

Appendix C. Wavefunctions in pyramidal nanostructures……………………….…………144

References ……………………………………………………………………..…………150

Publications and conference contribution…………………….……………………………162

CV Mikhail Lazarev………………………………………………………………………..163

Chapter 1

Introduction to semiconductor nanostructures

In this Chapter, we introduce the reader to the general concepts related to low-dimensional semiconductor heterostructures and the impact of dimensionality on their optical properties. We start with general aspects of light-matter interaction and nanotechnology (Section 1.1). In Section 1.2 we introduce semiconductor nanostructures, in particular low-dimensional nanostructures and the impact of dimensionality on their band structure. Section 1.3 is dedicated to a review of specific quantum wire and quantum dot nanostructures realized in different experiments. Finally, in section 1.4 presents more complex nanostructure systems, in particular the pyramidal systems investigated in this thesis.

1.1 Light-matter interaction and nanotechnology

The story of nanoscience started in the past century, a “golden” century for physics, which led to great advances that humanity now enjoys. In the first part of the 20th century, the fundamental breakthrough of explaining the nature of light and matter happened. The discovery of quantum mechanics and especially the quantum nature of light and matter led to a fundamental review of nature understanding. Albert Einstein got his Nobel prize for the explanation of the photoelectric effect as due to the quantum nature of light. In parallel, many other fundamental theoretical and experimental works were done such as the demonstration of wave properties of ordinary matter like electrons [1] and other fundamental particles. The term nano comes from the size of interest that is measured in nanometers (1 nm = 10^{-9} m); at this scale quantum physics plays an important role and particles can no more be described by classical mechanics. Hence, the terms *nanoscience* or *nanotechnology* are applicable to describe phenomena and techniques relevent for structures of sub-μm scale. In the second part of the 20th century, with the development of new technological tools, it became possible to use quantum properties of matter for applications. Today, nanotechnology is an extensive industry with new products that we all use in everyday life.

Indeed, humanity started to use nanoscale objects long time ago. A good example is Roman glasses [2], in which metal nanoparticles are used to give color to glass for use, e.g., in cathedrals and churches. Depending on the nanoparticle size, they can efficiently diffract/absorb light of particular wavelengths due to so-called plasmonic resonance. Of course, the Romans did not know all of that but used the effects empirically. Nanoscience is also “used” by nature for different

purposes, maybe the most famous example is the color of butterfly wings. The special nanostructures there scatter the light of a specific wavelength, which gives the beautiful colored picture on the wings [3]. A Swiss symbol, the edelweiss flower, is another example; the flower is adapted to extreme UV radiation at high altitudes by having filaments on leaves with a regular nanostructure on them [4].

As opposed to the natural nanostructures introduced in the previous paragraph, nanotechnology is a part of nanoscience that studies artificial ones. The rise of nanotechnology began with the development of microtechnology, which started from inventing of the transistor by Bardeen, Brattain and Schokly [5] and the integrated circuits by Kilby [6] in the 1950's. Transistors are the basic devices of modern computers; with time the transistor size decreased, and computers computation power increased according to Moore's law [7]. This would not be possible without understanding the physics of semiconductors [8] and the constant development and improvement of fabrication tools. Manipulation of matter on the microscale gave rise to a lot of other kinds of devices such as semiconductor lasers [9], solar cells [10], light emitting diodes (LEDs) [11] etc. [8]. Device miniaturisation led by technological progress and demands pushed the scale size from micrometers to nanometers. The realization of nanostructures became possible due to development of new fabrication techniques like electron-beam lithography, which allows fabricating structures with nm precision. New material deposition techniques such as molecular beam epitaxy (MBE) [12] and metal organic vapor phase epitaxy (MOVPE) [13] used for growth of high-quality heterostructures with nanometer precision, and techniques related to scanning tunneling microscopy (STM), make it possible to manipulate matter even at the single atom level [14]. The semiconductor nanostructures studies motivated the rise of new applications and the discovery of new materials such as graphene [15][16].

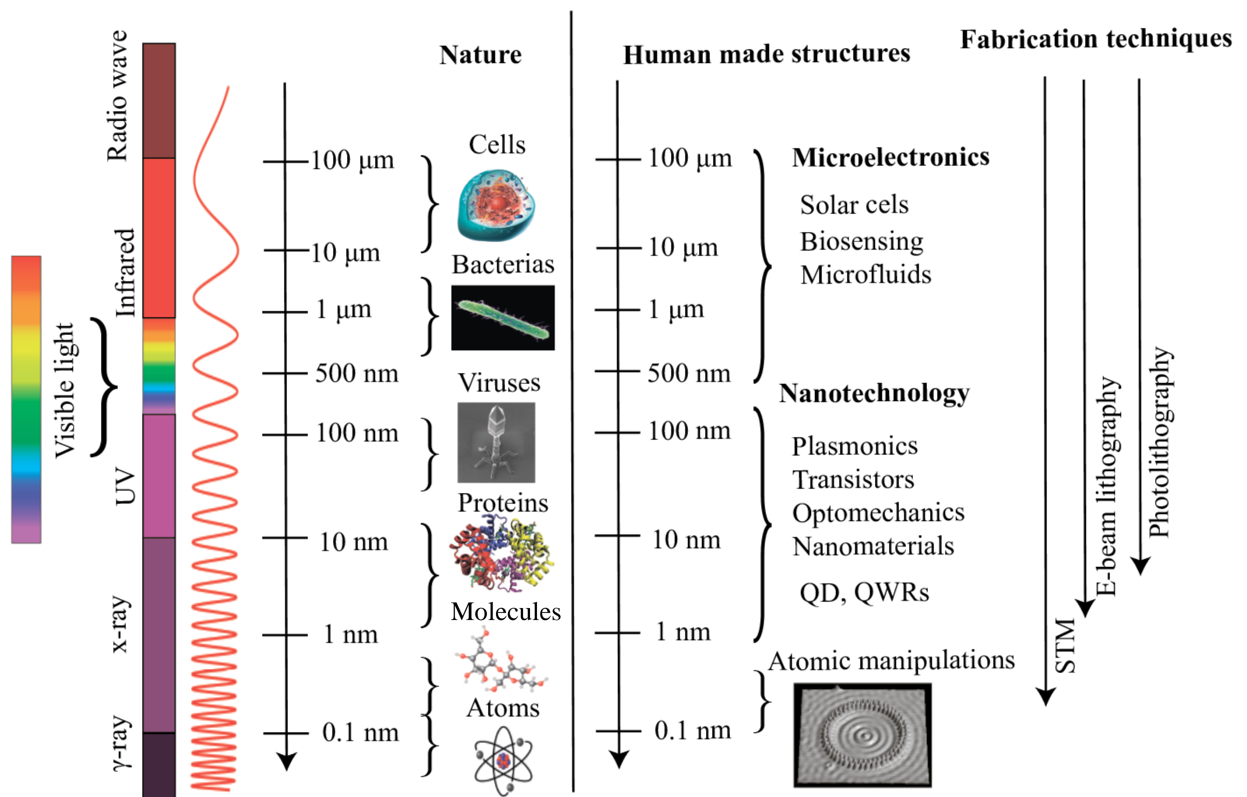

Figure 1.1 The nanoscale: natural and artificial nano-objects, compared with electromagnetic wavelengths and scales covered by fabrication techniques.

In figure 1.1 we present a size comparison between the wavelength of electrmoagnetic waves, natural micro and nano-objects (left side) such as bacteria, and proteins, artificial nano-objects (right side), and main fabrication tools that allow to operate in such scales. Modern nanotechnology allows to fabricate nanostructures in all size scales down to the atomic one, which makes them applicable to disciplines such as biology, chemistry and many others. A good example is plasmonic nanostructures [17] that permit the manipulation of light on a subwavelength scale, with numerous applications in imaging [18], biosensing [19][20][21] and lasing [22][23] at the nanoscale. The ability to achieve tight light focusing is useful for fundamental reserch [24][25][26], as well as in many applications [27][28][29]. This year (2018) the Nobel physics prize in physics was given for laser tweezers, a related technique [30]. Nowadays, demands for electronic device miniaturization and higher perfomance are challenging tasks, which pushes researchers to discover new matherials that may open new technology perspectives. Size reduction of electronic device size to the nanoscale faces problems like heating and the limit of classical beahvior. Already now the transistor size is so small that the quantum nature of matter is becoming more crucial. To overcome these problems, new breakthroughs are needed, and in the last decades nanophotonics was proposed as a possible direction. Active research goes in the direction of creating quantum computers [31]. The exact nature of the future quantum computers is still unknown, due to several factors that complicate their development such as low working temperature and quantum decoherence. Nevertheless, major companies like Intel, IBM [32] and Google already built quantum computers, based on the Josephson tunneling effect, with 40-50

qubits, the quantum analogs of bits. Recently [33], a record of quantum computer made of 51 qubits using cold atoms trapped in optical cavities was reported. Although such computers are useful for solving only specific problems, using these computers researchers already predicted several effects that would not be possible to calculate with conventional computers [33]. To avoid energy losses and reduce heating, the idea to use photons as carriers of information and photonic circuits for information processing has emerged; this is also relevant to quantum communication [34]. Possible efficient single photon sources in such quantum photonic circuits are semiconductor heterostructures such as quantum dots (QDs), also called "artificial atoms". QDs are also one possible candidate for the realization of a qubit in solids [31]. Besides, QDs have already now industrial applications, for example for next generation LEDs [35][36][37] and lasers [38][39]. Applications of QDs are not only sought in electronics; another example is the use of QDs as unique markers for biological applications [40] [41]. In this context, the ability to tune the QD properties via their shape and size is significant.

1.2 III-V semiconductors

III-V semiconductors, i.e., binary compounds composed of group III and group V elements of the periodic table, allow constructing heterostructures with nm features, making them useful for studying effects of low dimensionality on light-matter interaction. In this section we present a brief review of III-V semiconductors compound bulk and heterostructures properties.

1.2.1 III-V semiconductors bulk properties

In contrast to atoms in semiconductor crystals, electron wavefunctions are spatially delocalized in the periodic potential of the crystal lattice induced by the atom nuclei [42]. Usually, the crystal lattice is neutral, so the movement of an electron gives birth to a missing electron (hole) with opposite charge. It can be shown analytically that in a bulk semiconductor electrons and holes have a different band structure and dispersion curves, with corresponding conduction band (CB) and valence band (VB) (See Chapter 2). The energy difference between the minimums of CB and maximum of VB is called the bandgap. The bandgap is a fundamental characteristic parameter of the semiconductor. The bandgap size mainly depends on two parameters: material composition and crystal structure. In figure 1.2 we present different semiconductors with respect to the lattice constant and bandgap size. The curves in figure 1.2 show the same parameters for the respective alloys.

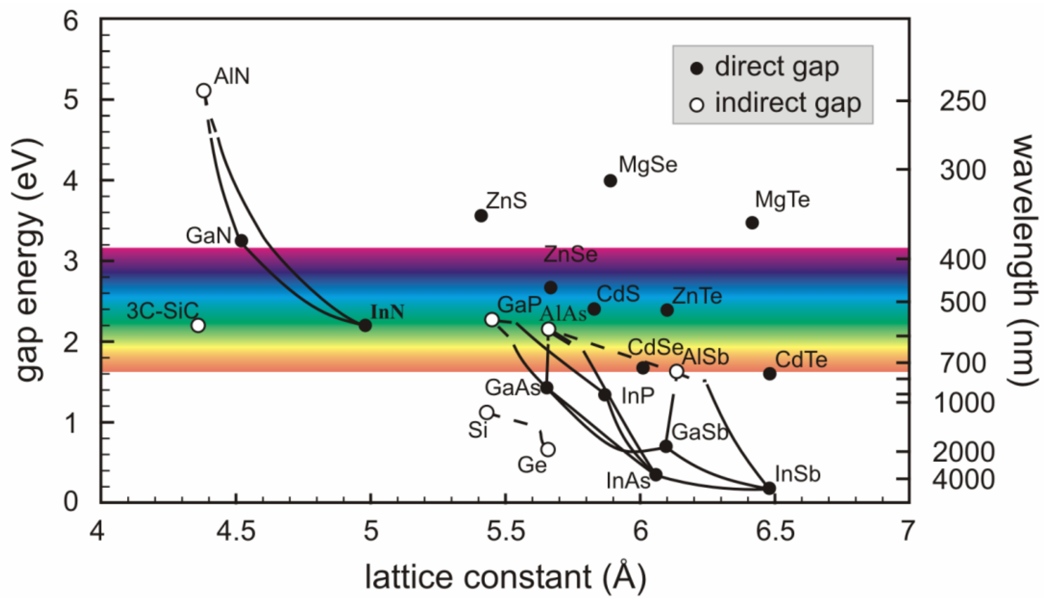

Figure 1.2. Semiconductors band gaps versus lattice constants. Adopted from [43]

Semiconductors can be of two different kinds, depending on their band structure. If the electrons and holes have minimum energy at the same k vector, the semiconductor is called a *direct bandgap semiconductor*, otherwise the semiconductor has *indirect bandgap*. Black and white circles in figure 1.2 correspond to materials with these different bandgap types. Examples of such typical band structures are presented in figure 1.3 for GaAs and Si. Indeed, the carrier dispersion curves are more complicated than just single electron and hole bands. The VB consists of two holes types, “light” and “heavy”, depending on the corresponding effective masses, and the so-called split off (SO) band. More details on the band structure of GaAs will be presented in Chapter 2 of this thesis.

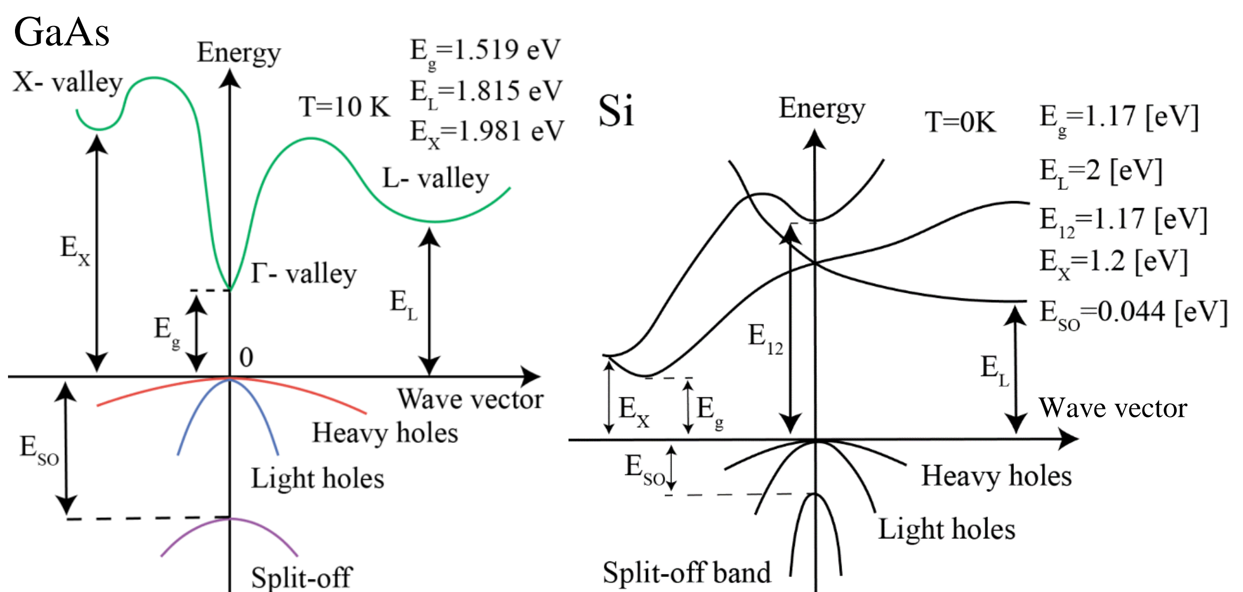

Figure 1.3. Band structures of GaAs and Si.

Both these semiconductors are very popular in optics (GaAs) and electronics (Si) applications. The crystal structure of Si is face-centered diamond cubic lattice. In this thesis, we focus on GaAs and its alloys with AlAs, both of which have zincblende crystal structure with a diatomic base. The unit cell of the GaAs crystal is presented in figure 1.4 (a), where red and blue colors mark As and Ga atoms, respectively.

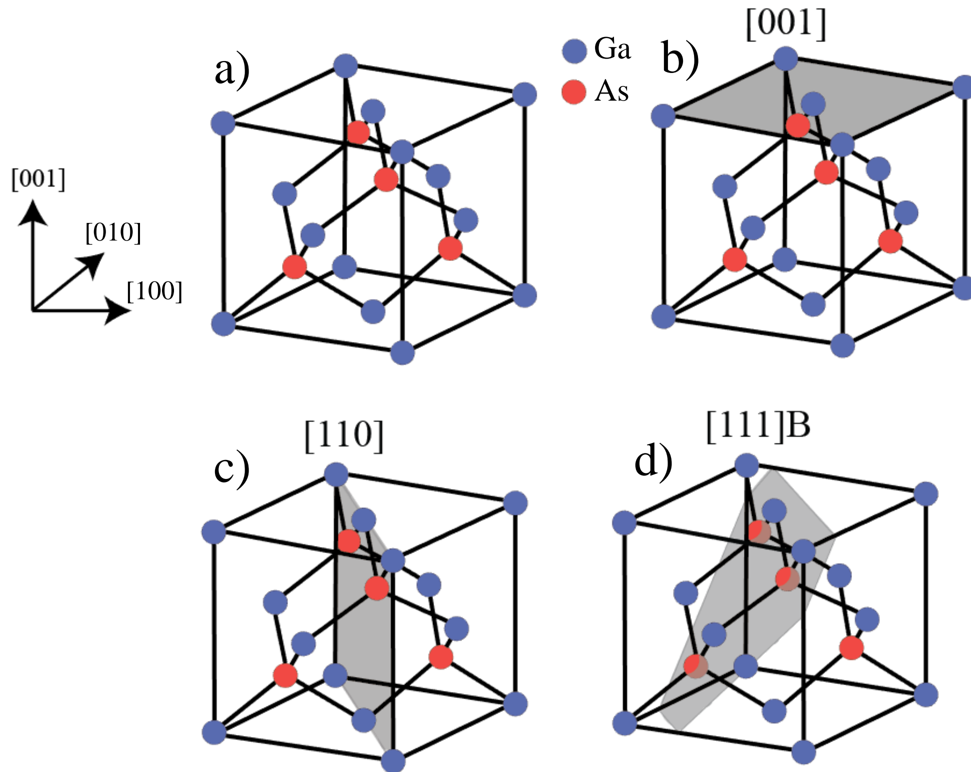

Figure 1.4. GaAs crystal structure and essential crystal planes.

The zincblende crystal structure has three important crystallographic directions: [001], [110] and [111] as illustrated in figure 1.4 (b)-(d). All three planes have an important role in different fabrication processes. For example, epitaxial growth is typically done on (100) planes, cleavage of GaAs usually takes place along the [110] direction. Different etching and growth rates for different planes is a crucial point in this thesis; [111] direction are used in patterning steps and nanostructures growth for this reason. The [111] direction, in case of GaAs, can contain either Ga or As atoms. Thus one distinguishes between (111)A crystallographic planes containing Ga atoms and (111)B planes containing As atoms (see figure 1.4 (d)).In this thesis, we will focus on GaAs and $Al_xGa_{1-x}As$ ($x<0.44$) alloy nanostructures that have direct bandgap, which are very useful as optical materials due to the fast radiative recombination of electrons and holes, as compared to indirect semiconductors or $Al_xGa_{1-x}As$ ($x>0.44$) [44].

1.2.2 Low-dimensional semiconductor nanostructures

Modern optoelectronics owes its appearance to the research of heterostructure systems starting from homo- and hetero- junctions studied in the 1960s [45]. Heterojunctions are contact interfaces between two types of semiconductors with different bandgap size. The heterojunction is a fundamental building block for many devices such as diodes and transistors. A homojunction, on the other hand, is the interface between two semicondusters with the same bandgap size but different doping; a typical example is the Si p-n junction used in diodes. Since the 1960s the semiconductor growth techniques have been significantly improved, which allowed to grow increasingly complex structures. The primary semiconductor growth technologies nowadays are molecular beam epitaxy (MBE) [12] and metalorganic vapor phase epitaxy (MOVPE) [13] that allow growing semiconductors with monolayer precision. Variation of the material composition during the growth creates heterostructures on the sample surface; the simplest example is heterostructures that consist of one thin semiconductor layer sandwiched in between another semiconductor with a larger bandgap; for sufficiently thin core layer, such heterostructures are called quantum wells (QWs). The use of such heterostructures was successfully implemented in double heterostructure laser diodes by Z. I. Alferov [46]. High quality heterostructure growth requires low difference in lattice constant of the semiconductors involved. For that purpose, the AlGaAs alloy is a good candidate due to the small difference of GaAs (0.565 nm) and AlAs (0.566 nm) lattice constants. This makes AlGaAs nanostructures strain free, in opposite to InGaAs/GaAs ones where the InAs lattice constant is about 0.606 nm, which induces strain.

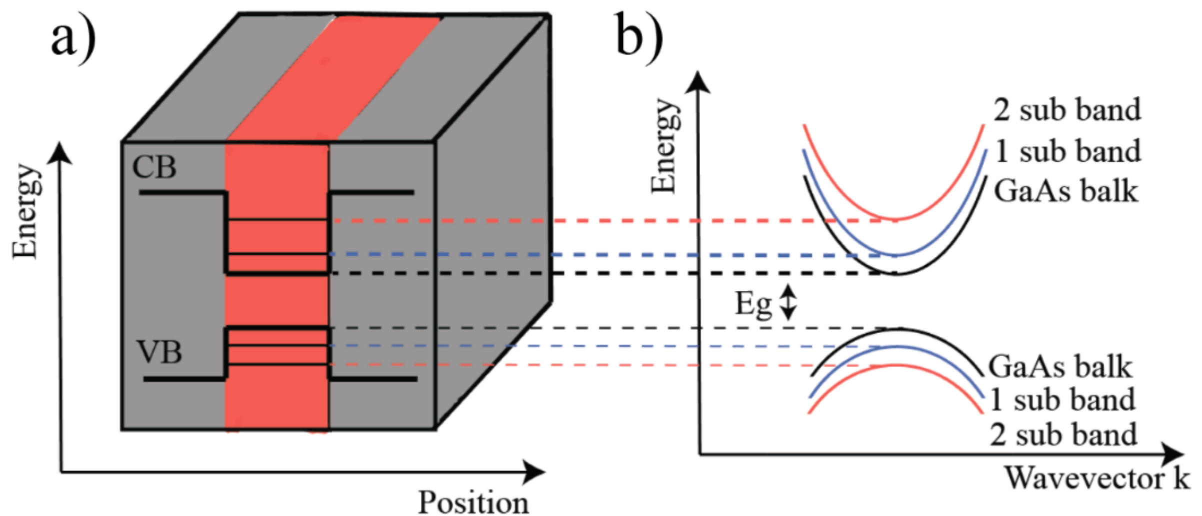

Figure 1.5. Quantum well band structure a) in real space; b) in k-space.

One way of tailoring light-matter interaction in semiconductors is the construction of semiconductor heterostructures of different degrees of quantum confinement. This can be done by fabrication of heterostructures layer systems of different bandgap size and/or by variation of

confinement dimensions at the nanoscale. The resulting nanostructures have specific band structure of charge carriers, which, in turn, impacts their transport and optical properties.

Reducing the heterostructure size in one dimension, comparable to the De Broglie electron wavelength (in bulk material), leads to quantum effects and states energy splitting. An example, shown in figure 1.5, is that of quantum wells (QWs). In a simple approximation, the electron states structure can be obtained by solving the Schrodinger equation with a rectangular potential well. Changing the potential profile in one direction leads to different states structure and optical emission wavelengths; such flexibility is beneficial for applications in optics [47][48][49]. Reduced dimensionality dramatically changes transport and optical properties of the nanostructure; for example, decreasing the threshold currents in diode lasers [50].

A key characteristic of the nanostructure is the density of states (DOS) functions. Figure 1.6 schematically shows the DOS for bulk and quantum confined semiconductors. In case of an ideal QW with rectangular potential profile, the energy spectra and DOS for electrons are:

$$E_{2D,l}(k_x,k_y)=\frac{\hbar^2\pi^2 l^2}{2m^* L_z^2}+\frac{\hbar^2\left(k_x^2+k_y^2\right)}{2m^*}\quad l=1,2,3\ldots$$

$$\rho_{2D}(E)=\frac{2m^*}{\pi\hbar^2 L_z}\sum_l \Theta\left(E-E_{2D,l}(k=0)\right)$$

Where L_z is QW width, l state number, m* effective electron mass, k_x and k_y electron **k** vector projections, E energy measured from the band edge, and Θ the Heaviside function ($\Theta = 0$ for $x < 0$; $\Theta = 1$ for $x \geq 0$).

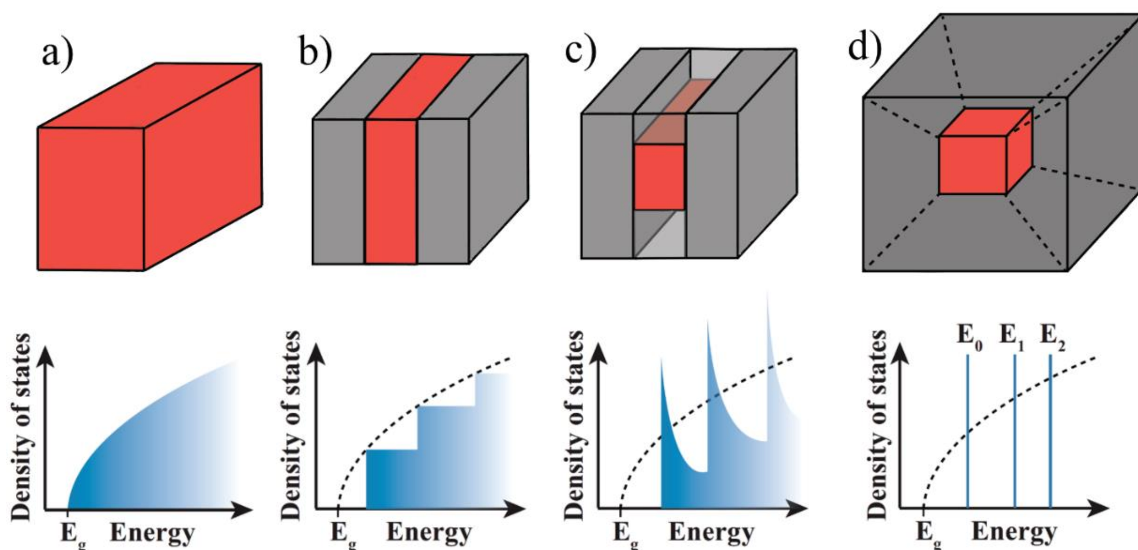

Figure 1.6. Schematic structure (top) and density of states (bottom) of (a) bulk (b) quantume well (QW), c) quantum wire (QWR) and (d) quantum dot (QD) semiconductors. DOS graphics are adopted from [51].

Reducing QW dimensionality in one more direction, we confine carriers in two directions and let them be free only in one direction. Such systems are called quantum wires (QWRs). In this case the corresponding energy and electron DOS expressions are

$$E_{1D,l,m}(k_y) = \frac{\hbar^2\pi^2}{2m^*}\left(\frac{l^2}{L_z^2} + \frac{m^2}{L_x^2}\right) + \frac{\hbar^2 k_y^2}{2m^*} \quad l,\ m=1,\ 2,\ 3\ldots$$

$$\rho_{1D}(E) = \frac{\left(2m^*\right)^{\frac{1}{2}}}{\pi\hbar^2 L_z L_x}\sum_{l,m}\left(E - E_{1D,l,m}(k=0)\right)^{\frac{1}{2}}$$

Further dimensionality reduction brings us to the ultimate quantum nanostructure type, where charged carriers are confined in all three directions like free electrons in atoms, called the quantum dot (QD). In this case the spectra consist of discrete states, the corresponded electron energies and DOS are:

$$E_{0D,l,m,n} = \frac{\hbar^2\pi^2}{2m^*}\left(\frac{l^2}{L_z^2} + \frac{m^2}{L_x^2} + \frac{n^2}{L_y^2}\right) \quad l,\ m,\ n=1,\ 2,\ 3\ldots$$

$$\rho_{0D}(E) = \frac{2}{L_z L_y L_x}\sum_{l,m,n}\delta\left(E - E_{0D,l,m,n}(k=0)\right)$$

In atoms, electrons are confined by the Coulomb force induced by the nuclei, which results in a specific energy structure. In the case of QD nanostructures, 3D confinement is a result of the heterostructure environment. Hence, low dimensional systems are susceptible to their environment. This requires the fabrication of high-quality nanostructures with high purity and excellent interface quality, which makes the fabrication process challenging.

1.3 Specific low-dimensional III-V nanostructures

The first low dimensional nanostructure QWs has been demonstrated in 1960th QW. Since then, material quality and techniques of 2D nanostructures have been significantly improved; the main techniques of growth of high-quality QWs are MOVPE and MBE. QWs have wide applications, for example in solar cells [49], LEDs [48], photodetectors [52] and lasers [50]. Decreasing the dimensionality of a nanostructure, i.e., increasing the number of quantum confinement directions, leads to dramatic changes in light-meter interactions and carrier properties. In this section, we will present examples of experimental, QWR and QD systems.

1.3.1 Quantum Wires

Fabrication of high-quality QWRs [53] still remains challenging despite recent progress. Here we list the main types of QWR structures and their fabrication methods.

T-shaped QWR. This type of QWR is formed by the crossing two QWs, as shown schematically in figure 1.7 (a). The fabrication process consists of two main parts. The first step is to grow a QW in an MBE chamber; next step is cleaving the sample in high vacuum; and finally another QW is grown on the exposed cleaved surface [54]. This method has a number of disadvantages: complicated technology, weak confinement. and limited design flexibility [55]

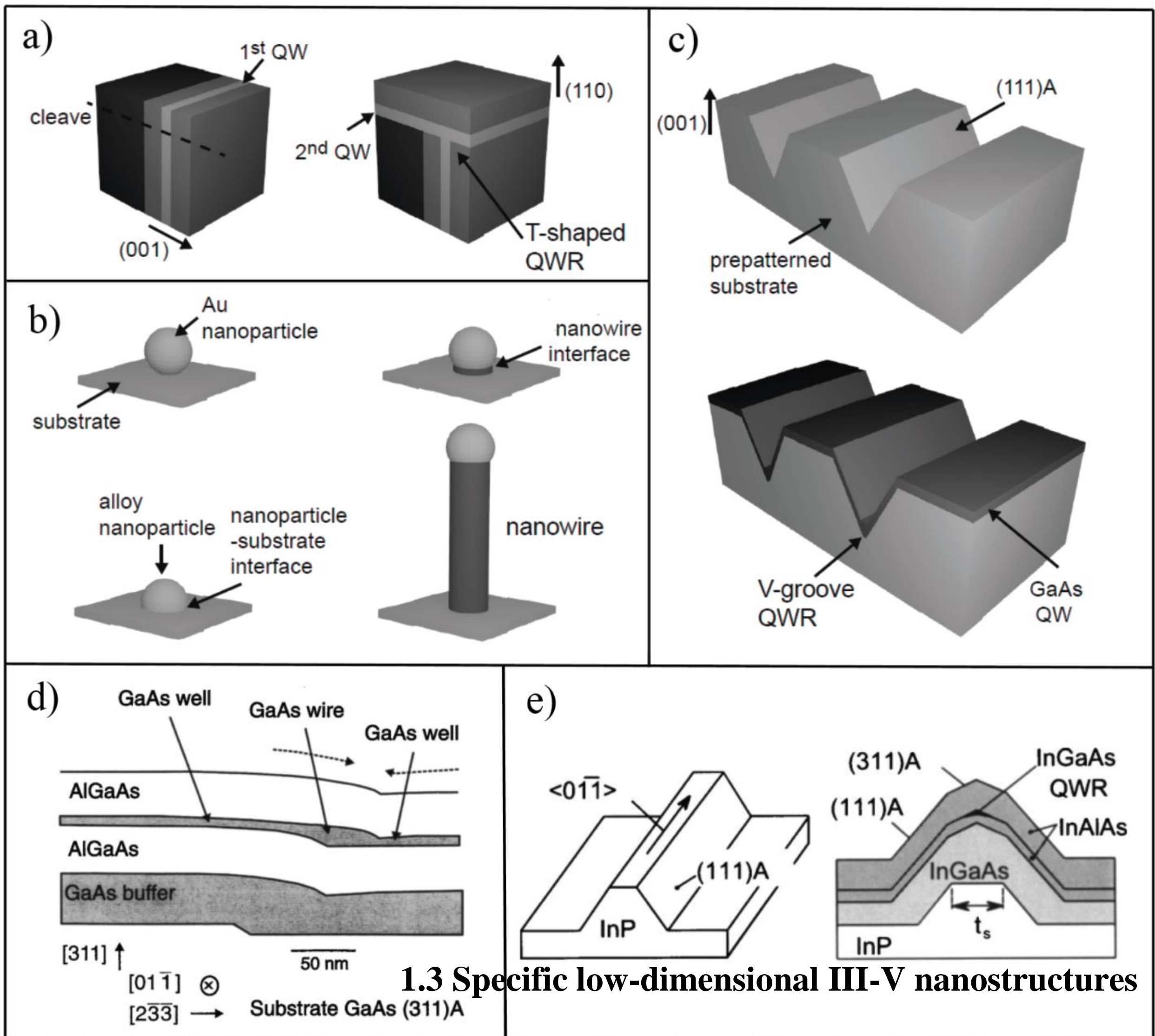

Figure 1.7. Schematic illustration of different QWR systems and their fabrication methods. a) T-shaped QWR b) Nanowire growth process on gold nanoparticle c) V-groove QWR on V-shaped pattern. (a-c) adopted from [56]. *d) Schematic picture of QWR formation on side walls* [53], *e) Ridge-type QWRs* [53]

Nanowires. Semiconductor nanowires are extremely popular nowadays, and many fabrication techniques have been developed in this area. These include top-down or bottom-up approaches [57][58], from self-organized [59][58] to site-controlled [60][58] growth by MBE [61][58] or MOVPE [60] [62][58]. The idea was first introduced almost 50 years ago by Wagner et al. in [63]. The nanowire formation mechanism, the so-called "vapor-liquid-solid" mechanism, is illustrated in figure 1.7 (b) that shows one example of bottom-up nanowire formation. The first step is Au or Ag droplet formation on the substrate, the metal droplet acting in this process as growth catalyst. The second step is the growth of the semiconductor nanowire by MOVPE or MBE. Among the wide variety of growth techniques, the size and geometry of the nanowire can be very different. The nanowire height can be more than few μm [58] with different widths; it has been shown that lateral quantum confinement as in a QWR can be achieved at nanowire diameters of 20 nm [64]. Generaly speaking, nanowires are a very attractive fabrication plarform for realization of nanostructures of different kinds. The wide variety of nanowires types also provides much flexibility for different applications in photonics [65][66][67][68][69].

QWRs grown on patterned surfaces. Generally speaking, this method consists of few steps including lithography, etching, and regrowth by MOVPE or MBE. One particular example is illustrated in figure 1.7 (c), where the substrate is patterned by V-shaped channels [70]. The V-shaped pattern made on a (001) GaAs substrate is composed of two {111}A crystal facets, exposed after selective wet chemical etching. The second part of figure 1.7 (c) presents the same sample after the self-ordered MOVPE growth. The nature of the self-ordered growth will be further explained below (see figure 1.10).

There are also many other related non-planar growth techniques, like QWRs made on side walls [71], ridge-type QWRs [72], and QWRs based on multiatomic and monoatomic steps [53]. QWRs grown on sidewalls are presented in figure 1.7 (d); the QWR growth is initiated by the presence of sidewalls of shallow mesa structure on the sample surface with height small enough to confine charge carriers (few nanometers). Similar ideas are realized in QWRs based on multiatomic steps, due to segregation processes and the attachment rates of adatoms on different parts of the steps. Figure 1.7 (e) illustrates the ridge-type InGaAs/InP QWR growth by MBE. A problem with this method is a significant spatial variation of In composition, which results from the large difference in diffusion length of the material components [53].

1.3.2 Quantum dots

Three-dimensional quantum confinement is possible in a variety of systems, for example nitrogen-vacancy centers in diamonds [72], that have a number of potential applications [73]. Here we focus on semiconductor QDs, that have already found many applications, such as in photovoltaic devices [41][74], QD displays [37][36], photodetectors [41], a number of applications in biology [40][75], and as sources of non-classical light [76][77][78]. Here we present the main semiconductor QD fabrication approaches.

Colloidal quantum dots are widely used in many research directions [22] and already found their place in applications [79][80][74]. The big advantage of colloidal QDs is their relatively easy way of fabrication. The colloidal QDs are nanocrystals that consist of a core and a shell the size of which can be modified. Thus, by modulation of the quantum confinement one can tune their emission wavelength, as schematically shown in figure 1.8 (a). It has been shown that colloidal QDs are good sources of single photons [81]. Since the discovery of colloidal QDs in the 1980s, their quality has been significantly improved and the family of structures expanded. Unique fabrication procedures allow using colloidal QDs as ink for printing them on surfaces of interest [22]. However, the small size QD core placed close to a low-quality interface causes emission disturbance and undesiarable blinking effects.

QD formation by QW/QWR thickness fluctuations. In ideal QW and QWR nanostructures, charged carriers are confined only in one or two directions, respectively. In real QW/QWRs material fluctuations always take place and can lead to 3D confinement, or formation of QD regions (see figure 1.8 (b)). Examples of such QD formation are demonstrated in [82]. However, this method of QD formation has no control on QD size or positioning.

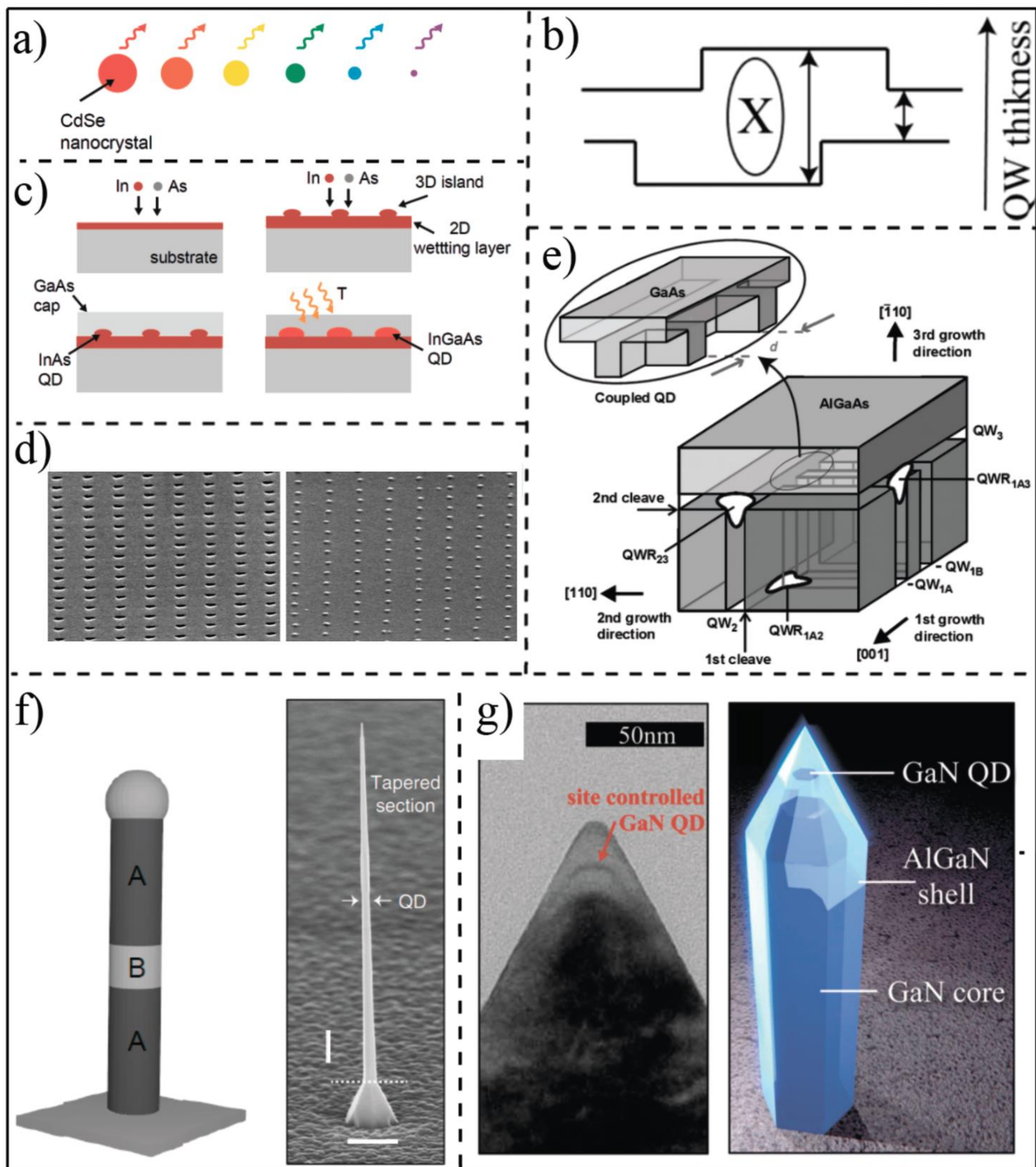

Figure 1.8. Schematic pictures of different QD structures and formation processes. a) Colloidal QDs, adopted from [56] *b) QD formation by quantum well thickness fluctuation (X denotes confined exciton) c) InGaAs QDs formation by Stranski-Krastanow growth method, adopted from* [56] *d) Site-controlled QDs by Stranski-Krastanow growth on a patterned substrate, adopted from* [83] *e) QD formation via the cleaved-edge overgrowth method, adopted from* [84] *f) Schematic illustration of nanowire containing a QD and SEM image of free standing nanowire, adopted from* [85] *g) QD formed on a pyramid tip, adopted from* [76].

Self-assembled QDs. Probably the most popular approach nowadays is the *Stranski Krastanow* growth mode, yielding QDs of high optical quality. Stranski-Krastanow (SK) QDs result from self-organized growth originating from lattice mismatch between the substrate and the QD material. This growth technique was proposed by I. Stranski and L. Von Krastanow in 1939.

Few monolayers, deposited by epitaxial growth, form islands of QDs on the substrate surface by the following mechanism: first, adatoms form a thin layer on the top of the substrate (a wetting layer). Next, adatoms diffuse and form islands to minimize energy due to strain induced by lattice mismatch. Most of the SK QDs are fabricated by MBE, and the most popular material system is InAs/GaAs [86]; figure 1.8 (c) schematically illustrates an example of InGaA/GaAs SK QDs growth. The typical SK QD size is about 5 nm height and 10-20 nm in width. Post-growth processes can modify the QDs size; for example, during rapid thermal annealing process is used after covering the QDs by GaAs cap. SK QDs have high optical quality and show narrow spectral linewidths [87][83], which makes them very useful for integration into photonic cavities [88][89][90][38][91][92][93] or waveguides [94][95] and other photonic devices [77]. However, SK QDs have a disadvantage due to their random position. In addition, due to the self-organized growth mechanism they have broad size distribution that leads to relatively high inhomogeneous spectral broadening. Another self-assembled growth technique is the MBE-based *droplet epitaxy,* which does not require the strain and is used for producing GaAs/AlGaAs QDs [96]. The fabrication process consists of two steps: (i) Ga deposition on the GaAs forms nm-size droplets; (ii) crystallization into GaAs QDs is performed under As beam.

Site controlled SK QDs on a patterned substrate. The lack of position control is a huge disadvantage of self-assembled QDs that, e.g., complicates integration into photonic devices. Many research groups fabricate a large number of ordered cavities or other photonic structures on the same substrate after the SK QDs growth, and search for QD position and spectral match by photoluminescence (PL) spectroscopy. This procedure is highly inefficient, and several groups reported QD position control [83][97][98] that can improve the fabrication process. In figure 1.8 (d), an example of site-controlled QD pattern with 300 nm period is shown [83]. Prior to the MBE growth, the substrates were patterned by electron beam lithography (EBL) with small circles; the circle pattern was then transferred to the substrate and created nanoholes that serve as QD nucleation centers.

QD formation via cleaved-edge overgrowth is a further elaboration of T-shaped QWRs, just with one more cleaving- overgrowth step; the resulting structure is schematically shown in figure 1.8 (e) [84]. In this case, the QD is formed by a crossing of three QWs in one place. The MBE growth technique involved gives fine control over QW thickness and, as a consequence, QD dimensions. This technique also demonstrated the formation of coupled QDs [99].

QDs in nanowires. The fabrication principle of nanowires has been demonstrated in the previous subchapter. The QD formation in nanowires occurs via changing of the material composition during the growth, with different band gaps leading to QD formation inside the nanowire (figure 1.8 (f)). This approach was used with different material systems, such as InAsP/InP [85] or GaAs/GaP [100][101]. Self-assembled QDs in core-shell GaAs/AlGaAs nanowires were reported [102]. GaN QDs in AlN nanowires were also reported; an example is shown in figure 1.8 (g). Site control GaN QDs were shown as candidates for single photon emitters at room temperature [76].

1.4 Tailored-potential quantum nanostructures

Semiconductor quantum wires/dots with tailored heterostructure potential along their axis represent an interesting low-dimensional system, intermediate between one-dimensional (1D) QWRs and 0D quantum dots (QDs). One interest in such systems stems from the possibility it offers for tailoring the degree of quantum confinement of valence band states, which can be used to adjust the admixture between heavy and light hole states and the related optical polarization properties. More generally, it makes possible the realization of a variety of quasi-1D potential charge carrier traps with unique features of carrier interactions and single-photon emission.

1.4.1 Mixed-geometry nanostructures

Nanostructures with mixed dimensionality could combine advantages of QDs and QWRs, but their fabrication is even more challenging than that of QDs or QWR separately. Among the fabrication techniques presented above, only few are suitable for flexible potential tailoring or creation of more complex structures such as quantum dot molecules (QDMs). The cleaved edge overgrowth technique is suited both for QWR and QD fabrication, as well as for the realization of QDMs were the QDs are connected by a QWR [99]. This approach has a significant disadvantage due to its low flexibility in terms of structural design and composition control. Several alternative methods are presented in figure 1.9.

Quantum post systems [103], schematically shown in figure 1.9 (a), consist of vertically-stacked SK InGaAs QDs grown on a GaAs substrate. The distance in between of QDs is such that carriers states are hybridized. In these structures, the first QD layer forms strain pattern on the substrate surface. For thin enough GaAs barriers, the residual strain pattern may be used for aligning the next layer of QDs. Such process can be repeated many times yielding a vertical, quasi-one-dimensional nanostructure as shown in figure 1.9 (a). The resulting quantum posts show width and composition variations along their axis because of fluctuations in the QD structures.

V-groove QWR structures were also explored for modifying the confinement potential along their axis. One way is to use E-beam lithography to modify the substrate pattern geometry [104]. Modification of the V-groove geometry leads to modification of confinement potential as shown in Figure 1.9 (c). But this method does not provide abrupt variations in potential between the different segments of the QWR.

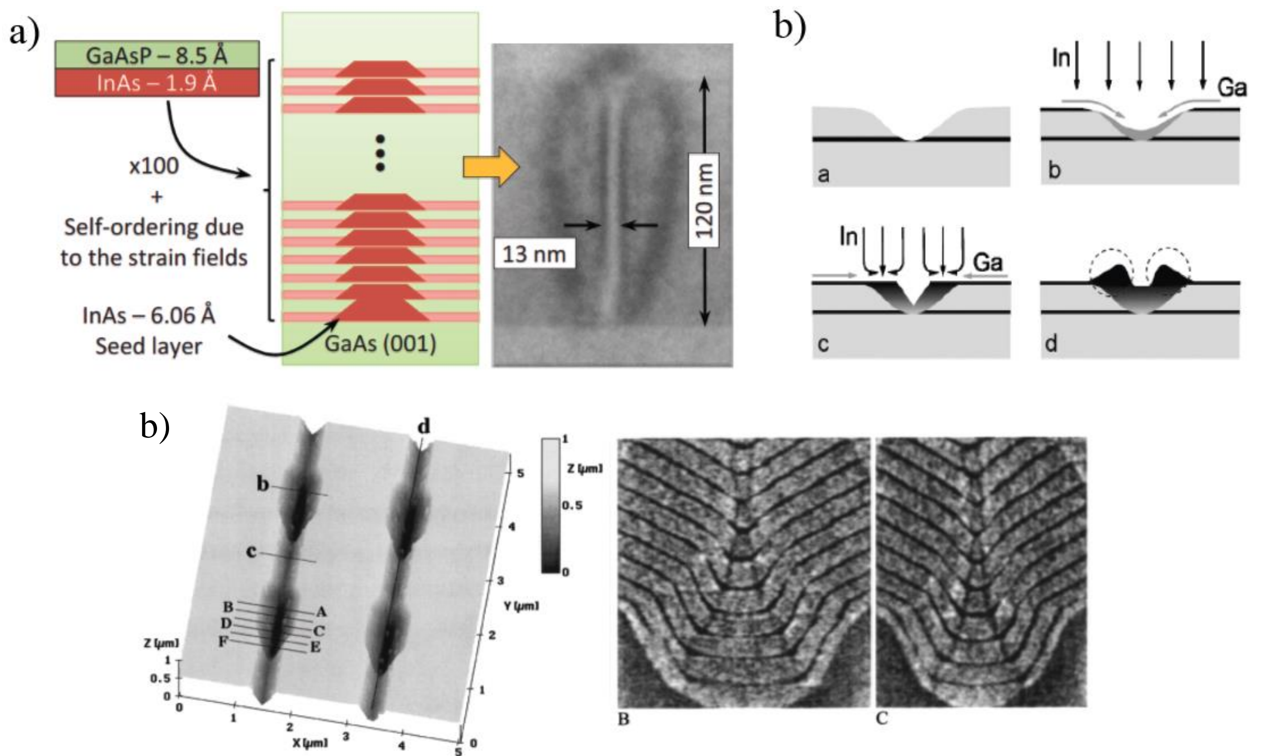

Figure 1.9. Examples of mixed-geometry quantum nanostructures. a) Quantum post structure [103], *b) InGaAs QD molecule example* [105] *c) V-QWR with modulated potential along its axis* [104].

Another promising technique is to use nanowires that have been presented before, by tailoring their composition along their axis during the growth [69]. One particular way to do this is by modulating crystal phase of the nanowire [106][107][108].

1.4.2 Quantum nanostructures formed in inverted pyramids

A major part of this thesis deals with the control of the polarization of light emitted by quantum nanostructures. Most of the reports on the valence band (VB) structure of single QDs and the polarization state of photons they emit rely on self-assembled QDs, in which the polarization properties are fixed by their peculiar geometry and strain distribution. Comprehensive understanding of the effect of QD heterostructure-potential distribution on polarization requires a QD system in which the shape and composition can be closely controlled. This could be achieved, in principle, using the quantum posts (figure 1.9 (a)) or by applying additional stress. However, strain effects split the heavy hole (HH) and light hole (LH) states and hence minimizes VB mixing (see Chapter 2). The pyramidal heterostructure system introduced here is a useful approach for controlling quantum confinement in 3D by the built-in geometry of the heterostrcuture potential. These pyramidal quantum structures result from MOVPE growth of GaAs/AlGaAs heterostructures in inverted pyramid, and consist of different types of QDs and QWRs. To

understand the formation mechanisms of these structures, we will consider first a related nanostrcuture system, the V-groove QWRs that were studied previously in detail [109].

The V-groove QWRs are made by MOVPE growth of AlGaAs heteristrcutures on (100) GaAs substrates patterned with V-grooves aligned along the [011] crystal directions (see figure 1.10). The V-groove pattern is prepared using photolithography or electron beam lithography and wet chemical etching. The higher growth rate on the exposed (111)A facets, as compared with the bottom (100) one yields sharp V-grooves. Surface fluxes of adatoms induced by the sharply concave bottom compensate for this growth rate anisotropy and result in self-limiting growth of an AlGaAs template serving as the nucleation site of GaAs or AlGaAs crescent-shaped QWR [109]. The QWR size is independent of the size of the etched V-groove, and can be tuned to the desired scale of 2D quantum confinement (as small as few nm) with prescribed quantum confinement energy [109]. A transmission electron microscope (TEM) image of the cross section of such GaAs/AlGaAs V-groove QWR is shown in figure 1.10. We note the reproducibility in QWR size for the vertically stacked QWRs, a signature of the self-ordering mechanism involved. An important feature relevant to the pyramidal QD heterostructures introduced later, are the segregated AlGaAs regions evident in the TEM cross section of figure 1.10. These are formed due to the different surface diffusion lengths of the Ga and Al adatoms, resulting in Ga-enrichment of narrow regions forming an AlGaAs vertical QW at the center of the V-groove. In addition, thin GaAs QWs are formed on the (111)A groove facets.

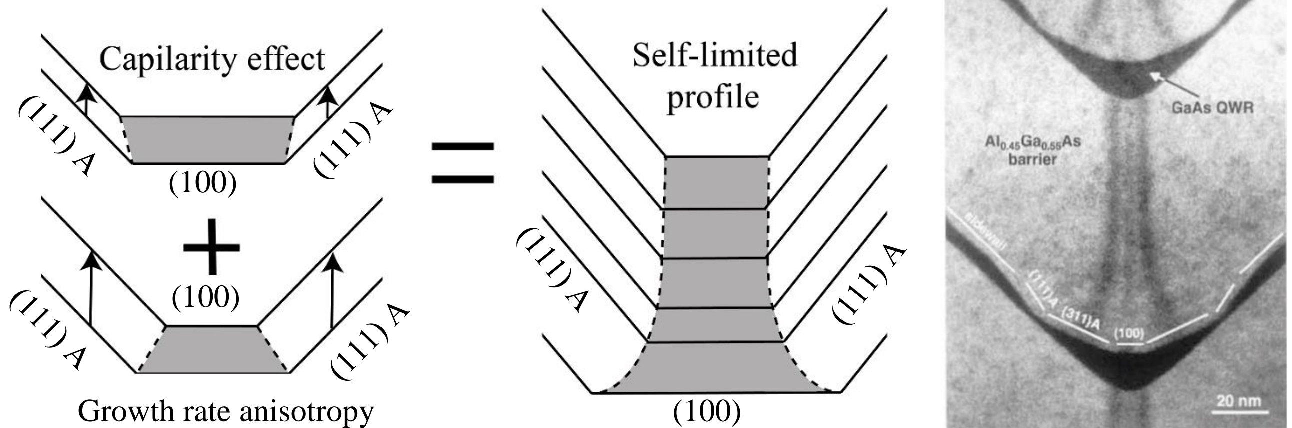

Figure 1.10 Schematic illustration of the self-limited growth process and cross-sectional TEM image of $Al_xGa_{1-x}As$/GaAs V-groove QWRs. *TEM picture adapted from* [109]

The nanostructures formed in inverted pyramids rely on similar site-controlled self ordering as for V-groove QWRs. They are produced by MOVPE of GaAs/AlGaAs heterostructures in inverted tetrahedral pyramids made on (111)B GaAs substrates [110]. Different than the case of the V-groove QWRs, growth takes place only inside the pyramids, exposing (111)A facets, due to the negligible rate of decomposition of the metallorganic precursors on the (111)B facets [111]. The growth rate anisotropy (between side-(111)A and bottom-(111)B planes) results in self-limiting nano-sized templates at the bottom of the pyramids, where lens-shaped QDs subsequently grow [112]. The Al-Ga segregation mechanism, driven by nano-

capilarity, gives rise to Ga-enriched nm-wide regions resulting in a variety of quantum nanostrcutures with controlled compositions and sizes [113].

Figure 1.11 illustrates schematically several important QWR/QD structures that have been realized with the pyramidal system.

Vertical QWRs (VQWRs). The detailed realization and studies of AlGaAs VQWRs grown in inverted pyramids were presented in [114][115] [113]. An example of such structures is shown in figure 1.12 (a). The QWR is colored in orange color and has the lowest Al content in the structure due to the strong Al-Ga segregation induced by the high curvature at the bottom of the pyramid. Typical QWR diameter is 15 - 20 nm, and it is surrounded by segregated QWs and bulk material of higher Al content, which provides strong lateral carrier confinement. Changing the nominal Al content in the growth directions directly yields tailoring of the heterostructure potential and 1D confined states along the QWR axis.

Pyramidal QDs. A QD heterostructure can be formed by growing a sufficiently thin layer of lower bandgap material inside the VQWR [116] [110] (see figure 1.11(b). One way to realize this is to reduce the AlGaAs VQWR length, embedded between two higher bandgap cladding layers. This was accomplished in [113] where the VQWR length was systematically reduced from 600 nm to 10 nm. Another approach is to insert a thin layer of smaller bandgap (e.g., GaAs or InGaAs) inside the pyramidal structure [117].

Quantum dot-in-dot (DiD). Motivated by the desire to tailor of the VB structure of QDs, dot-in-dot (DiD) structures were realized in the pyramidal system [118] [119] (see figure 1.11(c)). In this case, a thinner QD is embedded inside a thicker QD potential well, which can be easily realized in the pyramidal system by simply changing the nominal AlGaAs alloy composition in the growth direction. These DiD structures proved useful for controlling the hole type in the QD-confined states [118].

QD molecule (QDM). The pyramidal structure is a useful platform for vertically stacking QDs separated by thin barriers, with perfect alignment in the plane of the wafer. This makes possible the realization of QD molecules with a controlled degree of coupling between the QD wells [120] (see figure 1.11(d)).

Bandgap-engineered QWRs. More generally, the effective bandgap along the VQWR can be tailored with monolayer (sub-nm) accuracy by tailoring the Al content during growth in almost arbitrary profiles (fig. 1.11 (e). This was first demonstrated in linearly graded AlGaAs QWRs used to study exciton localization [121] and drift [122].

Summing up the advantages of the QD heterostructures grown in inverted pyramids:

- *Site control*. Prior to the growth, one can control the QD position and its distance from the substrate by changing pattern parameters such as pyramid size and distance in between pyramids. With large enough distance between the pyramids, one can readily excite and

collect light emission from a single QD heterostructure. Another possibility is to isolate not special but spectrally by changing the pyramid size of the single pyramid [123].

– *High reproducibility*. The details of the pyramidal nanostructures depend weakly on the pattern dimensions due to the self-formation growth process. This also results in small inhomogeneous broadening of the emission of QD ensembles, as compared to self-assembled systems [98].

– *Controllable quantum confinement*. The degree of quantum confinement can be controlled by the size of the nanostrcutures, which can be tuned by the thickness of the grown layers and material composition distribution.

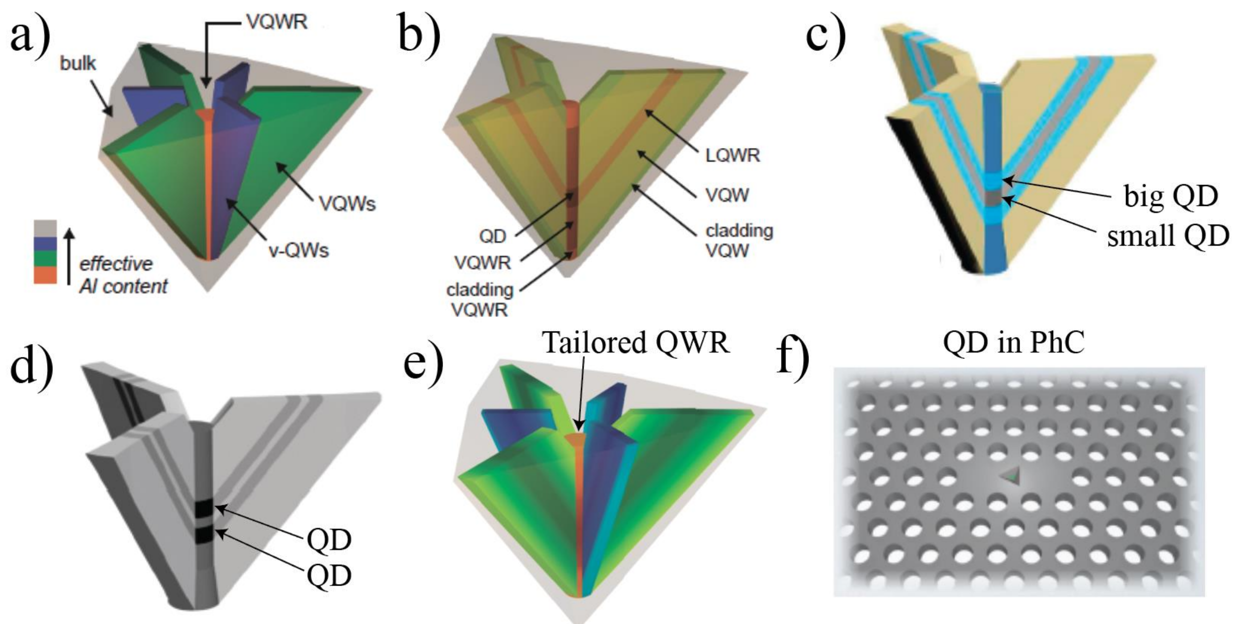

Figure 1.11. Schematic illustration of pyramidal QWR/QD nanostrcutures and integration in a phootnic cavity. (a) Vertical QWR, (b) QD, (c) Dot-in-dot, (d) QD molecule, (e) tailored potential QWR/QD (f) pyramidal QD integrated in a photonic crystal cavity.

The concept of the AlGaAs pyramidal QD heterostructures was also extended to the strained InGaAs/GaAs system [124]. In this case, the smaller bandgap of InGaAs, as compared with GaAs, allows the integration of the pyramidal InGaAs/GaAs QDs with photonic elements based on GaAs. In particular, such pyramidal QDs were employed for integrating single QDs in photonic crystal (PhC) membrane structures (see fig. 1.11(f)) [125] [126]. The thin membranes (~100-200 nm) require the fabrication of the QDs in sub-µm sized inverted pyramids. The exact (~10-50 nm precision) site control of the pyramidal QDs is essential for integrating systems (as opposed to single) QDs overlapping in an optimal way with the confined photonic modes of the

PhC structures [51]. The reproducibility in terms of emission wavelength is also helpful in achieving spectral matching with PhC cavities [98].

One of the current research directions is the integration of QDs with tailored positions and optical spectra into photonic circuits. Figure 1.12 (a) and (b) schematically show some possible photonic circuit construction, where in (a) the QD could be pumped optically and/or electrically using selective doping regions (red and blue), and in (b) just optically. Although Si-based photonic circuits are of great importance especially for industrial applications, they are not directly compatible with III-V compound QD technologies. The main difficulty of growing III-V QDs on Si substrates is the different lattice constants, which results in defects at the interfaces. Significant progress in this field has been achieved in the past few years. One interesting example of integrated QDs on Si-based photonic circuits was demonstrated in [127], as shown in figure 1.12 (c)-(f). Efficient coupling of light emitted by a GaAs-based QD into a Si_3N_4 waveguide was evidenced. Using the pyramidal, site-controlled QDs described above instead of self-assembled SK QDs would offer a big improvement for such devices and would open opportunities for integrated photonic circuits utilizing QD systems.

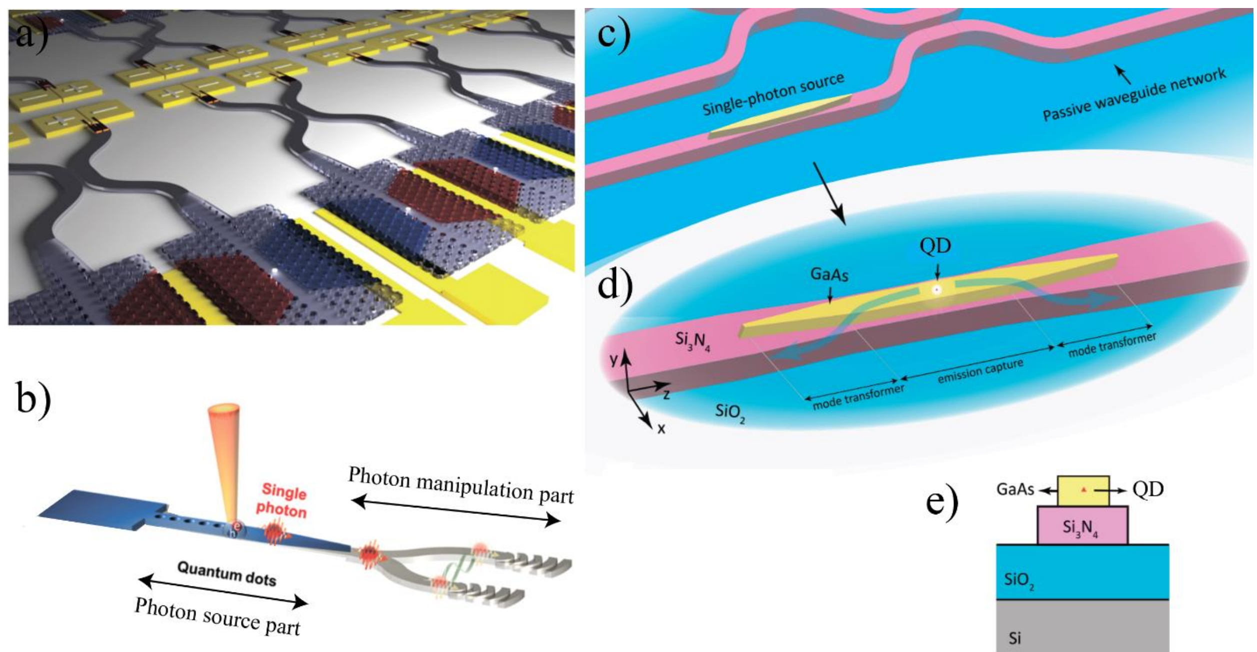

Figure 1.12 (a) Schematic figure of photonic circuits with integrated QDs. Blue and red corresponds to N and P doped region, yellow describes gold pads. Bright spot represents QDs in a waveguide. Adopted from [128]. *(b) Schematic illustration of possible design of photonic circuit pumped by a laser beam* [129]. *(c)(d)(e) A scheme of Si-based device with GaAs based QDs. Adopted from* [127] *(c) Waveguide network with GaAs based photon source regions. (d) Magnified image of photon source region (e) Cross-section of photon source region.*

1.5 Thesis goal and outline

The goal of this thesis is the study of GaAs/$Al_xGa_{1-x}As$ quantum nanostructures with tailored potential formed in inverted pyramids and the influence of quantum confinement on their optical properties. In particular, we were interested in the connection between the VB structure and the polarization state of the emitted light.

In **Chapter 1** we present a general introduction to the field of nanoscience as well as an introduction to semiconductor nanostructures formed in inverted pyramids.

Chapter 2 gives the theoretical background on band structure and optical properties of semiconductor, which we use in our computer code to simulate the optical properties of the pyramidal nanostructures. We start from the basics of the physics of semiconductors using the *k.p* approximation to describe the conduction and valence bands. We further show how Lowdin's perturbation leads to the 4x4 Luttinger Hamiltonian formalism used. At the end of the chapter, we give an example of the simulation of the optical spectra of AlGaAs pyramidal QDs.

Chapter 3 describes the fabrication processes and tools used for the realization of QD nanostructures in the inverted pyramids. This includes substrate patterning, epitaxial growth and post-growth processing. In addition, various optical characterization tools used in the optical spectroscopy part are presented.

Chapter 4 presents the grown AlGaAs/GaAs pyramidal nanostructures with different degree of quantum confinement that were investigate: a QWR, a "thin" QD and three QDs with parabolically shaped potential of different gradients formed via tailoring the Al content. The effect of the systematic variation of the degree of quantum confinement is studied by optical spectroscopy and numerical simulations.

Chapter 5 is dedicated to polarization resolved photoluminescence studies of the pyramidal nanostructures. For each structure, sets of polarization-resolved photoluminescence spectra were acquired and analyzed with corresponding numerical simulations. The influence of valence band mixing on the polarization features and its evolution with the degree of quantum confinement are discussed.

Chapter 6 discusses ways for dynamic control of the polarization properties of pyramidal nanostructures. Single QDs, QD molecules and QD superlattices are analyzed in order to identify structural parameters for which energy position between heavy hole and light hole states is almost perfectly balanced. Then, the effect of an external electric field in switching the valence band character, and therefore the emission polarization, is explored in numerical simulations.

Chapter 7 is a concluding chapter that summarizes all essential results and gives some proposals for future directions of the research. As a preliminary result, photoluminescence spectra of a parabolic QD under an external electric field introduced by a Schottky structure are presented.

Chapter 2

Band Structure and Optical Transitions in Pyramidal Quantum Nanostructures

Quantum confinement in low-dimensional semiconductors significantly modifies the electronic states in the conduction and valence bands and can be used to tailor their optical spectra. This chapter presents the theory permitting the evaluation of the impact of quantum confinement on the band structure (Section 2.1) and the optical transitions (Section 2.2). The important role of excitons in confined structure is reviewed in Section 2.3. The numerical model permitting the calculation of the optical spectra for comparison with experimental studies is described (Section 2.4). The effect of the quantum confinement on valence band mixing and the role of the latter in determining the degree of linear polarization of the emitted light are discussed in particular.

2.1 Hamiltonian formulation

To compute the band structures we use a model based on k.p approximation [130] and Lowdin's perturbation [131], eventually leading to the formulation based on the Luttinger Hamiltonian [132] [133].

2.1.1 From general Hamiltonian to k.p approximation

The general Hamiltonian for a crystal reads [134]:

$$H = \sum_i \frac{\mathbf{p}_i^2}{2m_i} + \sum_j \frac{\mathbf{P}_i^2}{2M_j} + \frac{1}{2}\sum_{j',j}^{j'\neq j} \frac{Z_j Z_{j'} e^2}{4\pi\varepsilon_0 \left|\mathbf{R}_j - \mathbf{R}_{j'}\right|} - \sum_{i,j} \frac{Z_j e^2}{4\pi\varepsilon_0 \left|\mathbf{R}_j - \mathbf{R}_{j'}\right|} + \frac{1}{2}\sum_{i',i}^{j'\neq j} \frac{e^2}{4\pi\varepsilon_0 \left|\mathbf{r}_i - \mathbf{r}_{i'}\right|} + H_{SO}$$

where m_i is the electron mass, $\boldsymbol{r}_i$ the electron position, M_j the mass of the nucleus, $\boldsymbol{R}_j$ the nucleus position with charge Z_j, and H_{SO} the spin-orbit interaction term. To make the problem solvable, we perform some simplifications. First, we assume that the nuclei are much heavier than the electrons, and so we may neglect their motion (Born–Oppenheimer approximation):

$$H = \sum_i \frac{\mathbf{p}_i^2}{2m_i} + \frac{1}{2}\sum_{j',j}^{j'\neq j} \frac{Z_j Z_{j'} e^2}{4\pi\varepsilon_0 \left|\mathbf{R}_j - \mathbf{R}_{j'}\right|} + \frac{1}{2}\sum_{i',i}^{j'\neq j} \frac{e^2}{4\pi\varepsilon_0 \left|\mathbf{r}_i - \mathbf{r}_{i'}\right|} + H_{SO}$$

Second, since almost all electrons are trapped by the nuclei and only few have localization lengths larger than the lattice constant, we consider just the latter ones. Third, we use the so-called mean field (Hartree-Fock) approximation. The result is a mean-field Hamiltonian for single electrons,

$$H = \frac{\mathbf{p}^2}{2m_0} + V(\mathbf{r}) + H_{SO}$$

where *V(**r**)* is mean field potential, and the spin-orbit interaction term reads $H_{SO} = \frac{\hbar}{4m_0^2c^2}\sigma \cdot \left[\nabla V \times \mathbf{p}\right]$, and m_0 is the electron mass.

Exploiting the lattice periodicity a, we first look for solutions in the form of Bloch waves:

$$\psi_k^{(n)}(\mathbf{r}) = u_k^{(n)}(\mathbf{r})e^{i\mathbf{kr}} \text{, with } u_k^{(n)}(\mathbf{r}) = u_k^{(n)}(\mathbf{r}+\mathbf{a})$$

Substituting the Bloch wave function into the Hamiltonian and neglecting parts with fast oscillations we get [135]: $H = H^{k \cdot p} + H_{SO}$, where

$$H^{k \cdot p} = \left[\frac{\mathbf{p}^2}{2m_0} + V(\mathbf{r})\right] + \left[\frac{\hbar}{m_0}\mathbf{k}\cdot\mathbf{p} + \frac{\hbar^2\mathbf{k}^2}{2m_0}\right]$$

Thus the Schrödinger equation becomes:

$$\left(\left[\frac{\mathbf{p}^2}{2m_0} + V(\mathbf{r})\right] + \left[\frac{\hbar}{m_0}\mathbf{k}\cdot\mathbf{p} + \frac{\hbar^2\mathbf{k}^2}{2m_0}\right] + \frac{\hbar}{4m_0^2c^2}\sigma\cdot\left[\nabla V \times (\mathbf{p}+\hbar\mathbf{k})\right]\right)u_k^{(n)}(\mathbf{r}) = \varepsilon_k^{(n)}u_k^{(n)}(\mathbf{r})$$

where σ are Pauli matrixes and ∇V the gradient of atomic mean field potential. The next step is to find solutions around the point ***k***=*0* for that, we consider as an approximation the 4 closest bands, where the states have S and P symmetries: $\left|u_0^{(S)}\right\rangle = \left|S\right\rangle$, $\left|u_0^{(X)}\right\rangle = \left|X\right\rangle$, $\left|u_0^{(Y)}\right\rangle = \left|Y\right\rangle$, $\left|u_0^{(Z)}\right\rangle = \left|Z\right\rangle$ [136].

This yields the matrix elements of the ***k.p*** Hamiltonian, neglecting spin:

$$H^{k.p} = \begin{pmatrix} E_C+\varepsilon & iP_0k_x & iP_0k_y & iP_0k_z \\ -iP_0k_x & E_V+\varepsilon & 0 & 0 \\ -iP_0k_y & 0 & E_V+\varepsilon & 0 \\ -iP_0k_z & 0 & 0 & E_V+\varepsilon \end{pmatrix},\; H_{SO} = \frac{\hbar}{4m_0^2c^2}\begin{pmatrix} 0 & 0 & 0 & 0 \\ 0 & 0 & -\gamma_{X.Y} & -\beta_{X,Z} \\ 0 & \gamma_{Y,X} & 0 & -\alpha_{Y,Z} \\ 0 & \beta_{Z,X} & \alpha_{Z,Y} & 0 \end{pmatrix}$$

where $\frac{\hbar}{m_0}\langle S|\mathbf{k}\cdot\mathbf{p}|Y\rangle = iP_0k_Y$, $\frac{\hbar}{m_0}\langle S|\mathbf{k}\cdot\mathbf{p}|Y\rangle = iP_0k_X$, $\frac{\hbar}{m_0}\langle S|\mathbf{k}\cdot\mathbf{p}|Y\rangle = iP_0k_Z$,

$$\langle X|\frac{\mathbf{p}^2}{2m_0}+V(r)+\frac{\hbar^2\mathbf{k}^2}{2m_0}|X\rangle = \langle Y|\frac{\mathbf{p}^2}{2m_0}+V(\mathbf{r})+\frac{\hbar^2\mathbf{k}^2}{2m_0}|Y\rangle = \langle Z|\frac{\mathbf{p}^2}{2m_0}+V(\mathbf{r})+\frac{\hbar^2\mathbf{k}^2}{2m_0}|Z\rangle = E_V+\varepsilon$$

$$\langle S|\frac{\mathbf{p}^2}{2m_0}+V(\mathbf{r})+\frac{\hbar^2\mathbf{k}^2}{2m_0}|S\rangle = E_C+\varepsilon,$$

and $\varepsilon = \frac{\hbar^2\mathbf{k}^2}{2m_0}$, $\alpha_{Y,Z} = \langle Y|\left(\frac{\partial V}{\partial y}p_z - p_y\frac{\partial V}{\partial z}\right)|Z\rangle$, $\beta_{X,Z} = \langle X|\left(\frac{\partial V}{\partial x}p_z - p_x\frac{\partial V}{\partial z}\right)|Z\rangle$,

$$\gamma_{Y,X} = \langle Y|\left(\frac{\partial V}{\partial x}p_y - p_x\frac{\partial V}{\partial y}\right)|X\rangle.$$

Solving the eigenvalue problem for this Hamiltonian we obtain the dispersion curves of the corresponding 4 bands: conduction band, heavy hole band, light hole band and split-off band, schematically shown in figure 2.1. However, this 4x4 Hamiltonian is not sufficiently accurate enough and needs to be further elaborated. To this end, we use a model based on Lowdin's [131] perturbation theory including spin [1], which finally yields a 8x8 Luttinger Hamiltonian.

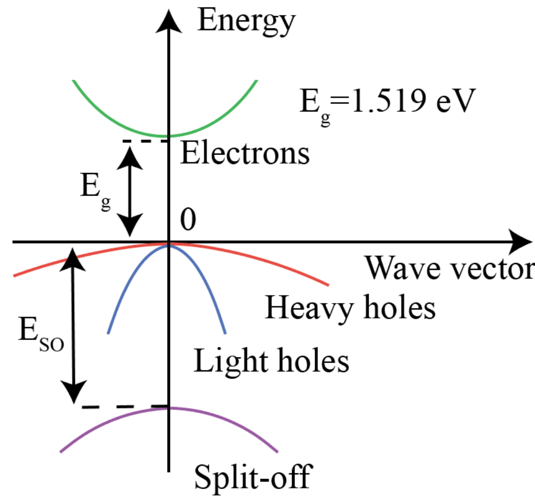

Figure 2.1 Band structure of GaAs according to the ***k.p*** *model.* $E_g = E_C - E_V$

2.1.2 Lowdin's Perturbation: beyond simple k.p

In the development above we considered only 4 bands, but in fact, there is an infinite number of bands that have a non-negligible influence on the band structure. This influence can be taken into account as a perturbation [130]. Suppose we have a group of states of class A and another group of class B, both solutions of our Hamiltonian *H*. We focus on the eigenfunctions of class A and take into account the influence of class B states as a perturbation. This is known as

Lowdin's Perturbation approach [131]. From the standard Schrodinger equation in martrix form we have the term

$$\left(E-H_{m,m}\right)a_m=\sum_{n\neq m}^{A}H_{m,n}a_n+\sum_{\alpha\neq m}^{B}H_{m,n}a_\alpha$$

where we split the basis into the two classes A and B. Next, we find an equation for *a*:

$$a_m=\sum_{n\neq m}^{A}h_{m,n}a_n+\sum_{\alpha\neq m}^{B}h_{m,n}a_\alpha \text{ where } h_{m,n}=\frac{H_{m,n}}{\left(E-H_{m,m}\right)}$$

Therefore,

$$a_m=\sum_{n\neq m}^{A}h_{m,n}a_n+\sum_{\alpha\neq m}^{B}h_{m,\alpha}\sum_{\alpha\neq n}^{A}h_{\alpha,n}a_\alpha+\sum_{\alpha\neq m}^{B}h_{m,\alpha}\sum_{\alpha\neq\beta}^{B}h_{\alpha,\beta}a_\beta$$

and the initial expression becomes:

$$\left(E-H_{m,m}\right)a_m=\sum_{n\neq m}^{A}\left(H_{m,n}+\sum_{\alpha\neq m}^{B}\frac{H_{m,\alpha}H_{\alpha,n}}{E-H_{\alpha,\alpha}}+\ldots\right)a_n=\sum_{n\neq m}^{A}U_{m,n}a_n$$

The perturbed Hamiltonian is then:

$$U_{m,n}=H_{m,n}+\sum_{n\neq m}^{B}\left(\frac{H_{m,\alpha}H_{\alpha,n}}{E-H_{\alpha,\alpha}}+\ldots\right)$$

where $H_{m,\alpha}=\langle m|H|\alpha\rangle$ are matrix elements of the non-perturbed Hamiltonian.

To apply this technique to our case, we take as class A states our first 4 bands in the Kane picture (originating from the 1 S and 3 P states) and as class B states we limit ourselves to D-symmetry states.

To first order in the perturbation, $H'_{m,n}=\sum_{n\neq m}^{B}\left(\frac{H_{m,\alpha}H_{\alpha,n}}{E-H_{\alpha,\alpha}}\right)$. The resulting Hamiltonian (without spin) is $H=H_0+H'$ where:

$$H'=\begin{pmatrix} A'k^2 & Bk_zk_y & Bk_xk_z & Bk_xk_y \\ Bk_yk_z & L'k_x^2+Mk_y^2+Mk_z^2 & N'k_xk_y & N'k_xk_z \\ Bk_zk_x & N'k_xk_y & Mk_x^2+L'k_y^2+Mk_z^2 & N'k_zk_y \\ Bk_xk_y & N'k_xk_z & N'k_zk_y & Mk_x^2+Mk_y^2+L'k_z^2 \end{pmatrix}$$

A’, *B*, *L*’, *M*, *N*’ constants due to Löwdin renormalization involving states outside the (S, P) subspace. In the case of GaAs, B=0.

The total Hamiltonian, including spin, is $H = H_0 + H' + H^{SO}$ where:

$$H_0 = \begin{pmatrix} E_C+\varepsilon & iP_0k_x & iP_0k_y & iP_0k_z & 0 & 0 & 0 & 0 \\ -iP_0k_x & E_V+\varepsilon & 0 & 0 & 0 & 0 & 0 & 0 \\ -iP_0k_y & 0 & E_V+\varepsilon & 0 & 0 & 0 & 0 & 0 \\ -iP_0k_z & 0 & 0 & E_V+\varepsilon & 0 & 0 & 0 & 0 \\ 0 & 0 & 0 & 0 & E_C+\varepsilon & iP_0k_x & iP_0k_y & iP_0k_z \\ 0 & 0 & 0 & 0 & -iP_0k_x & E_V+\varepsilon & 0 & 0 \\ 0 & 0 & 0 & 0 & -iP_0k_y & 0 & E_V+\varepsilon & 0 \\ 0 & 0 & 0 & 0 & -iP_0k_z & 0 & 0 & E_V+\varepsilon \end{pmatrix} \quad H^{SO} = \frac{\Delta_0}{3}\begin{pmatrix} 0 & 0 & 0 & 0 & 0 & 0 & 0 & 0 \\ 0 & 0 & -i & 0 & 0 & 0 & 0 & +1 \\ 0 & +i & 0 & 0 & 0 & 0 & 0 & -i \\ 0 & 0 & 0 & 0 & 0 & -1 & +i & 0 \\ 0 & 0 & 0 & 0 & 0 & 0 & 0 & 0 \\ 0 & 0 & 0 & -1 & 0 & 0 & +i & 0 \\ 0 & 0 & 0 & -i & 0 & -i & 0 & 0 \\ 0 & +1 & +i & 0 & 0 & 0 & 0 & 0 \end{pmatrix}$$

$$H' = \begin{pmatrix} 0 & 0 & 0 & 0 & 0 & 0 & 0 & 0 \\ 0 & +L'k_x^2+Mk_y^2+Mk_z^2 & N'k_xk_y & N'k_xk_z & 0 & 0 & 0 & 0 \\ 0 & N'k_yk_x & Mk_x^2+L'k_y^2+Mk_z^2 & N'k_yk_z & 0 & 0 & 0 & 0 \\ 0 & N'k_zk_x & N'k_zk_y & Mk_x^2+Mk_y^2+L'k_z^2 & 0 & 0 & 0 & 0 \\ 0 & 0 & 0 & 0 & 0 & 0 & 0 & 0 \\ 0 & 0 & 0 & 0 & 0 & +L'k_x^2+Mk_y^2+Mk_z^2 & N'k_xk_y & N'k_xk_z \\ 0 & 0 & 0 & 0 & 0 & N'k_yk_x & Mk_x^2+L'k_y^2+Mk_z^2 & N'k_yk_z \\ 0 & 0 & 0 & 0 & 0 & N'k_zk_x & N'k_zk_y & Mk_x^2+Mk_y^2+L'k_z^2 \end{pmatrix}$$

where $\varepsilon = \dfrac{\hbar^2 k^2}{2m_0}$ and Δ_0 is the spin-orbit splitting:

$$\Delta_0 = \frac{-3i\hbar}{4m_0c^2}\langle X|\frac{\partial V}{\partial x}p_y - \frac{\partial V}{\partial y}p_x|Y\rangle$$

This Hamiltonian contains the 4 atomic bands, the kinetic terms, the spin-orbit term, the perturbation of the 5 d-bands, and the atomic potential in terms of a mean field. I remind the reader that this Hamiltonian is written in the basis of atomic-like states. Because the optical transition rate is proportional to $\langle \varphi_{cb}|\mathbf{e}\cdot\mathbf{p}|\varphi_{vb}\rangle$ where ***p*** is the momentum and ***e*** is a polarization vector (see Section 2.2), for optical studies it is more convenient to change the basis of this Hamiltonian to the basis of the eigenfunctions of momentum operator. The states of this new basis are presented in table 2.1 [134].

Eigenvalues and corresponding eigenstates at $\boldsymbol{k} = 0$

Energy	First Kramers Set	Second Kramers Set	Name
E_c	$\left\|\frac{1}{2},\frac{1}{2}\right\rangle = \left\|S\uparrow\right\rangle$	$\left\|\frac{1}{2},-\frac{1}{2}\right\rangle = \left\|S\downarrow\right\rangle$	Electron
E_v	$\left\|\frac{3}{2},\frac{3}{2}\right\rangle = \frac{i}{\sqrt{2}}\left\|(X+iY)\uparrow\right\rangle$	$\left\|\frac{3}{2},-\frac{3}{2}\right\rangle = \frac{-i}{\sqrt{2}}\left\|(X-iY)\downarrow\right\rangle$	Heavy Hole
E_v	$\left\|\frac{3}{2},\frac{1}{2}\right\rangle = \frac{-i}{\sqrt{6}}\left\|(X+iY)\downarrow -2Z\uparrow\right\rangle$	$\left\|\frac{3}{2},-\frac{1}{2}\right\rangle = \frac{i}{\sqrt{6}}\left\|(X-iY)\uparrow +2Z\downarrow\right\rangle$	Light Hole
$E_v-\Delta_0$	$\left\|\frac{1}{2},\frac{1}{2}\right\rangle = \frac{-i}{\sqrt{3}}\left\|(X+iY)\downarrow +Z\uparrow\right\rangle$	$\left\|\frac{1}{2},-\frac{1}{2}\right\rangle = \frac{-i}{\sqrt{3}}\left\|(X-iY)\uparrow -Z\downarrow\right\rangle$	SO Hole

Table 2.1 Eigenvalues and corresponding eigenstates of the CB and VB states in momentum basis.

The Hamiltoian in this basis is:

$$H_0 = \begin{pmatrix} E_C+\varepsilon & 0 & V & 0 & \sqrt{3}V^* & -\sqrt{2}U & -U & \sqrt{2}V \\ 0 & E_C+\varepsilon & -\sqrt{2}U & -\sqrt{3}V & 0 & -V^* & \sqrt{2}V^* & U \\ V^* & -\sqrt{2}U^* & E_V & 0 & 0 & 0 & 0 & 0 \\ 0 & -\sqrt{3}V^* & 0 & E_V & 0 & 0 & 0 & 0 \\ \sqrt{3}V & 0 & 0 & 0 & E_V & 0 & 0 & 0 \\ -\sqrt{2}U^* & -V & 0 & 0 & 0 & E_V & 0 & 0 \\ -U^* & \sqrt{2}V & 0 & 0 & 0 & 0 & E_V & 0 \\ \sqrt{2}V^* & U^* & 0 & 0 & 0 & 0 & 0 & E_V \end{pmatrix} \qquad H^{SO} = \frac{\Delta_0}{3}\begin{pmatrix} 0 & 0 & 0 & 0 & 0 & 0 & 0 & 0 \\ 0 & 0 & 0 & 0 & 0 & 0 & 0 & 0 \\ 0 & 0 & 1 & 0 & 0 & 0 & 0 & 0 \\ 0 & 0 & 0 & 1 & 0 & 0 & 0 & 0 \\ 0 & 0 & 0 & 0 & 1 & 0 & 0 & 0 \\ 0 & 0 & 0 & 0 & 0 & 1 & 0 & 0 \\ 0 & 0 & 0 & 0 & 0 & 0 & -2 & 0 \\ 0 & 0 & 0 & 0 & 0 & 0 & 0 & -2 \end{pmatrix}$$

$$H' = \begin{pmatrix} 0 & 0 & 0 & 0 & 0 & 0 & 0 & 0 \\ 0 & 0 & 0 & 0 & 0 & 0 & 0 & 0 \\ 0 & 0 & -P+Q & -S^* & R & 0 & \sqrt{3/2}S & -\sqrt{2}Q \\ 0 & 0 & -S & -P-Q & 0 & R & -\sqrt{2}R & \sqrt{1/2}S \\ 0 & 0 & R^* & 0 & -P-Q & S^* & \sqrt{1/2}S^* & \sqrt{2}R^* \\ 0 & 0 & 0 & R^* & S & -P+Q & \sqrt{2}Q & \sqrt{3/2}S^* \\ 0 & 0 & \sqrt{3/2}S^* & -\sqrt{2}R^* & \sqrt{1/2}S & \sqrt{2}Q & -P & 0 \\ 0 & 0 & -\sqrt{2}Q & \sqrt{1/2}S^* & \sqrt{2}R & \sqrt{3/2}S & 0 & -P \end{pmatrix}$$

Where

$$\varepsilon = \frac{\hbar^2 k^2}{2m_0}, U = \frac{P_0}{\sqrt{3}}k_z, V = \frac{P_0}{\sqrt{6}}\left(k_x + ik_z\right), P = \frac{\hbar^2}{2m_0}\gamma_1\left(k_x^2+k_y^2+k_z^2\right),$$

$$Q = \frac{\hbar^2}{2m_0}\gamma_2\left(k_x^2+k_y^2-2k_z^2\right),\ S = 2\sqrt{3}\frac{\hbar^2}{2m_0}\gamma_3\left(k_x k_z - ik_y k_z\right), R = -\sqrt{3}\frac{\hbar^2}{2m_0}\left(\gamma_2\left(k_x^2-k_y^2\right)-2i\gamma_3 k_x k_y\right),$$

$$\gamma_1 = -\frac{2}{3}\frac{m_0}{\hbar^2}\left(L'+2M\right)-1\ , \gamma_2 = -\frac{1}{3}\frac{m_0}{\hbar^2}\left(L'-M\right),\ \gamma_3 = -\frac{1}{3}\frac{m_0}{\hbar^2}N'.$$

The dashed lines in these matrices separate the valence band of the Hamiltonian from the coupled conduction band part. Δ is spin-orbit splitting and $\gamma_1,\gamma_2,\gamma_3$ are known as the Luttinger

parameters. For GaAs, $\gamma_1 = 6.98$ $\gamma_2 = 2.06$ $\gamma_3 = 2.93$, whereas for AlAs $\gamma_1 = 3.76$ $\gamma_2 = 0.82$ $\gamma_3 = 1.42$ [137]. The parameters for $Al_xGa_{1-x}As$ are obtained by a linear combination of the parameters for the binaries, weighted by the Al content x.

To calculate the band structure in bulk material, we have to diagonolize the Hamiltonian and obtain the dispersion relations for the conduction, heavy hole (HH), light hole (LH) and split-off bands. To simplify this process, we decouple the conduction and split-off bands and leave the HH and LH bands coupled. In this approximation, the conduction band dispersion is $E_{CB}(\mathbf{k}) = E_g + \frac{\hbar^2\mathbf{k}^2}{2m_e^{GaAs}}$, with $m_e^{GaAs} \approx 0.067m_0$, and the split-off one is $E_{SO}(\mathbf{k}) = E_{SO} + \frac{\hbar^2\mathbf{k}^2}{2m_{SO}}$, with $m_{SO}^{GaAs} \approx 0.172m_0$. The remaining 4x4 Hamiltonian for the LH and HH bands is

$$H_{4x4}^{k.p} = \begin{pmatrix} -P+Q & -S^* & R & 0 \\ -S & -P-Q & 0 & R \\ R^* & 0 & -P-Q & S^* \\ 0 & R^* & S & -P+Q \end{pmatrix}$$

and the eigenvalues are $E = -P \pm \sqrt{Q^2 + S^2 + R^2}$ (two times degenerate, due to the spin). Substituting P, Q, S, R and reassembling the non-k dependent coefficients we have:

$$E_{hh} = -A\mathbf{k}^2 - \sqrt{B^2\mathbf{k}^4 + C^2\left(k_x^2k_y^2 + k_y^2k_z^2 + k_z^2k_x^2\right)}$$
$$E_{lh} = -A\mathbf{k}^2 + \sqrt{B^2\mathbf{k}^4 + C^2\left(k_x^2k_y^2 + k_y^2k_z^2 + k_z^2k_x^2\right)}$$

where k_x, k_y, k_z are the components of the wavevector and A, B, C are constants related to momentum matrixes defined above [136]. The off-diagonal matrix terms R and S give a non-trivial VB-mixing. From the last equations, the direction dependence of the effective masses tensor can be extracted as $m_{ij} = \left(\frac{\partial^2 E}{\partial k_i \partial k_j}\frac{1}{\hbar^2}\right)^{-1}$. Thus, the effective masses along the [100], [110], [111] crystal directions are:

$$m_{hh}^{[100]} = \frac{m_0}{\gamma_1 - 2\gamma_2} \quad m_{lh}^{[100]} = \frac{m_0}{\gamma_1 + 2\gamma_2}, \quad m_{hh}^{[110]} = \frac{m_0}{2\gamma_1 - \gamma_2 - 3\gamma_3} \quad m_{lh}^{[110]} = \frac{m_0}{2\gamma_1 + \gamma_2 + 3\gamma_3}, \quad m_{hh}^{[111]} = \frac{m_0}{\gamma_1 - 2\gamma_3}$$
$$m_{lh}^{[111]} = \frac{m_0}{\gamma_1 + 2\gamma_3}$$

2.1.3 Effect of low dimensionality on the conduction band

The approach outlined above considers that the CB is totally decoupled from the VB states. In the case of AlGaAs heterostructures, the Schrodinger equation for the decoupled conduction band wavefunctions reads

$$\frac{\hat{p}^2}{2m_{(r,\varphi,z)}}\phi_{(r,\varphi,z)} + V_{(r,\varphi,z)}\phi_{(r,\varphi,z)} = E\phi_{(r,\varphi,z)}$$

where $V_{(r,\varphi,z)}$ is the heterostructure potential created by the inhomogeneous distribution of the Al atoms. We resort here to a cylindrical coordinate system, which approximately matches the geometry of the pyramidal nanostrcutures discussed in this thesis. In bulk $Al_xGa_{(1-x)}As$ the effective electron mass is given by (x < 0.4) [137] $m_e^{AlxGa(1-x)As} = (0.067 + 0.083x)m_0$. The spin-dependent wavefunctions are given by $\varphi_{cb} = \phi_e \left|S\uparrow\right\rangle$ or $\varphi_{cb} = \phi_e \left|S\downarrow\right\rangle$. In computer simulations later presented we take into account the effective mass dependence on the Al content. However, due to the relatively low Al content (x < 0.1) in the central QWR in the pyramidal nanostructures, for analytic considerations we can consider it as constant. The Schrodinger equation reads

$$-\frac{1}{2m_e\hbar^2}\left(\frac{1}{r}\frac{\partial}{\partial r}\left(r\frac{\partial\phi_{(r,\varphi,z)}}{\partial r}\right) + \frac{1}{r^2}\frac{\partial^2\phi_{(r,\varphi,z)}}{\partial\varphi^2} + \frac{\partial^2\phi_{(r,\varphi,z)}}{\partial z^2}\right) + V_{(r,\varphi,z)}\phi_{(r,\varphi,z)} = E\phi_{(r,\varphi,z)}$$

With separation of variables, $\phi_{(r,\varphi,z)} = \phi_{(r,\varphi)}\phi_{(z)}$, we get

$$\begin{cases} -\frac{1}{2m_e\hbar^2}\left(\frac{\partial^2\phi_{(z)}}{\partial z^2}\right) + V_{(z)}\phi_{(z)} = E_1\phi_{(z)} & (1) \\ -\frac{1}{2m_e\hbar^2}\left(\frac{1}{r}\frac{\partial}{\partial r}\left(r\frac{\partial\phi_{(r,\varphi)}}{\partial r}\right) + \frac{1}{r^2}\frac{\partial^2\phi_{(r,\varphi)}}{\partial\varphi^2}\right) = E_2\phi_{(r,\varphi)} & (2) \end{cases}$$

Equation (2) can be further split into equations for the radial and angular parts. The solution for (2) is written in terms of Bessel functions as $\phi_{(r,\varphi)} = J_m(k_\alpha r)\cos(m\varphi)$ $m \in N$ $\alpha \in N$ where α , m are quantum numbers.

In some cases, equation (1) can also be treated analytically, e.g., for parabolically shaped heterostrcuture potential V. Using the well known solutions for parabolic potentials in terms of Hermite polynomials then gives

$$\phi_{m,\alpha,n}(\zeta, r, \varphi) = N_{m,\alpha,n}J_m(k_\alpha r)\cos(m\varphi)H_n(\zeta)e^{-\frac{1}{2}\zeta^2}$$

where α, n, m are quantum numbers, $N_{m,\alpha,n}$ are normalization constants and $H_n(\zeta)$ are Hermite polynomials. The numerical model we will use takes into account barriers with finite height and also specific geometry features of the nanostructures in the inverted pyramids, but the CB wavefunctions will have a similar shape as in these simple analytic solutions.

2.1.4 Effect of low dimensionality on valence band structure

1D confinement, QW

In the bulk (zero confinement) the VB states (HH and LH) are degenerate at $\mathbf{k}=0$ (see figure 2.1). As it was mentioned in Chapter 1 first QW structures were made from AlGaAs/GaAs heterostructure, by modifying Al content along the growth direction. In the presence of 1D confinement (QW), due to the higher effective mass the HH band edge is lower than the LH one, as schematically shown in figure 2.2. Thus, ground state optical transition occurs between the CB and the HH band.

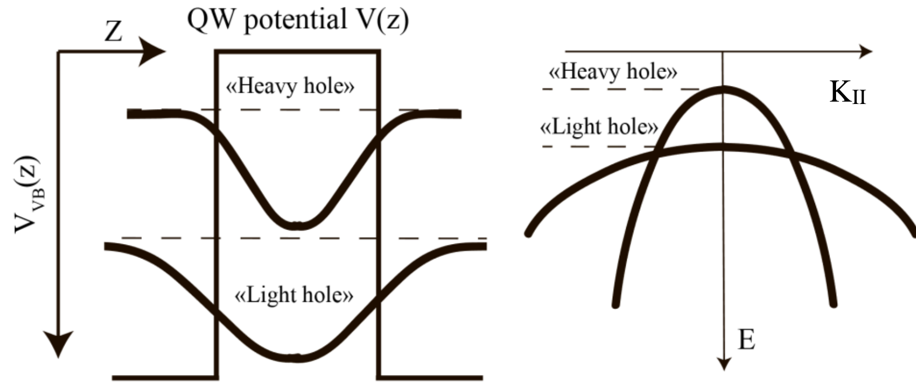

Figure 2.2 Schematic picture of the first VB states in a QW and the corresponding dispersion curve.

The QW Hamiltonian (in case of confinement in the z direction) can be obtained by replacing $k_z \to \left(-i\frac{\partial}{\partial z}\right)$; all material parameter are functions from z (band gaps, Luttinger parameters, etc.). In the bulk optical transitions mainly occur at $\mathbf{k}=[0,0,0]$ of the charged carriers. In QWs, in case of infinitely high potential barriers, $\mathbf{k}=\left[0,0,\frac{\pi n}{L_z}\right]$, where L_z is the QW width. The 4X4 Luttinger Hamiltonian reads

$$H_{4x4}^{k.p} = \begin{pmatrix} -P+Q & -S^* & R & 0 \\ -S & -P-Q & 0 & R \\ R^* & 0 & -P-Q & S^* \\ 0 & R^* & S & -P+Q \end{pmatrix} + V(z)$$

where $P = \frac{\hbar}{2m_0}\gamma_1(z)\left(k_x^2 + k_y^2 - \frac{\partial^2}{\partial z^2}\right), Q = \frac{\hbar}{2m_0}\gamma_2(z)\left(k_x^2 + k_y^2 + 2\frac{\partial^2}{\partial z^2}\right),$

$S = 2\sqrt{3}\frac{\hbar}{2m_0}\gamma_3(z)\left(-ik_x\frac{\partial}{\partial z} - k_y\frac{\partial}{\partial z}\right), R = -\sqrt{3}\frac{\hbar}{2m_0}\left(\gamma_2(z)\left(k_x^2 - k_y^2\right) - 2i\gamma_3(z)k_x k_y\right)$

In the *k.p* 4x4 Luttinger Hamiltonian, the off-diagonal components *R* and *S* are responsible for HH-LH mixing (VB mixing). In the case of a QW they vanish at the center of the Brillouin zone, and VB mixing happens only at $k_{x,y} \neq 0$. The confinement potential defines the VB structure; an example of band structure simulation of a GaAs QW is shown in figure 2.3.

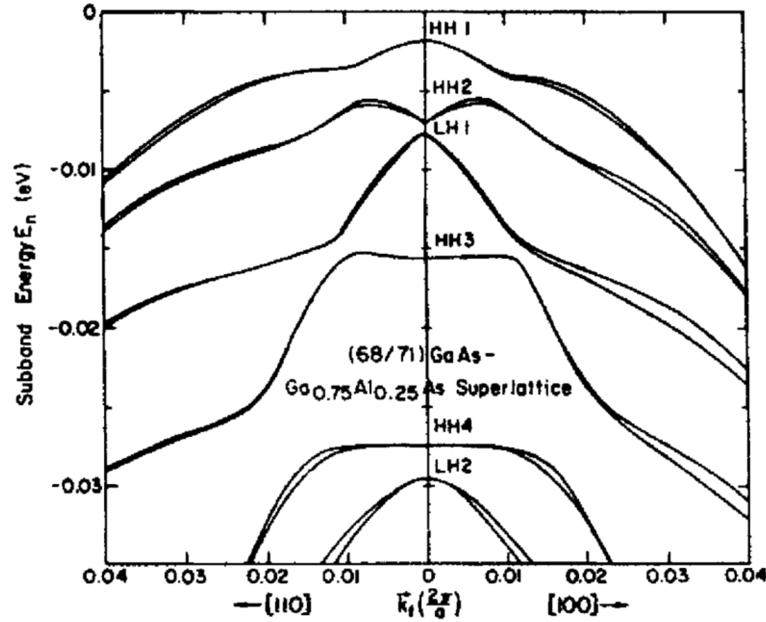

Figure 2.3 Valence-band structure of a GaAs QW grown along [001] as a function of k vector along two directions in the QW plane [138].

Another important way of modifying the VB structure is to introduce strain and remove the degeneracy of the LH and HH bands [130]. Under effect of non-uniform strain the crystal lattice potential changes according to the displaced atom position *r'*: $\mathbf{r}_i' = \mathbf{r}_i + \sum_{j=x,y,z} \varepsilon_{ij}\mathbf{r}_j$ where *r* is the original position without strain. Displacement modifies the operators, for example $\mathbf{k}_i' = \mathbf{k}_i - \sum_{j=x,y,z} \varepsilon_{ij}\mathbf{k}_j$, as well as the total Hamiltonian. Analytic computations of the band structure with strained lattice can be found in [139]. In GaAs/AlGaAs nanostructures, effect of strain is

negligible due to the small lattice constant difference of GaAs and AlAs. but cannot be avoided for GaAs/InGaAs nanostructures or with external stress.

2D confinement, QWR

The case of 2D confinement (QWR) is an extension of the 1D (QW). The VB Hamiltonian has the same form as for QWs, but now its elements are given by:

$$H_{4x4}^{k.p} = \begin{pmatrix} -P+Q & -S^* & R & 0 \\ -S & -P-Q & 0 & R \\ R^* & 0 & -P-Q & S^* \\ 0 & R^* & S & -P+Q \end{pmatrix} + V(z)$$

where $P = \frac{\hbar}{2m_0}\gamma_1(z,y)\left(k_x^2 - \frac{\partial^2}{\partial y^2} - \frac{\partial^2}{\partial z^2}\right), Q = \frac{\hbar}{2m_0}\gamma_2(z,y)\left(k_x^2 - \frac{\partial^2}{\partial y^2} + 2\frac{\partial^2}{\partial z^2}\right),$

$S = 2\sqrt{3}\frac{\hbar}{2m_0}\gamma_3(z,y)\left(-ik_x\frac{\partial}{\partial z} + i\frac{\partial}{\partial y}\frac{\partial}{\partial z}\right), R = -\sqrt{3}\frac{\hbar}{2m_0}\left(\gamma_2(z,y)\left(k_x^2 - k_y^2\right) - 2i\gamma_3(z,y)k_x k_y\right)$

As in the QW case, the QWR band structure depends strongly on the confinement potential shape (size and depth). Considering the simplest case of QWRs with rectangular symmetry and infinitely high potential walls, the momentum vector has one more quantization axis, and $\mathbf{k} = \left[0, \frac{\pi j}{L_y}, \frac{\pi n}{L_z}\right]$. In this case, the off-diagonal coefficients of the k.p 4x4 Hamiltonian (*R* and *S*) are not equal to 0 at the lowest energy states. Thus, VB mixing is always taking place and impact son optical properties. The reduced dimensionality also affects the lower energy VB states, resulting in LH-like states [140].

3D confinement, QD

The 3D quantum confinement regime can be achieved if we limit the charge carrier motion in all 3 dimensions. In this case the energy spectra consist of discrete states instead of bands, and each VB state has HH and LH portions (components). Similarly to the QW (or QWR) cases, in the case of QDs a set of differential equations for valence band wavefunctions is obtained by changing the ***k*** vector by operator $k_\mu \rightarrow \left(-i\frac{\partial}{\partial \mu}\right)$. Plus, now all material parameters are dependent on all position coordinates. The valence band Luttinger Hamiltonian is derived in [141]. In order to facilitate setting the boundary conditions at the heterostructure interfaces, we modify the terms involving Q as [142]

$$Q(\mathbf{r})k_\mu \rightarrow \frac{Q(\mathbf{r})}{2}\left(i\frac{\partial}{\partial x_\mu}\right)+\left(-i\frac{\partial}{\partial x_\mu}\right)\frac{Q(\mathbf{r})}{2}$$

$$Q(\mathbf{r})k_\mu k_\nu \rightarrow \left(-i\frac{\partial}{\partial x_\mu}\right)\frac{Q(\mathbf{r})}{2}\left(-i\frac{\partial}{\partial x_\nu}\right)+\left(-i\frac{\partial}{\partial x_\mu}\right)\frac{Q(\mathbf{r})}{2}\left(-i\frac{\partial}{\partial x_\mu}\right)$$

The Hamiltonian then becomes

$$H=\begin{bmatrix} D_{HH} & -S & R & 0 \\ -S^\dagger & D_{LH} & 0 & R \\ R^\dagger & 0 & D_{LH} & S \\ 0 & R^\dagger & S^\dagger & D_{HH} \end{bmatrix}$$

with

$$D_{HH}=-\frac{\hbar}{2m_e}\left[\frac{\partial}{\partial x}(\gamma_1+\gamma_3)\frac{\partial}{\partial x}+\frac{\partial}{\partial y}(\gamma_1+\gamma_3)\frac{\partial}{\partial y}+\frac{\partial}{\partial z}(\gamma_1-2\gamma_3)\frac{\partial}{\partial z}\right]+V$$

$$D_{HH}=-\frac{\hbar}{2m_e}\left[\frac{\partial}{\partial x}(\gamma_1-\gamma_3)\frac{\partial}{\partial x}+\frac{\partial}{\partial y}(\gamma_1-\gamma_3)\frac{\partial}{\partial y}+\frac{\partial}{\partial z}(\gamma_1+2\gamma_3)\frac{\partial}{\partial z}\right]+V$$

$$R=\frac{\hbar}{2m_e}\sqrt{3}\left[\frac{\partial}{\partial x}\left(\frac{2\gamma_3+\gamma_2}{3}\right)\frac{\partial}{\partial x}-\frac{\partial}{\partial y}\left(\frac{2\gamma_3+\gamma_2}{3}\right)\frac{\partial}{\partial y}-i\frac{\partial}{\partial x}\left(\frac{2\gamma_3+\gamma_2}{3}\right)\frac{\partial}{\partial y}-i\frac{\partial}{\partial y}\left(\frac{2\gamma_3+\gamma_2}{3}\right)\frac{\partial}{\partial x}\right]+$$
$$+\frac{\hbar}{m_e}\frac{2}{\sqrt{6}}\left[\frac{\partial}{\partial x}(\gamma_3-\gamma_2)\frac{\partial}{\partial z}+\frac{\partial}{\partial z}(\gamma_3-\gamma_2)\frac{\partial}{\partial x}+i\frac{\partial}{\partial y}(\gamma_3-\gamma_2)\frac{\partial}{\partial z}+i\frac{\partial}{\partial z}(\gamma_3-\gamma_2)\frac{\partial}{\partial y}\right]$$

$$S=-\frac{\hbar}{2m_e}\sqrt{3}\left[\frac{\partial}{\partial x}\left(\frac{\gamma_3+2\gamma_2}{3}\right)\frac{\partial}{\partial z}+\frac{\partial}{\partial z}\left(\frac{\gamma_3+2\gamma_2}{3}\right)\frac{\partial}{\partial x}-i\frac{\partial}{\partial y}\left(\frac{\gamma_3+2\gamma_2}{3}\right)\frac{\partial}{\partial z}-i\frac{\partial}{\partial z}\left(\frac{\gamma_3+2\gamma_2}{3}\right)\frac{\partial}{\partial y}\right]-$$
$$-\frac{\hbar}{2m_e}\sqrt{\frac{2}{3}}\left[\frac{\partial}{\partial x}(\gamma_3-\gamma_2)\frac{\partial}{\partial x}-\frac{\partial}{\partial y}(\gamma_3-\gamma_2)\frac{\partial}{\partial y}+i\frac{\partial}{\partial x}(\gamma_3-\gamma_2)\frac{\partial}{\partial y}+i\frac{\partial}{\partial y}(\gamma_3-\gamma_2)\frac{\partial}{\partial x}\right]$$

where $\gamma_1,\gamma_2,\gamma_3$ are, as before, the Luttinger parameters.

The solution of this Hamiltonian yields the total VB wavefunctions:

$$|\varphi_{vb}\rangle=\varphi_{HH\uparrow}\left|\frac{3}{2},\frac{3}{2}\right\rangle+\varphi_{LH\uparrow}\left|\frac{3}{2},\frac{1}{2}\right\rangle+\varphi_{HH\downarrow}\left|\frac{3}{2},-\frac{3}{2}\right\rangle+\varphi_{LH\downarrow}\left|\frac{3}{2},-\frac{1}{2}\right\rangle$$

where $\varphi_{HH\uparrow}$ is the heavy hole part with spin up, $\varphi_{HH\downarrow}$ with spin down, and $\varphi_{LH\downarrow}$ the light hole part with spin down and $\varphi_{LH\uparrow}$ with spin up. Coming back to the atomic basis, the VB function reads

$$|\varphi_{vb}\rangle = |\varphi_{vb\uparrow}\rangle + |\varphi_{vb\downarrow}\rangle = \left(\frac{1}{\sqrt{2}}\varphi_{HH\uparrow} - \frac{1}{\sqrt{6}}\varphi_{LH\downarrow}\right)|X\uparrow\rangle + i\left(\frac{1}{\sqrt{2}}\varphi_{HH\uparrow} + \frac{1}{\sqrt{6}}\varphi_{LH\downarrow}\right)|Y\uparrow\rangle - \sqrt{\frac{2}{3}}\varphi_{LH\uparrow}|Z\uparrow\rangle +$$
$$+\left(\frac{1}{\sqrt{2}}\varphi_{HH\downarrow} - \frac{1}{\sqrt{6}}\varphi_{LH\uparrow}\right)|X\downarrow\rangle - i\left(\frac{1}{\sqrt{2}}\varphi_{HH\downarrow} + \frac{1}{\sqrt{6}}\varphi_{LH\uparrow}\right)|Y\downarrow\rangle + \sqrt{\frac{2}{3}}\varphi_{LH\downarrow}|Z\downarrow\rangle$$

2.2 Optical transitions

2.2.1 Charge carrier-photon interaction

The Hamiltonian describing the interaction between an electron and an electromagnetic field is [143]:

$$H(t) = \left[\frac{\left(\hat{p} + e\hat{A}(r,t)\right)^2}{2m_e} + V(r) + e\phi_{(r,t)}\right]$$

Where $\hat{A}(\mathbf{r},t) = \frac{2E_0\hat{e}}{i\omega}\left(e^{i(\mathbf{kr}-\omega t)} - h.c.\right)$ is the vector potential of the photon, $V(r)$ is a confinement potential and $\phi_{(r,t)}$ is a scalar electric potential, and m_e the effective electron mass. We consider the electromagnetic field as a weak perturbation, thus we neglect quadratic terms in the vector potential. The Gauge field is chosen such that $\phi = 0$. The perturbation Hamiltonian then reads as:

$$\hat{V}_{photon}(\mathbf{r},t) = \frac{2E_0 e}{i\omega m_e}\left(e^{i(\mathbf{kr}-\omega t)} - h.c.\right)\hat{e}\hat{p}$$

where $\hat{e}$ is the field polarization vector, $\hat{p}$ is the momentum operator and E_0 the electric field amplitude. In the case of our nanostructures, the confinement potential confines charged carriers to regions much smaller than the wavelength, thus effectively $\omega \to 0$. The perturbed Hamiltonian part then represents a dipole operator $\hat{V}_{photon}(r,t) = A_0\hat{e}\hat{p}$.

Using time-dependent perturbation theory, the transition rate between an initial and a final state of the electrons is given by Fermi's golden rule [143]:

$$w_{i\to f} \propto A_0^2 \langle f|\hat{e}\hat{p}|i\rangle^2 \delta\left(E_f - E_i - \hbar\omega\right)$$

The total transition rate, taking into account all states within the bands, is given by [143]:

$$W = \sum_f w_{i \to f} \rho_{ij} f_i \left(1 - f_f\right)$$

where ρ_{ij} is density of states and f_f , f_i are Fermi distributions functions. In our study, we will thus be mostly interested in the optical transition matrix elements $M_{fi} = \langle f | \hat{e}\hat{p} | i \rangle$, which define in particular the optical-polarization selection rules.

2.2.2 Valence band mixing and light polarization

Since the valence band states in our nanostructures have specific angular momentum, the transition rates depend on the polarization state of the absorbed or emitted photons. Using the result from previous section and table 2.1 we can calculate the dipole matrix elements in single crystal lattice unit cell:

$$\langle \varphi_{cb} \downarrow | \mathbf{e} \cdot \mathbf{p} | \varphi_{vb} \downarrow \rangle \propto \left(\frac{1}{\sqrt{2}} \varphi_e \cdot \varphi_{HH\uparrow} - \frac{1}{\sqrt{6}} \varphi_e \cdot \varphi_{LH\downarrow} \right) e_x + i \left(\frac{1}{\sqrt{2}} \varphi_e \cdot \varphi_{HH\uparrow} + \frac{1}{\sqrt{6}} \varphi_e \cdot \varphi_{LH\downarrow} \right) e_y - \left(\sqrt{\frac{2}{3}} \varphi_e \cdot \varphi_{LH\downarrow} \right) e_z$$

$$\langle \varphi_{cb} \uparrow | \mathbf{e} \cdot \mathbf{p} | \varphi_{vb} \uparrow \rangle \propto \left(\frac{1}{\sqrt{2}} \varphi_e \cdot \varphi_{HH\uparrow} + \frac{1}{\sqrt{6}} \varphi_e \cdot \varphi_{LH\downarrow} \right) e_x - i \left(\frac{1}{\sqrt{2}} \varphi_e \cdot \varphi_{HH\uparrow} - \frac{1}{\sqrt{6}} \varphi_e \cdot \varphi_{LH\downarrow} \right) e_y - \left(\sqrt{\frac{2}{3}} \varphi_e \cdot \varphi_{LH\downarrow} \right) e_z$$

where φ_e is the electron component, φ_{HH} heavy hole (HH) component, φ_{LH} light hole component,

which yields the emission/absorption intensity as: $I \propto \langle \varphi_{cb} \downarrow | \mathbf{e} \cdot \mathbf{p} | \varphi_{vb} \downarrow \rangle^2 + \langle \varphi_{cb} \uparrow | \mathbf{e} \cdot \mathbf{p} | \varphi_{vb} \uparrow \rangle^2$

Integration of this expression over the crystal (all unit cells) leads to total emission intensity. Since spin states are not resolved, the total intensity is the sum over terms with different sin states: $\varphi_{LH\downarrow} = \varphi_{LH\uparrow}$ $\varphi_{HH\downarrow} = \varphi_{HH\uparrow}$ As a result, the total emission intensity is isotropic in the XY plane:

$$I_{xy} \propto \left(\langle \varphi_e | \varphi_{HH} \rangle^2 + \frac{1}{3} \langle \varphi_e | \varphi_{LH} \rangle^2 \right)$$

and anisotropic in the XZ or YZ planes. The intensity in z direction can be expressed as:

$$I_z \propto \left(\frac{4}{3} \langle \varphi_e | \varphi_{LH} \rangle^2 \right)$$

The hole character involved in the transition is not a directly measurable quantity. However, using a polarization resolved PL setup scheme (see Chapter 3 and 5) one can distinguish between two different linear polarizations of the emitted light, and derive linear polarization

defined as: $DOLP = \frac{I_z - I_{xy}}{I_z + I_{xy}}$. Substituting the expression for the intensities we get:

$$DOLP = \frac{\langle \varphi_e | \varphi_{LH} \rangle^2 - \langle \varphi_e | \varphi_{HH} \rangle^2}{\frac{5}{3}\langle \varphi_e | \varphi_{LH} \rangle^2 + \langle \varphi_e | \varphi_{HH} \rangle^2}$$

Thus, using this DOLP value one can find the VB hole character, represented by the ratio of LH and HH projections on the CB wavefunction:

$$\frac{\langle \varphi_e | \varphi_{LH} \rangle}{\langle \varphi_e | \varphi_{HH} \rangle} = \sqrt{\frac{1 + DOLP}{1 - \frac{5}{3} DOLP}}$$

It can further be shown that the intensity of emitted light in the plane of the nanostructure growth direction (ZX for example) is proportional to the following expression:

$$I(\alpha) \propto \langle \varphi_e | \varphi_{HH} \rangle^2 \cos^2\alpha + \frac{4}{3}\langle \varphi_e | \varphi_{LH} \rangle^2 \sin^2\alpha + \frac{1}{3}\langle \varphi_e | \varphi_{LH} \rangle^2 \cos^2\alpha - \frac{2}{\sqrt{3}}\langle \varphi_e | \varphi_{HH} \rangle \langle \varphi_e | \varphi_{LH} \rangle \sin 2\alpha$$

where a is the angle in the XZ plane with respect to the QD growth direction. In particular, for LH-like VB ground state with very high purity, $\langle \varphi_e | \varphi_{HH} \rangle = 0$, we get

$$I \propto \langle \varphi_e | \varphi_{LH} \rangle^2 \sin^2\alpha + 0.25 \langle \varphi_e | \varphi_{LH} \rangle^2 \cos^2\alpha$$

Thus, a maximum DOLP value of GS of 0.6 is obtained. In the other extreme case where QD VB state is purely HH-like, $\langle \varphi_e | \varphi_{LH} \rangle = 0$ and hence $I \propto \langle \varphi_e | \varphi_{HH} \rangle^2 \cos^2\alpha$. Thus the DOLP value is -1.

2.3 Excitons

Electron-hole pairs excited in an otherwise electrically neutral semiconductor attract each other due to the Coulomb interaction. This gives rise to bound electron-hole pairs called excitons. Excitons have finite lifetimes and can decay radiatively into photons following the electron-hole recombination.

2.3.1 General concept of excitons

There are two types of excitons, depending on the material properties. Semiconductors with a small dielectric constant support Frenkel excitons. Because of the small dielectric constant, Coulomb interaction is strong as a consequence the size of the exciton is comparable with the

lattice constant. The second type is the Wannier-Mott excitons observed in semiconductors with large dielectric constants [144]. In contrast to Frenkel excitons, Coulomb interaction is weak and the exciton size can rich tens of lattice constants. GaAs and related compounds have high dielectric constant, hence we consider in more detail the Wannier-Mott excitons.

The Hamiltonian for an oppositely charged electron-hole pair in a semiconductor is:

$$\left[\left(E_{cb}-\frac{\hbar^2}{2m_e}\nabla_e^2\right)-\left(E_{vb}+\frac{\hbar^2}{2m_h}\nabla_h^2\right)-\frac{e^2}{4\pi\varepsilon_0\varepsilon_m\left|\mathbf{R}_e-\mathbf{R}_h\right|}+V_e(\mathbf{R}_e)+V_h(\mathbf{R}_h)\right]\psi(\mathbf{R}_e,\mathbf{R}_h)=E\psi(\mathbf{R}_e,\mathbf{R}_h)$$

where m_e, m_h are effective electron and hole masses $\mathbf{R}_h$, $\mathbf{R}_e$ electron and hole positions, $V_e(\mathbf{R}_e)$, $V_h(\mathbf{R}_h)$ confinement potentials, $\psi(\mathbf{R}_e,\mathbf{R}_h)$ exciton wavefunction, E_{cb}, E_{vb} conduction and valence band energies and ε_m dielectric constant. It contains three parts: kinetic energies of the electron and hole, Coulomb interaction and confinement potential. In case of free excitons (no confinement potential), this equation can be solved by defining the coordinates of the center of mass of the exciton $\mathbf{R}_c=\frac{m_e\mathbf{R}_e+m_h\mathbf{R}_h}{m_e+m_h}$, the relative electron-hole position $\mathbf{R}=\mathbf{R}_e-\mathbf{R}_h$, and the reduced mass defined by $\frac{1}{m_{eh}}=\frac{1}{m_e}+\frac{1}{m_h}$.

The Hamiltonian in the new coordinate system is [143]:

$$\left[\left(E_g-\frac{\hbar^2}{2(m_e+m_h)}\nabla_{CM}^2\right)+\left(-\frac{\hbar^2}{2m_{eh}}\nabla^2-\frac{e^2}{4\pi\varepsilon_0\varepsilon_m\left|\mathbf{R}\right|}\right)+V(\mathbf{R}_{CM},\mathbf{R})\right]\psi(\mathbf{R}_{CM},\mathbf{R})=E\psi(\mathbf{R}_{CM},\mathbf{R})$$

For free electron and holes in bulk, the Hamiltonian separates into two independent parts, first describing the free center of mass motion, and the second, hydrogen-atom like Hamiltonian for the relative motion. Thus, the solution can be written $\psi(R_{CM},R)=\psi_{CM}(R_{CM})\psi(R)$ the Schroedinger equation for the relative particle motion becomes:

$$\left[-\frac{\hbar^2}{2m_{eh}}\nabla^2-\frac{e^2}{4\pi\varepsilon_0\varepsilon_m\left|\mathbf{R}\right|}\right]\psi(\mathbf{R})=E\psi(\mathbf{R})$$

For free excitons, the energy spectra are thus similar to the case of the hydrogen atom, with energies $E_n^{3D}=-\frac{m_{eh}}{2n^2}\left(\frac{e^2}{4\pi\varepsilon_0\varepsilon_m\hbar}\right)^2$ where n is a state number. Thus the exciton energy for the ground state is $E_{EX}=-\frac{m_{eh}}{2}\left(\frac{e^2}{4\pi\varepsilon_0\varepsilon_m\hbar}\right)^2$. In analogy with the hydrogen atom, one also has the

exciton Bohr radius: $a_{Bohr} = \frac{4\pi\varepsilon_0\varepsilon_m\hbar^2}{m_{eh}e^2}$. For bulk GaAs, this binding energy $E_X = -E_{EX}$ is 4.2 meV and the exciton Bohr radius is ~11 nm.

2.3.2 Excitons in low-dimensional structures

Excitons can also form in low dimensional systems such as QWs, QWRs, and QDs. The exciton binding energy in these systems is usually larger than in bulk because of the electron and hole are confined by the potential and this increases their Coulomb interaction. In bulk the total exciton energy is a sum of energy of free electron-hole pair plus exciton binding energy.

$$E_X = E_g - E_{Coulomb}^{e-h}$$

The expression for arbitrary dimension α can be derived analytically using fractional dimensional theory [145].

$$E_x^b = \frac{E_x^b(bulk)}{\left(1+(\alpha-3)/2\right)^2}$$

For strictly 2D systems, the limit of highly confined QWs ($\alpha = 2$), the binding energy is 4 times higher than in bulk [145]. In finite-potential GaAs QWs, observed exciton binding energies are as high as < 20 meV [146] [147][148]. That makes excitonic spectra features dominant even at room temperatures. The nanostructure dimensionality can be estimated by using formula 3.1, QW dimensionality α from 2 to 3, for QWR α from 1 to 2. Fractional dimensional theory approach also have been used for calculation real QWR structures in [149].

The exciton binding energy in strictly 1D QWRs approaches infinity. In real structures it is finite and depends on the confinement potential; binding energies as high as ~27 meV were reported for T-shaped GaAs QWRs [150].

In confined systems the total exciton energy is:

$$E_X = E_g + E_{cb} + E_{vb} - E_{Coulomb}^{e-h}$$

where E_{cb} and E_{vb} confinement energies of CB and VB. As a conscience the exciton energy depends on the confinement potential of the nanostructure. Thus QDs, the excitonic structure depends on the relative size of quantum confinement energy and the electron-hole Coulomb energy. Usually in small QDs confinement is strong compared to the Coulomb interaction. Thus, exciton spectra are dominated not by Coulomb interaction as in bulk or QWs but by QD single-particle energy levels structure. The Coulomb interaction in the case of strong

confinement can be considered as a perturbation [151]. The perturbation Hamiltonian is then written as:

$$E_{Coulomb}^{e-h} = \iint \psi_{cb}\psi_{vb} \frac{e^2}{4\pi\varepsilon_0\varepsilon|\mathbf{r}_{cb}-\mathbf{r}_{vb}|}\psi_{cb}^{*}\psi_{vb}^{*}d\mathbf{r}_{cb}d\mathbf{r}_{vb}$$

where ψ_{vb}, ψ_{cb} are the valence and conduction band wavefunctions, r_{cb}, r_{vb} the electron and hole positions. This approach is applicable to the pyramidal QDs investigated in subsequent chapters.

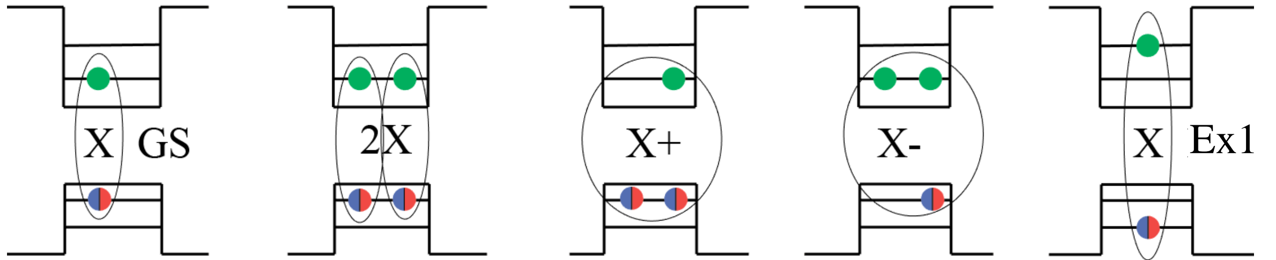

Figure 2.4 Schematic picture of possible exciton states in a QD.

Thus, for strongly confined QDs the features of the QD “excitons” are largely determined by the 3D confined CB (electron) and VB (hole) states. Some important types of QD excitons are illustrated schematically in figure 2.4. A QD can accommodate a finite number of charge carriers, limited by the number of confined states and subject to the Pauli principle. As a result, the QD can accommodate a single exciton X, biexciton 2X and eventually multi-exciton nX neutral states. Carriers at excited states of the QD can form excited exciton states such as the Ex1 state in figure 2.4. The QD can also confine charged exciton states such as the negatively charged X- and the positively charge X+ trions (see figure 2.4). Correspondent total energies

$$E_{X-} = E_g + 2E_{GS}^{e} + E_{GS}^{h} - 2E_{Coulomb}^{e-h} + E_{Coulomb}^{e-e}$$

$$E_{X+} = E_g + E_{GS}^{e} + 2E_{GS}^{h} - 2E_{Coulomb}^{e-h} + E_{Coulomb}^{h-h}$$

$$E_{2X} = E_g + 2E_{GS}^{e} + 2E_{GS}^{h} - 4E_{Coulomb}^{e-h} + E_{Coulomb}^{e-e} + E_{Coulomb}^{h-h}$$

Multiple-charged excitons have been observed in pyramidal QDs [152] and quantum rings [153]. Depending on the carrier configuration and the nanostructure geometry/composition, the QD exciton binding energy can be positive or negative [151][154][155]. Expressions for binding energies are following:

$$E^{b}_{X-} = -E^{e-h}_{Coulomb} + E^{e-e}_{Coulomb}$$

$$E^{b}_{X+} = -E^{e-h}_{Coulomb} + E^{h-h}_{Coulomb}$$

$$E^{b}_{2X} = -2E^{e-h}_{Coulomb} + E^{e-e}_{Coulomb} + E^{h-h}_{Coulomb}$$

2.4 Numerical simulation

The analytical expressions for the wavefucntions and optical spectra presented above were used in order to numerically simulate these parameters for the specific pyramidal nanostructures studied in Chapters 4, 5 and 6. Here we describe how a given pyramidal nanostructure is modelled.

2.4.1 Modelling of pyramidal nanostructures

Consider first the modelling of a uniform, vertical AlGaAs QWR formed in the inverted pyramid (figure 2.5 (a)); the QWR length is limited by vertical barriers with higher Al content (cladding layers, not shown). The gray region corresponds to nominal (bulk) Al content, and the other different colors correspond to the different nanostructure types, which differ from each other in Al content; the lowest Al concentration is at the center QWR (orange). Figure 2.5 (b) shows a schematic cut of the pyramid through a plane containing the vertical QWs. Figure 2.5 (c) presents a top-view SEM of a grown structure after surface etching. The different crystallographic planes are visible and the main quantum nanostructures are indicated.

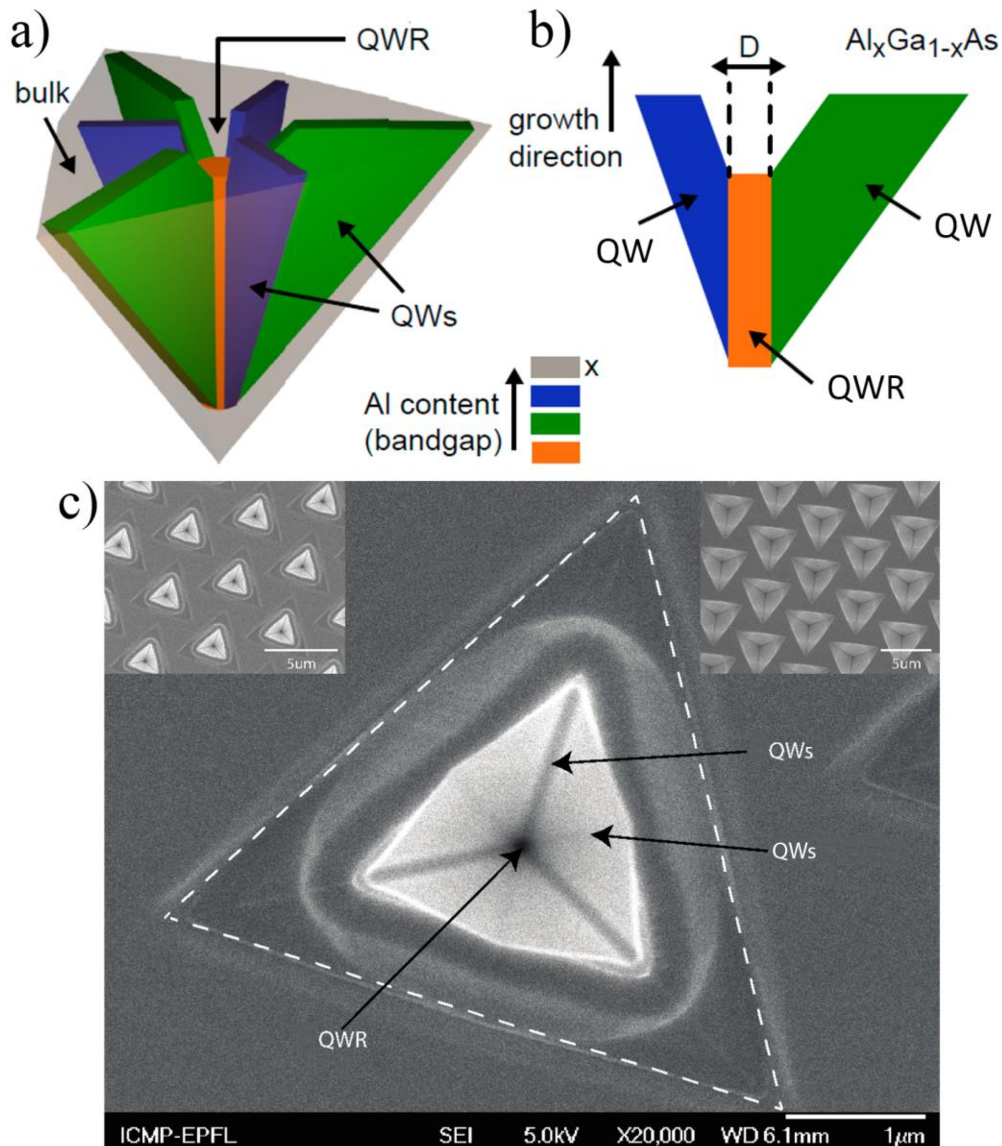

Figure 2.5 Schematic presentation of QWR/QD nanostructures in inverted pyramids: (a) 3D view, and (b) cross-section along one of the QWs (adapted from [56]*). (c) Top SEM image of a pyramidal structure after growth and surface etching. The left inset shows the array of etched pyramids after growth; the right one shows the patterned substrate before growth.*

We introduce several simplifications in order to facilitate the modelling. For long QWR structures, we use a cylindrical QWR core of constant diameter (typically 18 nm) and (segregated) Al content with slab-shaped side-QWs only with the correspondingly segregated AlGaAs composition. By modifying the Al content distribution along the growth direction, we may then form QDs or other tailored-potential 1D nanostructures. Figure 2.6 presents schematically such a AlGaAs QD system. Note that changing the Al content along the growth direction gives rise to higher-dimensionality nanostructures in the side-QWs.

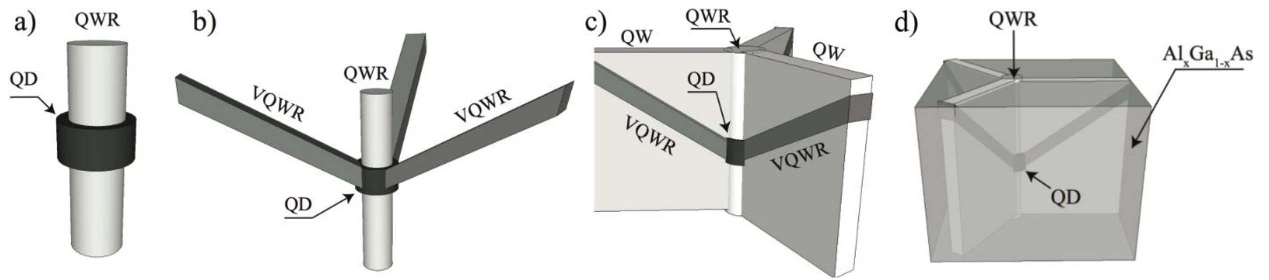

Figure 2.6 Schematic presentation of the components of the modeled QD nanostructures in pyramids. (a) Vertical QWR with QD (b) Central QWR/QD with Vicinal QWRs (c) addition of VQW regions (d) entire modeled system with bulk AlGaAs region.

From simple assumptions, one may estimate the effective AlGaAs composition in each segregated nanostructure type by following the formula for the segregated Al content [156]:

$$Al_{segr} = \frac{x}{x + K(1-x)}$$

Where x is the nominal (bulk) Al concentration of the grown alloy. This formula fits the measured emission line energy position by corresponding AlGaAs bandgap energy. By using this formula we can calculate the effective composition for each nanostructure shown in figures 2.5 and 2.6 (in our analysis we will neglect the vicinal QW/QWRs where the segregation effect is small). This was reported for the pyramidal nanostructures as shown in figure 2.7 [157]. This study showed that the segregated AL content in the side-QW region (green QW in figure 2.5 (a)) is characterized by K=2.1, and for vertical QWR (orange region in figure figure 2.5(a)) by K=8.6. The K parameters depend weakly on the growth temperature; the above-mentioned values will be used in all modelling in this thesis.

Knowing the composition of a given AlGaAs region in the pyramidal structure, the semiconductor bandgap and band edges can be determined using the well-established expression for the bandgap of $Al_xGa_{(1-x)}As$ at 0 K [137]:

$$E_g\left(Al_xGa_{1-x}As\right) = \left(1-x\right)E_g\left(GaAs\right) + xE_g\left(AlAs\right) - x\left(1-x\right)C$$

Where C is the so-called bowing parameter $C = -0.127 + 1.31x$, $E_g(GaAs)$= 1.519 eV and $E_g(AlAs)$= 3.1 eV. The ratio between the CB and VB offsets is taken as $\Delta_{CB}/\ \Delta_{VB}$ ~67/33 [158][159].

However, the effective Al content is not the same as the actual (segregated) one inside the nanostructure. In low dimensional quantum nanostructures (such as QD, QWR and QW) the emission line energy is a sum of the band gap energy, the confinement energy of electron and holes plus, in case of back etched pyramids, the effect of surface charges. The effect of the surface-related electric field can be estimated by comparing the QD/QWR ground state (GS) energy position after the surface etching and back-etching; this gives typically a spectral red shift of ~ 10

meV. All these effects need to be taken into account when comparing the experimental results and the simulated ones [113].

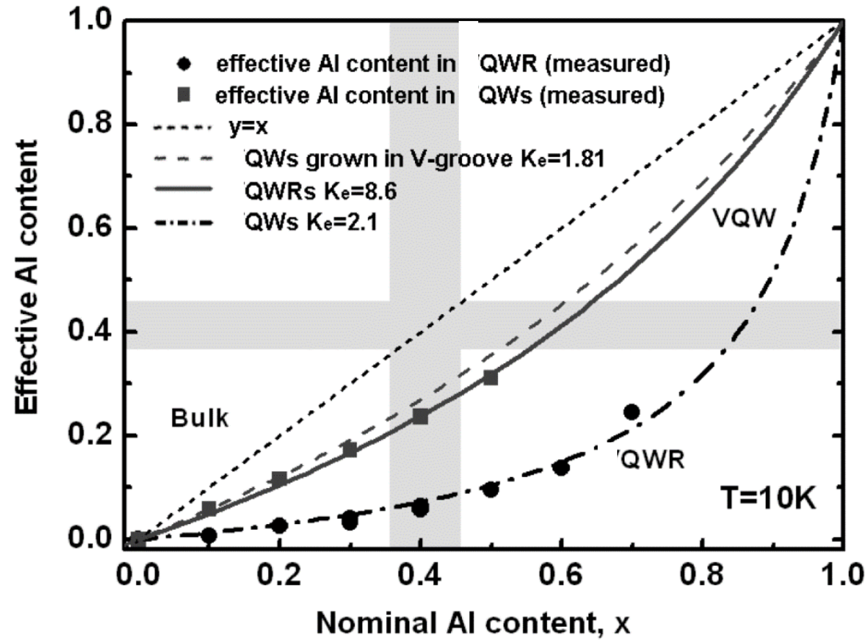

Figure 2.7. Actual (segregated Al content in different segregated nanostructures formed in inverted AlGaAs pyramids versus the nominal Al content of the parent alloy. Adopted from [113]

For the pyramidal structures consisting of an AlGaAs VQWR with a tailored Al content along the growth direction, we model the QWR as a cylinder of constant 18 nm diameter, with composition that varies along the pyramid axis according to the Al content tailoring. The vertical QWs formed on the side are added as slabs of the corresponding thickness and composition. In the case of thin GaAs QDs, with thickness<10 nm (see figure 2.8), the modeled structures have to take into account the lens shape of the QD.

The CB structure is calculated using the single band approximation described in Section 2.1.2, and the VB structure is calculated using the 4X4 Luttinger Hamiltonian presented in Section 2.1.3. The numerical solution of the obtained differential equations system was performed by using the method described in [142][160], applying the standard material parameters for GaAs and AlGaAs compounds [137]. The Hamiltonian was solved numerically using Matlab codes that were programed by Prof K.F. Karlsson. Effects of external electric fields, discussed in Chapter 6, were analyzed with the same approach, except that a term $H_E = qV_r$ was added to the Hamiltonian.

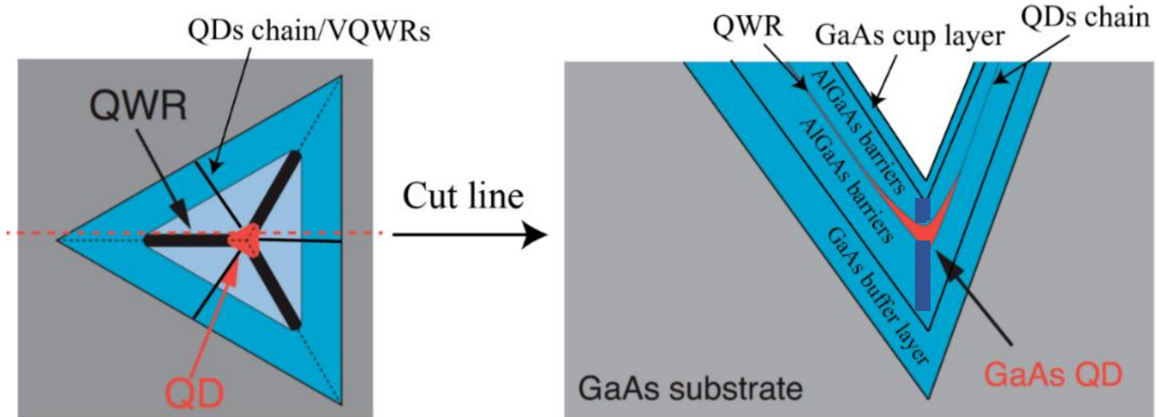

Figure 2.8 Schematic top view (left) and cross section (right) picture of a thin-GaAs QD pyramidal structure.

2.4.2 Example of simulation results

As an example of the numerical simulation, we simulate here a thin cylindrical AlGaAs QD nanostructure. The modeled volume is 40x40x100 nm with the QD in the center (as in schematic figure 2.6 d) and infinitely high potential barriers in the borders of this area. For simplicity, we consider the QD as a cylinder imbedded in a long QWR of the same diameter. The QD radius is 9 nm and its height is L=7 nm. The modeled Al content distribution is: in the QD 3%, in the side QWRs 10%, in the vertical QWR barriers 8%, in the QWs 23%, and in the bulk 40%.

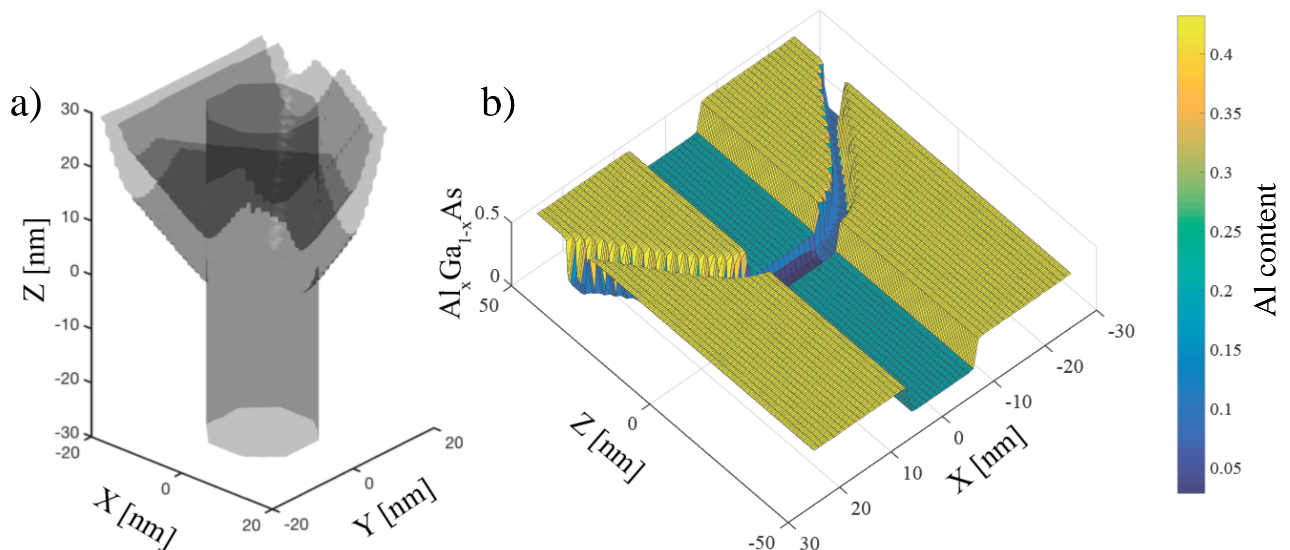

Figure 2.9. (a) 3D isosurface of Al content (x=0.4) in a simulated 10 nm thick GaAs QD nanostructure. (b) Z-X cut of the simulated nanostructure showing Al content distribution.

Figure 2.10 shows the calculated wavefunction isosurfaces for the electron (green), light hole (blue) and heavy hole (red) ground states and first excited ones. Red and blue correspond to

HH and LH parts of the VB wavefunction. The overlaps of given pairs of CB and VB states determine the strength of the transitions involved.

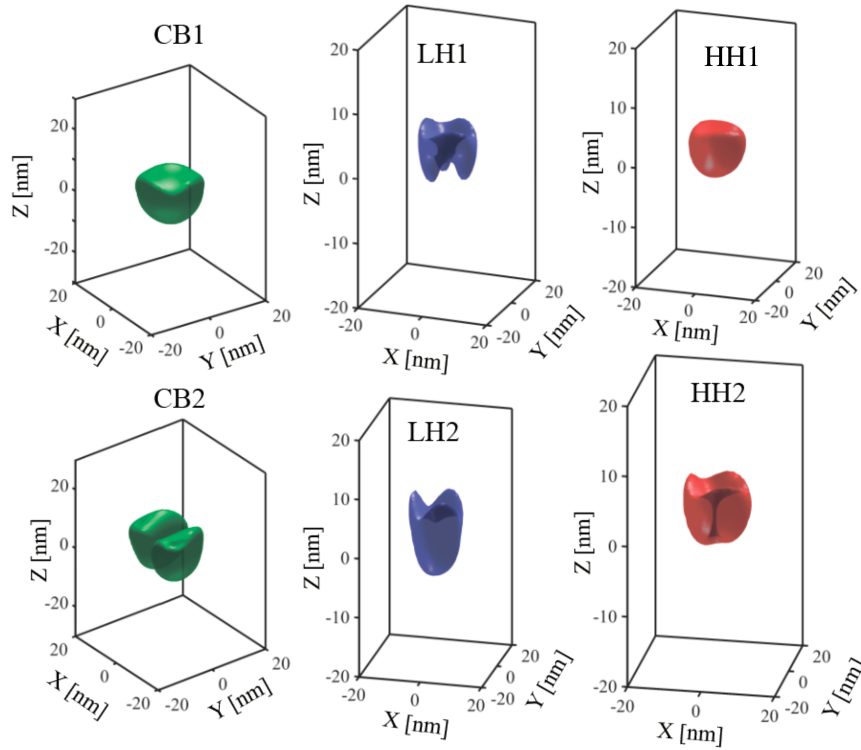

Figure 2.10. WFs isosurfaces of two lowest CB states (CB1, CB2) and VB states (LH1, HH1; LH2, HH2) of the $Al_{0.2}Ga_{0.8}As$ pyramidal QD. Correspondent energies from the CB (VB) edge indicated below each isosurface.

The resulting (normalized) optical spectra are presented in figure 2.11. The spectral lines in figure 2.11 (a) were calculated without taking into account Coulomb interaction between charged carriers. The different colors correspond to different transitions types: blue for the CB and LH component of the VB state and the red for CB and the HH part. Figure 2.11 (b) presents the spectra of the same structure but taking in to account Coulomb interaction as a perturbation and with artificial broadening of 2 meV, with different colors corresponding to polarization of the emitted light parallel or perpendicular to the growth direction.

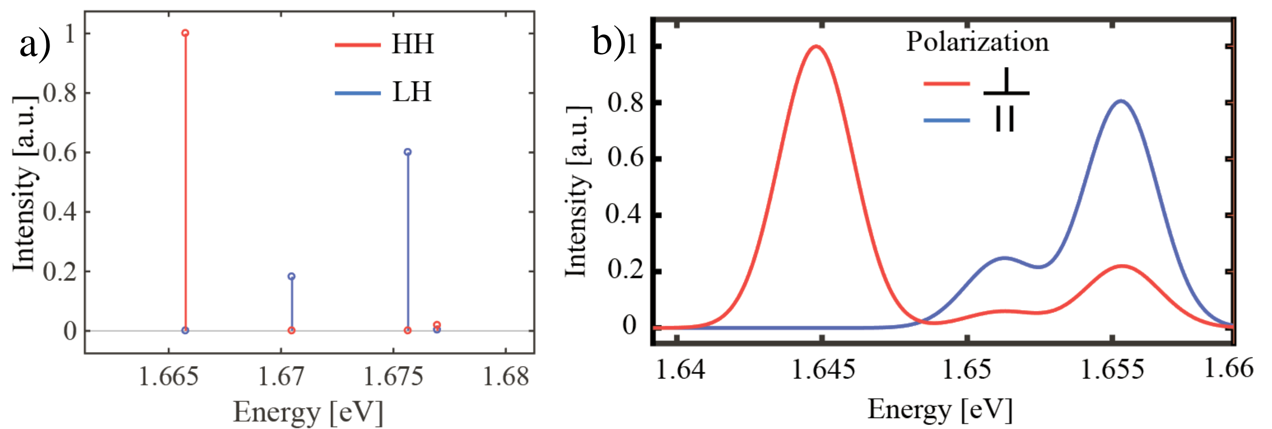

Figure 2. 11. Simulated optical absorption spectra for the $Al_{0.2}Ga_{0.8}As$ pyramidal QD: (a) without Coulomb interaction or broadening; (b) with Coulomb interaction as perturbation and artificial line broadening of 2 meV.

It can be seen that the ground state transition is polarized perpendicular to the growth direction due the HH character of the VB state involved. The excited states emission lines are polarized more along the growth direction (with a ratio of 4 to 1, or DOLP=0.6) due to the LH character of the VB states involved.

2.5 Summary

This chapter described the theoretical tools that we use to understand the impact of quantum confinement on the optical spectra in pyramidal quantum nanostructures and to interpret the experimental results obtained in the course of this thesis. The numerical model employed is sufficiently flexible in order to model and discuss the wide range of 3D nanostructures presented in this thesis. It will be a key tool for proposing specific designs of such nanostructures, eventually for constructing single photon sources with polarization control.

Chapter 3

Fabrication and characterization of pyramidal quantum nanostructures

Pyramidal quantum wires and dots are perfect systems for studying the effect of quantum confinement on optical properties due to the fine control over composition and nanostructure dimensions they offer. In this chapter, we present the fabrication and characterization tools and techniques we used for the realization of site-controlled heterostructures in inverted pyramids. In Section 3.1, we present the fabrication processes, including substrate patterning, MOVPE growth, post-growth processing and sample preparation for optical characterization. In Section 3.2 we describe the fabrication and characterization tools, including electron microscopy and different kinds of photoluminescence spectroscopy.

3.1 Fabrication of pyramidal heterostructures

In this section, we present the structure and growth techniques of site-controlled QWRs/QDs in pyramidal heterostructure and briefly review results of growth studies from previous works.

3.1.1 Substrate patterning

The first, important fabrication step is the substrate patterning. Substrate patterning defines the QD arrangement and QD density on the substrate. This makes the morphological quality and homogeneity of the substrate pattern crucial for obtaining high-quality QD ensembles. The steps of the process are illustrated in figure 3.1.

We use standard 2-inch wafer GaAs (111)B-oriented wafers and coat them by 60 nm thick SiO_2 or SiN layer using *plasma enhanced chemical vapor deposition* (PECVD) for mask deposition (see section 3.2). To remove moisture on the substrate prior to photoresist deposition we heat the substrate till 160^0C for 5 minutes. Next, we deposit photoresist as schematically shown in figure 3.1 (a). The resulting photoresist thickness after spinning is 0.5-1 μm. To remove the solvent from the photoresist, we bake the wafer for 5 min at 90 ^{0}C. For the photolithography step we used a mask aligner (see 3.10 b) to transfer the pattern to the photoresist using UV irradiation. The mask consists of circles placed at 5 μm distances, which allows easy subsequent access to single pyramids with optical spectroscopy. After exposure, a developing solution (MF-319) is

used to open circular holes above the mask layer (figure 3.1 (b)). Substrate baking at 115 ^{0}C is performed in order to produce smooth photoresist profiles, and later cleaning from residues in O_2 plasma etching step. For pattern transfer to the oxide layer, we use reactive ion etching (RIE) (see section 3.2). To remove the photoresist mask we use acetone and then cleaning with isopropanol and water rinsing (figure 3.1 (c)).

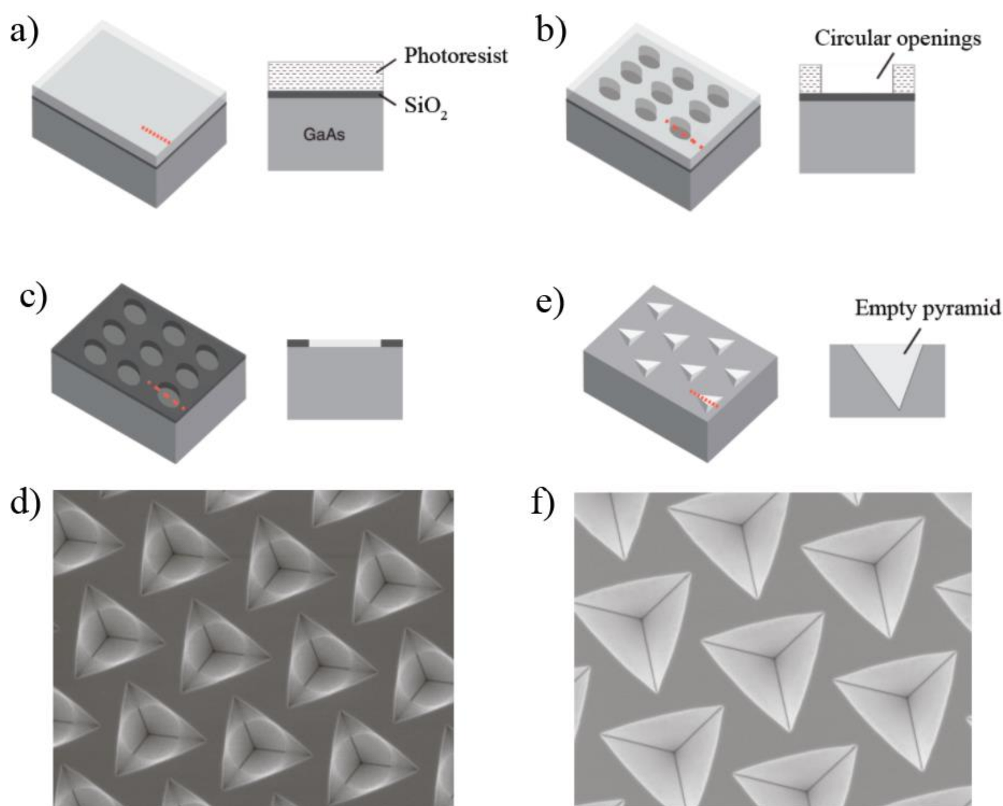

Figure 3.1. Schematic illustration of the substrate patterning process and its schematic cross-sections (a,b,c,e). a)The substrate after SiO_2 and photoresist deposition; b) substrate after photolithography step; c) pattern after RIE and photoresist removal; d) SEM image of a substrate with the patterned SiO_2 after the wet etching step; e) Schematic illustration of the patterned pyramids after SiO_2 removal; f) SEM image of substrate ready for growth. (a,b,c,e) adapted from [125].

Wet chemical etching is used for patterning the substrate by pyramidal openings, with the SiO_2 (or SiN) mask defining the dimensions of the pattern. We use 1% Br-Methanol solution for this step, which provides faster etching in the (111) B direction than in the (111)A ones [116] [110]. The result is an inverted tetrahedral pyramid, suitable for the growth of the site-controlled pyramidal heterostructure. Figure 3.1 (d) shows a scanning electron microscope (SEM) image of a sample after the wet etching step. Before MOVPE growth, we remove the SiO_2 (or SiN) layer by dipping in HF acid and removal of residues by O_2 plasma. A schematic picture of the resulting pattern is shown in figure 3.1 (e), and a SEM picture of a real sample is shown in figure 3.1 (f).

The exact procedure of substrate patterning including the important process parameters are described in detail in Appendix A.

3.1.2 MOVPE growth

The working principle of MOVPE is based on the gas carrier used to transport specific adatoms bounded to organic molecules in a gas phase to the substrate surface. As a carrier gas we use N_2, Al is transported by $Al_2(CH_3)_6$ (trimethyl-aluminium, TMAl), Ga by $Ga(CH_3)_3$ (trimethyl-gallium, TMGa), In (if needed) by $In(CH_3)_3$ (trimethylindium, TMIn), and As by Ultima II 6N5 grade arsine (AsH_3) from Matheson (also called as precursor molecules). Compounds including Group-III Al, Ga, In and group-V As atoms can thus be grown. Before the actual material deposition on the substrate, the substrates were deoxidized in the reactor under AsH_3 during ~ 4 min. All gases flow in the reactor chamber at low pressure (20 mbar) and high temperatures from 600-800ºC, depending on the deposited alloy. The reactor is made from materials inert to the reaction compounds. The reaction occurs on the substrate surface, which is mounted on a horizontal rotating support in order to obtain uniform growth.

The formation of GaAs crystalline layers relies on the reaction on the heated sample surface:

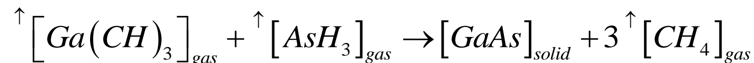

$$^{\uparrow}\left[Ga\left(CH\right)_3\right]_{gas} + {}^{\uparrow}\left[AsH_3\right]_{gas} \rightarrow \left[GaAs\right]_{solid} + 3\,{}^{\uparrow}\left[CH_4\right]_{gas}$$

This process is schematically shown in figure 3.2 (a), with TMGa and Arsine molecules in the reaction input dragged by N_2 and the substrate mounted on a reactor with rotating support. Figure 3.2 (b) is schematic illustration of the reaction process on the sample surface Showing the atomic arrangement near a monolayer step. The right panel shows a photo of the MOVPE installation at LPN-EPFL, with the glove box part and the reactor during growth (bright spot in the photo center).

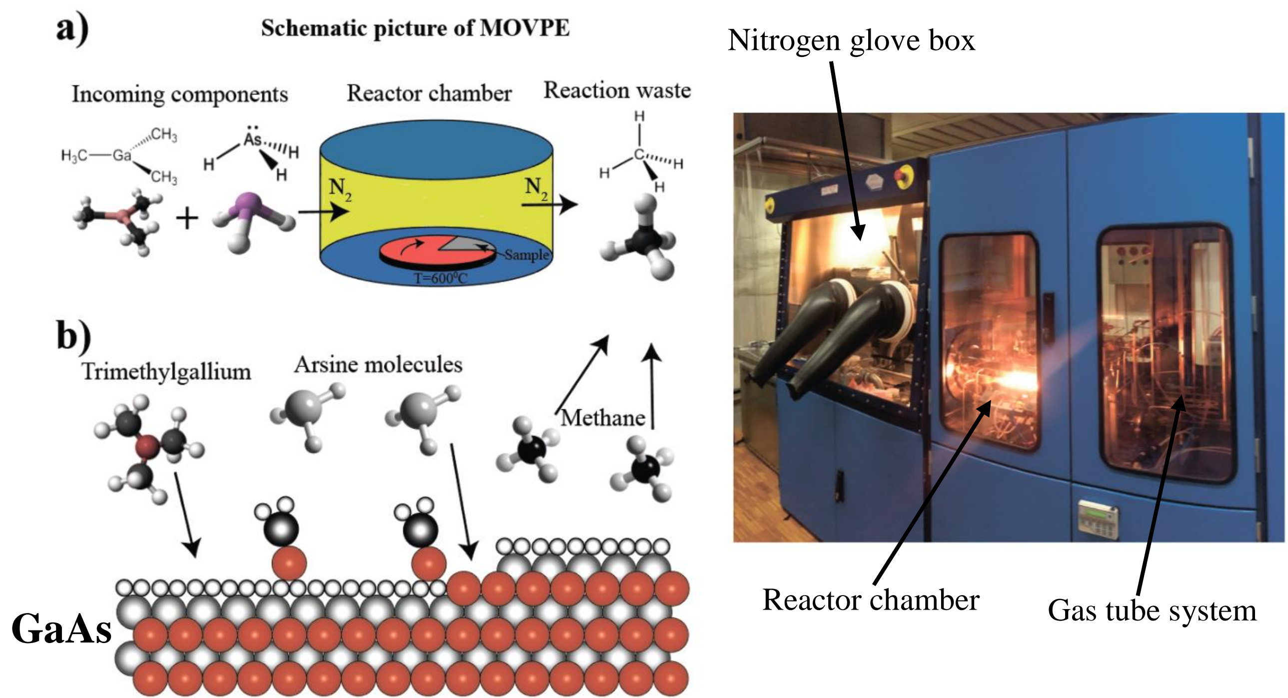

*Figure 3.2. Left: schematic of the MOVPE growth process (an example of GaAs): (a) schematic picture of growth reaction in the reactor chamber b) surface of substrate (*red: Ga, gray: As, black: C, white: H)*. Right: the MOVPE system in LPN-EPFL.*

For epitaxial growth of $Al_xGa_{1-x}As$ and $In_xGa_{1-x}As$ alloys, the analogous reactions with the replacement of Ga by Al or In is used. Of course, numerous important details are involved in this reaction, which has an impact on growth speed and the composition of the III/V compounds [109]. Starting from gas phase thermodynamics, parameters such as partial pressures and gas velocity that affect the "mass transport" or the growth rate can be set. By "mass transport", we mean gas phase diffusion of adatoms (Ga, As, Al, In) from the gas carrier to the substrate surface. The partial pressures determine the ratio III/V of adatoms on the substrate surface. Another significant parameter is the substrate temperature that affects the reaction kinetics of gas phase diffusion and the adatom surface diffusion and incorporation processes. The latter eventually determine the QWR/QD compositions in our pyramidal nanostructres. For example, it has been shown experimentally that the width of the self-limiting profile of the non-planar substrates increases with increasing temperature [109][161].

Prior to MOVPE growth, the purity of the deposited material must be assessed. For that purpose, we routinely grow a 15 nm-thick GaAs QW sandwiched between AlGaAs barriers, and by PL spectral analysis we are able to compare current system purity and growth quality with a reference QW sample. Following a design of the desired pyramidal nanostructures and programming the growth sequence into the computer-controlled MOVPE system, the corresponding III/V semiconductors layers are deposited on the patterned substrate. The growth parameters used in nanostructures growth in this thesis, including the V/III ratio, reactor chamber pressure, and substrate temperature are presented in appendix B. The nominal growth rates (as

measured on (100) GaAs surfaces) are about 0.06 nm/s, much smaller than the actual ones measured inside the inverted pyramids. The actual growth rate on the nonplanar pattern is a complex parameter determined by substrate pattern size and deposited alloy composition. The actual growth rates were calibrated by growing GaAs/AlGaAs superlattices and measuring the grown thicknesses using cross-sectional SEM imaging. For more details about the growth process in inverted pyramids on an example of parabolically shaped QDs see our publication [162].

3.1.3 Post-growth processing

To remove the irregular growth on the substrate (non-patterned) (111) B planes we used surface etching. Then, depending on the chosen study, we either cleave the sample or continue with back-etching for substrate removal. The aim of the back-etching step is to increase the emission efficiency of the nanostructure in order to facilitate the PL spectroscopy steps [124]. For polarization-resolved PL measurements, important for studies of VB mixing (see Chapter 5), we need to collect light perpendicular to the growth direction, and for that purpose we cleaved the sample through the pyramids and collected the PL from the cleaved edge [163]. The post-growth processing steps are described below in some detail.

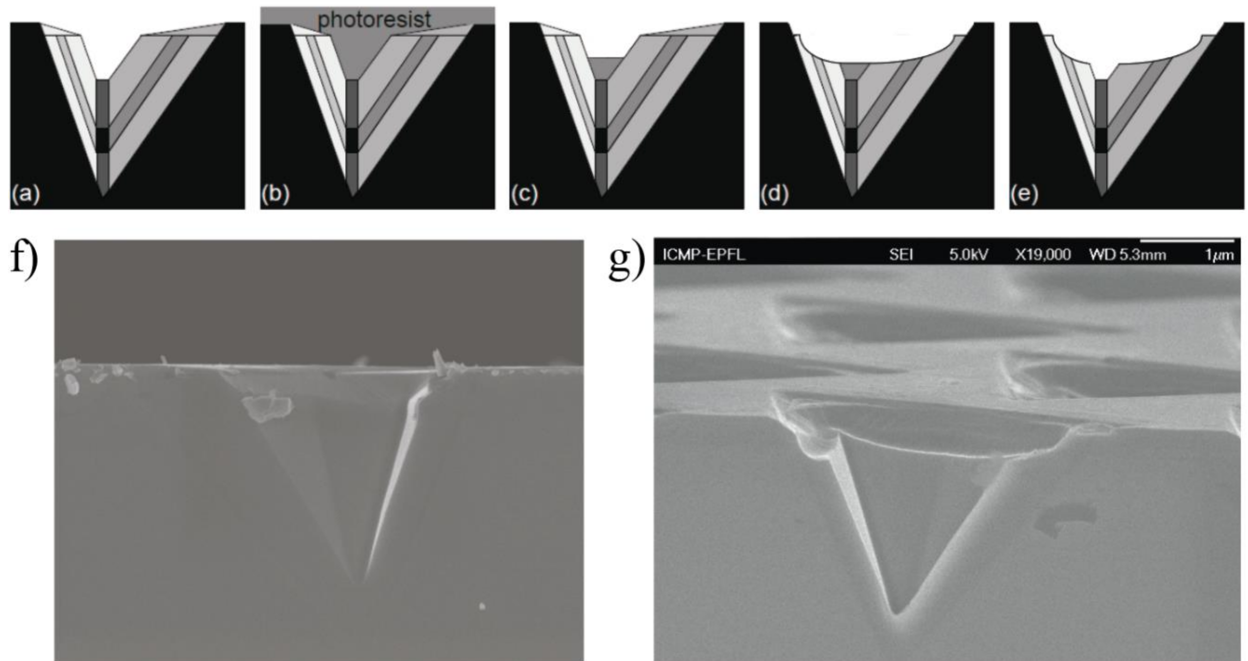

Figure 3.3 (a)-(e) Schematic pictures of post-growth surface etching process step by step. f) SEM picture before the surface etching g) SEM picture after surface etching. (a)-(e) adapted from [56]

Surface etching. Due to the finite growth rate on the (111) B "no-growth" planes, irregular growth takes place. This leads to spectral lines masking the PL emitted by the core quantum nanostructures inside the pyramids. The process of removing this irregular growth is illustrated in Fig. 3.3. Starting with the sample after growth (figure 3.3 (a)), we deposit photoresist

(S1805) homogeneously at 3500 rpm spin speed (figure 3.3 (b)), and then etch the sample by RIE with O_2 plasma till only resist inside the pyramidal opening is left (figure 3.3 (c)). The next step is wet chemical etching of the exposed surface, using H_2SO_4: H_2O_2:H_2O solution (figure 3.3 (d)). The final step is photoresist removal by acetone and cleaning in isopropanol and water (figure 3.3 (e)). The full process description with etching times and other parameters is presented in Appendix A. Figure 3.3 (f) and (g) show SEM images of the cleaved sample before and after the surface etching.

Back-etching. The main goal of the back-etching procedure is to increase the light collection efficiency by flipping the pyramidal structure and by GaAs substrate removal [110]. The substrate thickness is about 300 μm, thus the major part of it (200-220 μm) can be removed by mechanical polishing and the rest can be removed by slow selective wet etching.

Mechanical polishing. First, we deposit 20 nm Ti and 200 nm Au layers on top of the substrate by electron beam evaporation; the result is schematically shown in figure 3.4 (a). There are two reasons to do this. First, the metal film serves as a mirror reflecting light to the microscope objective during PL measurement, and second, it serves as mechanically stable support. Next, we glue the "golden" side with black wax onto another (111) B GaAs substrate that was cleaved in advance to have the same (or a bit bigger) size (figure 3.4 (b)). We then polished the sample under a certain mechanical pressure by Al_2O_3 microparticles with size of 5-15 μm, and constantly measure the sample size with 5 μm precision.

Chemical etching. The final and most important step is slow selective etching of the remaining thin GaAs substrate layer. For selective etching we used constant flow of NH_4OH : H_2O_2 (1:30) solution; the solution ratio may be adjusted to change etching speed. Due to the selective etching, islands of exposed pyramids appear on the sample surface; an example is shown in figure 3.4 (c). The etching is selective not only with respect to crystallographic directions but also to Al content. The etching reaction almost completely stops at the $Al_{0.75}Ga_{0.25}As$ cap layer deposited during the growth, which prevents damage of the core structure. Figure 3.4 (d) presents a top SEM image of a back-etched pyramid.

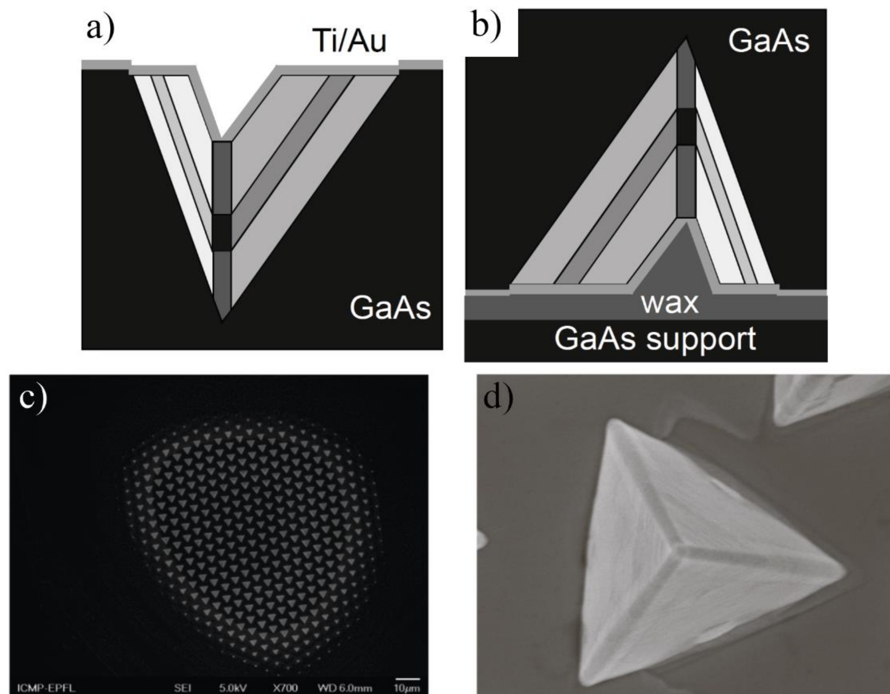

Figure 3.4 (a)-(b) Schematic pictures of the back etching process, step by step. c) SEM image of the substrate with the island of pyramids after the back etching process d) SEM picture of a single back etched pyramid. (a) and (b) adapted from [56] .

The back-etching results in increasing the excitation and light collection efficiency as compared to surface-etching by a factor of ~10^3 (see insets in figure 3.5) [164]. On figure 3.5 (a) are presented measured spectra and a schematic image of the pyramidal structure before the back-etching; yellow and red lines mark the excitation and emitted light ray, respectively. Two factors affect the intensity of the emitted light. First, it is the nanostructure excitation efficiency. The nanostructure is about 2-3 μm inside the substrate that absorbs the excitation laser. Moreover, due to the shape of the air/GaAs/AlGaAs interface (inverted pyramid), light is defocused inside the pyramid. Second, the fact that GaAs has high dielectric constant ε_{GaAs} =12.9 [165], the emitted light undergoes total internal reflection, which traps the emitted light. The result (figure 3.5 (a)) is that no emission is observed from the QD (expected to be at ~1.55 eV). Conversely, in case of the back-etched pyramid (figure 3.5 b), the excitation light focuses on the QD region and part of emitted light refracts in the direction of the collection objective lens. Indeed, in the spectrum of the back etched sample the QD emission is clearly seen at 1.55 eV.

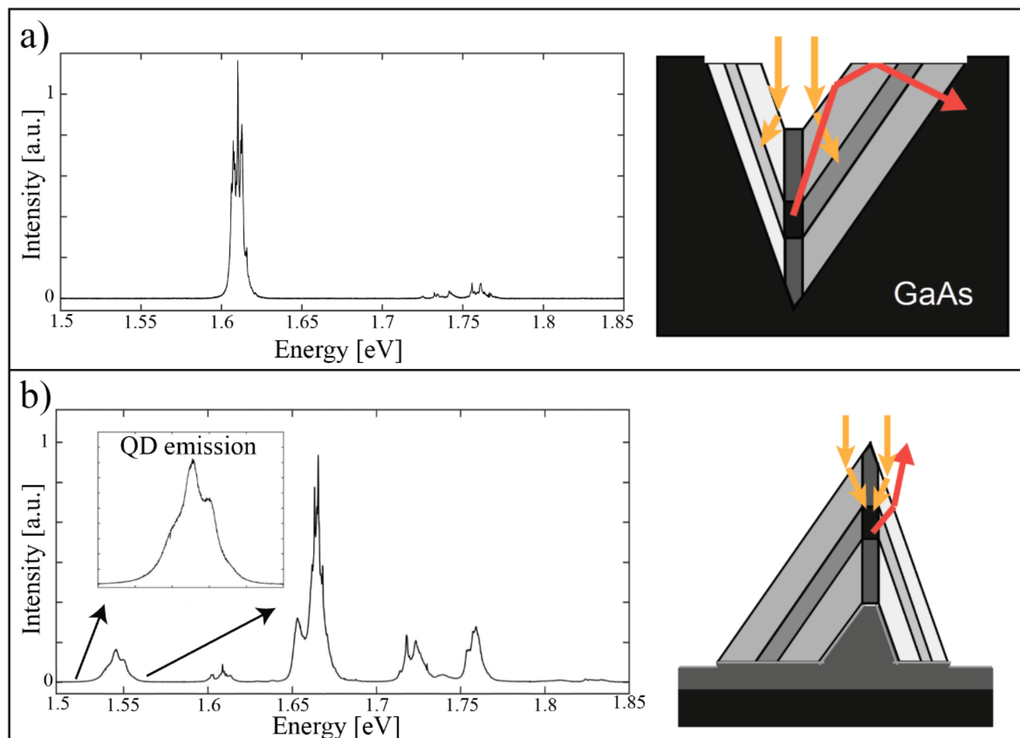

Figure 3.5 PL emission spectra before (a) and after back etching (b). Insets show schematically light rays inside the pyramid. Schematic parts adapted from [56]

3.2 Tools and techniques

Study and fabrication of such a complex system like QWR/QD in pyramidal heterostructures require a broad variety of characterization tools and techniques. In this subchapter, we will cover all used techniques for investigation of structural and optical properties of the pyramidal heterostructure.

3.2.1 Fabrication tools.

Figure 3.6 presents a part of the clean room facilities at the institute of Physics, showing fabrication equipment used in this thesis. These include:

RIE. Reactive Ion Etching (RIE) is a common plasma etching technology used widely for microfabrication applications. The great advantage of RIE is its etching depth precision (~1 nm), which makes RIE great solution for mask transferring. The main elements of the RIE tool are a vacuum chamber, a radio radio-frequency (RF) generator, electrodes and feed gas. The sample is placed in between the two electrodes, usually on top of the lower one. Plasma is created by the RF generator via the electric field between the electrodes. Electrons, due to their lower mass compared to ions, efficiently ionize the gas atoms under the high frequency electric field. Positively charged atoms, accelerated towards the lower electrode by the electric field, chemically etch the substrate. In our work we used Oxford Instruments Plasmalab 80 RIE system.

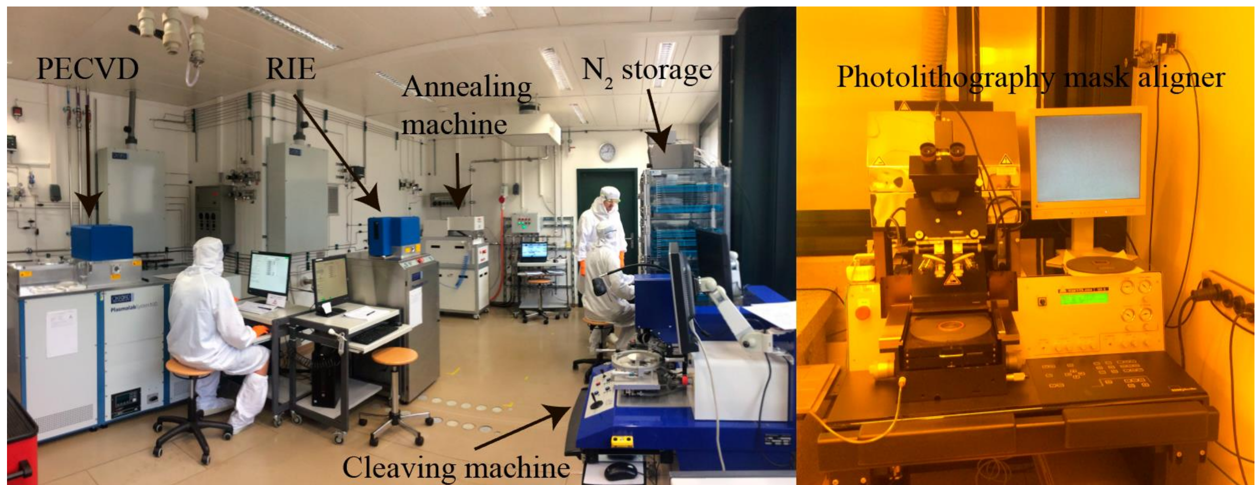

Figure 3.6. Clean room facilities. Mask aligner used for photolithography (right).

PECVD. Plasma-enhanced chemical vapor deposition (PECVD) is a widely used technique for thin film deposition; it allows to deposit a large variety of dielectric materials with high thickness accuracy. PECVD machine looks similar to RIE machine and its components are: vacuum chamber, RF generator and feed gas. The advantages of PECVD low operation temperatures, uniform coating and etc. Precursor gas and carrier gas ionized to plasma by RF generator thus decreasing temperature needed for chemical reaction on the substrate surface. In this thesis PECVD is used to coat samples with SiO_2/SiN layers.

Photolithography. Photolithography is used in microsructure fabrication, more particularly to write photoresist masks of microstructures with ~100 nm resolution. The photoresist layer coated on the substrate is sensitive to UV radiation, projected through a proper mask in a mask aligner (see figure 3.6). Exact power of the UV lamp is a very important, thus it is important to calibrate exposure time on dummy samples in advance. Resolution limit is compatible with masks for the pyramid processing, with opening size of ~2 µm.

Cleaving. For polarization resolved photoluminescence spectroscopy experiments, we need to cleave the pyramidal samples to collect emission from the side (cleave in plane of QD/QWR growth direction). Usually, we use standard scribers, and after scratching the sample cleave goes along a crystalline direction. In case of more precise cleaving or small samples, an automatic scribing machine is used.

Electron beam metal deposition. We used such evaporator for thin metal layer deposition. It consists of a vacuum chamber, material source, electron gun and sample holder with shatter. The electron beam heats the material source until the metal starts to evaporate in all directions isotropically, at a constant flux if electron beam power is kept constant. This method allows the deposition of thin films with nm precision.

Rapid Thermal Annealing (RTA). This annealing machine can rapidly heat the sample and keep it at a certain temperature. The annealing process takes place in a chamber with a special atmosphere in order to prevent undesirable chemical reaction on the sample surface. Annealing is useful for many purposes, e.g., to active dopants, change interfaces, etc. We used annealing as a Schottky diode fabrication process step, to create ohmic contact by mixing the semiconductor/metal interface due to diffusion at high temperature.

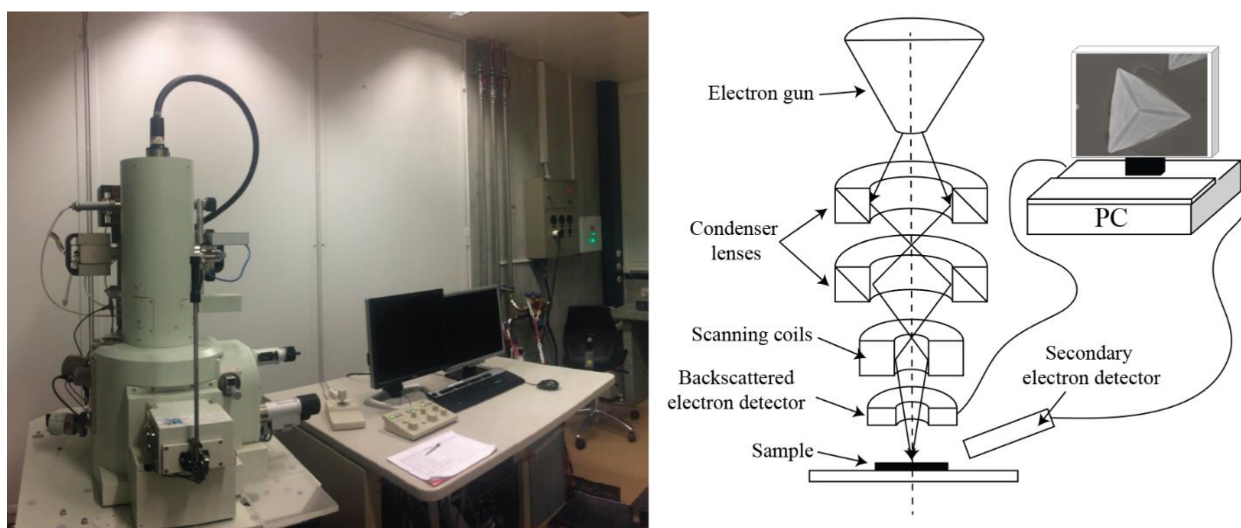

Figure 3.7. Scanning electron microscope (left) and schematic illustration of its components (right).

SEM. Observation of the pyramidal structures using scanning electron microscopy (SEM) is useful for calibrating growth parameters and characterizing the resulting structures with a spatial resolution much better than with optical microscopy (as high as ~10 nm). In the SEM chamber, under vacuum, electrons from an electron gun are accelerated and pass through condenser lenses that focused the electron beam on the sample (figure 3.7). Scanning coils are used to scan the electron beam across the sample's surface, and the secondary or backscattered electrons from each point are collected by proper detectors. The reconstructed image corresponds to contrasts produced by surface topography and composition/doping distributions. The obtained resolution depends mainly on the size of the generated electron cloud underneath the surface.

3.2.2 Polarization-resolved photoluminescence spectroscopy

In photoluminescence (PL) spectroscopy, the structure is photo-excited, typically with a laser beam focused on the surface of the sample, and the light emitted gives useful information about the structure studied. The electron-hole plasma generated by the exciting light is out of equilibrium and the product of its relaxation (through radiative and nonradiative channels) is excitons or electron-hole pairs at the ground states of the nanostructure. The spectrum of the PL gives important information on the bandstructure and confined states of the tested samples.

In order to collect the PL from a single pyramid, we use the micro-PL setup illustrated in figure 3.8. The PL setup consists of three main parts: its laser pumping system, cryostat with the mounted sample, and emission collection and dispersion. The sample is cooled to a low temperature and pressure of 10 K and 10^{-5} mbar correspondently, using a liquid He flow in optical cryostat (Janis Research, CO., Inc. ST-500, or Cryovac Konti). Excitation light was generated using a Ti:sapphire laser (Spectra-Physics Tsunami 3960 or CoherentMira 900) with tunable wavelength at 700-1000 nm, which is optically pumped by 532 nm laser (Nd:YVO4 Spectra Physics Millenia) or 514.5 nm (Nd:YAG Coherent Verdi V10) that can be used as excitation laser for non-resonant excitation. The exciting beam is focused to a 1-2 μm spot using a microscope objective lens (50*X*, f= 3.6 mm, NA = 0.5), permitting selection of a single pyramid (4-5 μm big). The cryostat is mounted on an x-y position stage, allowing to control the sample position with 50 nm precision. The emitted light, collected through the same objective lens and focused on spectrometer slit. The emission is dispersed by with 1200 mm^{-1} grating of spectrometer (55 cm Jobin Yvon TRIAX550 or HR460), yielding a spectral resolution of ~80 μeV. The dispersed light is collected by CCD (Jobin Yvon). The actual excitation power on the sample ~20 times less powerful than measured at the entrance to microscope due to the loses on beam splitters inside the microscope.

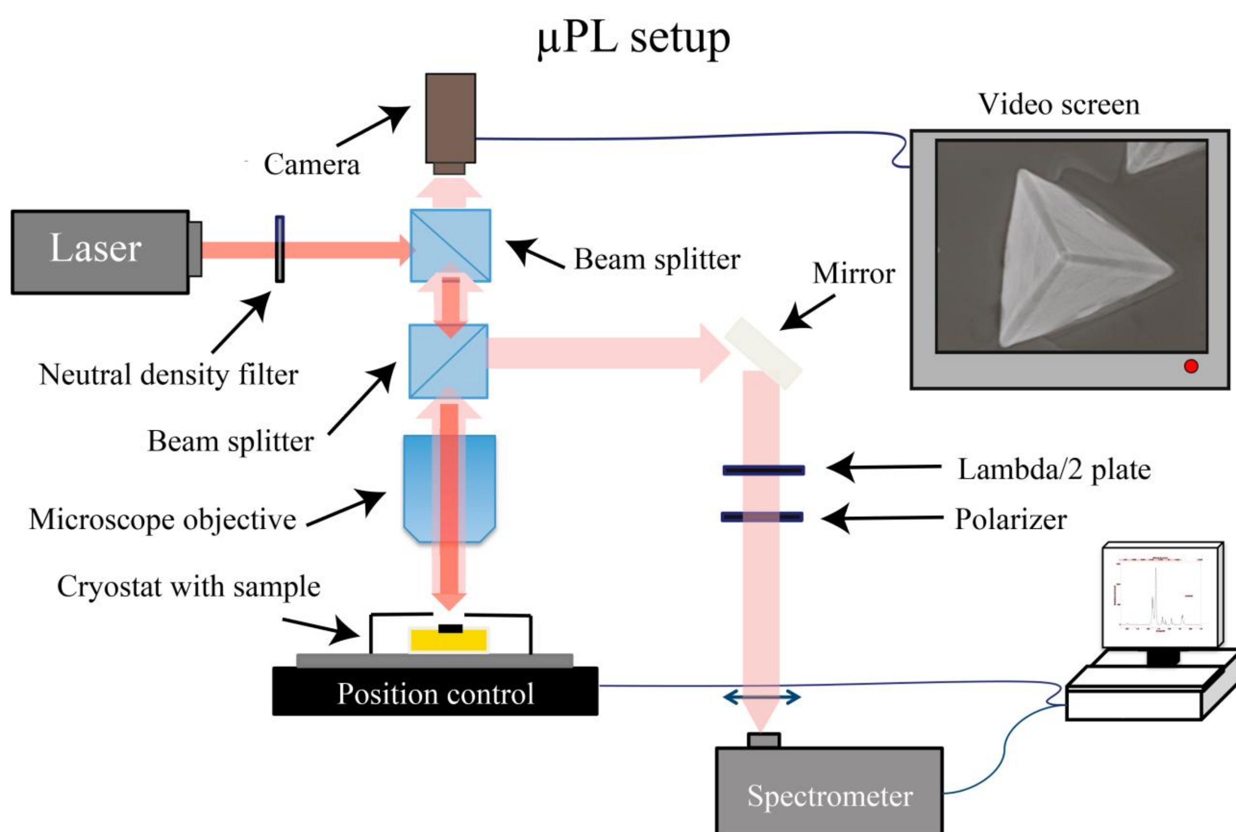

Figure 3.8. Schematic diagram of the polarization-resolved micro-PL setup.

For polarization-resolved PL spectra measurements, a half-lambda plate and a polarizer are added to the set up, as shown in figure 3.8. Such measurements are especially useful in the cleaved-edge geometry (fig 3.9 b), yielding information about valence band mixing effects (see Chapter 5).

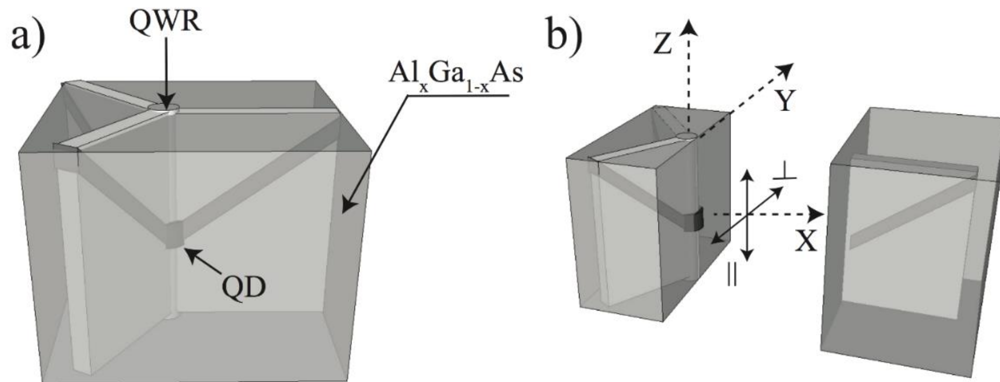

Figure 3.9. (a) Schematic 3D picture of a grown QD in a pyramid. (b) Cleaved edge geometry for side-view polarization-resolved measurements.

3.2.3 Time-resolved photoluminescence

To investigate carrier capture-relaxation dynamics, time-resolved PL spectra have been measured. In this type of measurements a pulsed laser source (ps pulses) with pulse period larger than the duration of the PL process. The simplest setup is the one that we use in our lab. The setup is the same as in figure 3.8, except that in the exit slit of the monochromator a micro-channel plate photomultiplier tube (MCP-PMT) is used for detection. The MCP-PMT provides the stop signal for the start signal provided by the exciting laser pulse. In between the start-stop signals, one counts the detected phonons and their arrival time. This kind of setup gives approximately 100 ps time resolution.

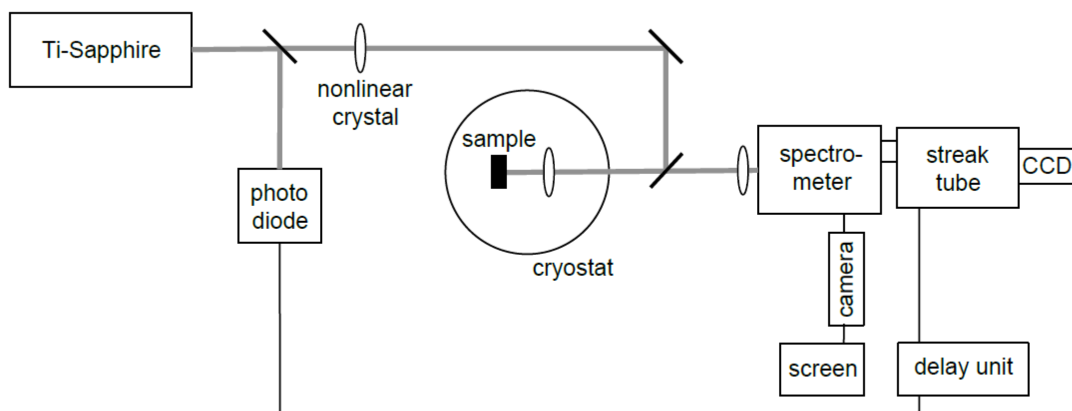

Figure 3.10. Schematic diagram of the time-resolved setup employing a streak camera. Adopted from [56]

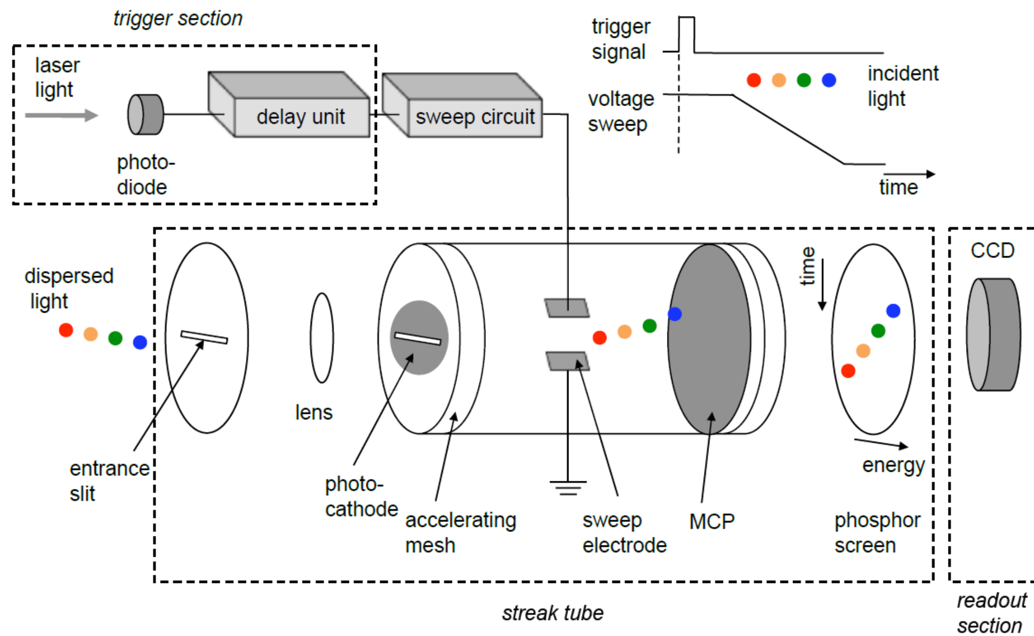

Figure 3.11. Schematic description of the streak tube of a streak camera setup. Adopted from [56]

The second type of time-resolved PL set-up makes use of a streak camera. The streak camera allows to obtain time-resolved PL spectra in the two-dimensional energy-time domain, with time resolution in the order of a few ps. A general description of the streak camera is schematically presented in figure 3.10 and figure 3.11. PL signal from the sample is dispersed by the monochromator and enters the slit of the streak camera tube, and then is focused by the lens on the photocathode. The photocathode is a part of an acceleration tube. The photocathode translates the optical signal into an electron beam, which is accelerated and passes through a sweep (vertical) electrode. Electrons are converted into photons by the MCP, and are detected by a CCD. Thus, a two-dimensional energy-time image is obtained, representing the time-resolved PL spectra. The excitation laser in the experimental PL setup for time resolved measurements used was a Ti-Sapphire laser pumped by a Nd:YVO4 laser, with 2.5 ps long pulses at a repetition rate of 76 MHz. The PL dynamics was measured with a Hamamatsu C5680 spectrometer that provides sub-meV spectral resolution. Typical time resolved resolution achieved is ~10 ps.

In figure 3.12 we show an example of such streak camera image. Here, spectrally and temporally resolved PL of a single parabolically-shaped-potential QD (see Chapter 4) at excitation power of 210 μW is displayed. All experiments with streak camera reported in this Thesis were performed in the laboratory of Prof. N. N. Sibeldin by Dr. V. Tsvetkov and Dr. M. Skorikov at Lebedev Physical Institute of the Russian Academy of Sciences in Moscow.

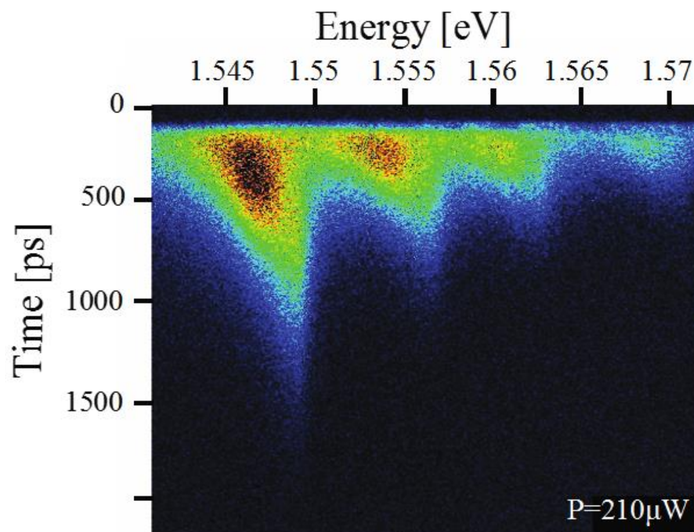

Figure 3.12. Representative spectra-temporal image of the time-resolved PL spectra obtained with the streak camera (10K).

3.3 Summary

In this chapter, we presented the fabrication methods and experimental tools that we used in this thesis work. Fabrication consists of three phases: substrate patterning in the form of arrays of inverted pyramids, MOVPE overgrowth, and post-growth processing. The AlGaAs nanostructure formation mechanism inside the inverted pyramids is based on Ga-Al segregation and capillarity effects that takes place along the symmetry axe of the inverted pyramid. The presented PL spectroscopy techniques give access to important information on the nanostructure and the confined carrier states, as discussed in subsequent chapters.

Chapter 4

Transition from 2D to 3D Quantum Confinement Studied in Pyramidal Nanostructures

The degree of quantum confinement of the charge carriers in semiconductors can modify significantly their optical properties. Whereas the difference in optical properties between 1D and 0D systems has been investigated extensively, the gradual transition between these two dimensionalities (1D->0D) has not been considered in detail, mainly because of the difficulty in identifying a single system in which such gradual transition can be implemented. In this chapter, we exploit the high degree of control of the quantum confinement in vertical AlGaAs/GaAs QWR/QD structures grown in inverted pyramids in order to investigate this transition. A general overview of the structural features of the pyramidal nanostructures studied is presented in Section 4.1. The 1D and 0D extreme limits are studied in QWRs of finite length (Section 4.2) and in a thin GaAs/AlGaAs QD (Section 4.3). The intermediate case is explored with potential profiles of parabolic shapes with different gradients (Section 4.4). Section 4.5 summarizes the results.

4.1 Fabricated structures

In Chapter 3, we described how Ga-Al segregation in AlGaAs layers grown in inverted pyramids yields a vertical-QWR (VQWR) with well-defined heterostructure potential. By varying the nominal Al content of the AlGaAs alloy along the growth direction (or wire axis), it is possible to shape an additional confining potential along the otherwise uniform QWR, with nm-scale accuracy. This yields strain-free QDs in which their confining potential along one direction can be designed on nm scale corresponding to a fraction of the confined exciton diameter (~10 nm). In this section, we present the set structures of different confinement configurations studied.

4.1.1 Design and fabrication

Three types of nanostructures were fabricated and studied (see figure 4.1): a "long" AlGaAs QWR representing an idealized 1D structure; parabolically shaped AlGaAs QDs (PQDs) with height much larger than the width; and a "thin" GaAs QD with a height/width aspect ratio smaller than 1. The structures were grown by MOVPE in inverted pyramids as described in some detail in Chapter 3. The designed Al-contents in the grown heterostructures are displayed in figure 4.1. A total of five structures were fabricated, with L_{QWR}= 480 nm, L_{PQD}= 480 nm, 240 nm and 120 nm and L_{QD}= 5 nm (GaAs thin QD). The growth layer sequence for each structure presented in

Appendix B. Note that these are the actual lengths in the growth directions, determined by growth calibrations and SEM measurements of the corresponding structures. The corresponding MOVPE growth parameters are shown in Appendix B. Qualitative examples of the actual distributions of the Al-content in the x-z plane are shown in the lower panel of figure 4.1. These estimated local Al-contents, which set the quantum confinement parameters in the different structures, were estimated based on earlier reports of the segregation effects in such structures [113]. The z-variation in the bandgap along the growth direction translates into similar profiles of the conduction and valence band edges. Random fluctuations in Al-content and VQWR width along z are expected to result in corresponding fluctuations in confinement energy.

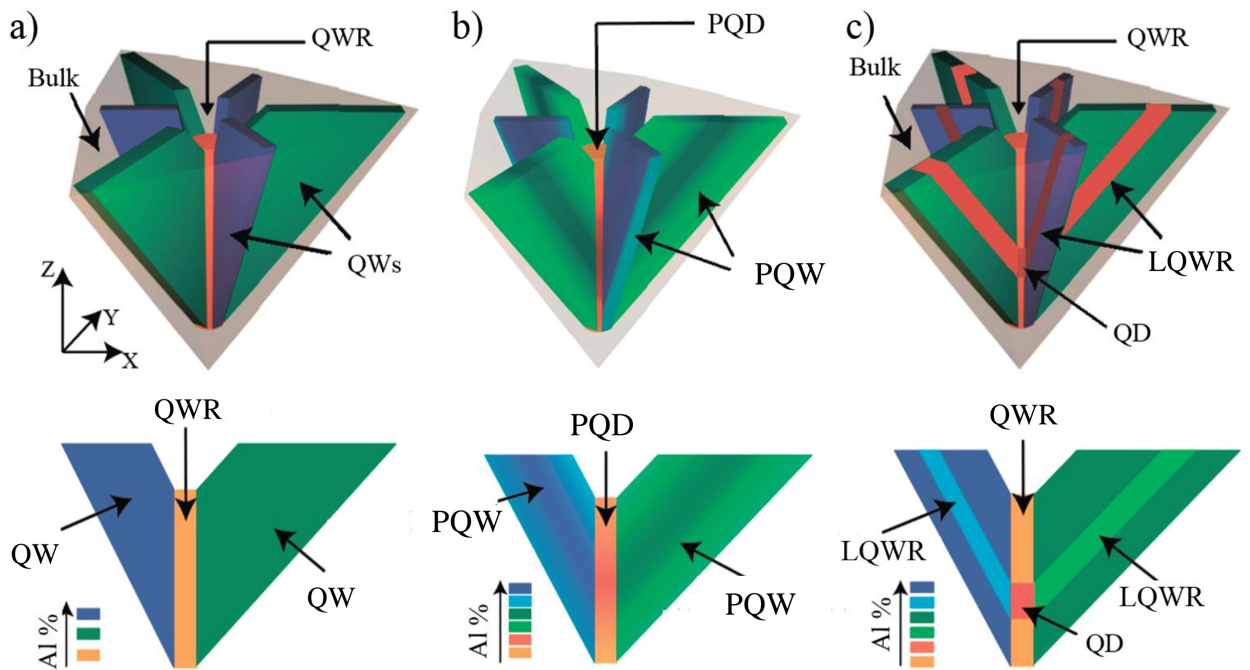

Figure 4.1 Schematic presentation of AlGaAs pyramidal nanostructures with different confinement geometries. Top panels: 3D illustration; bottom panels: cross-section in the x-z plane. (a) finite-length QWR (b) parabolic-QD (c) Thin QD. Color scale represents Al-contents.

4.1.2 Structural features

Figure 4.2 schematically shows a comparison of the designed structures with the actual confinement potentials. Besides the difference between the nominal and actual lengths, random fluctuations in the effective heterostructure potential are expected due to the nature of the MOVPE growth process (figure 4.2 lower panel). In particular, the otherwise smooth and uniform potential along the VQWR fluctuates due to random variations in Al-content and diameter of the VQWR Al content fluctuation (on order of 1%) lead to exciton localization effects at low lattice temperatures (close to 0 K). However, since we expect the potential fluctuations to be on a few-

nm scale, which is smaller than the exciton diameter (~10 nm), potential disorder should not have a large effect on resulting potential profile.

Structural characterization using SEM and optical microscopy was used to obtain general information about the grown structures. However, it is not possible to infer details about the material composition in the nanostructures with these methods. Rather, PL measurements were used to get information about the sample quality and AlGaAs composition across the pyramidal structure.

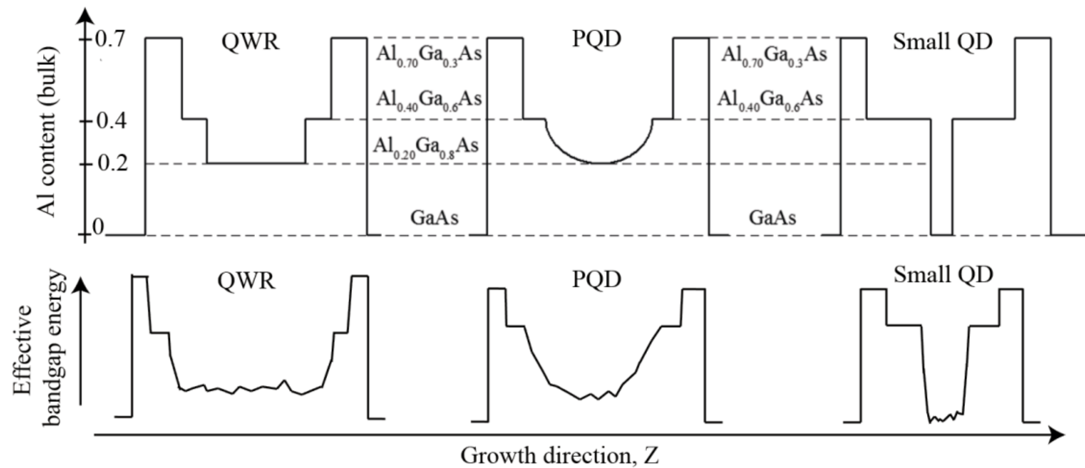

Figure 4.2 Schematic presentation of the Al-content and the confinement potential along the growth direction at the VQWR. Top panel: nominal Al content; bottom panel: illustration of the bandgap variation including disorder effects. (a) QWR (b) PQD (c) "thin" QD.

4.1.3 Spectral analysis of the pyramidal nanostructures

The Al-Ga segregation yields different nanostructures within the same pyramid, as summarized schematically in figures 4.1 and 4.2.The core nanostructure part we call region with Al content nominal $0.2<x<0.4$ which is sandwiched in between the barrier layers with $x=0.4$. Each QWR/QD nanostructure in the central QWR is accompanied by QW/QWR nanostructures in side QWs (the same for barrier layer) as shown in figure 4.1 (c). A more detailed structural description is presented in Chapter 2. To analyze quantitatively these structures, we used low-temperature photoluminescence (PL) spectroscopy of single pyramids in a back-etched configuration. Figure 4.3 shows wide-range (panoramic) PL spectra of a 480 nm long AlGaAs QWR and a "thin" (5 nm thick) GaAs/AlGaAs QD (detailed MOVPE growth sequence layers parameters are given in Appendix B). The upper horizontal scale shows the equivalent Al content of an AlGaAs bulk alloy emitting at the same photon energy, derived from the relationship of the bandgap of AlGaAs and the nominal Al content [166] [109]. With the help of this relationship, we can attribute each group of spectral lines to luminescence from the different zones in the pyramid. The equivalent Al contents thus found correspond well to studies of the segregation reported earlier in [113].

For the 480nm QWR sample, the peak at lowest energy corresponds to the nominal $Al_{0.2}Ga_{0.8}As$ QWR region where the actual (effective) Al content is about ~3%. The peak at 1.675 eV is related to QWs of the lower Al content (green color in figure 4.1 a) and the barrier central QWR 1.65 eV (nominal x=0.4 actual ~0.08). The one at 1.725 eV is related to the QWs with higher Al content (blue color in figure 4.1 a). Considering such long QWR such of 480 nm length, due to weak vertical quantum confinement and the low energy difference between confined states (much lower than kT), we may consider it as a model of a QWR system. The barriers QW are not presented in the spectra due to high Al content in the barriers, the expected effective Al content is ~23%.

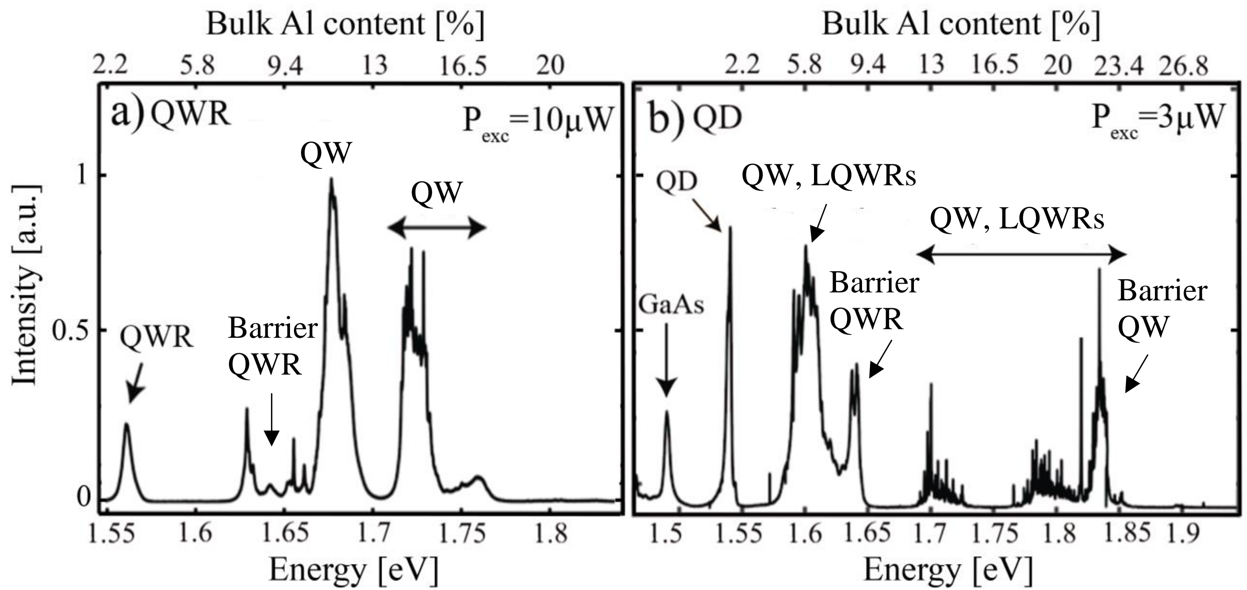

Figure 4.3 Panoramic spectra (after back etching) measured at T=10 K (a) 480 nm QWR sample, excitation power 10 μW. (b) "thin" (5 nm) GaAs QD sample, excitation power P=3 μW.

Figure 4.3 b shows PL spectra of the thin lens-shaped GaAs QD in $Al_{0.4}Ga_{0.6}As$ vertical barriers (nominal Al content). Due to the high potential barriers and the small thickness, the QD ground state emission line is blue shifted (~50 meV) from the bulk GaAs free exciton emission. The other lines are interpreted in Fig. 4.3(b) (compare to figure 4.1(c)). The major difference from the QWR spectra is the multitude of sharp lines (1.7-1.85 eV). These lines are a sign of localized of excitonic states inside the thin LQWRs and the thin QWs on the pyramid facets.

4.2 Finite-length quantum wire

In this Section, we focus on the QWR nanostructure, which represents the limit of 2D quantum confinement in our study. First, modeling of the electron and hole confinement energies and wavefunctions, as well as the expected radiative transitions, are presented. The transitions are then observed experimentally in low-temperature PL) spectra. Conclusions are drawn about the characteristic signatures of 2D confinement in this system.

4.2.1 Modeling of the QWR system

Summarizing all assumptions, we end up with QWR system as shown schematically in figure 4.1 a, but neglecting the "vicinal" QWs with the higher Al content [166] (figure 4.1 blue colored QWs). More details on the model are given in Chapter 2. According to the segregation model, we assume the material parameters (actual Al content) for the 480 nm $Al_{0.2}Ga_{0.8}As$ QWR in $Al_{0.4}Ga_{0.6}As$ barriers as follows: QWR core ~3 %, QWs in core ~10%, bulk 20% of Al content; barrier QWR ~7%, barrier QWs ~23%, barrier bulk 40%. As modeled area, we take 550x30x30 nm space about the center of modeled QWR.

4.2.1.1 Band structure

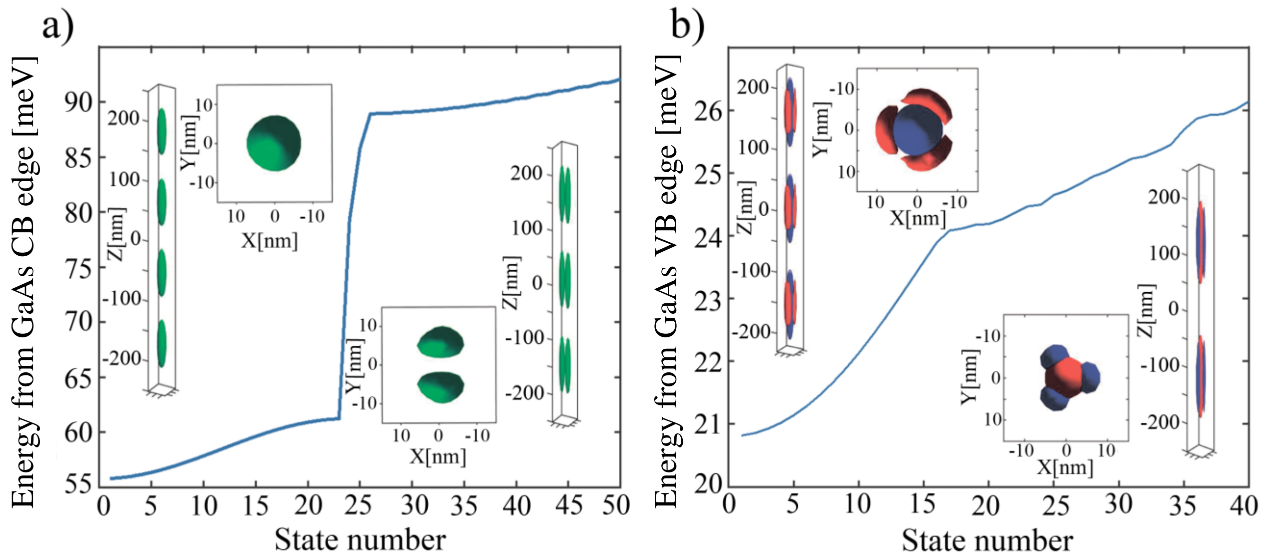

Figure 4.4 Calculated energy of confined conduction band (a) and valence band (b) states (energies with respect to bulk) for the 480 nm QWR. The insets show the calculated wavefunctions for several states at the indicated energies in (a) third excited state of first subband, (b) second excited state of second subband. Green: electrons; red- heavy holes; blue: light holes.

Figure 4.4 shows modeling results for the (simplified) 480 nm $Al_{0.2}Ga_{0.8}As$ QWR. For electrons (figure 4.4 a) the separation between adjacent confined states is less than 1 meV due to

the finite (long) length. Examples of typical electron wavefunctions are presented in the insets, demonstrating the formation 1D transverse subbands. Such “cigar” WF shape is a sign of weak confinement in the growth direction. The energy separation between the two subbands, about 30 meV, is in good agreement with analytical. From these results, we can estimate the confinement energy of the ground electron state (GS) to be about ~25 meV from the AlGaAs CB edge Figure 4.4 b presents calculated confined energy states for the VB. Insets show examples of the calculated wavefunctions; blue and red color indicated light hole (LH) and heavy hole (HH) parts of the wavefunction, correspondently. The VB states separation is ~0.1 meV, thus the model represents an infinitely long QWR for the temperatures used in the experiments (>10 K). The 3D confinement energy of the ground state is ~6 meV from the AlGaAs CB edge.

Left insert in 4.4 (b) presents second excited VB state. LH VB part is in the center with the same shape as corresponding CB state. Due to the fact that LH and HH wavefunctions are perpendicular to each other HH part almost not crossing with LH one and as a consequence with CB. For illustration purpose the ratio of HH and LH probability density isosurfaces were changed in the insert figures, the real ratio LH/HH is about 100/1 order in this structure. In the right side shown high excited state where HH and LH VB parts switched places. VB dispersion curve as CB at the beginning repeats parabolic shape, such behavior is a sign of free carriers in one direction. Such order of state separation in CB and VB put 480 nm QWR very close to the condition of infinite QWR system. Due to phonon presents in a real QWR at the temperature higher than 2 K the carriers will not feel the influence of confinement. This fact makes 480 nm QWR a good model structure to explore “ideal” (infinitely long) QWR optical properties.

4.2.1.2 Optical spectra

The left panel of figure 4.5 presents the calculated optical transitions rate spectra of the 480 nm $Al_{0.2}Ga_{0.8}As$ QWR structure, neglecting Coulomb interaction and broadening effects. The parts related to transitions of the HH and LH parts of the wavefunctions (see Chapter 2) are colored red and blue, respectively. Evidently, the LH components of these low energy transitions are dominant in the QWR spectra, which is a consequence of two facts. First, the LH portion in these VB states is 50-100 times larger, depending on the state number involved in the emission process. Secondly, the CB and LH wavefunctions have similar and hence much larger overlaps than the CB-HH ones. For higher energy transitions, there are states where the HH portion is higher and the transitions exhibit larger HH flavor.

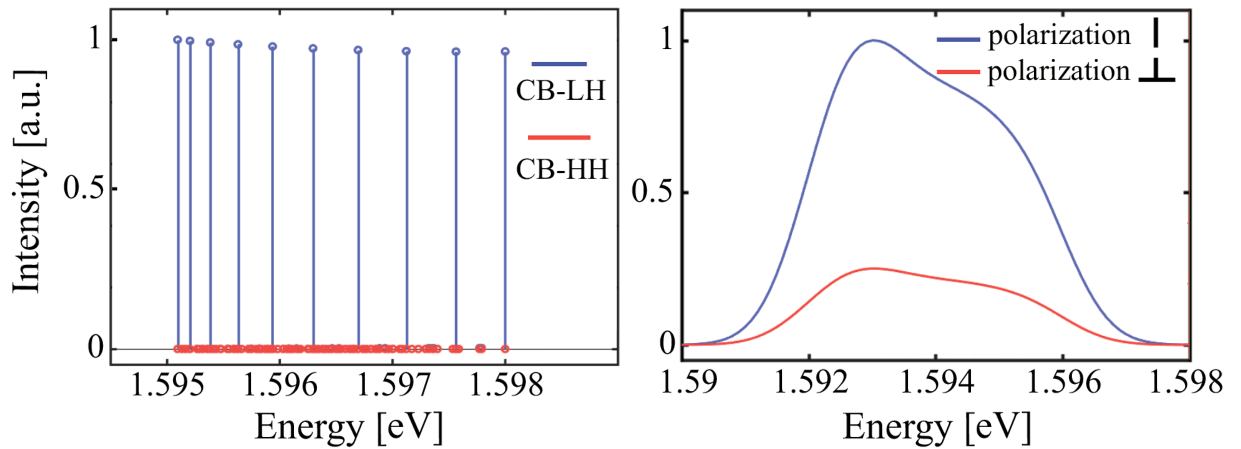

Figure 4.5. Calculated optical spectra of the 480nm QWR structure. Left panel: relative transition rates, excluding Coulomb interaction and broadening. Blue and red colors show HH and LH parts. Right panel: calculated absorption spectra taking into account Coulomb interaction as a perturbation and 2 meV broadening of transitions. Blue and red colors indicates linear polarization along and transverse to pyramid axis, respectively.

The right panel of figure 4.5 presents spectra of the same structure, but taking into account Coulomb interaction as a perturbation as described in Chapter 2. Also, an artificial broadening of ~2 meV for each transition has been added to be consistent with experimental results (see next Section). The Coulomb interaction red shifts the spectrum, whereas the broadening causes a merging of the individual transitions into a board peak. Note that by the red and blue colors are denoted the different linear polarization components of the QWR emission with respect to the pyramid axis: blue for light polarization along the QWR, and red – perpendicular to the QWR. Such polarization resolved spectra is a very important tool of investigation nanostructure quantum state properties. As shown in Chapter 2, HH-related transitions emit light only perpendicular to the QWR axis, while LH ones emit light with a stronger polarization component along the QWR axis. If we compare left and right sides of figure 4.5 we see that taking into account Coulomb interaction leads to spectra red shift by ~12 meV.

4.2.2 QWR structure – experimental results

4.2.2.1 Power-dependent PL spectra

Figure 4.6 shows the PL spectra of the 480 nm $Al_{0.2}Ga_{0.8}As$ QWR structure for several excitation power levels at T=10 K (back-etched sample, top excitation/emission geometry). Spectra were normalized to the same maximum value. The spectral line shape obtained under low excitation power (0.2 μW) closely resembles the calculated one (figure 4.7, right panel). Such broad spectra under low excitation power can be explained by the low energy separation between adjacent in CB and VB states. As the thermal energy at 10 K (~1 meV) is comparable or higher than the energy separation between confined states, the charge carriers can easily hop from one state to another due to the carrier-phonon interaction. The absence of sharp lines also indicate that

potential fluctuations along the QWR axis are < 1 meV. Due to the same reason, increasing excitation power does not change significantly the spectral line shape.

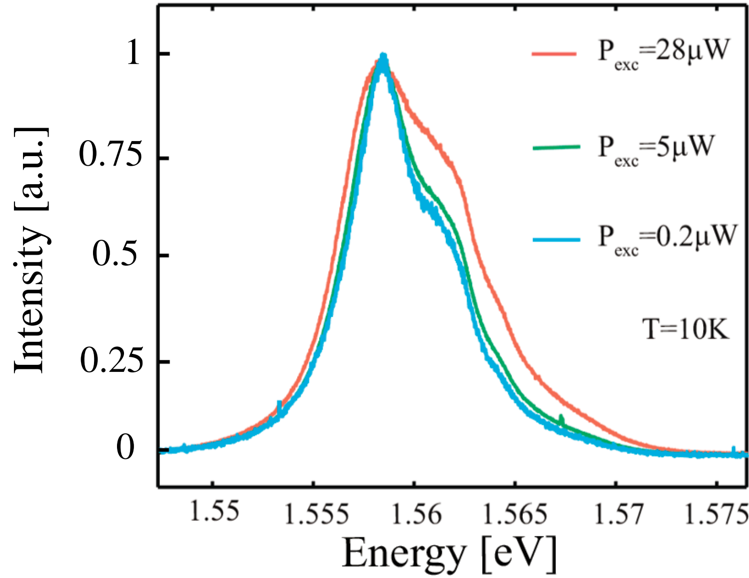

Figure 4.6 PL spectra of the 480 nm QWR structure for several excitation powers.

Note that calculated absorption spectra (figure 4.5) are blue shifted by ~20 meV as compared to the measured emission spectra (figure 4.6). As described in Chapter 2, our numerical model uses a simplified version of the actual geometry of the nanostructures. It is also quite simplified in terms of accounting for multi-particle states and electric fields set by charged carriers and impurities around the nanostructure. Surface charges induced by the back-etching geometry apply an electric field resulting in an additional redshift of the emission spectra. Compared to inverted geometry (just after the growth), we find that spectra collected in back-etched geometry are redshifted by ~ 10 meV.

4.2.2.2 Time-resolved PL measurements

Figure 4.7 presents time-resolved PL spectra of the 480nm QWR structure obtained with the streak camera set up shown in Chapter 3, for different excitation powers P=1200 μW, 2700 μW, and 4080 μW; different colors correspond to different emission intensities (T=1.8 K). For P=1200 μW excitation power, mostly the GS transition (1.555 eV) persists for less than 1 ns. Weak PL is observed also at the transition of the second QWR subband (1.61 eV), see figure 4.4 (a). At increasing excitation power *P*, state filling gives rise to emission from higher energy states (figure 4.7 (b-c). Increasing emission tails at low energies (<1.56 eV) evidence formation of multi-exciton states [167]. Figure 4.7 (d) presents the PL spectra at several excitation powers *P* as well as the measured decay times of the main spectral peaks. The peak at ~1.561 eV is better resolved than in the cw spectra of figure 4.6, probably due to the lower sample temperature. The shorter decay times of the higher energy features evidence efficient carrier relaxation from the excited to the ground states.

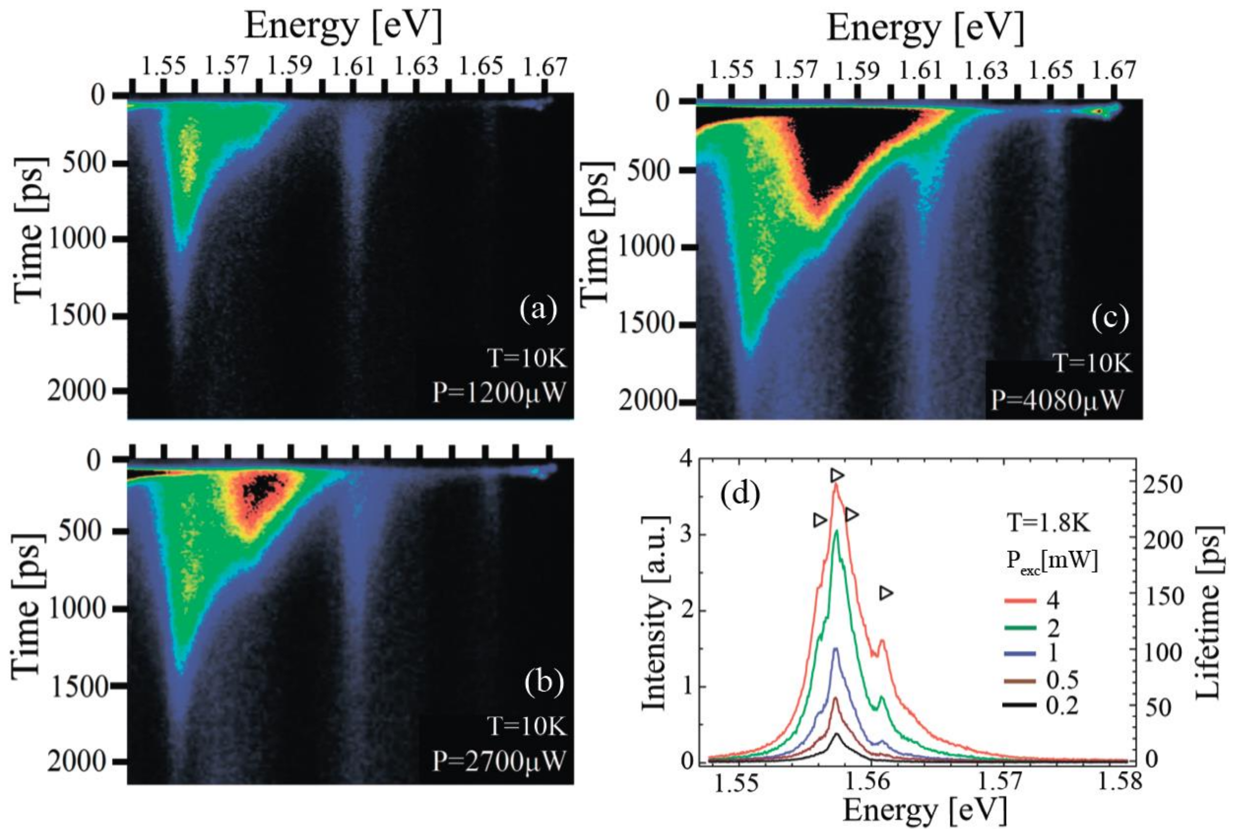

Figure 4.7 Time-resolved photoluminescence spectra of the single 480 nm QWR structure sample (T=1.8 K). (a)-(c) Spectral-temporal images obtained under pulsed excitation for different average excitation powers P. (d) Integrated PL spectra at different excitation powers. Triangles show the decay times of the corresponding spectral peaks. Different colors indicate different PL intensities.

4.2.3 QWR structure: summary

The 480nm long $Al_{0.2}Ga_{0.8}As$ QWR structure represents our model of a 1D system, since the CB and VB states confined along the wire axis have a small energy separation (<1 meV). Thus, although in the numerical model one can resolve many densely spaced states and transitions in the calculated spectra, the experimental PL spectra show emission from spectrally smooth QWR subbands. The modelling indicates that the VB states responsible for emission from the ground states are virtually pure LH-states, and predict emission polarized mainly along the wire axis. Verification of this latter feature is taken up in Chapter 5.

4.3 "Thin" quantum dot

This section is dedicated to a GaAs QD nanostructure that exhibits 3D quantum confinement with large state energy separation. The thin QD nanostructure in the inverted pyramid has a specific lens shape due to nature of the MOVPE growth. We first focus on modeling of the structure and the differences with respect to the QWR modeling. PL measurements, including power dependence and time-resolved are then presented and discussed.

4.3.1 Modelling of the quantum dot system

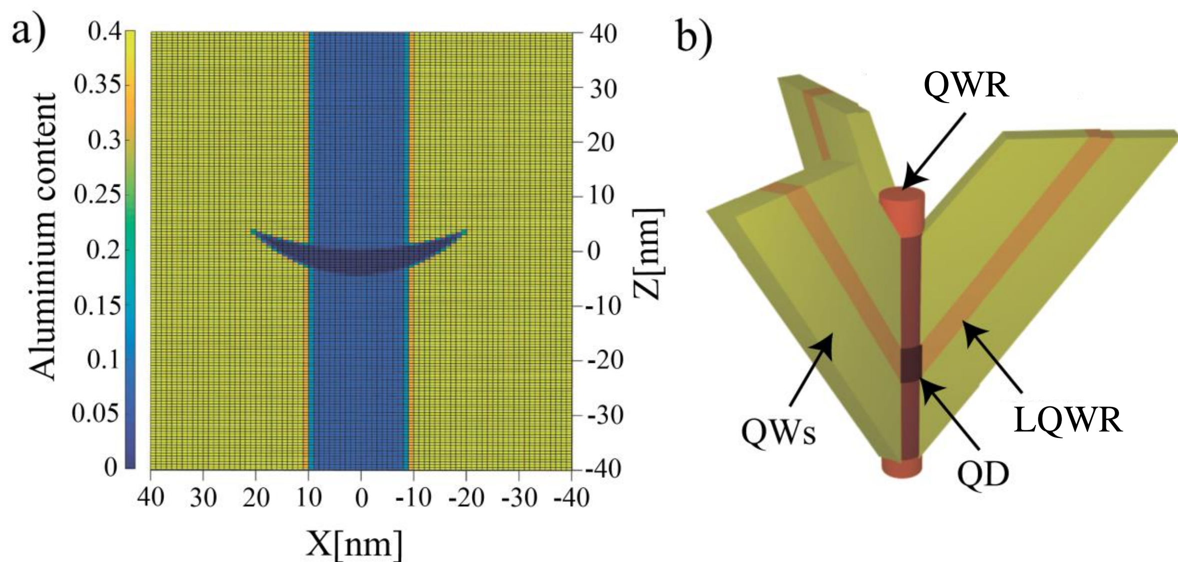

Figure 4.8 Geometry of the modeled QD structure. (a) Cross section in the XZ plane at the center of the nanostructure. Different colors corresponds to different AL content. (b) Schematic picture of the QD nanostructure in the inverted pyramid.

The thin QD structure more complex to model, due to the MOVPE growth nature that results in a lens shape dot. Here, we present simulation results for such GaAs lens shaped QD with 5 nm center thickness embedded in a vertical QWR with nominal $Al_{0.2}Ga_{0.8}As$ composition. Figure 4.8 (a) shows a cut of through the structure. For simplicity, we neglect the GaAs side QWRs (see figure 4.8 b), because at such thin GaAs layers these wires turn into chain of QDs due to thickness fluctuations and should not affect the optical properties of the central QD. The vertical QWR (blue area in figure 4.8 a) is modeled as a cylinder with uniform 18 nm diameter and constant Al content. Starting with nominal $Al_{0.4}Ga_{0.6}As$ barriers, the model parameters were as follows: QD diameter 18nm, barrier vertical QWR ~8% Al, barrier QWs ~23% Al, barrier bulk 40% Al. As modeled area, we take 550x30x30 nm volume about the center of the structure. Bandgap energies were calculated using the formula introduced in Chapter 2.

4.3.1.1 Band structure and wavefunctions

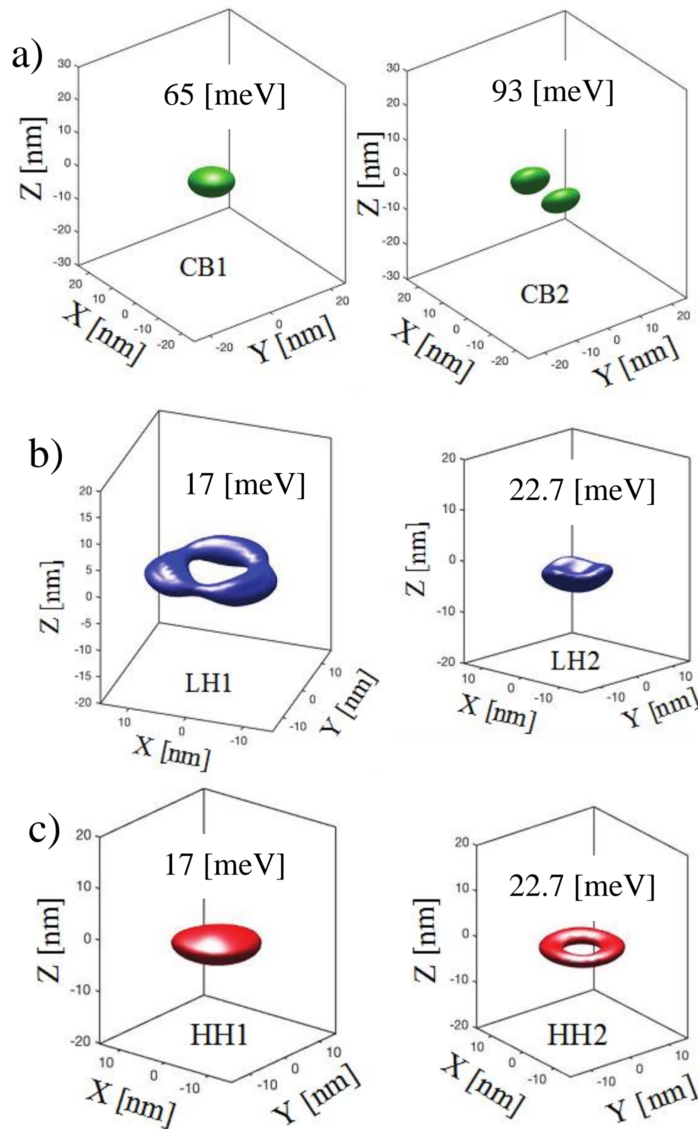

Figure 4.9 Calculated electron, light, heavy hole wavefunctions of the lowest energy states for the 5 nm thick lens-shaped GaAs pyramidal QD. Red and blue colors indicate HH and LH characters, respectively.

On figure 4.9 we show wavefunction (WF) isosurfaces of the conduction band (green, (a)), light hole component (blue, (b)) and heavy hole component (red, (c)) lowest energy CB and VB states: ground states (CB1, LH1, HH1) and first excited states (CB2, LH2, HH2). The corresponding confinement energies are also indicated. The lowest energy VB state has a dominant HH character. The thin QD potential results in wavefunctions with aspect ratios (z/xy dimensions) <1. Notice that for such thin QD, the WF of the lowest energy VB state overlaps well the CB ground state WF, whereas the lowest energy LH state component has almost zero overlap with this CB state.

4.3.1.2 Optical spectra

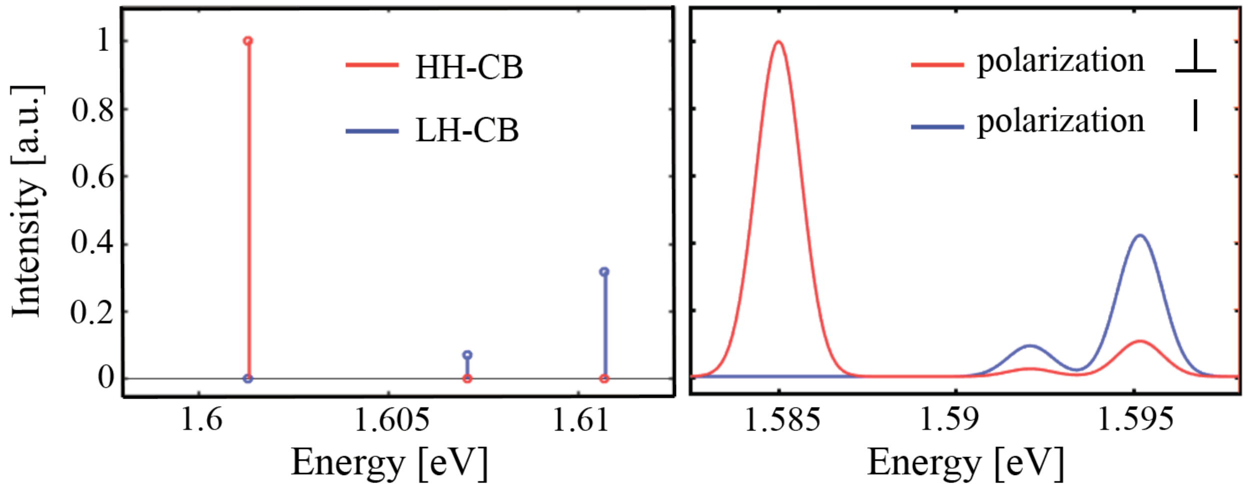

Figure 4.10 Calculated optical spectra of the "thin" (5 nm) GaAs QD structure. Left panel: relative transition rates, excluding Coulomb interaction and broadening. Blue and red colors show HH and LH parts. Right panel: calculated optical spectra taking into account Coulomb interaction as a perturbation and 2 meV broadening of transitions. Blue and red colors indicates linear polarization along and perpendicular to the growth direction, respectively.

Figure 4.10 (left panel) presents the calculated absorption spectra for the 5 nm lens-shaped QD in the case of single carriers (no coulomb interaction). As expected, the ground state transition is polarized perpendicular to growth direction since it is only due to recombination of the CB and HH-like ground state of the VB. The two excited state transitions are related to the indirect transitions CB1-LH1 and CB1-LH2 (see figure 4.9). The right panel of figure 4.10 presents the optical spectra of the same structure, with an artificial broadening of ~2 meV, but taking into account Coulomb interaction as a perturbation. This Coulomb interaction gives rise to spectral red shift of ~16 meV. Notice that because of the large energy separations of the transitions, the assumed broadening does not change qualitatively the polarization features of the optical spectra even with such broadening included.

4.3.2 Experimental results – “thin” QD structure

4.3.2.1 Power-dependent PL spectra

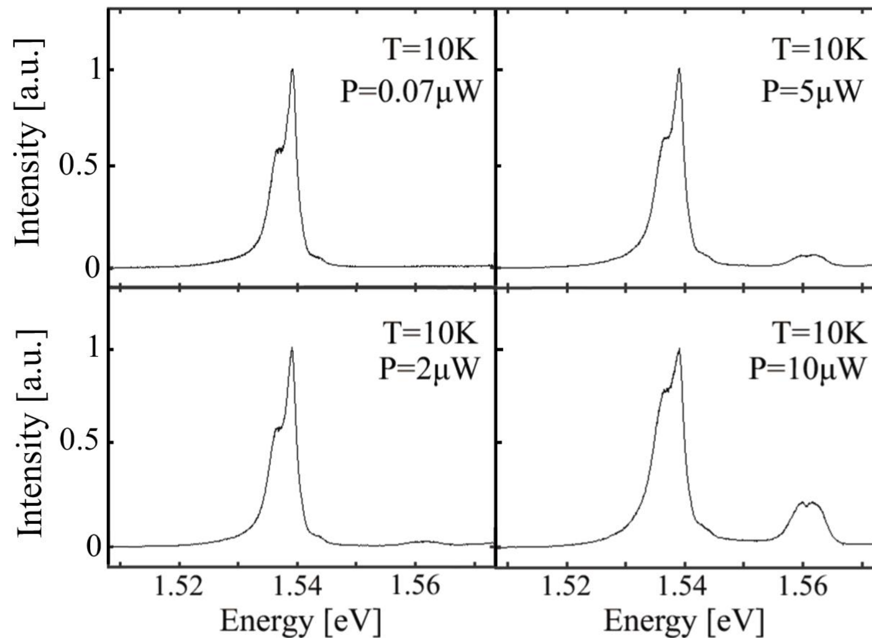

Figure 4.11 Excitation power dependence of the PL spectra of 5 nm-thick GaAs QD, measured at T= 10K. Excitation powers are indicated.

Figure 4.11 shows PL spectra of the lens-shaped GaAs QD, taken at different excitation powers in top view measurements geometry at T=10 K. For comparison convenience, spectra have been normalized to their maximum value. Even at low excitation power, the 2X transition appears together with the GS exciton at ~1.54 eV, red shifted by 2.2 meV. The excited transitions appear at ~1.56 eV, with two peaks resembling the ones predicted by the model (figure 4.10). The difference in the energy separation from the GS (~20 meV versus calculated ~10 meV) can be due to a different actual QD shape as compared with the simple model.

4.3.2.2 Time-resolved PL measurements

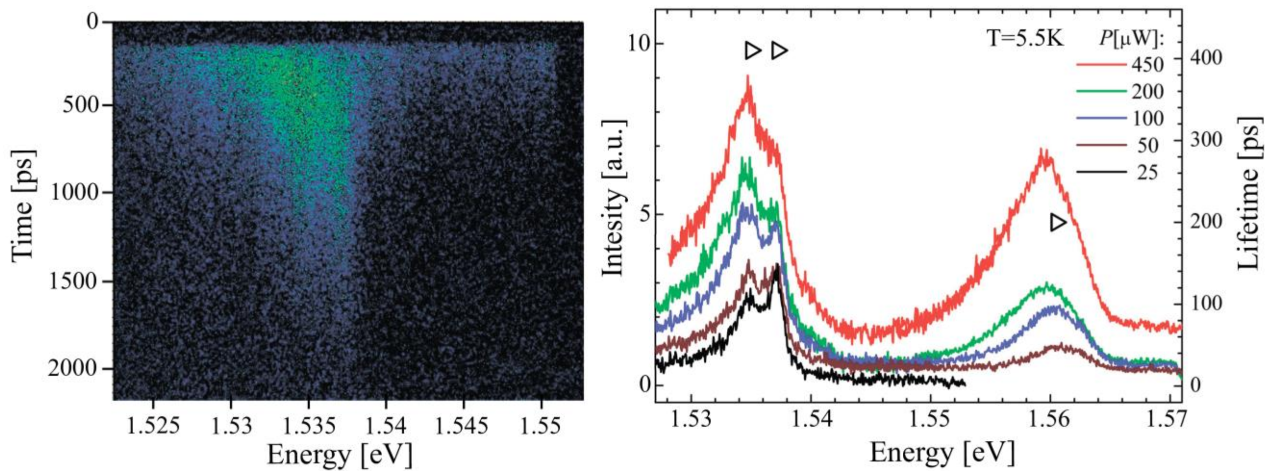

Figure 4.12 Left panel: spectrally and temporally resolved PL of the thin GaAs QD (P=200µW T=5K). Right panel: the average laser power is written at the bottom right corner of each image. Right panel, time- integrated PL spectra of the same structure versus excitation power. Triangles show the decay times at a given energy.

Figure 4.12 presents time-resolved PL spectra and transition decay times of the 5 nm lens-shaped GaAs QD obtained using the streak camera setup at T=5.5 K. From the time-resolved PL we see that the GS and 2X lines appear and decay at the same time. The GS transition demonstrates the longest decay time (~400 ps), as compared with the shorter decay time (~200 ps) of the excited state transition, evidencing efficient relaxation of the carriers to the ground state.

4.3.3 Summary: comparison of QD and QWR systems

The two cases considered so far, the thin QD and the finite-length QWR, are extreme ones in terms of confinement strength along the growth direction. The QD system simulation results demonstrate large energy state separation in the CB, in the order of 30 meV, and in the VB about 6 meV. On the other hand, in the finite-length QWR case the CB state separation of the first states is ~0.1 meV and in the VB it is ~0.05 meV (these numbers depend on the state number), much smaller than the line broadening and thermal energies concerned. The large energy separations and VB hole characters lead to HH-like GS transition, as opposed to the LH-like ones in the QWR case.

4.4 Parabolically-shaped quantum dots

This Section is dedicated to studying the evolution of the optical properties under different degree of quantum confinement strength in parabolically shaped QD nanostructures. Our fabrication method makes possible to realize not only 1D or 0D nanostructures but also nanostructures with variable confinement strength along the growth axis. Parabolically shaped QD potentials is the model structure we chose for defining the degree of confinement. We have realized three types of parabolically shaped QDs with a potential different gradient, where the total length L is 120 nm, 240 nm, and 480 nm [162]. This profile was obtained by dividing the growth sequence into 2x20 steps of equal Al content step Δx and linearly grading the Al content *x* in each segment by properly adjusting the TMGa and TMAl partial pressures (see Appendix B for structure details). This parabolic section, with nominal Al contents changing between 0.2 and 0.4, was sandwiched between barriers of nominally x=0.4 Al content, defining QWR barriers for the parabolic QD. Each structure was studied theoretically and experimentally.

4.4.1 Parabolic QD modeling: evolution with confinement

First, we present modeling results for each structure, including energies of the confined states and their wavefunctions, as well as their optical spectra. The model of the parabolic QDs (PQDs) is essentially the same as the finite-length QWR (Section 4.2.1), except that the QWR core is replaced by the parabolically-shaped QD heterostructure. The actual Al content in the X-Z plane cutting the PQD (L=120nm) at the center of the pyramid is shown on the left part of figure 4.13; the simulated volume is 30x30x300nm (XxYxZ). The core of the structure includes the PQD where the lowest Al content is ~3%, vertically sandwiched between vertical QWR barriers of ~7% Al content and side QWRs with a parabolic distribution of Al content (lowest content of ~10%). These actual Al contents were calculated as described in Chapter 2. On the right side of figure 4.13 is shown the Al content profile assumed along the growth Z-direction at the QD center, along with the calculated electron WF isosurfaces (green).

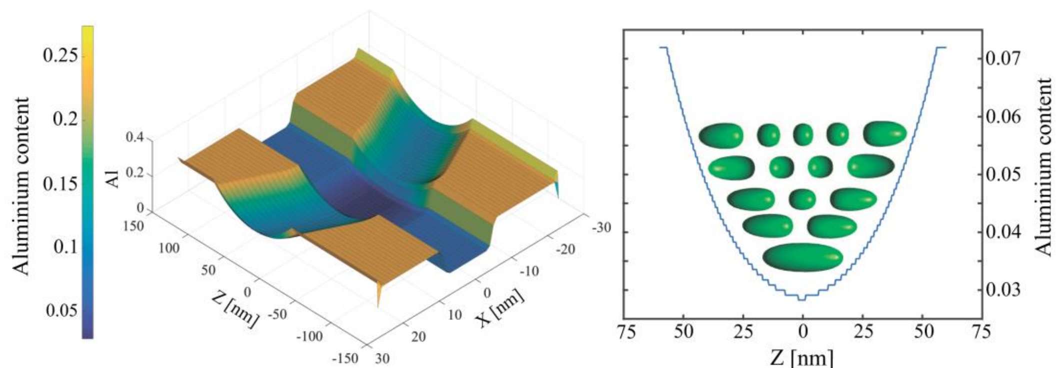

Figure 4.13 Modeled Al content profile of the 120 nm PQD. Left: 3D plot of (actual) Al content; right: profile at QD center along the growth direction (Z). Green: calculated confined electron WFs inside the QD. (Note: WF energy position does not represent the actual corresponding energy).

4.4.1.1 Band structure and optical spectra

120 nm parabolically shaped QD

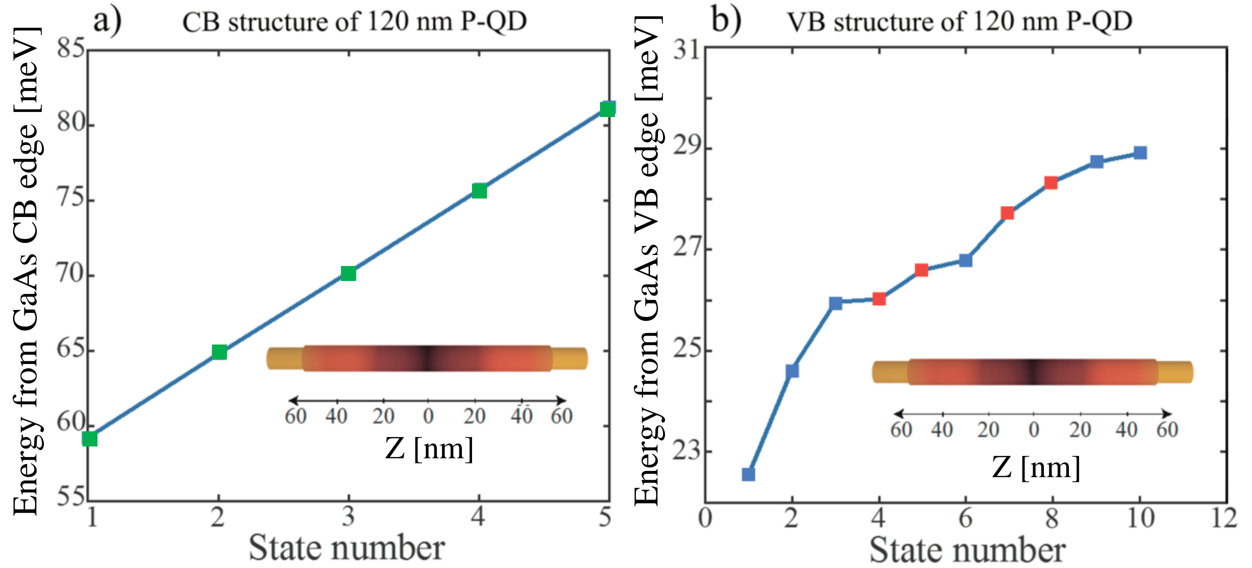

Figure 4.14 Band structure of the 120 nm PQD. (a) Calculated confinement energy of electron states (from the GaAs conduction band edge). (b) Calculated energy of hole states (from the GaAs valence band edge); red squares present VB states with significant HH part, blue squares – LH parts. Insets show schematic pictures of the PQD.

Figure 4.14 displays the calculated band structure of the 120 nm PQD: the confinement energies of the first 5 CB (part a), and the first 12 VB states (part b). As expected for simple harmonic oscillator potential well, the CB states are equally spaced in energy. It can be shown analytically that in infinitely long parabolic potential localized states are equally spaced from each other [143]. Our numerical simulations of CB are in agreement with analytic results. Figure 4.14 b shows the modeling results for the VB; red or blue squares show the energy positions of the VB states for which CB states overlap more with HH (red) or LH (blue) VB states. The details about the WFs overlaps are displayed in figure 4.17. The VB has a more complex structure compared to the CB due to VB mixing, different effective masses and the more complex non-diagonal Hamiltonian structure (see Chapter 2). Moreover, the CB and the VB have different heterostructure potential gradients, which also contributes to different energy spacing. The confinement energy of the CB GS is ~ 29 meV, and that of VB GS is ~7 meV.

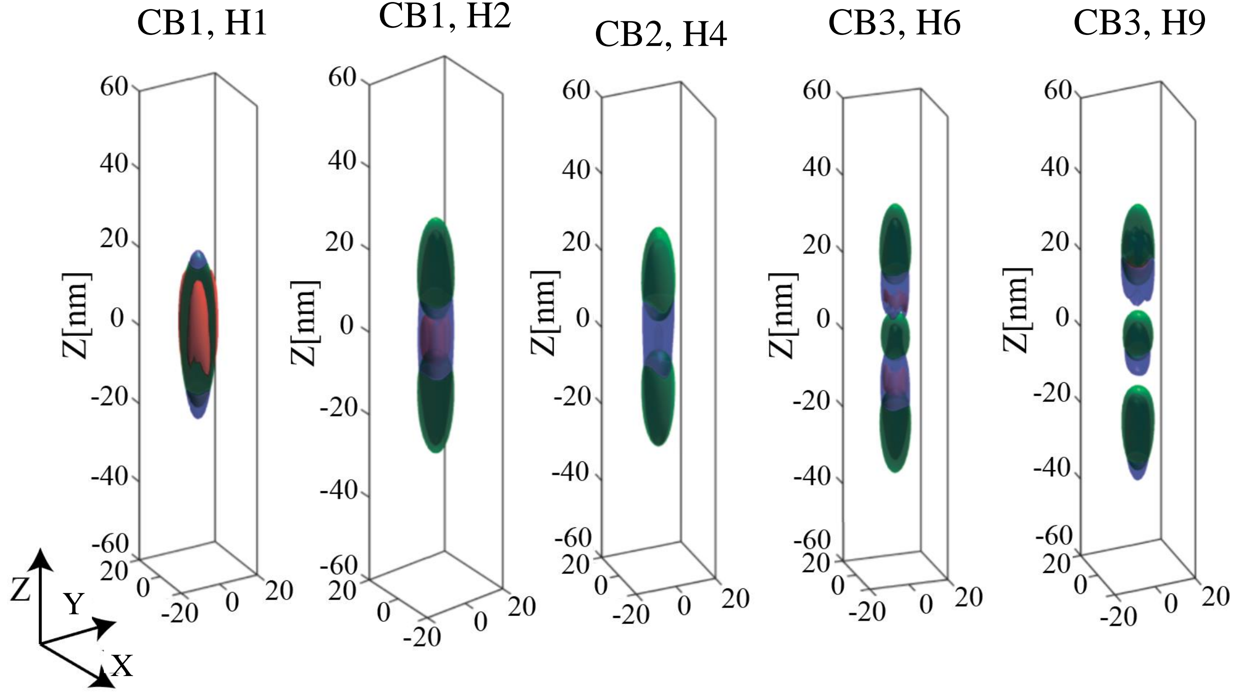

Figure 4.15 CB and VB wavefunctions (Green: CB, blue: LH component, red: HH component) of the first 5 main transitions in the 120 nm PQD). Probability densities at the iso-surfaces are chosen arbitrarily to illustrate WFs geometries.

Figure 4.15 presents the WFs (isosurfaces) of the first 5 states that have strongest overlap with CB, En CB state number Hn VB state number. For illustration purposes, the isosurface probability density values were chosen such that all bands (LH, HH, CB) are visible in the figure. Different colors correspond to different WF type: green for electron, blue for LH-component and red for HH-component. As expected from the WF overlaps, the strongest transitions should correspond to those between CB and the LH parts of the VB states. Figure 4.16 shows examples of WF isosurfaces involved in transitions between CB states and other VB states, where overlaps with the HH components are more significant and dominant HH-like transitions are expected.

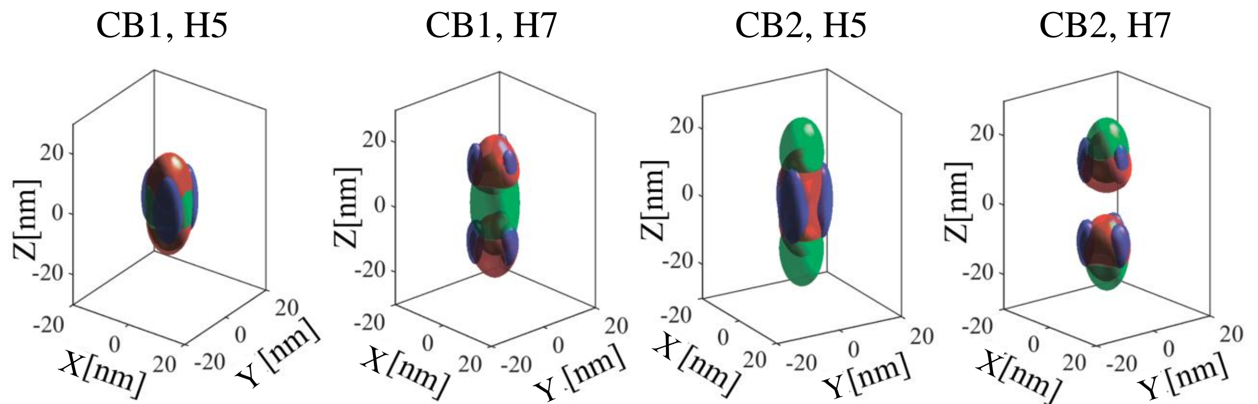

Figure 4.16 CB and VB wavefucntions (Green: CB, blue: LH component, red: HH component) for additional transitions in the 120 nm PQD). Probability densities at the iso-surfaces *are chosen arbitrarily to illustrate WFs geometries.*

Figure 4.17 presents a summary of the overlaps between the CB and VB states in the 120nm PQD (blue and red for the LH and HH components, respectively). The GS CB and the GS (essentially LH) VB states have the largest overlap, due to the similarity in the CB and LH WF shapes. The excited states of the CB overlap with HH and LH components of different VB states to different degrees, depending on the details of the WF shapes.

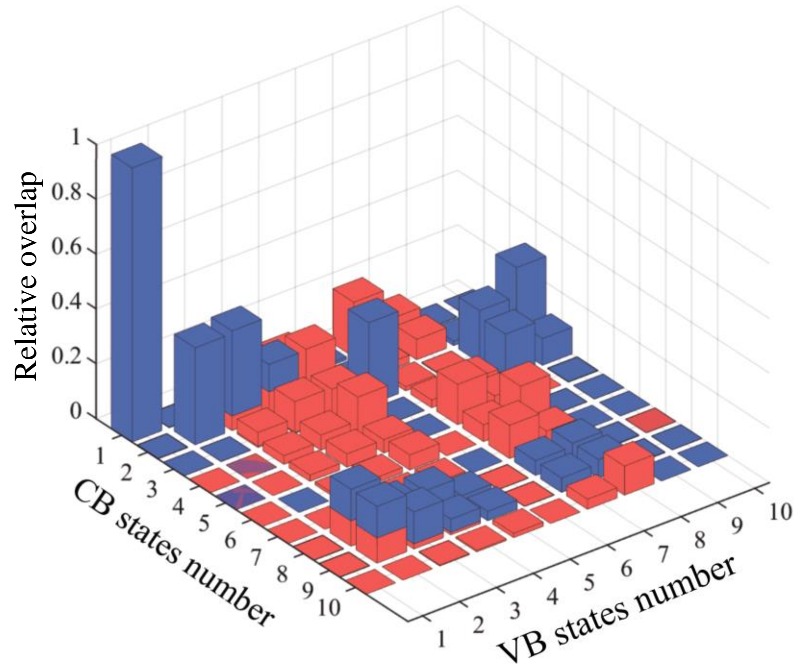

Figure 4.17 Normalized wavefunction overlaps between the CB and VB states confined in the 120 nm PQD. Color corresponds to the transition type: blue and red for LH and HH components, respectively.

The left panel of figure 4.18 presents the calculated optical transitions rate spectra neglecting Coulomb interaction and broadening effects. The GS transition has a strong LH character, whereas spectra of the excited states have either LH or HH character. Still, the strongest transitions around a given energy have a LH character. The first HH transitions appear just above the GS one (at ~1.605 eV), and are related to the first CB state and excited VB states H5 and H7 (see figure 4.16, E1-H5, E1-H7). We should note that, despite the fact that the CB states in this parabolically shaped QD potentials are equally spaced, the resulting optical spectra are more complicated due to the complex structure of the VB. But if we consider only the LH transitions clusters related to the different CB states, we can identify clusters of main transitions with a spacing of ~ 9 meV. The right panel of the figure 4.17 presents the optical spectra for the same PQD structure, but including Coulomb interaction as a perturbation and artificial broadening of 2 meV. The broadening merges the LH transitions clusters with nearby HH transitions into broader peaks. Note that the parallel and vertical polarization components of the merged lines have intensity ratios that are neither pure LH-like or pure HH-like, but rather depend on the details of the transitions involved.

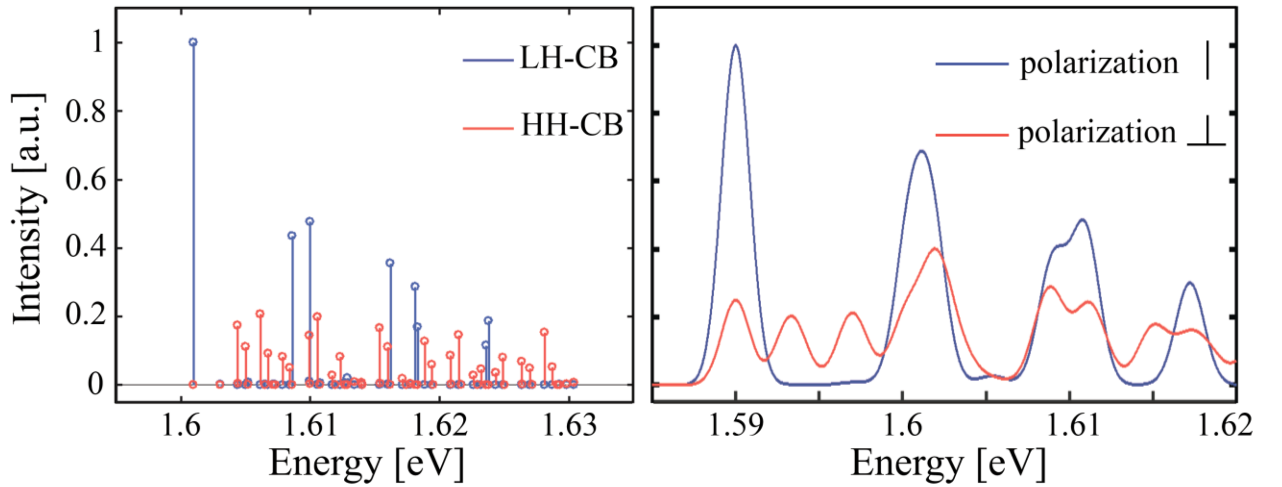

Figure 4.18 Calculated optical spectra of the 120 nm PQD structure. Left panel: relative transition rates, excluding Coulomb interaction and broadening. Blue and red colors show HH and LH parts. Right panel: calculated absorption spectra taking into account Coulomb interaction as a perturbation and 2 meV broadening of transitions. Blue and red colors indicates linear polarization along and transverse to pyramid axis, respectively.

240 nm parabolically shaped QD

The calculated band structure of the 240 nm PQD is presented in figure 4.19. As evident for the CB (figure 4.19 a), the states have smaller energy spacing due to the lower potential gradient as compared with the 120 nm PQD structure (higher density of states). The confinement energy of the CB GS is ~ 26 meV, and that of the VB GS it is ~5 meV. The first 12 CB states are equally spaced with a spacing of ~ 3 meV, with harmonic-oscillator like WF patterns. Figure 4.19 b presents the VB band structure calculation results by the blue or red colors we show VB states for which the LH (blue) or HH (red) components have significant overlap with CB states. In the insert schematic picture of confinement potential and first 5 VB WFs states that have strongest overlaps with CB. Generally speaking, VB states are not equally spaced, but as shown later (figure 4.21) the VB states that have the strongest overlaps with the CB states are equally spaced. We see a trend towards a QWR structure in the sense that HH WFs have a larger quantum number as compared with the 120 nm PQD where the fourth VB state was already a HH character. In Appendix B, the calculated wavefunction overlaps and their type are presented, as in figure 4.17 for the 120 nm PQD.

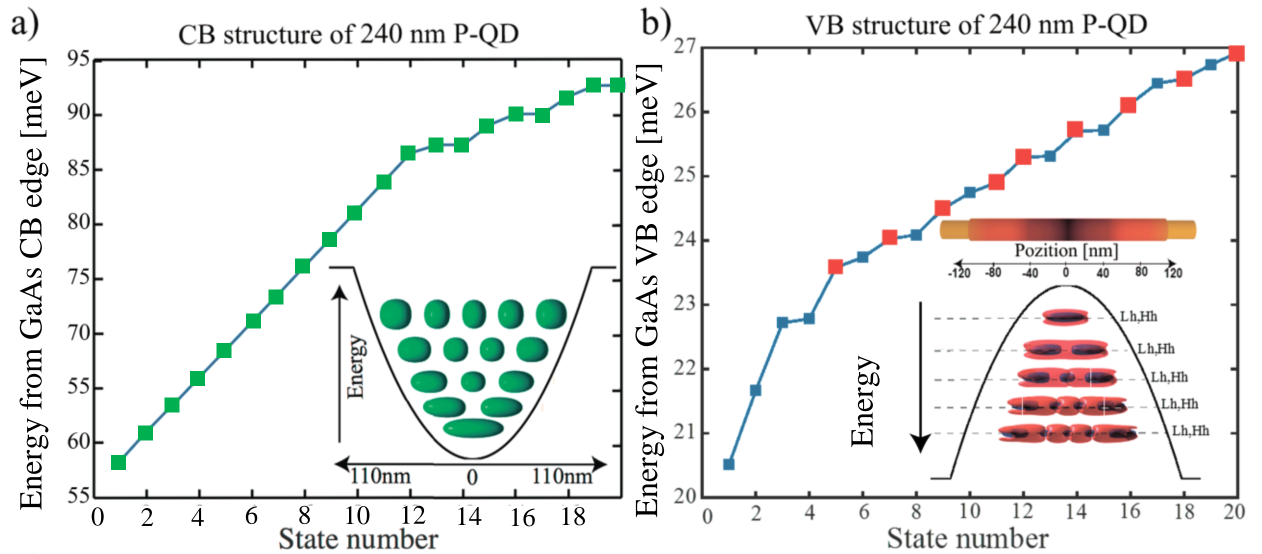

Figure 4.19 Band structure of the 240 nm PQD. (a) Calculated energy of the CB states. (b) Calculated energy of the hole states; red squares present VB states with significant HH part, blue squares present energies of LH ones. Insets show calculated corresponding WFs.

Figure 4.20 shows side view and top view illustrations of the calculated WFs of the first 5 strongest optical transitions in the 240nm PQDs. More detailed information about the WF geometries for each calculated state can be found in Appendix C. Clearly, the CB WFs overlap almost perfectly with the LH WFs, whereas their overlap with the HH WFs are very small due to the hole in the HH WFs along the axis of the PQD.

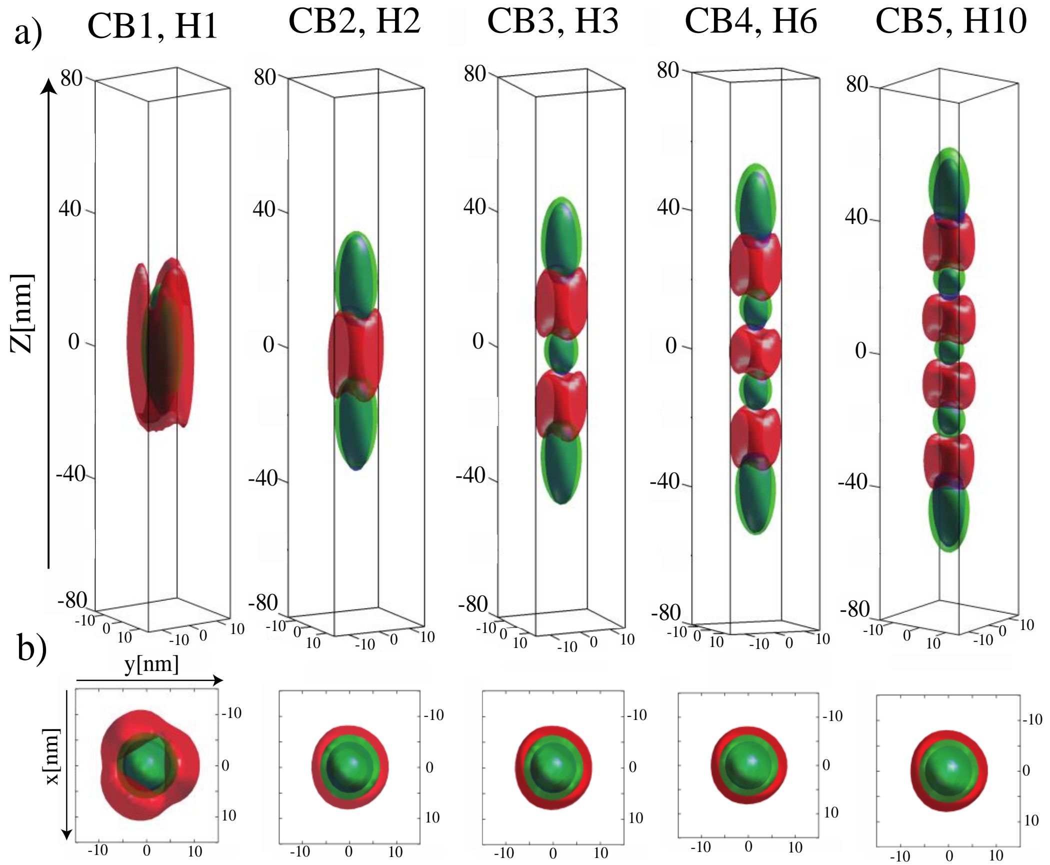

Figure 4.20 CB and VB WFs (Green CB, blue LH, red HH) of first 5 main transitions in the 240 nm PQD. (a) Side view. (b) Top view.

Figure 4.21 (left part) presents the calculated optical transitions rate spectra neglecting Coulomb interaction and broadening effects, for the 240nm PQD. The transitions between the CB and the LH part of the VB WFs are indicated in blue, and for the HH parts in red. We see that, compared to the 120 nm PQD case, the strength of the HH related transitions is significantly smaller, and they are more blue shifted towards the main excited transitions. The spacing between the main transitions is ~4 meV. The right panel of figure 4.21 shows the calculated optical spectra with artificial broadening and including Coulomb interaction as a perturbation. The Coulomb interaction affects on spectra by inducing a redshift in transition energies that, generally speaking, depends on the confinement potential and modifies the spacing between the transition lines. In particular, the spacing between the GS and excited states becomes larger, since the WFs involved are more localized in the nanostructure center.

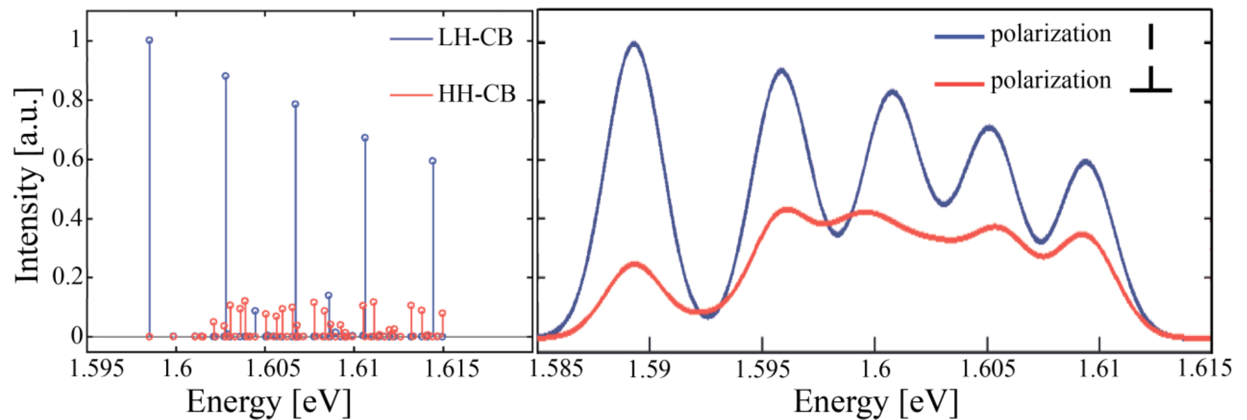

Figure 4.21 Calculated optical spectra for the 240 nm PQD structure. Left panel: relative transition rates, excluding Coulomb interaction and broadening. Blue and red colors show HH and LH parts. Right panel: calculated absorption spectra taking into account Coulomb interaction as a perturbation and 2 meV broadening of transitions. Blue and red colors indicate linear polarization along and transverse to the pyramid axis, respectively.

480 nm parabolically shaped QD

The 480 nm PQD has the lowest parabolic gradient that we realized experimentally, making it close to a uniform QWR structure in terms of confinement geometry. The calculated band structure and absorption spectra of the 480 nm PQD are presented in figure 4.22. Part a of the figure presents the energies of the first 5 equally spaced CB states, with state separating of ~1.5 meV. Figure 4.22 b presents the VB energies of first 12 states; different colors shows which component of the VB state has a stronger overlap with the corresponding CB state, LH (blue) or HH (red) VB part. The first 5 VB states show the same behavior as the CB states with energy spacing of about ~0.5 meV. Such small state separation in the VB makes this structure sensitive to the temperature due to the phonon-carrier interaction. Thus, around 10 K (~1 meV) the VB states are basically populated as in a QWR, while the CB states separation is still high for phonon induced transitions. The VB states with significant CB-HH overlap start from state number 10. These results show the trend of the HH-like transitions to lose strength at the low energy part of the spectrum with decreasing confinement strength along the growth direction (see appendix C.8, transition strength histogram for the 480 nm PQD).

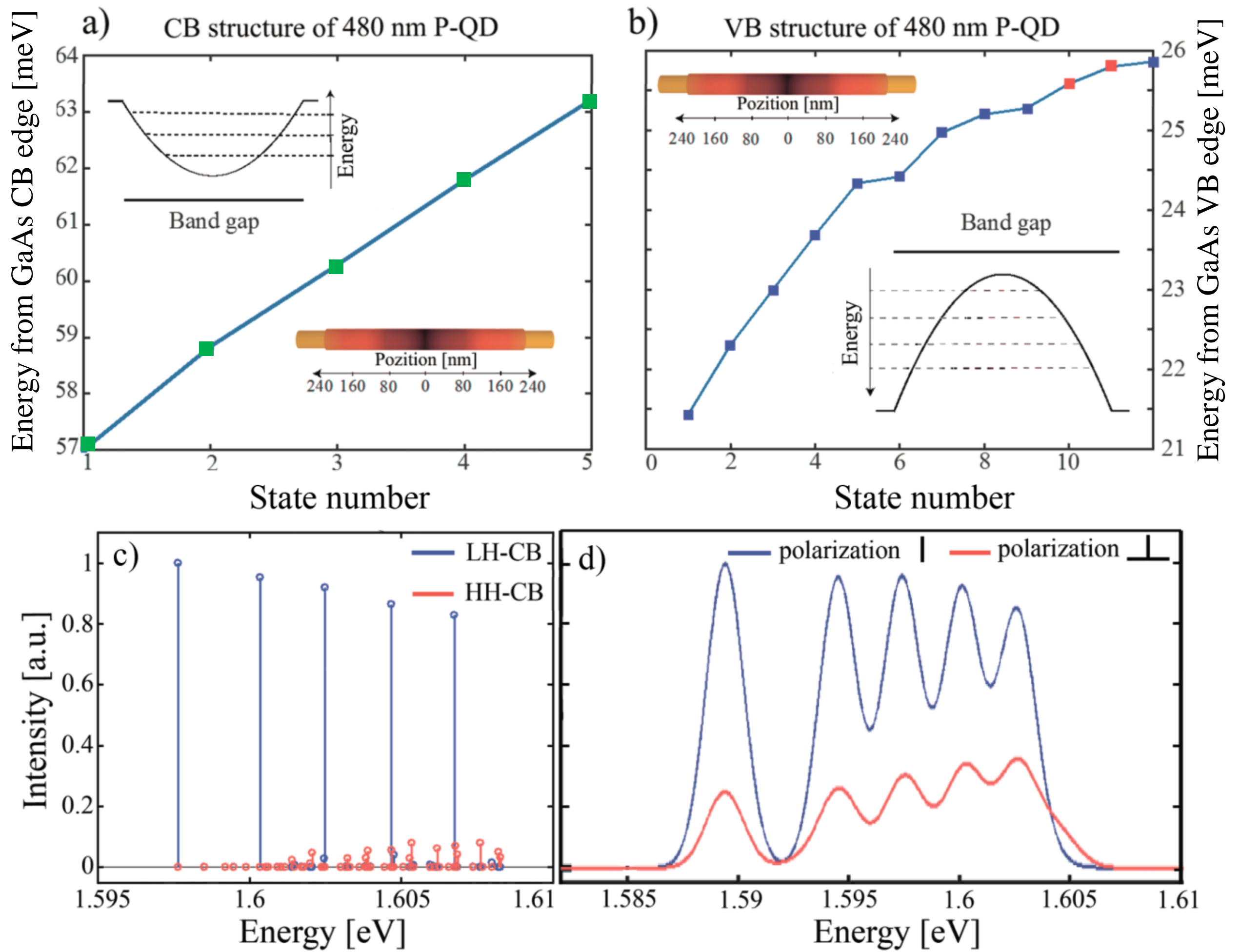

Figure 4.22 Modeling of the 480nm PQD structure. (a) Calculated energy of the first CB states. (b) Calculated energy of the first VB states. Inserts show schematic representation of states inside modeled potential. Calculated optical spectra showing (c) relative transition rates, excluding Coulomb interaction and broadening (blue and red colors show HH and LH parts) and (d) taking into account Coulomb interaction as a perturbation and 2 meV broadening of transitions (blue and red colors indicate linear polarization along and transverse to pyramid axis, respectively).

The calculated CB and VB WFs of the 480nm PQD are qualitatively similar to the WFs of 240 nm PQD, except that the state numbers involved into the strongest transitions are different. Figure 4.22 (c) and (d) show the optical spectra of the 480nm PQD structure. The first 5 transitions have similar features as the lowest energy transitions in the corresponding QWR structure (see figure 4.5 and Appendix C) Comparing to figures 4.18 and 4.21, we see that the influence of HH-related transitions is gradually decreasing with decreasing the confinement potential gradient, leading to LH transition domination (see figure 4.5). Figure 4.22 d, where the optical spectra take into account Coulomb interaction as a perturbation, and an artificial broadening of 2 meV, shows that the energy spacing of the transitions stays the same, except for the GS transition that becomes more red shifted due to the WF concentration in the center of the nanostructure (as already seen in the 240 nm PQD structure).

Comparing the three PQD structures, we see that with increasing confinement (potential gradient), the spacing between the confined states and transitions increases. However, the CB have a simple harmonic-oscillator like behavior that can be predicted analytically, whereas the VB states are defined by the Luttinger Hamiltonian and have a more complex structure. The overlap of the LH WF components with the CB WFs decreases with increasing confinement strength, and the presence of the HH components in the optical spectra becomes more and more significant. As a consequence, the excited states transitions demonstrate a more significant HH-like flavor in the polarization resolved spectra.

4.4.2 Experimental results

The PQD samples presented above were measured and characterized using the PL setups described in Chapter 3. The conventional PL studies presented in this chapter were done with cw laser excitation, whereas the time resolved spectra obtained by pulsed excitation. Excitation was done at 532 nm wavelength in top-view geometry of the back-etched pyramids, with 1-2 μm (~5 μm for time resolved) laser spot permitting excitation of single pyramids. In the following Sections, we will discuss the low temperature PL spectra and carrier scattering (relaxation) properties in these PQDs.

4.4.2.1 Power dependence of PL spectra

Figure 4.23 presents the excitation power dependence of the PL spectra acquired from the PQDs (L=120 nm, 240 nm, 480 nm) at T=10 K. All structures demonstrate effective state filling with increasing excitation power and several equally spaced peaks, which spacing that depends on the potential gradient. In addition, the binding energy of the 2X peak increases with increasing potential gradient. In general, we observe that decreasing the potential gradient leads to a slight red shift (~2 meV) of the GS due to the reduction in confinement energy. This value is comparable to the GS peak position homogeneity of the PQD, also ~2 meV [119].

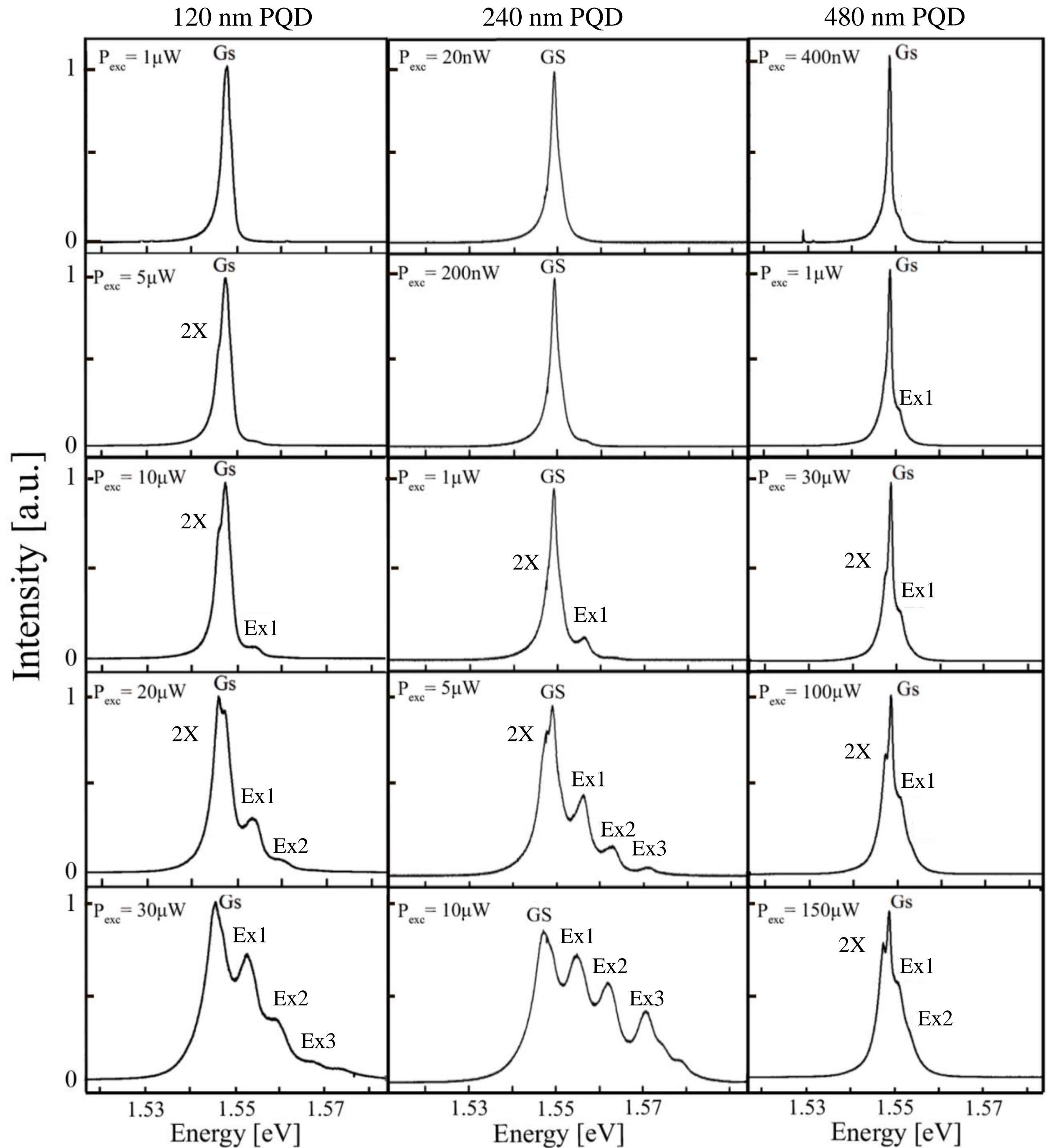

Figure 4.23 Excitation power dependence of the PL spectra of the PQDs (120 nm PQD: left column, 240 nm PQD: central column, and 480 nm PQD: right column; T= 10 K). Excitation powers are indicated, as well as the resolvable transition peaks.

In such top excitation measurements of back-etched pyramids, the GS energy position is also affected by electric fields due to surface charge carriers. Moreover, alloy disorder with ~0.2% in Al content would also give comparable energy shifts. In the low power spectra of the 120 nm PQD (P=1 μW), only the GS transition is exited; the GS line asymmetry is assigned to the

appearance of the 2X state. The 2X peak starts appearing at P= 5 μW, although it is hard to resolve; numerical fitting which gives 1.5 meV red shift of the 2X transition compared to the GS position. The first excited state also starts to show up at this excitation level (at ~1.554 eV). The 240 nm PQD shows medium transition spacing of ~5 meV. It shows a bit different states filing dynamics: the 2X and first excited state transitions appear at a similar excitation level. In the 480 nm PQD, the 2X line appears at higher excitation than the first excited state. Here, the energy spacing of the transitions is ~2 meV. Thus, the states separation in the CB or VB are ~1 meV, which is comparable with crystal temperature. Such low states separation in general leads to properties similar to those of a QWR. The experimental energy spacings are in good agreement with the simulation result presented earlier in this chapter. The temperature dependence of the PQD spectra are presented in Appendix C (figure C.9).

4.4.2.2 Carrier relaxation dynamics

120 nm parabolically shaped QD

Figure 4.25 presents the power dependence of the time-resolved PL spectra obtained by streak camera measurements on a single pyramid with a 120 nm PQD. In the first column (P<100 μW) the first GS is visible, and with increasing power it saturates and multiexcitonic states show on its low energy side. For P >100 μW, excited state transitions show up. The almost equal transition spacing (~ 8 meV) is similar to that observed in the cw spectra (8 meV, figure 4.23). In the time resolved spectra, it is well seen that the GS lineshape is asymmetric, a sign of the presence of multiexcitonic states, and the same asymmetry repeats for the excited states at the higher excitation powers. As in the case of the QWR, the GS has the longest decay time due to fast scattering of carriers from the excited states to the GS. We can see the decay time of the GS, ~350 ps (see figure 4.26). The excited states demonstrate faster decay for first excited state ~300 ps, second ~ 200 and etc. (see figure 4.26).

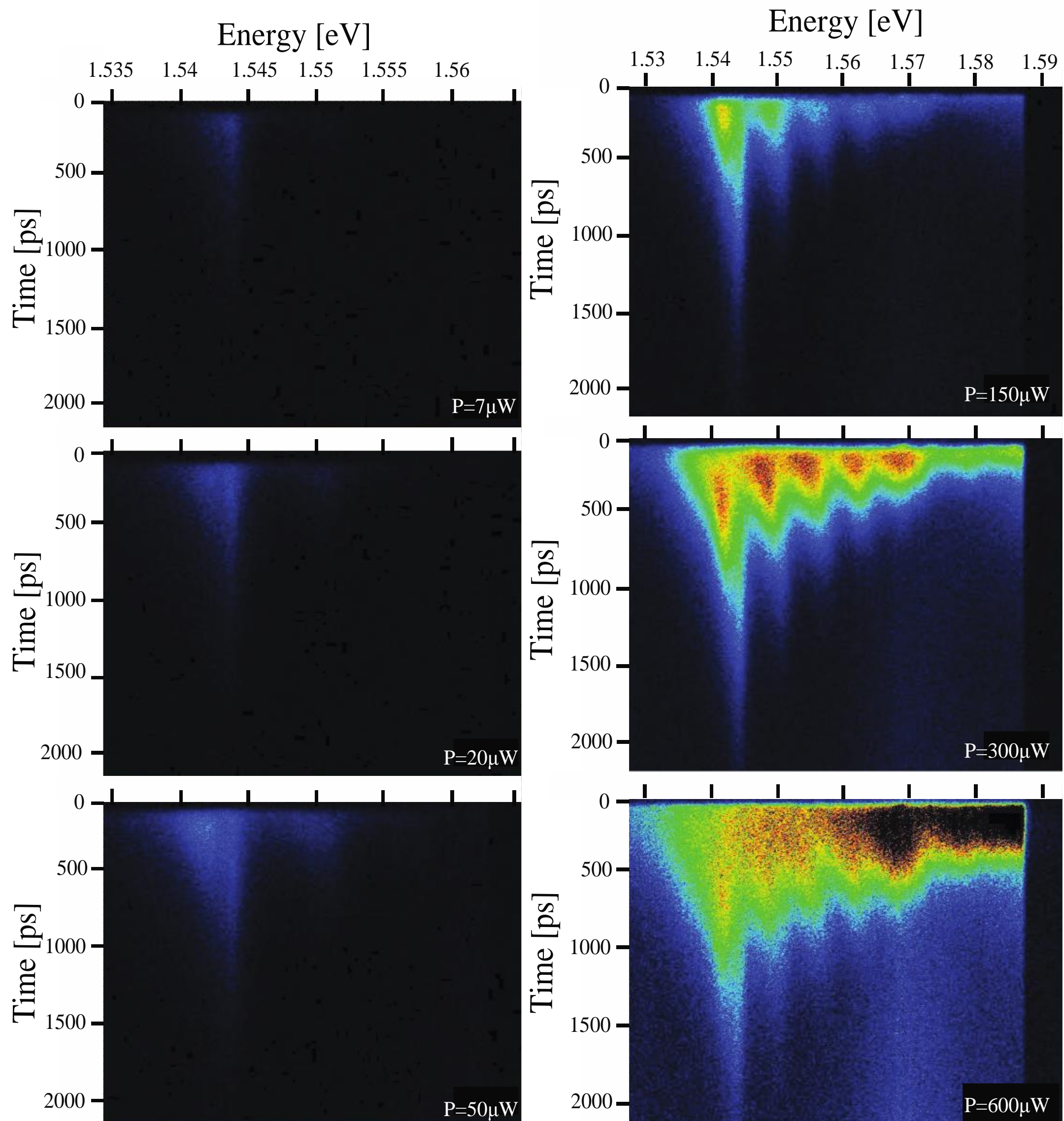

Figure 4.25 Time-resolved photoluminescence spectra of a single 120 nm PQD structure. Spectral-temporal images were obtained under pulsed excitation for the different average excitation powers P indicated.

This effect is presented quantitatively in figure 4.26, which shows time-integrated PL for different excitation powers, and (by the triangles) the decay time at a given energy, measured at P=150 μW. The decay time peak is aligned in energy with peaks of 150 μW spectra. Shorter decay times are observed for higher excited states indicating faster carrier relaxation for these states. The 300 μW spectrum is a bit red shifted suggesting multi-excitonic effects.

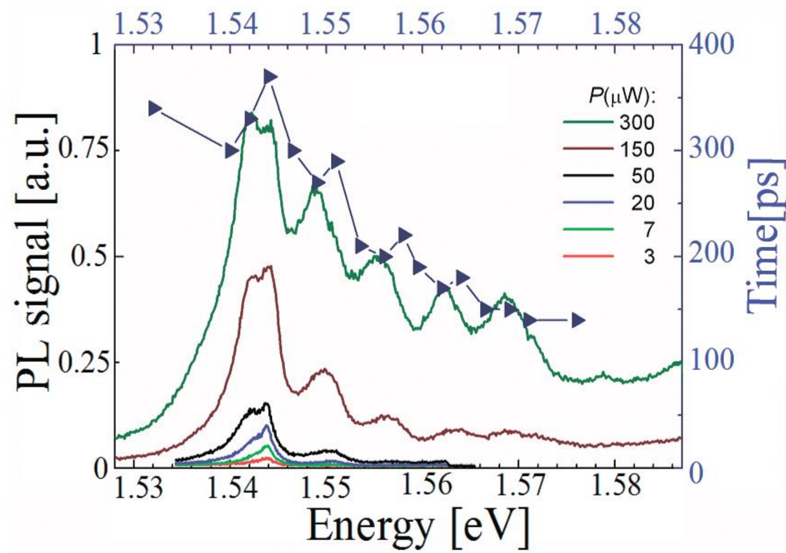

Figure 4.26 Power dependence of (time integrated) PL spectra of the 120 nm PQD sample obtained at T=5 K; excitation power indicated in the insert. Triangles show the decay time at the corresponding energy, obtained from the time-resolved measurements at P=150μW.

240 nm parabolically shaped QD

The same measurements were carried out on the 240 nm PQD structure. The corresponding time resolved spectra are shown in figure 4.27, and the extracted decay times are displayed in figure 4.28. The results are similar to those for the 120 nm PQD structure except that the state spacing is larger and the decay times are slightly shorter. The GS exciton decay time is ~280 ps and first excited state ~220 ps. The difference in decay time occurs due to the different nanostructure confinement strength. This should be compared to the decay time for thin pyramidal GaAs QD, for which the GS decay time is ~400 ps (see figure 4.12).

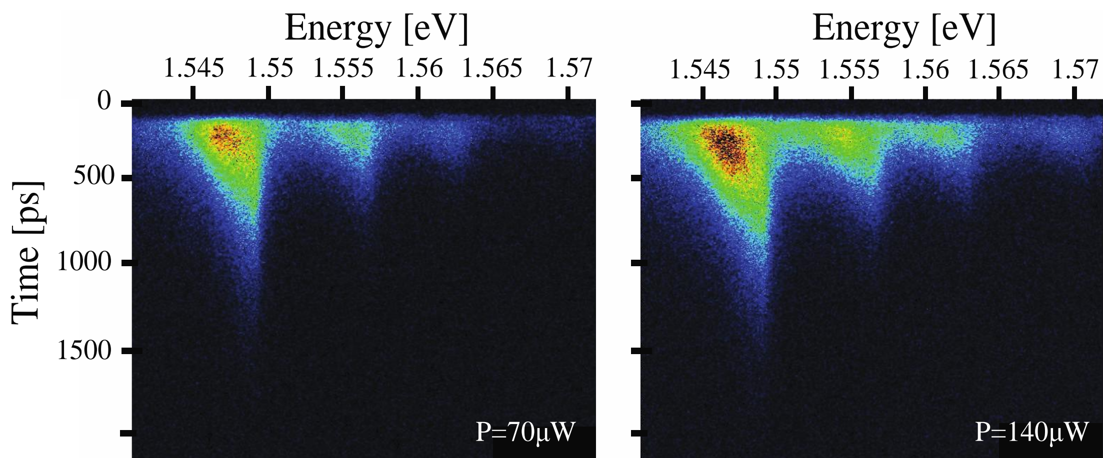

Figure 4.27 Time-resolved photoluminescence spectra of a single 240 nm PQD structure, obtained at T=5 K and two average excitation powers P.

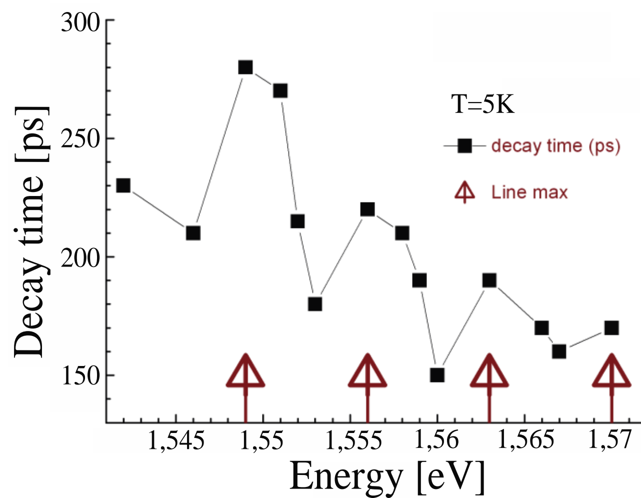

Figure 4.28 Decay time versus energy for the 240 nm PQD structure of figure 4.27. Sample temperature is T=5 K, excitation power is P= 210 μW. Triangles show the energy positions of the spectral peaks.

480 nm parabolically shaped QD

The time resolved PL spectra for the 480 nm PQD (figure 4.29) remind those of the QWR structure. Figure 4.29 show power depended on time resolved PL spectra measurements result obtained at T=5 K. Compared to the 120 nm and the 240 nm PQD structures, the dynamics of the different excited states are more difficult to resolve.

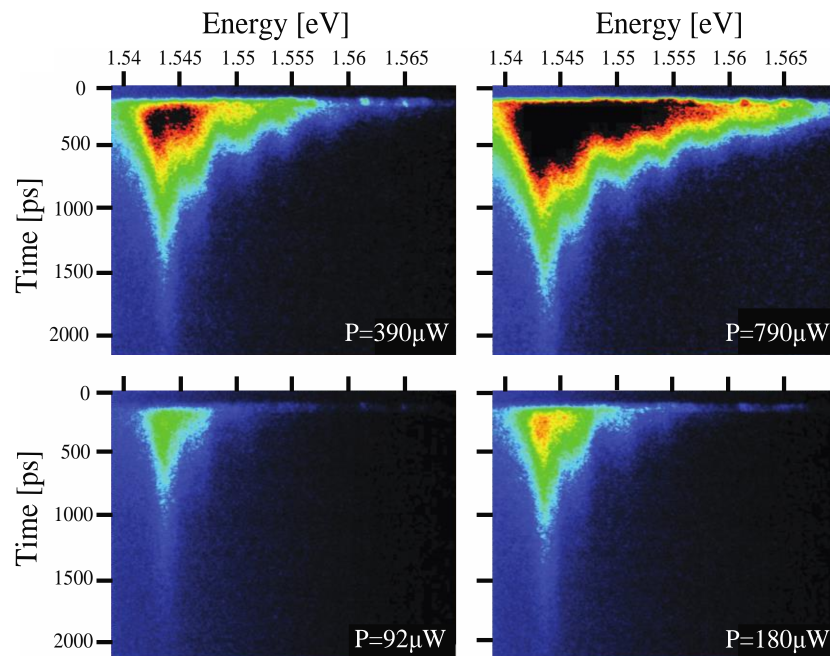

Figure 4.29 Time-resolved PL spectra of the single 480 nm PQD structure, measured at T=5 K for several average excitation powers P.

4.4.3 Discussion

Here we summarize all collected results of 1D-0D nanostructures in this chapter. First, we will review obtained results of quantum confinement influence on confined carrier states using the results of power dependent spectra and states filing by temperature dependent PL.

Quantum confinement strength and exciton decay time

We have presented grown structures (figure 4.1) and PL results at low temperature, each structure presented has unique confinement potential. In the literature confinement energy, is a well-established term in case of rectangular potential as difference between the ground state energy and the bottom of confinement potential. In the more complex case where potential depends on position (like in PQDs) it is not clear how to identify the confinement energy. To give the qualitative meaning of confinement in 0-1 D nanostructures we need to introduce a new variable, confinement strength. I propose to define the confinement strength as the energy difference between GS and first excited state in CB. The similar definitions could be proposed, per example energy difference between GS and first excited state in VB or more complicated ones. I propose the simplest definition, that in some cases can be even treated analytically. Figure 4.30 shows "map of nanostructures" where as coordinated were taken size of the nanostructure and its calculated confinement strength. Blue curve correspond to pyramidal nanostructure with parabolic and red rectangular potential, with the bottom of $Al_{0.2}Ga_{0.8}As$, barrier heights $Al_{0.4}Ga_{0.6}As$ (nominal parameters). By changing Al content in the nanostructure we can realize almost all points on this map. To obtain this curves a number of structures have been simulated it is shown as small squares in the figure, by the black stars fabricated structures.

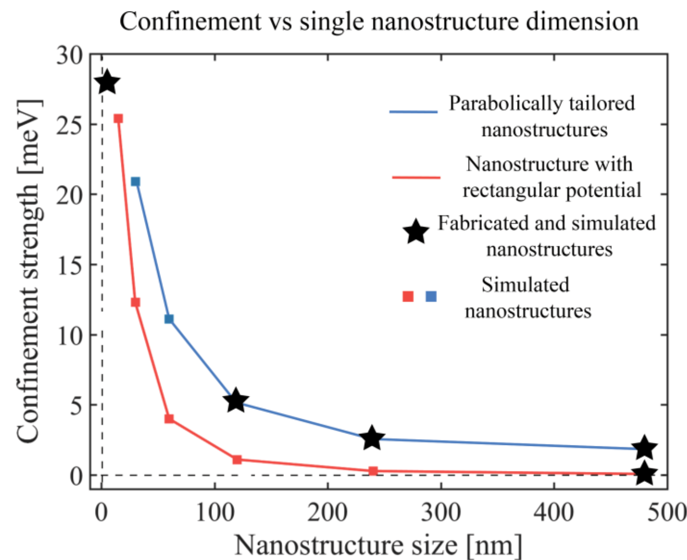

Figure 4.30 Map of grown and modeled nanostructures. As a coordinate on the map were taken the nanostructure confinement strength and actual nanostructure size. Confinement strength of the nanostructure by definition was taken as the energy difference between first and second CB confined states.

Figure 4.31 presents a summary of the measured decay time of the observed transitions in the investigated structures. Different colors lines correspond to different number of studied state (see figure legend), the structures are indicated by dashed lines. We see the tendency of increasing difference of the decay time between the GS and excited ones with increasing confinement strength. Also decreasing the decay time with the number of excited states.

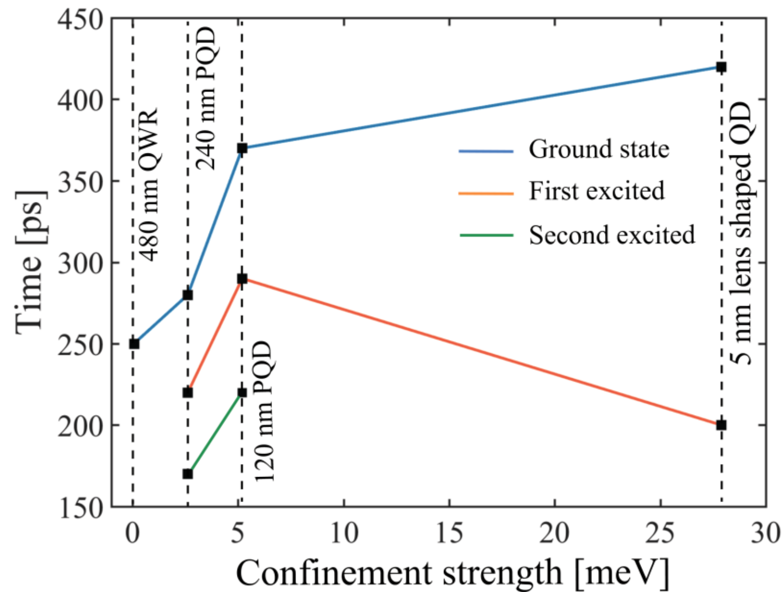

Figure 4.31 Summary of the observed decay time for all grown PQD structures.

Band gap renormalization and confinement strength

In all spectra of presented structures we see the redshifted to GS peak that serve as indication of presents of malty particles states (biexcitons, charged excitons and etc.). We cannot resolve all myltiexcitonic states due to the broadening of excited states, but we can resolve myltiexcitonic peak correspondent to the GS. Figure 4.32 shows the energy difference between the GS transition and multiexcitonic one as a function of confinement strength (log scale). By dashed lines shown the positions of the nanostructures in confinement strength axis, the insert shows an example of a fitting process for "thin" (5 nm) GaAs QD, the red dashed lines in the insert is a fit curve and the black one is center position. The fitting is quite a delicate process and can give a bit different line positions depending from fitting parameters, the error bars shows this uncertainty. As a result for presented structure is presented in the figure 4.32. The energy difference depends as *log* of confinement strength from 0 meV to 2 meV. Note that 0 energy difference (as in QWR) does not mean that there are no multyexcitonic states, there are, but too close to the correspondent excitonic transition to resolve them. Our numerical simulations supports the experimental results and tell us that GS multiexcitonic binding energies lies in the same energy range.

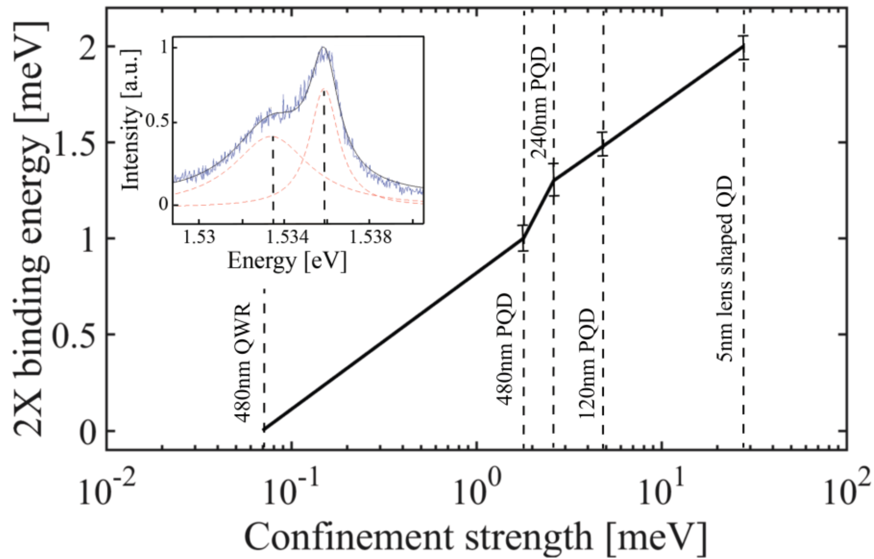

Figure 4.32 Summary picture of the red shift of multiexciton line from the ground state line position.

4.5 Summary

We have shown that vertical AlGaAs QWRs grown in inverted pyramids serve as a good system for simulating ideal QWR structures as well as tailored potential QDs. In particular, the transition between 2D and 3D quantum confinement was investigated in such QD structures with parabolically-shaped potential profiles, fabricated by varying the Al content along the growth direction in the AlGaAs pyramidal QWRs. The conduction band wavefunctions exhibit harmonic oscillator-like features, with energy spacing determined by the potential gradient. The calculated optical transitions show dominant CB-LH transitions, due to the elongated confinement geometry. However, with increasing confinement strength along the growth direction, the CB-HH transition components become more significant. Photoluminescence spectroscopy reveals the main expected features of the optical transitions between the confined states, including the decay times of the transition lines. Experimental evidence for the predicted evolution of the VB states with confinement via analysis of the polarization of the optical emission is presented in Chapter 5, where we discuss the role of HH and LH characters of the VB states considered.

Chapter 5

Valence band mixing and emission polarization of tailored-potential quantum dots

Modification of the band structure of electron and hole states in semiconductors via quantum confinement has been broadly exploited in the quantum engineering of their electronic and optical properties. Quantum confinement in two or three directions introduces mixing of the heavy hole (HH) and the light hole (LH) valence band (VB) states in III-V direct gap semiconductors (center zone), which should impact the polarization states of emitted light.

In this chapter, we investigate theoretically and experimentally the relationship between VB mixing and the polarization states of light emitted by tailored-potential QDs. After introducing some details of the experimental techniques in section 5.1, polarization-resolved, side-view PL spectra of thin pyramidal QDs and parabolic QDs are presented and discussed in sections 5.2 and 5.3. Section 5.4 presents estimations of the effective carriers temperature and state occupation numbers. The relationship between light polarization and VB mixing, line broadening and state occupation is explained in section 5.5, and conclusions are summarized in section 5.6.

5.1 Measurement of emission polarization in pyramidal nanostructures

As shown in Chapter 2, the measured degree of linear polarization (DOLP), is directly related to the hole character of the corresponding transition. Consider a QWR or QD at the core of the inverted pyramid (see figure 5.1). The DOLP of the emitted light is defined as:

$$DOLP = \frac{I_z - I_{xy}}{I_z + I_{xy}}$$

Where I_z is the emission intensity of the light polarized along the QD growth direction and I_{xy} is the intensity of the light polarized in the x-y plane. For a pure LH transition, Chapter 2 2 yields the calculated polar plot of the emission intensity analyzed with a polarizer rotated in the x-z plane, as displayed in figure 5.1. Such intensity distribution corresponds to DOPL=0.6, as indeed observed for pyramidal QWR structures [115].

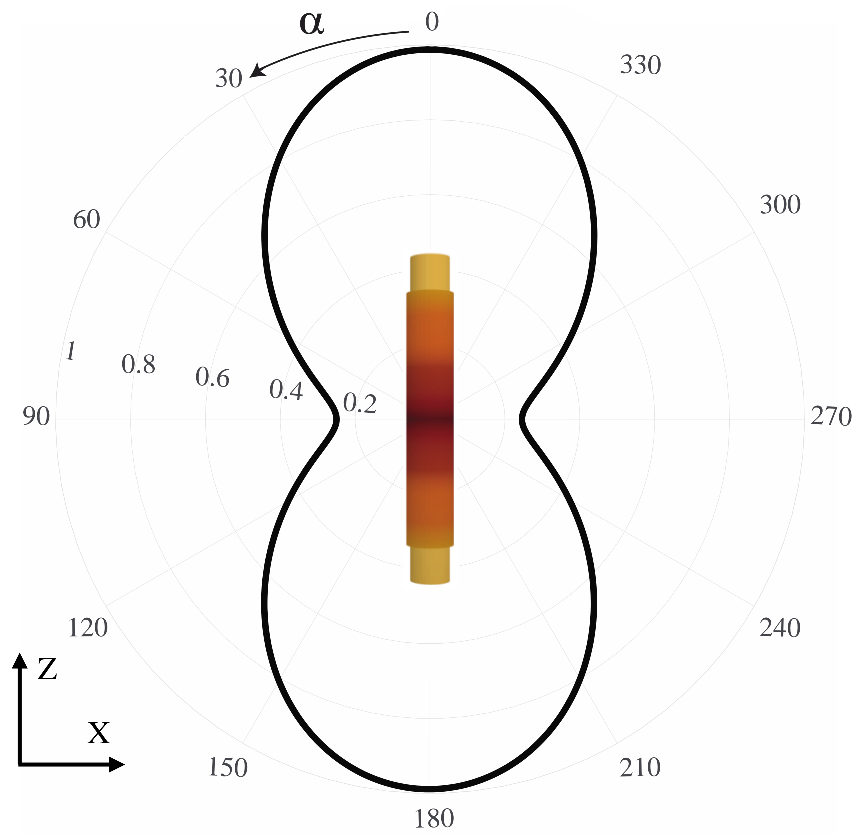

Figure 5.1 Calculated polar plot of the relative intensity variation for a pure LH transition (side-view measurement). The inset shows a schematic illustration of the QD structure and its relative orientation.

The polarization-resolved PL spectra discussed in this chapter were acquired employing the micro-PL system described in Chapter 3. All spectra were acquired at T=10 K in the cleaved edge geometry. Using the position controller we are able to fix the position of the excitation laser beam on the sample with a precision of ~300 nm as shown schematically in figure 5.2. Care should be taken to accurately align the laser spot with the QD since excitation levels may affect the measured DOLP (see section 5.5).

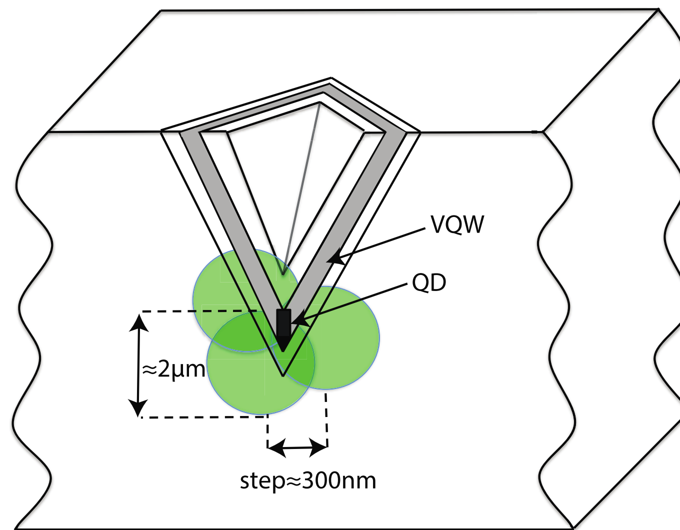

Figure 5.2 Schematic illustration of the cleaved sample with the pyramidal QD structure, with the green circle showing the excitation laser spot.

We used the following procedure for measuring the series of polarization-resolved PL spectra. First, we measured the maximum intensity of the PL spectra (QD line) with a polarizer parallel to the growth direction (α=0°). Next, the polarizer is rotated with 10° degree steps and each spectrum is normalized in intensity with respect to the one for 0°. Due to temperature and position fluctuations, the absolute measured intensity may fluctuate as well, thus the laser spot position has to be corrected for each measurement. An example of typical measurement deviations is shown in figure 5.3, which presents 4 PL spectra of different measurements sets acquired with polarizer angle α=30°. In spite of readjustments of the excitation spot, we observe fluctuations of ~4-6% of the PL intensity around the normalized value 0.8.

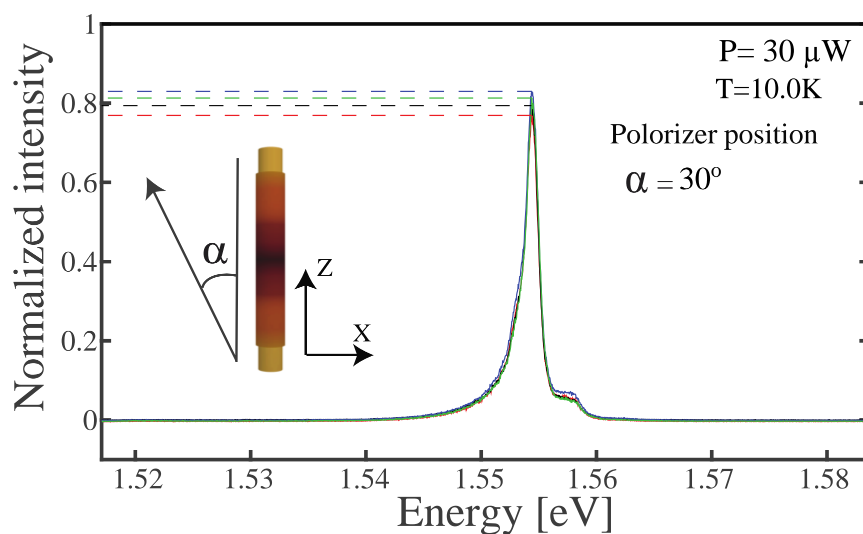

Figure 5.3 Polarization-resolved PL spectra of a 240 nm parabolic QD structure for several takes at polarizer position α=30°. Excitation power P=30 µW, T=10 K.

Based on polarization-resolved measurements as in figure 5.3, polarization polar plots could be constructed. Figure 5.4 shows such plot with polarizer steps of 10° for the 240 nm parabolic QD structure of figure 5.3 (see Appendix B for details of the structure). Different point at each angle α correspond to different takes. The solid black line is the fit to the theoretical curve shown in figure 5.1. It can be seen that despite the fluctuations in absolute intensity discussed above and charge fluctuation in surrounding medium, a concrete polarization characteristic can be derived by this measurement procedure. In fact, in this case the transition indeed corresponds to almost pure LH-transition, as further discussed in this chapter.

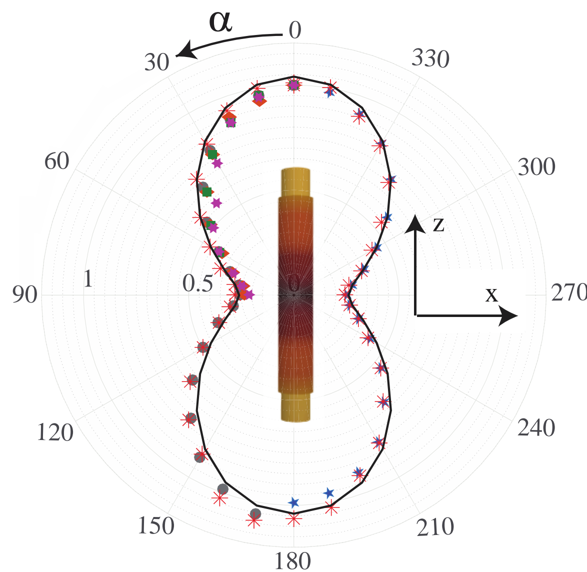

Figure 5.4 Symbols: experimental polar plot of the polarization state of the parabolic QD structure of figure 5.3. Solid line: calculated polar plot for a pure LH transition.

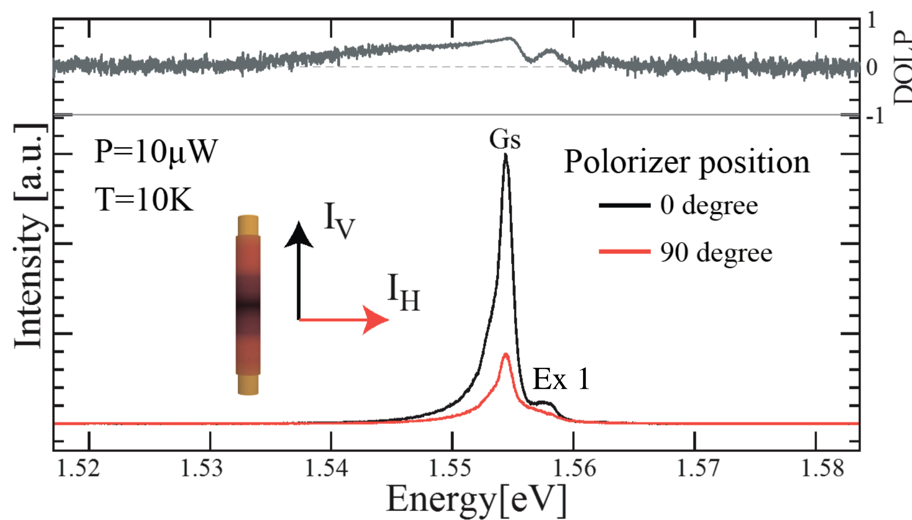

Figure 5.5 Polarization resolved PL spectra of the 240 nm parabolically shaped QD for two polarizer positions: α=0° (black curve) and α=90° (red curve). Top panel shows the corresponding DOLP spectrum. Laser excitation P=10 μW, temperature T=10 K.

A typical presentation of polarization-resolved PL and corresponding DOLP spectra discussed in this chapter is shown in figure 5.5, for the 240 nm parabolic QD structure. The ground state (GS) transition exhibits DOLP~0.6, as expected from a pure LH transition. However, other spectral lines show different DOLP values.

5.2 Emission polarization of 480 nm-QWR

As shown in Chapter 2, the DOLP can be written in terms of the overlaps of the CB and VB parts (LH and HH) of the WFs:

$$DOLP = \frac{\langle \varphi_e | \varphi_{LH} \rangle^2 - \langle \varphi_e | \varphi_{HH} \rangle^2}{\frac{5}{3}\langle \varphi_e | \varphi_{LH} \rangle^2 + \langle \varphi_e | \varphi_{HH} \rangle^2}$$

For transitions involving pure HH CB state, this yields DOLP=-1 where is for a pure LH transition it gives DOLP=0.6. For mixed LH/HH character, intermediate values of the DOLP are expected. As shown in Chapter 4 (Section 4.5), the calculated lowest energy transitions in the 480 nm QWR structure have (almost) pure LH character, and therefore are expected to show DOLP=0.6. We also note that the corresponding CB WFs have negligible overlap with the HH WF components, which further emphasize the LH character of the transitions. However, the calculated DOLP decreases with increasing transition energy due to slow increase in the HH character

Figure 5.6 presents polarization-resolved PL measurements of the 480 nm QWR at two different excitation powers of 7 μW and 300 μW. In each panel the lower part shows the relative PL spectra for two different polarizations, along (black) and perpendicular (red) to the growth direction. The measurements were done in the way described in section 5.1. The upper panels show DOLP spectra derived from the measured PL spectra. The general lineshape of the PL spectra is similar to the ones obtained in top view (see Section 4.6). The two subpeaks are formed due to the different densities of states and the finite line broadening at the corresponding energies (1.552 and 1.557eV). Figure 5.6 shows that the lower energy peak has DOLP=0.6 at both excitation levels, in agreement with the calculated DOLP (see figure 4.5). However, the higher energy peak shows much lower values of DOLP at lower excitation, and only approaches DOLP= 0.6 at higher excitation levels. There are two effects involved in this behavior: (i) the density of the VB LH-like states decreases with increasing energy (figure 4.5); and (ii) the occupation level of the LH versus the HH states can very at different excitation levels.

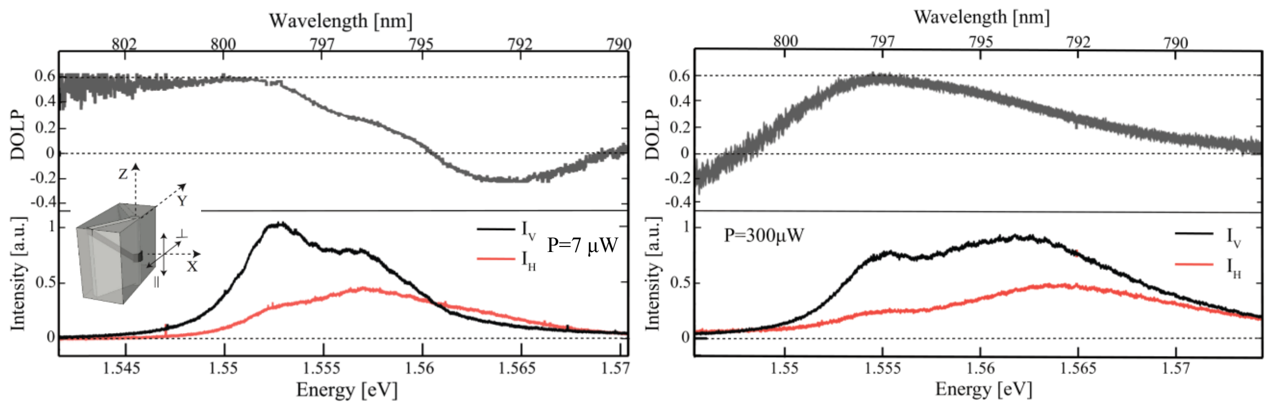

Figure 5.6 Polarization resolved PL spectra (lower panel) and DOLP spectra (upper panel) of 480 nm QWR at T=5.3 K: left panel P=7 μW; right panel P=300μW. Vertical (V) and horizontal (H) polarization components correspond to linear polarization along and perpendicular to the growth direction.

5.3 Emission polarization of thin QDs

In terms of confinement strength our lens shape QD represent another extreme case of nanostructure with strong confinement. In a contrary to 480 nm QWR, lens shaped QD exhibits GS polarization perpendicular to the growth direction, its indication of CB – HH transition type. Figure 5.7 presents side-view, polarization resolved PL and DOLP spectra of the lens shaped pyramidal GaAs QD discussed in Section 4.3.2, measured at several excitation levels in inverted pyramid. As for the top-view PL spectra (figure 4.11), we can identify the GS X and 2X transitions. Both transitions show GS DOLP close to -1 value, which corresponds to the HH related character of the VB states (see figure 4. 10). Consistent with the time-resolved spectra of this structure (figure 4.12 a), myltiexcitonic peaks disappear at low excitation levels, at the same time with the GS red shifted with respect to the GS emission lines. These transitions also show DOLP close to -1. Comparing the QD spectra with the QWR ones, we see also for the QWR red shifted tail of multiexcitoninc transitions appearing at high excitations, with DOLP<0.

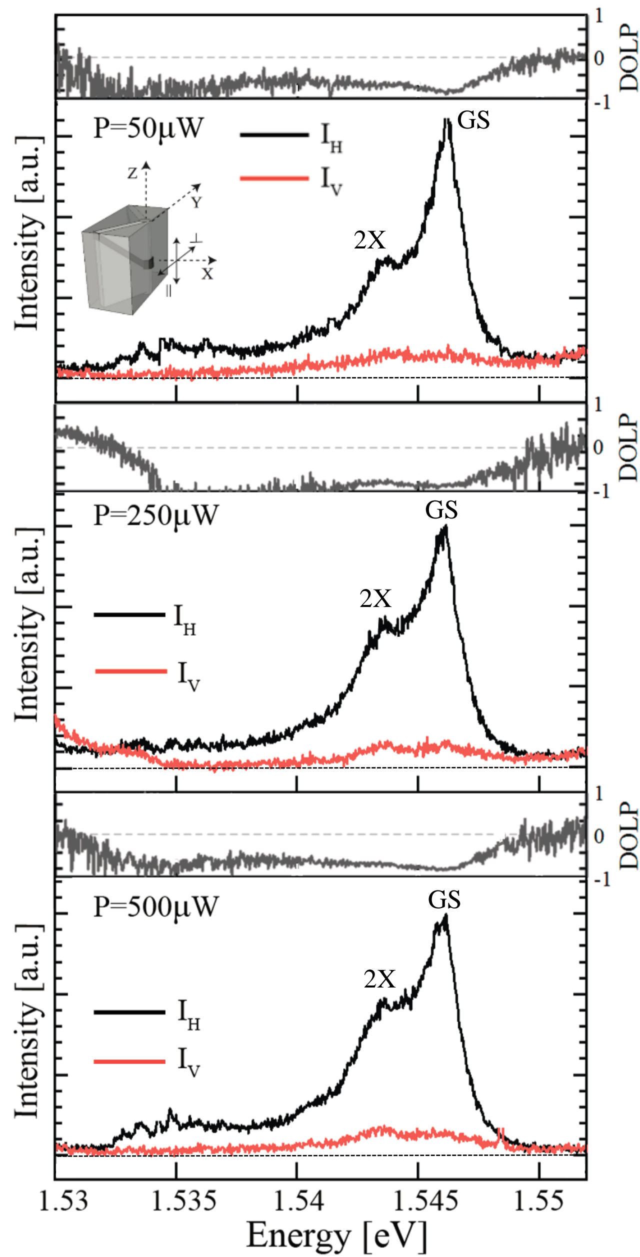

Figure 5.7 Polarization resolved PL spectra (lower panels) and DOLP spectra (upper panels) for the thin GaAs QD structure, at different excitation levels (T=10K). Vertical (V) and horizontal (H) polarization components correspond to linear polarization along and perpendicular to the QD growth direction.

5.4 Emission polarization of parabolic QDs

In this Section we focus on polarization resolved PL measurements of the parabolically shaped QDs (PQDs) discussed in Chapter 4 The three samples investigated are labeled 120 nm-PQD, 240 nm-PQD and 480 nm-PQD, according to the total length of the parabolic potential (see Chapter 4 and Appendix B for details of the structures).

5.4.1 120 nm-PQD

Figure 5.8 presents polarization resolved, power dependent PL study of the 120 nm PQD. As in previous sections, each panel shows PL spectra for the two different polarizations, along and perpendicular to the growth direction, and the upper parts show the derived DOLP spectra. At low excitation power, the PQD demonstrates properties similar line shape as for the thin, lens shaped QD of Section 5.2. The peak value of the DOLP around the GS emission is 0.6, as expected from the almost pure LH VB state dominating this transition (see figure 4.18). As in the case of the top-view PL spectra of Chapter 4, peaks separated by ~8 meV appear at increasing excitations, related to transitions between excited CB and VB states. The multiexcitonic tails on the low energy side of the GS transition approaches DOLP=0.6 at high excitation levels. The appearance of well-defined excited state transitions permits to follow the evolution of the DOLP as a function of state filling, as was already observed in the case of the QWR sample. As each excited state transition increases in intensity, DOLP>0 is observed for the transition, but the value reaches ~0.6 only gradually, with increasing excitation level.

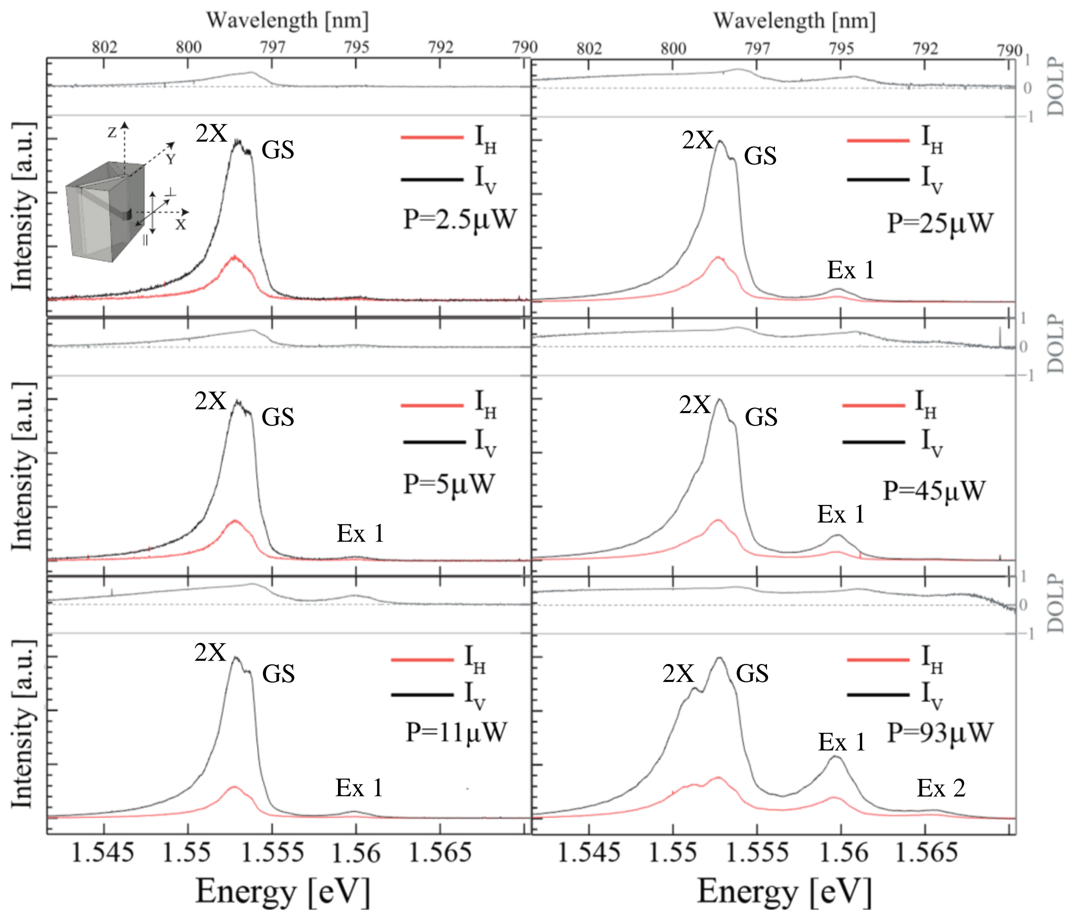

Figure 5.8 Polarization-resolved PL spectra (lower panels) and corresponding DOLP spectra (upper panels) for a parabolic AlGaAs QD (L=120 nm) measured at T=10 K and at different excitation laser powers. Vertical (V) and horizontal (H) polarization components correspond to linear polarization along and perpendicular to the QD growth direction.

This evolution of the DOLP of the excited transitions is more clearly observed in figure 5.9, which presents the power dependence of the DOLP spectra for DOLP values between 0 and 1. The GS peak shows DOLP=0.6 for all excitation powers used. Although the first excited state transition at ~1.56 eV is evident already at P=2.5 μW, the observed DOLP is close to 0 at that level, implying almost equal admixture of HH and LH states in the spectral line. Similarly, the next excited state transition appears at P~45 μW (~1.566 eV) with DOLP~0. Both excited-state transitions tend to DOLP~0.6 only at higher excitations levels. Examination of the calculated PL optical spectra without line broadening (see figure 4.18) reveals the major difference between the hole character of the GS and the excited state transitions. The main difference between the GS and the excited-state transitions is that around the GS energy (within ~2 meV) there are no HH-like transitions, whereas there many such HH-transitions near the excited state ones. This means that when line broadening is taken into account, the effective character of the excited state transitions is a mixed HH-LH character, depending on the broadening and the exact spectrum of the transitions. This explains why the excited states do not reach the value DOLP=0, as is the case for the GS transition. The gradual increase in the DOLP value with increasing excitation level suggests that the occupation of the HH-like and LH-like VB states does not remain constant but rather evolve with state filling, effectively changing the character of the line-broadened transition. In figure 5.9 some DOLP spectra demonstrate GS DOLP even larger than 0.6. This is due to the high sensitivity of the PL intensity on the exact excitation spot position, as was explained in section 5.1. The DOLP values greater than 0.6 are due to unusually large fluctuations in excitation spot position in these cases.

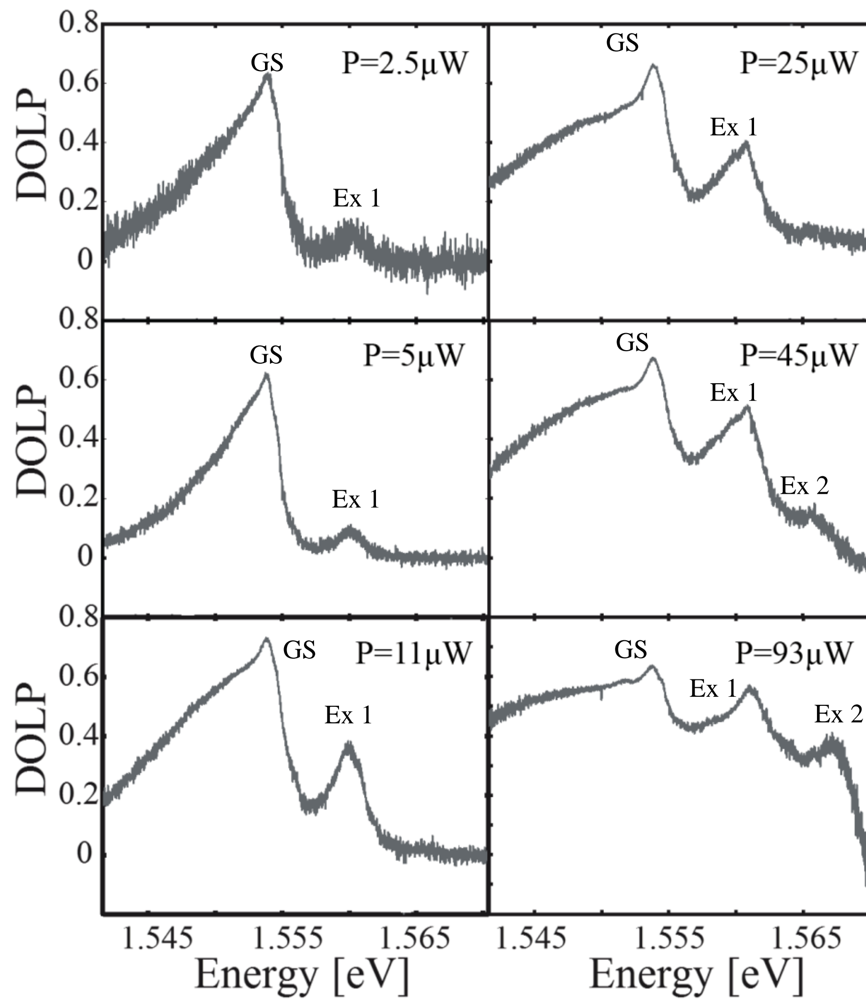

Figure 5.9 DOLP spectra for a parabolic AlGaAs QD (L=120 nm) at several excitation powers (T=10K), derived from the PL spectra of figure 5.8.

5.4.2 240 nm-PQD

Figure 5.10 displays the polarization resolved PL spectra for a parabolic QD structure of L=240 nm (T=10K, excitation powers indicated in each panel). At low excitation power, the GS transition is dominant and demonstrates pure LH behavior. The dominant V-polarization (along the growth direction) of the PL spectrum was predicted in chapter 4 (section 4.4.1) in terms of the hole character of the VB states. These polarization resolved measurements yield similar results for the transition separations ~4-5 meV as for the top-view PL measurements. Compared to the 120 nm PQD, the power dependence presents more efficient state filing due to the smaller state separations.

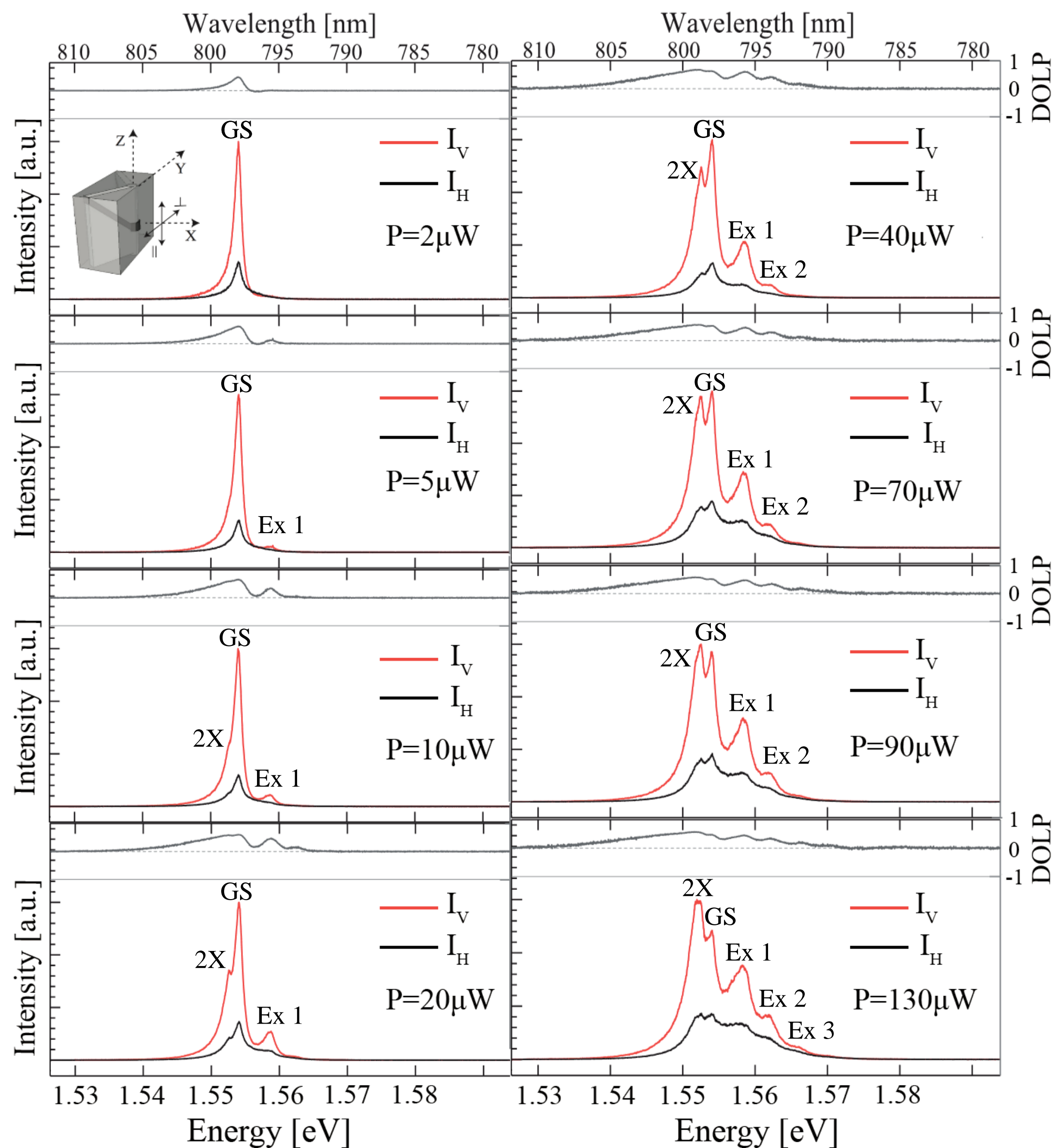

Figure 5.10 Polarization resolved PL spectra (lower panels) and corresponding DOLP spectra (upper panels) for a parabolic AlGaAs QD (L=240 nm) at T=10 K and at different excitation power P. Vertical (V) and horizontal (H) polarization components correspond to linear polarization along and perpendicular (horizontal) to the QD growth direction.

Figure 5.11 presents the P power dependence of the DOLP spectra of the 240 nm PQD, obtained from the polarization resolved measurements, in greater detail. The GS transition demonstrates DOLP of 0.6, as well as a corresponding myltiexcitonic tail. This indicates that the VB states involved in the ground state transitions have a strong LH state. This is consisted with the 120 nm PQD for which the GS also has 0.6 DOLP, despite weaker quantum confinement along growth direction. Stronger confinement introduces additional hole character mixing in the VB, which does not have an effect on the GS DOLP due to the different WFs geometry of LH and HHs. At low excitation power we see the result of the presence of weak HH states yielding negative value of DOLP. With increasing excitation power and increasing state filling, the DOLP of the

excited transitions increases from ~0 to maximum 0.6. Due to the lower state separation here, as compared with the 120 nm PQD, we did not see the presence of excited multiexcitonic states in the top emission PL spectra, but we see the effect of their presence at high excitation power in the DOLP spectra, where they fill the “gap” in between the excited states transitions. The simulation results do show that line broadening cover HH like transitions, which explains the lower maximum values of the DOLP at the excited transitions. However, the excited state transitions always show a lower DOLP than simulated ones, increasing with excitation level. This can be explained by states filing effects, as in section 5.5-5.6.

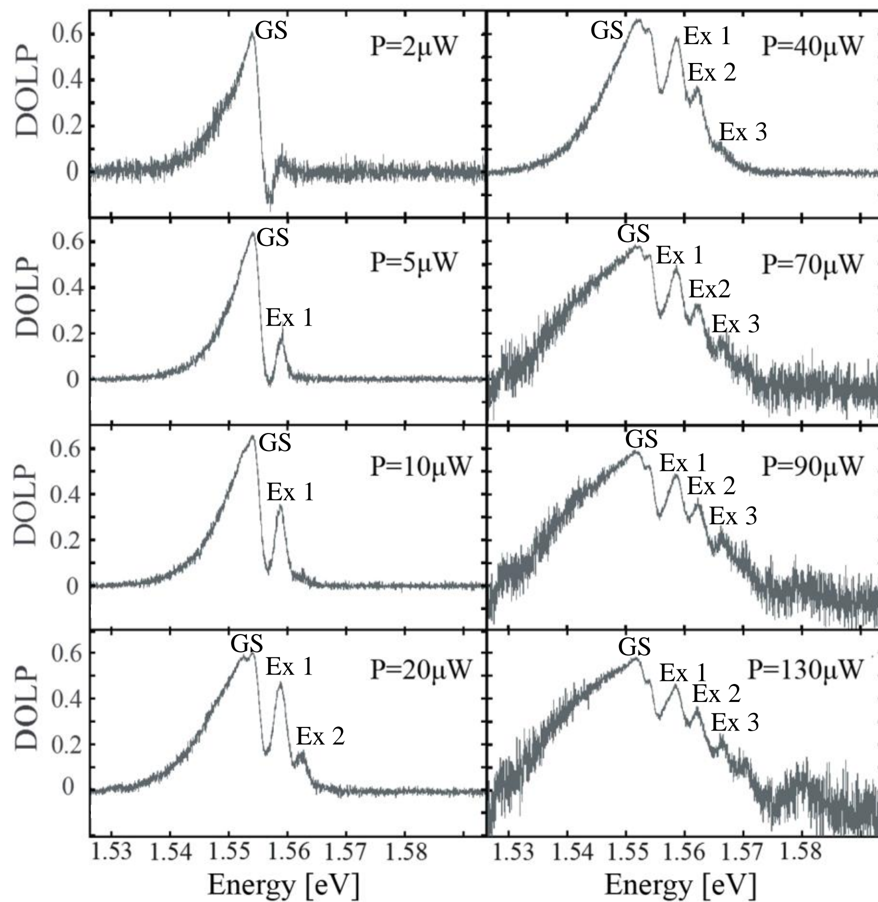

Figure 5.11 Closer look at the DOLP spectra of the 240 nm PQD at different excitation powers (T=10 K).

5.4.3 480 nm-PQD

The 480 nm PQD is an example of a nanostructure close to a QWR in terms of confinement strength, with similar VB structure and optical properties (see simulation results in chapter 4). Figure 5.12 shows the polarization resolved PL and DOLP spectra for this 480 nm PQD at different excitation levels. The excited states are barely resolvable even in the DOLP spectra; this is consistent with the small energy separation (~2 meV) expected for this structure (see Fig. 4.22). However, the GS DOLP is 0.6 as for the other PQD structures. Overall, the spectra reminds those obtained for the QWR (see figure 5.6, as expected).

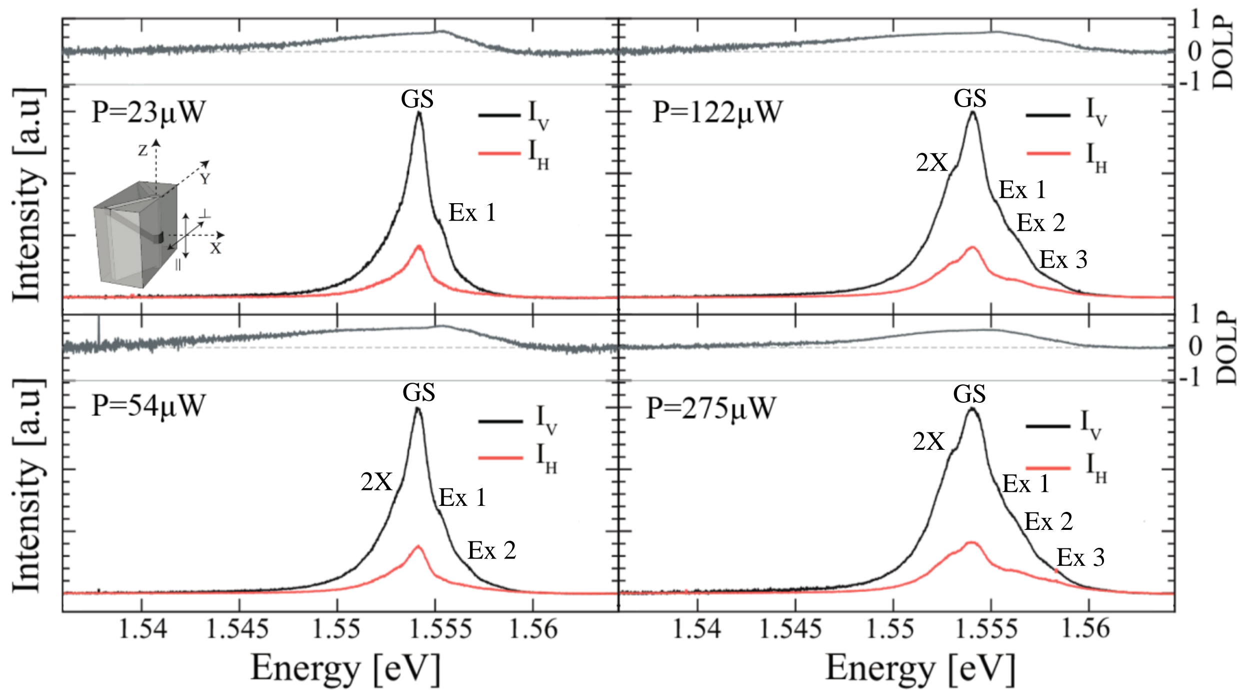

Figure 5.6 Polarization resolved PL spectra (lower panels) and DOLP spectra (upper panels) for a parabolic AlGaAs QD (L=480 nm) at T=5.3K and at different excitation laser powers. Vertical (V) and horizontal (H) polarization components correspond to linear polarization along (vertical) and perpendicular (horizontal) to the QD growth direction.

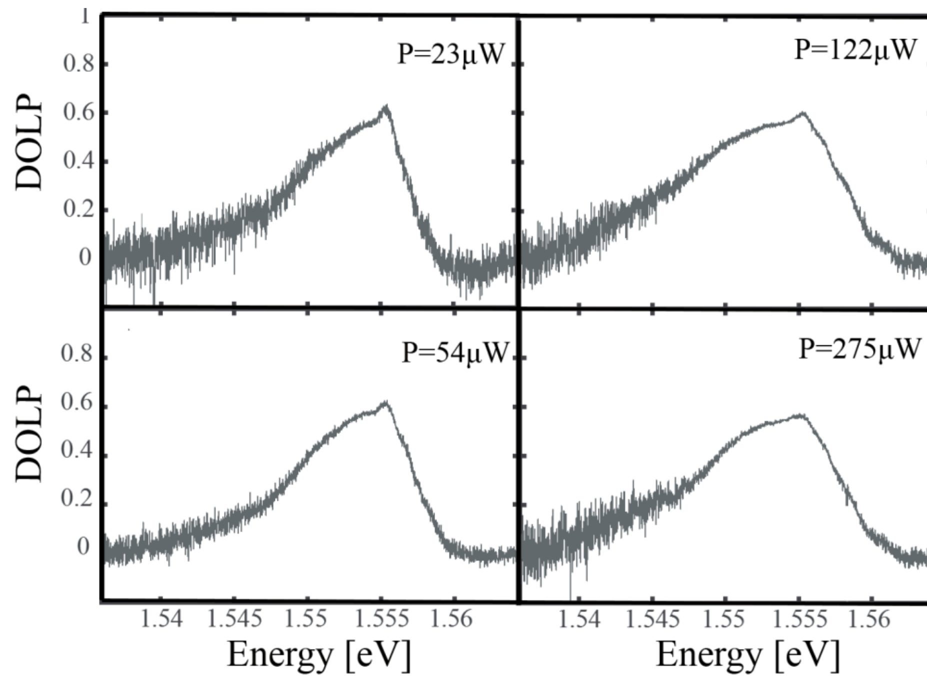

Figure 5.13 Power dependence of the DOLP spectra for a parabolic AlGaAs QD (L=480 nm) at T=5.3K.

5.5 Effective carrier temperature and Fermi level

Excitonic systems in quantum nanostructures, excited by optical or electrical pumping, are not in thermal equilibrium. However, relaxation and scattering processes in each band (CB or VB) are often faster than the interband recombination rates. This leads to thermal equilibrium of electrons and holes within their bands and allows the definition of quasi Fermi levels in each band. In addition, due to conversation of electric charge, the density of electrons and holes is approximately the same, which permits treating the system as a system of (neutral) excitons with characteristic densities, or effective Fermi levels.

From the PL measurement results, we may find exciton fermi level and effective exciton temperature. The measured integrated PL intensity at a given spectra line is proportional to the transition probability and the occupation probability of the corresponding states, at a given excitation power. Since the transition probability (matrix element) can be extracted from our modeling, the state occupation numbers can be found from the PL measurements. All LH and HH transitions have to be taken in to account for extracting the state occupation numbers, but due to the high broadening/spacing ratio, it is more complicated to extract them from top-view PL measurements. The side-view measurements allow some filtering of the VB states involved using the polarized spectra. Determination of the occupation numbers of the state corresponding to transition it yields the corresponding quasi Fermi energies and carrier temperature via the Fermi-Dirac distribution:

$$n_{i(t)} = \frac{1}{e^{\frac{E_i - E_\mu}{kT}} + 1}$$

This approach is illustrated here for the case of the 240 nm PQD. It is applied to the side view PL spectra polarized in the growth direction, which allows considering only the LH components of the VB states involved. The extracted occupation numbers (probability) are presented in figure 5.14 as a function of the excitation power for the three lowest energy transitions. The corresponding Fermi energies and carrier temperatures are presented in figure 5.15.

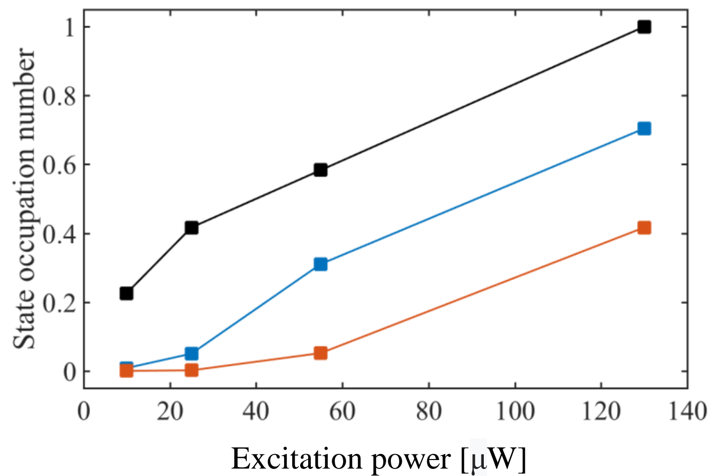

Figure 5.14 State occupation number versus excitation power for the 240 nm PQD. Black: GS, blue: first exited transition, red: second excited transition.

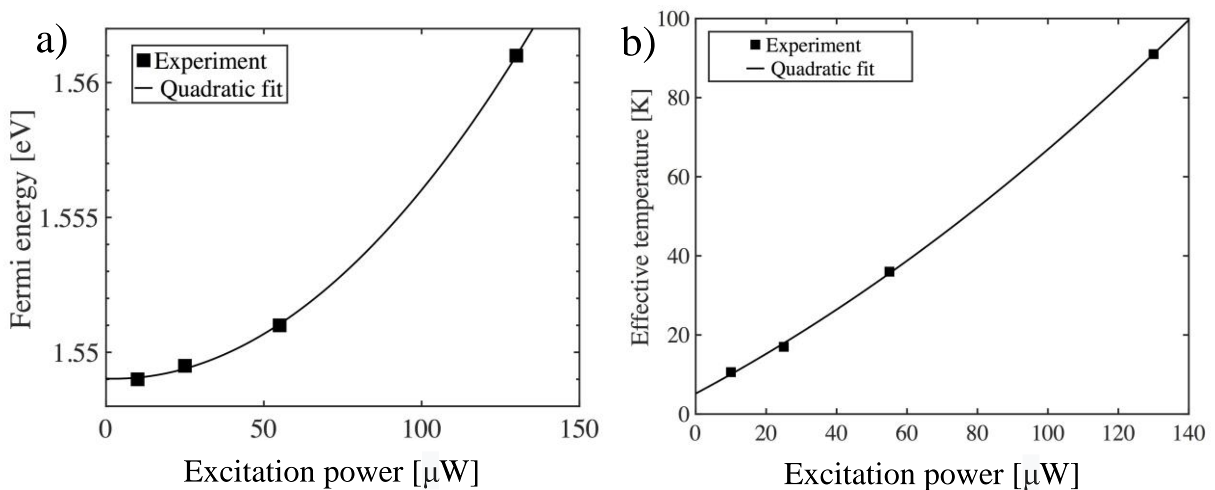

Figure 5.15 Fermi energy (a) and effective carrier temperature (b) as a function of the excitation power for the 240 nm PQD. Lattice temperature is 10 K. Solid lines are parabolic fits of the data.

5.6 Effects of VB mixing, broadening and state occupation

As shown in previous sections, the PL and DOLP spectra depend on several important factors: the VB mixing for each transition, the overlap of the CB WFs with the corresponding VB ones, the spectral density of transitions as compared to the line broadening, and the occupation of a given state. Here we discuss influence of these factors on the DOLP.

The LH and HH portions of a VB state are defined by:

$$LH = \frac{\langle \varphi_{LH} | \varphi_{LH} \rangle}{\langle \varphi_{LH} | \varphi_{LH} \rangle + \langle \varphi_{HH} | \varphi_{HH} \rangle} \qquad HH = \frac{\langle \varphi_{HH} | \varphi_{HH} \rangle}{\langle \varphi_{LH} | \varphi_{LH} \rangle + \langle \varphi_{HH} | \varphi_{HH} \rangle}$$

Figure 5.16 presents the calculated LH and HH portions for the 480 nm QWR structure. Here, the effect of VB mixing in QWR is negligibly small for the first 15 states, and the calculated optical spectra are in agreement with the dominance of the LH component.

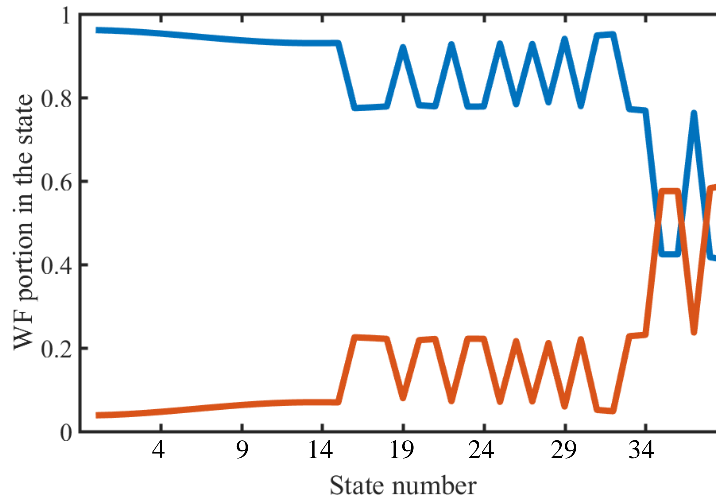

Figure 5.16 LH (blue) and HH (red) wavefunction portions versus the state number, for the 480 nm QWR structure.

A summary of the calculated and measured results for the 240 nm PQD is presented in figure 5.17. The calculated DOLP at the observed transitions are in agreement with the measured ones, provided the different state occupations are taken into account (square symbols in figure 5.17 (a)). For this structure, the occurrence of HH states at higher energies does reduce the DOLP values for the excited states (figure 5.17 (d)), but this by itself cannot explain the observed DOLP values and their dependence on excitation power. This illustrates the importance of the finite occupation levels on the DOLP level. In particular, the results suggest that the occupation levels of the HH components are higher as compared to the LH ones.

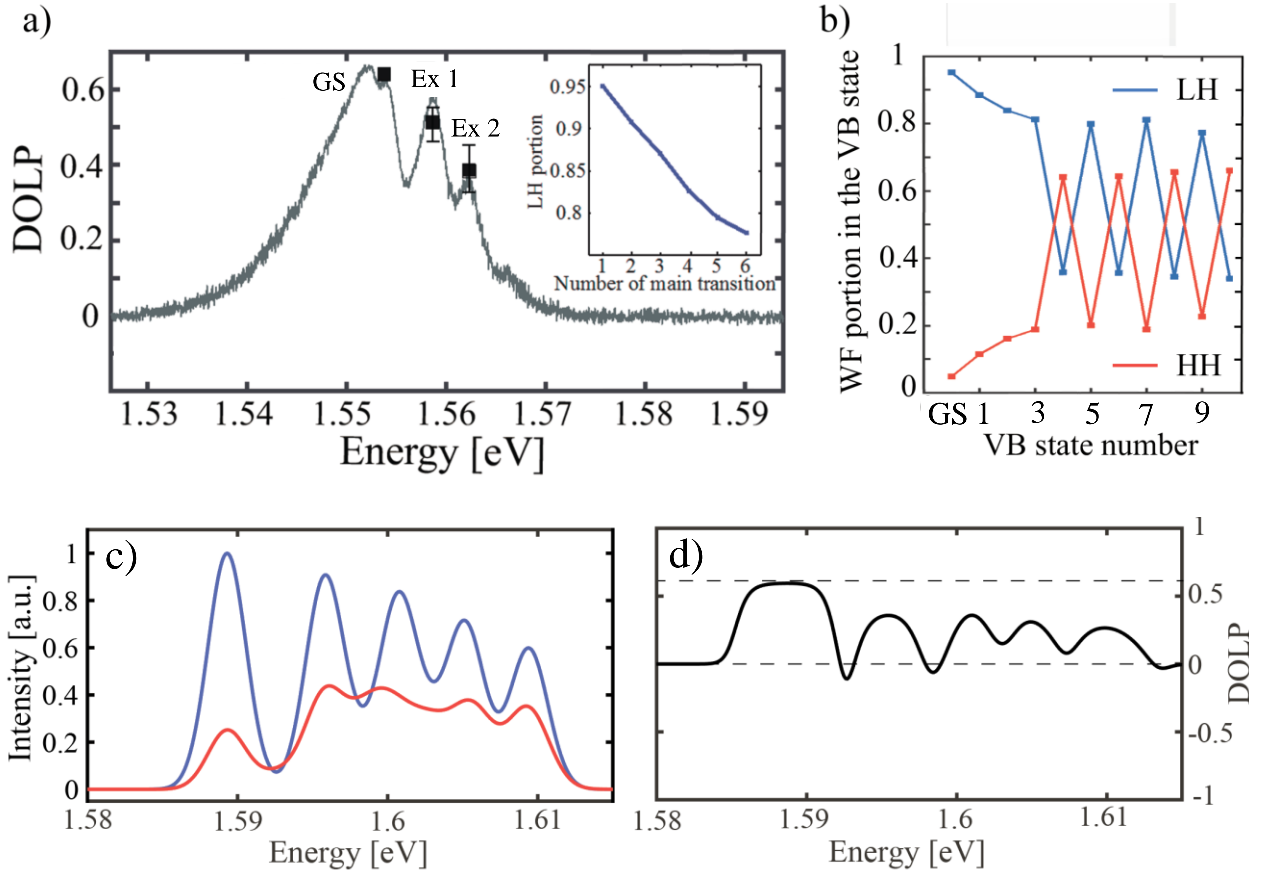

Figure 5.17 Summary of measured and calculated results for the 240 nm PQD. (a) Measured DOLP spectra (P=40 µW, T=10 K). Black squares are calculated DOLP values for 2 meV line broadening. Inserted figure shows LH portion dependence of the main transitions versus transition number. Error bars show DOLP deviations due to different state broadenings. (b) LH/HH portions versus state number. (c) Calculated optical spectra including Coulomb interaction and 2meV line broadening; blue and red lines correspond to vertical and horizontal polarizations. (d) DOLP spectra corresponding to (c).

The variation of the calculated DOLP values for the main transitions in the 240 nm PQD with increasing line broadening is presented in figure 5.18. Whereas the DOLP of the GS transition stays at 0.6 independent of broadening, the DOLP of the excited sates rapidly decrease with increasing broadening. The effect is more merged for higher energy transitions. This behavior is fully consistent with the increasing density of HH transitions at higher energies (see Chapter 4).

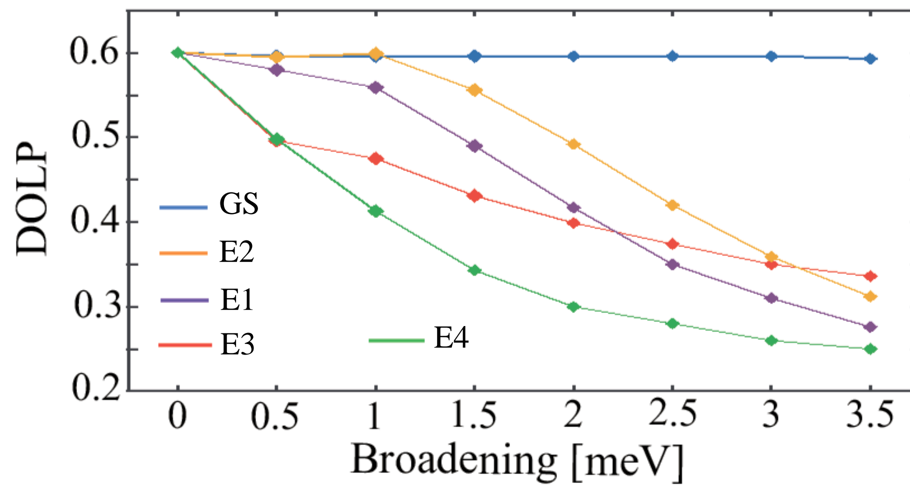

Figure 5.18 Calculated DOLP values for the main transitions in the 240 nm as a function of the line broadening.

A more detailed comparison of the measured and calculated spectra of the 240 nm PQD structure, in particular the effect of the excitation level, is presented in figure 5.19. The calculated polarized optical spectra and the derived DOLP spectra were constructed with the excitation power dependence as described above. It can be seen that the processes considered well account for the observed DOLP spectra at the considered excitation levels.

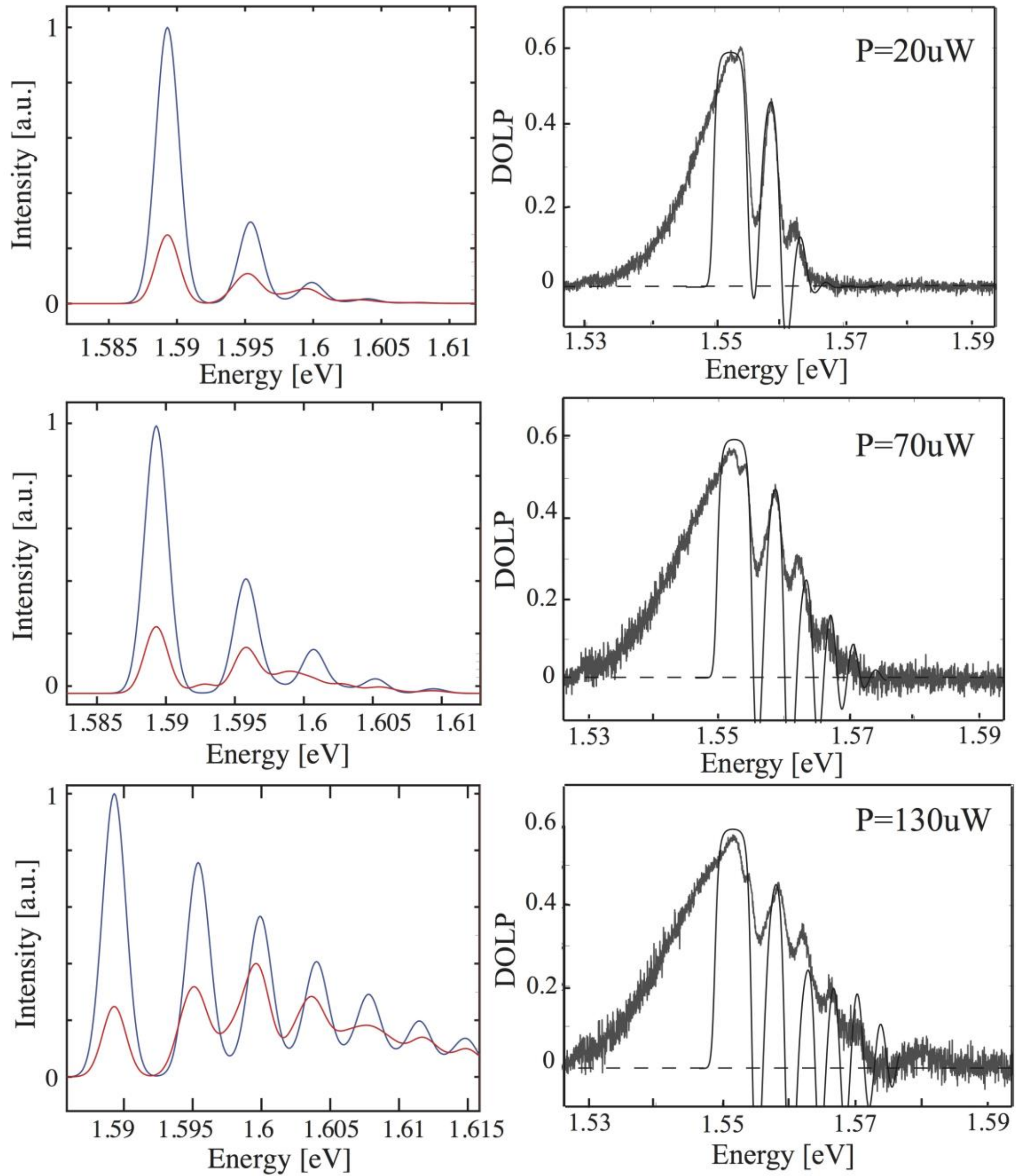

Figure 5.19 Comparison of calculated and experimental spectra of the 240nm PQD structure at different excitation levels. Left column: calculated optical spectra for vertical (blue) and horizontal (red) polarizations. Right column: measured DOLP spectra (thick lines) and simulated DOLP spectra (thin lines). Coulomb interaction as a perturbation and line broadening of 2meV were included.

Figure 5.20 presents the comparison between the measured and calculated optical spectra for the 120 nm PQD structure. The roles of VB mixing, spectral density of HH states, line broadening and state filling are similar as for the case of the 240 nm PQD structure. However, due to the stronger QD confinement along the growth direction, the transitions energy separation is larger and the role of the HH transitions is more important.

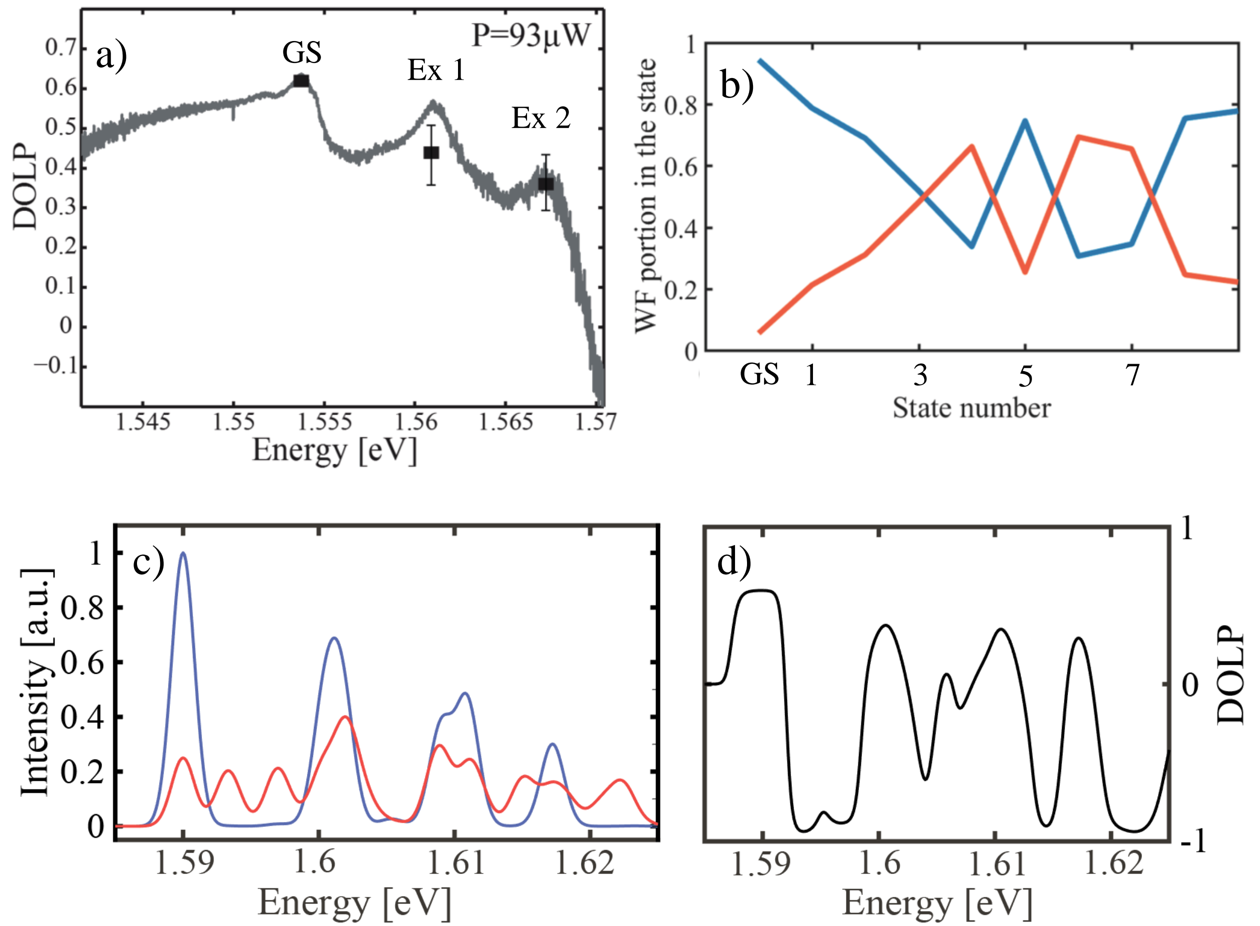

Figure 5.20 Summary of measured and calculated results for the 120nm PQD. (a) Measured DOLP spectra (P=93 µW, T=10 K). Black squares are calculated DOLP values for 2 meV line broadening. Error bars show DOLP deviations due to different state broadenings. (b) LH (blue)/HH (red) portions versus state number. (c) Calculated optical spectra including Coulomb interaction and 2 meV line broadening; blue and red lines correspond to vertical and horizontal polarizations. (d) DOLP spectra corresponding to (c).

As demonstrated by the summary of the results for the 480 nm QWR sample in figure 5.21, further decreasing the confinement strength brings the system closer to QWR structure. The error bars in part (a) are very small in this case due to the low presence of HH related transitions in this case, hence line broadening effects are less important here.

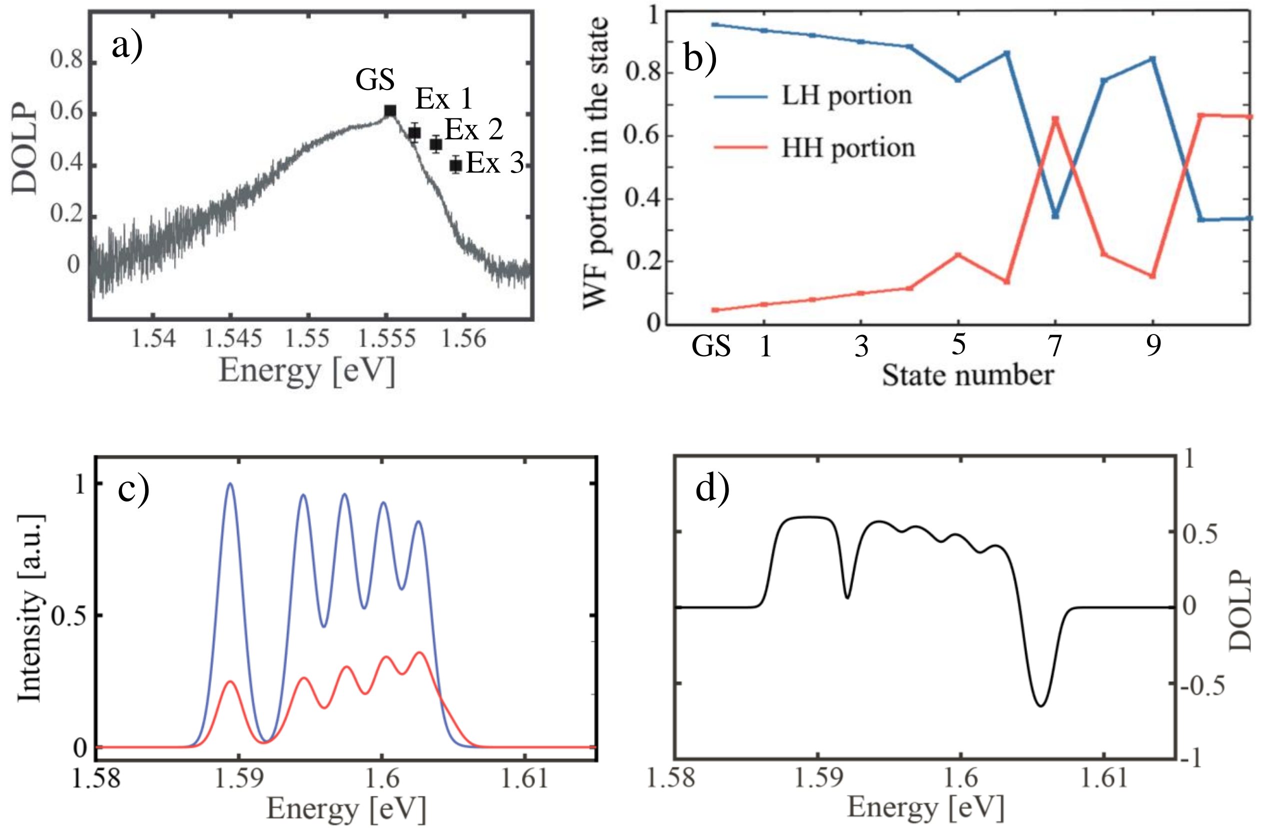

Figure 5.21 (a) Summary of measured and calculated results for the 480nm QWR. (a) Measured DOLP spectra (P=122µW, T=10K). Black squares are calculated DOLP values for 2 meV line broadening. Error bars show DOLP deviations due to different state broadenings. (b) LH (blue)/HH (red) portions versus state number. (c) Calculated optical spectra including Coulomb interaction and 2meV line broadening; blue and red lines correspond to vertical and horizontal polarizations. (d) DOLP spectra corresponding to (c).

An important effect influencing the DOLP is the overlap of the CB and VB wavefunctions corresponding the given transition. The CB wavefunctions overlap better with the LH WFs. LH portion decreasing in the VB states, with increasing QD confinement, thus the strength of the corresponding CB/LH decreases as well. The effect of the confinement on the VB mixing is illustrated in figure 5.22, which shows the LH portion of the 6 strongest transitions in the pyramidal nanostructures discussed.

In this Chapter we have presented power depended DOLP measurements by polarization resolved spectroscopy. We saw that VB mixing itself cannot explain DOLP characteristic behavior, even taking into account all HH related transitions. The reason is a different occupation states number and line broadening, in the model calculated states assumed to be occupied but in experiment (as we showed in previous section) it’s not, this fact changes everything. Different occupation numbers give a different “weight” for each transition lines, that have an impact on total DOLP.

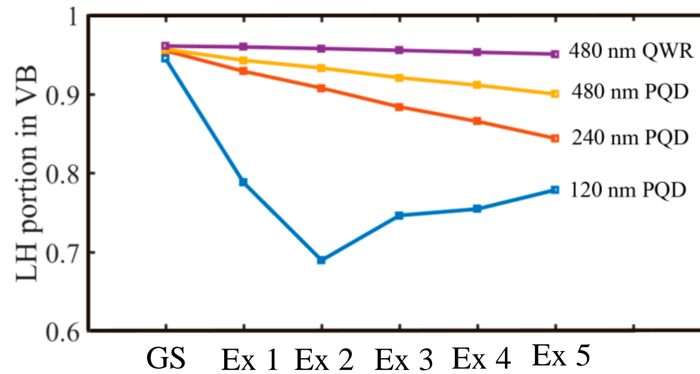

Figure 5.22 Comparison of the calculated LH portions of the lowest energy main transitions for all QWR/QD structures investigated.

In long PQD structures LH and CB states have much stronger overlap than HH (main transitions) so in this case VB mixing characteristic can tell only the trend of increasing strength of HH transitions with the number of VB states as a consequence decreasing of strength LH related transitions. PL spectra is a sum of all three effects, overlaps, occupation number and in the end VB mixing. VB mixing gives a maximum (minimum) ration of PL transitions intensities.

5.7 Summary

Quantum confinement in two or three directions introduces mixing of the HH and LH VB states in III-V direct gap semiconductors, with direct impact on exciton recombination and the optical emission spectra. In corresponding one-dimensional (1D) QWR structures, VB mixing between This results in a significant LH component and the emitted photons exhibit linear polarization oriented mainly along the QWR axis. In semiconductor QDs, quantum confinement along the remaining, third dimension further modifies the HH-LH mixing. In case of relatively low (additional) confinement strength, the QD ground VB state keeps its predominant LH character, but increasing this confinement strength gradually increases the impact of states with HH character. Using polarization-resolved PL spectroscopy and numerical simulations of pyramidal QWR/QD structures, we clarified the details of the relationship between this increasing confinement and the polarization state of the emitted light.

We showed that increasing confinement along the axis of a QWR introduces a “forest” of HH-like VB states with high spectral density around the LH states responsible for the main optical transitions. The finite linewidths of the broadened CB-VB transitions thus introduce a HH component to the observed lines. Whereas this effect is negligible for the ground state transitions, it is significant for the excited state transitions, and therefore their DOLP is lower than 0.6. With increased excitation and state filling, the DOLP of the excited states attains the value dictated by the high density HH states, transition strength and the finite transition linewidth. The pyramidal quantum nanostrcutures permitted understanding the evolution of the VB and optical transition characteristics for QWR-like (1D) to QD-like (0D) confinements. In this sense, QDs of finite size (length) behave in a way intermediate between QWRs and thin QDs.

Chapter 6

Control of emission polarization of quantum nanostructures

The ability to control the optical properties of QDs is important for fabrication of future nano-optical devices, since QDs are practical sources of single photons. In particular, the control over the energy and polarization of the emitted photons is important for quantum information technologies. In this chapter, we focus on dynamic ways to control the optical polarization properties of different nanostructure types realized by pyramidal heterostructures. Section 6.1 briefly reviews the main approaches for achieving such dynamic control and recent results obtained with pyramidal nanostrcutures. Section 6.2 concerns the modeling of single QDs of different geometries to find an "equilibrium" point for polarization switching and the effect of an external electric field applied to this nanostructure. Similarly, section 6.3 presents the simulation of these effects in QD molecules (QDMs) with different barrier heights between coupled QDs. Section 6.4 is dedicated to the study related effects in QD superlattice (QDSL) systems, including miniband formation and impact of electric field.

6.1 Dynamic control of QD optical properties

The online control of optical system properties is another very promising research direction. The ability to tune QD optical properties has great importance for applications since the QDs are considered as very promising components of future quantum devices. In previous chapters we showed how we can structurally modify the QD and thereby the polarization state of the emitted light. QDs are proven sources of single photons and are considered for integration in integrated quantum photonic circuits [127][168][128]. The coupling of the emitted single photons to optical elements such as cavities, waveguides, switches etc. depends on the photon (mode) polarization and energy [169]. Dynamic control over the polarization of the emitted photon would let us, e.g., to modulate the coupling to the optical mode of the nano optical elements.

Many ways to achieve dynamic control over QD optical properties exist, such as the application of external electro-magnetic fields [170][171] and strain [172]. Several groups have demonstrated electrically driven position control of QD in PhCs [173] and cavity and polarization control in micropillar cavities [90], [88]. Also, wavelength emission control by applying an additional stress [174] has been demonstrated.

Achievement of dynamic control over light polarization emitted by the nanostructures in the inverted pyramid should also be possible. In the previous chapter, we have discussed two extreme cases of small GaAs QD, AlGaAs QWR and an intermediate case of parabolically tailored

QDs, realized in inverted pyramids by MOVPE growth. The DOLP of each structure was measured; for the 120 nm PQD the GS emission showed DOLP=0.6 (LH emission), and for the thin GaAs QD we obtained DOLP=-1 (HH emission). This implies that in between of these degrees of confinement polarization switching originating from transition of VB character from LH to HH should take place. In earlier work [113], pyramidal AlGaAs QDs with heights in the range of 10-100 nm were realized, a range where this switching should occur. But in [113] not much attention was paid to the related VB states structure. Dynamic control of the GS emission polarization of quantum Dot in Dot (DiD) pyramidal nanosructure was demonstrated in [119] using magnetic fields. The magnetic field for polarization switching requires high field intensities, and hence not feasible for applications.

In this chapter, we first identify the structural parameters in pyramidal QDs, QD molecules and QD superlattices (SLs) for which small changes bring about switching of the polarization state. Then, we show how an applied external electric field can yield the modification of the VB states from LH-like to HH-like.

6.2 Single QD polarization control

6.2.1 Polarization control via structural parameters

We study here theoretically the transition process between LH- and HH-like character for a pyramidal QD of different geometries. In this chapter we use the same modeling approach as in chapter 4. The actual Al content in the core cylinder of the QD is ~3% (20% nominal Al content), and that in the vertical barrier cylinders it is ~7% (40% nominal Al content). The diameter of the QD/QWR cylinders is kept at 18 nm. The side QWR, QW and bulk structures and compositions are as described in Chapter 4. The height t of the QD cylinder (the QD “thickness) is varied between 8 to 23 nm (see inset in Fig. 6.1(a)).

Figure 6.1 presents the calculated confinement energies of the lowest CB and VB states versus the QD thickness *t*, without Coulomb interaction. Remarkably, the LH- and HH- states cross in energy, for QD thickness t~ 12 nm (figure 6.1 (b). For t < 12 nm, the ground state is HH-like and the structure behaves in his respect as a “thin” QD. For t > 12 nm, the ground state is LH-like and the structure behaves as a QWR or elongated QD. These results suggest the choice of QD parameters for achieving a structure at the border between HH- and LH- behavior of the VB ground state.

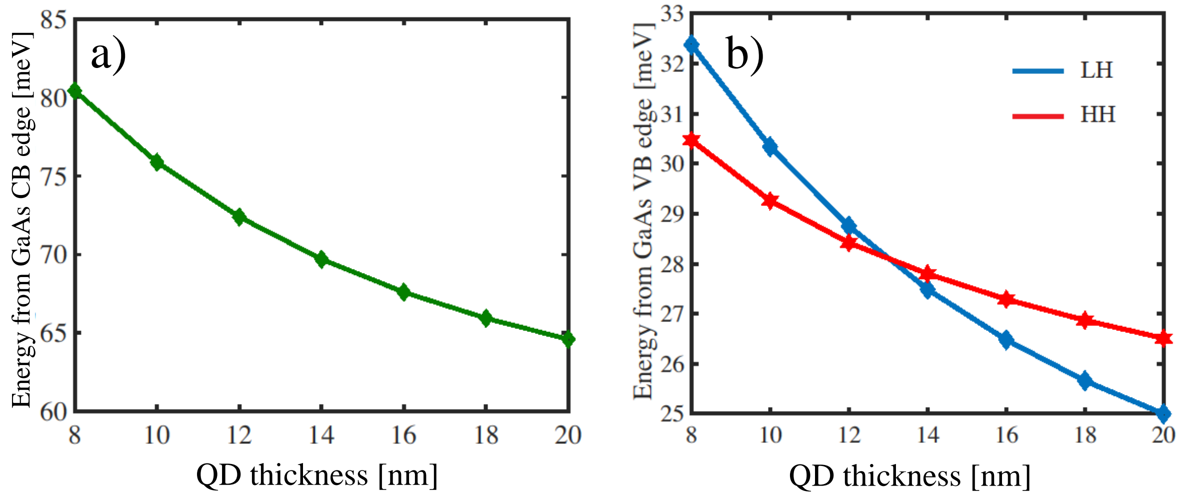

Figure 6.1 Modelling pyramidal QDs of different aspect ratios. (a) Energy of lowest CB state versus QD thickness t. (b) Energies of first two VB states versus QD thickness t. Blue line: LH-like state; red line: HH- like state.

The calculated polarization-resolved optical spectra of this QD structure are shown in figure 6.2 (a) for various thicknesses *t*; red and blue curves correspond to linear polarization normal and parallel to the growth direction. Line broadening of 2 meV was applied and Coulomb interaction was taken into account as a perturbation. From this set of spectra, we see the GS transition changes its character from LH to HH with reduction of QD thickness. Plotting the transition energies versus *t* (figure 6.2 (b)), we see that this transition happens for *t* between 12 and 14 nm. This transition also shows up in the VB mixing characteristic. Figure 6.2 (c) shows the HH and LH portions of the lowest VB states portions. Interestingly, the switching from HH to LH –like lowest energy state occurs near t=12 nm (as in figure 6.1(b)), different than for the switching thickness for the optical spectra due to the presents coulomb interaction.

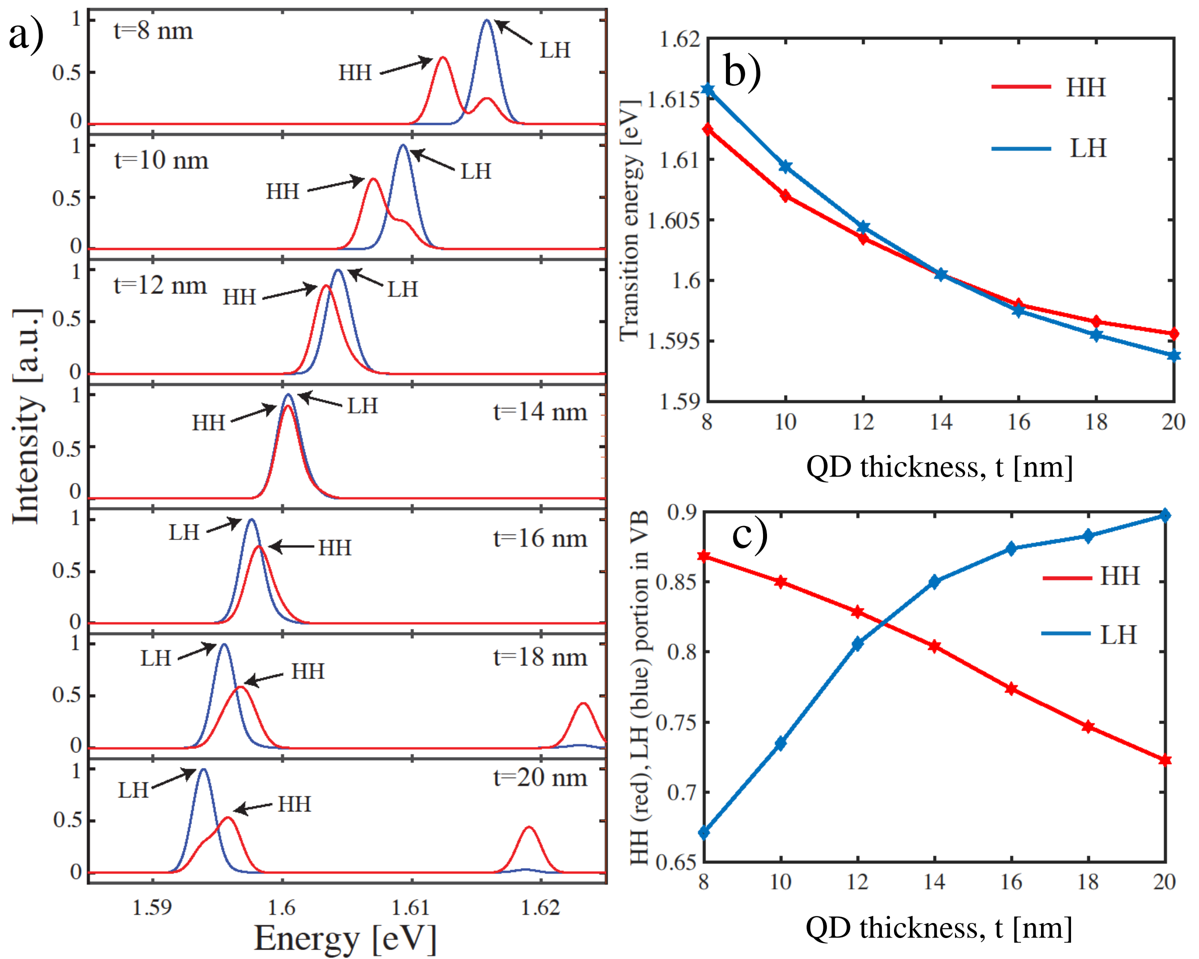

Figure 6.2 (a) Calculated polarization-resolved optical spectra of the QD structure of Fig. 6.1 for different QD thicknesses. Blue and red curves correspond to linear polarization parallel and perpendicular to the growth directions. Coulomb interaction and linewidth broadening accounted for as in Chapter 4. Lines corresponding to HH-like and LH-like transitions are indicated. (b) Calculated energies of the lowest energy transitions in (a) versus QD thickness t. (c) HH and LH portions of the lowest states presented in (b) versus QD thickness t.

6.2.2 Polarization control via external electric field

We have seen that in a range of t=12-14 nm, the QD GS transition changes its polarization with the switching of the VB ground state character from LH to HH. Since, around this point, small variations in the confinement potential can yield such switching, such QD can serve as a base for achieving the desired change using an electric field. Here we analyze the effect of an electric field on such "equilibrium": QD structure.

To illustrate the effect of an electric field, we consider the same QD structure discussed in 6.2.1, and fix the QD thickness at t=14 nm. The confined CB and VB states are then computed with the addition of an electric field E oriented in the growth direction z (see Chapter 2 for details on the numerical approach). We note the absence of reflection symmetry of the pyramidal QD

structure, with respect to a plane normal to the growth direction. Hence, application of the same electric field amplitude along +z or –z does not yield the same effect.

In figure 6.3(a) shows the calculated optical spectra of the QD structure for an electric field of amplitude E=20000 V/cm, oriented along the growth direction. Comparing to the spectrum for E=0 (figure 6.2(a)), we notice two major differences. First, the absorption edge is red shifted, which is due to a quantum confined Stark effect [170]. Secondly, the essentially single, lowest energy transition line with nearly equal LH and HH components develops for E>0 into a more rich structure with characteristic polarization features. This is further illustrated by the DOLP spectrum (figure 6.3(b)), which shows a HH-like feature at low energies instead of DOLP~0 for E=0. This is because the E-field changes the QD potential profile such that the lowest VB state is HH-like and the Stark shifts are different for the different VB states. Thus, the application of an electric field can dynamically tune the QD structure so as to switch the polarization state of light emitted by the QD ground states.

The impact of the E-field on the lowest transition states energy is displayed on the right panel of figure 6.3. The spectral lines near 1.595eV in figure 6.3 (a) are related to the CB1-VB1 and CB1-VB2 transitions. Note that the polarization is determined by the portion of the VB wavefunction that best overlaps with the CB state.

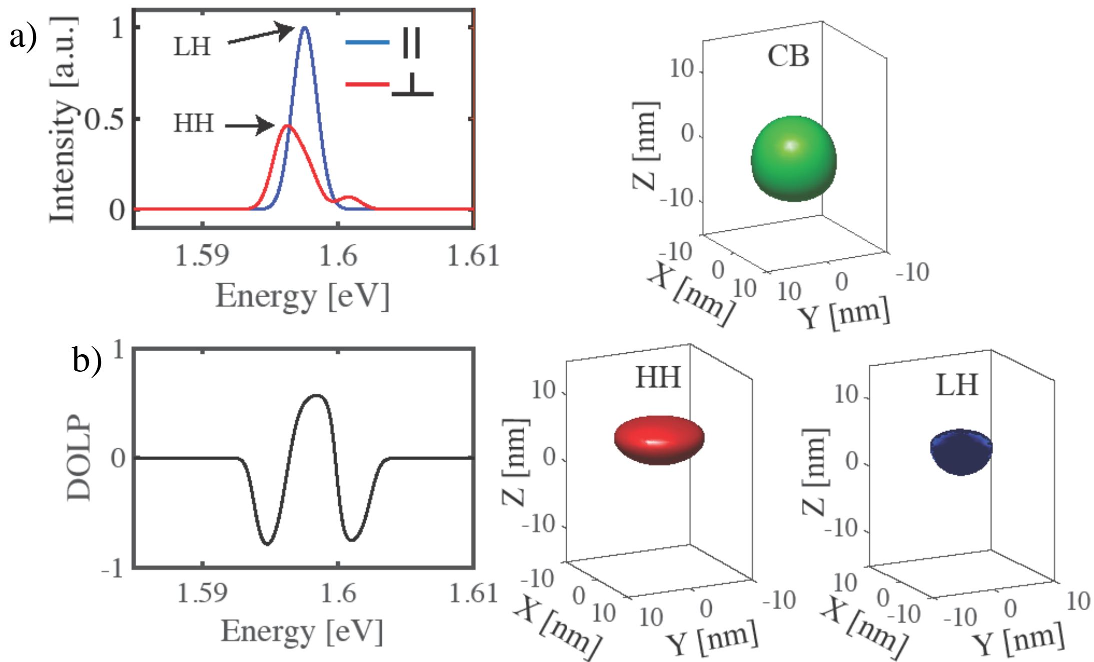

Figure 6.3 QD (t=14 nm), subject to an electric field E=20000 V/cm, applied in the z direction. Left panel: (a) Calculated optical spectra taking into account Coulomb interaction and 2 meV broadening. (b) DOLP spectra. Right panel: wavefunction iso-surfaces of the two lowest energy CB and VB states: green – electron; red – HH; blue - LH.

6.3 QD molecules

QD nanostructure properties as analogs to artificial atoms were broadly explored. A next step would be to realize QD molecules (QDMs), molecule-like nanostructures, for further investigation of nanostructure families and their optical properties. A QDM has more complex optical properties behavior due to the coupling of the CB and VB states. Although the QDM system is highly sensitive to structural details, our growth technique makes QDM possible to realize as already reported in [175][120]. In this section we will demonstrate by numerical simulations how the polarization properties of pyramidal QDMs depends on the potential barrier between the QDs and how to dynamically change the QDM polarization around the "equilibrium" point.

6.3.1 QDM states

Using our model, we have simulated a pyramidal system of two coupled $Al_{0.2}GaAs_{0.8}$ QDs in an $Al_{0.4}GaAs_{0.6}$ environment (nominal parameters). The actual material parameters in the central QWR and side barriers were estimated using formula 2.1 in chapter 2. As in Section 6.2, each QD is modelled as a cylinder with corresponding side QWRs. Figure 6.4 shows the calculation results for the CB energies of the first two states and their dependence on the barrier thickness d between the QDs (varied from 0 to 30 nm). Other QDM system parameters are kept constant, in particular each QD thickness is t=10 nm and the composition in the separation barrier is $Al_{0.5}GaAs_{0.5}$ (nominal composition).

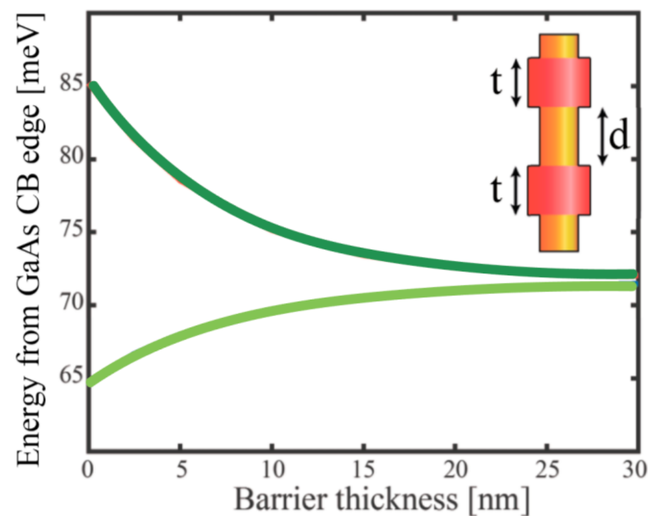

Figure 6.4 CB energy dependence of first 2 CB states in a pyramidal QDM (see text for detailed parameters). Insert shows schematic of the model.

For decreasing barrier separation *d*, the coupling of the two QDs increases, and the ground states split into bonding- and antibonding-like states [176][177]. Fig. 6.4 illustrates the dependence of the corresponding CB state energies in the QDM investigated. At large barrier thickness (d>30 nm), the effect of QD coupling is negligible, and the energy difference (<1meV) is related mainly

to the QD asymmetry (absence of reflection symmetry in the growth direction [120]). The same picture is valid for coupling of VB states, but the difference is that the VB states coupling has a more complex nature due to VB mixing. In particular, efficient coupling of QDs turns HH-like GS of the VB to become LH-like due to their extended wavefunctions along the growth direction.

Figure 6.4 shows one way to tune the coupling strength between two QDs. In the decoupled regime, each QD (with sufficiently small height to width aspect ratio) has a HH-like GS in the VB and, as a consequence, the emitted light is polarized perpendicular to the symmetry axis *Z* (growth direction). On the contrary, in case of a thin barrier, the QDM behaves like a single QD structure with larger height to width aspect ratio, with LH-like GS and emitted light polarization mainly along the growth direction. Basically, the situation is the same as in single QD case in terms of confinement strength. It appears that the states structure in QDM also very sensitive to the barrier height, which makes it also another effective way of controlling the states coupling in QDM.

6.3.2 Polarization control by barrier adjustment

In this section, we show the effect of barrier height on the polarization switching of the QDM GS emission. Figure 6.5 presents the dependence of the lowest CB and VB states on the nominal Al content in the outer barrier (nominal Al content in QD core: 20%; in external barriers: 40%, QD thickness t=7 nm; barrier thickness d=5 nm). The GS of the CB increases with increasing Al content, as the potential energy of the barrier increases. The VB states dependence is more complex: in between the two extreme barrier heights the VB GS changes its character from LH- to HH- like with increasing barrier height (see figure 6.5 b).

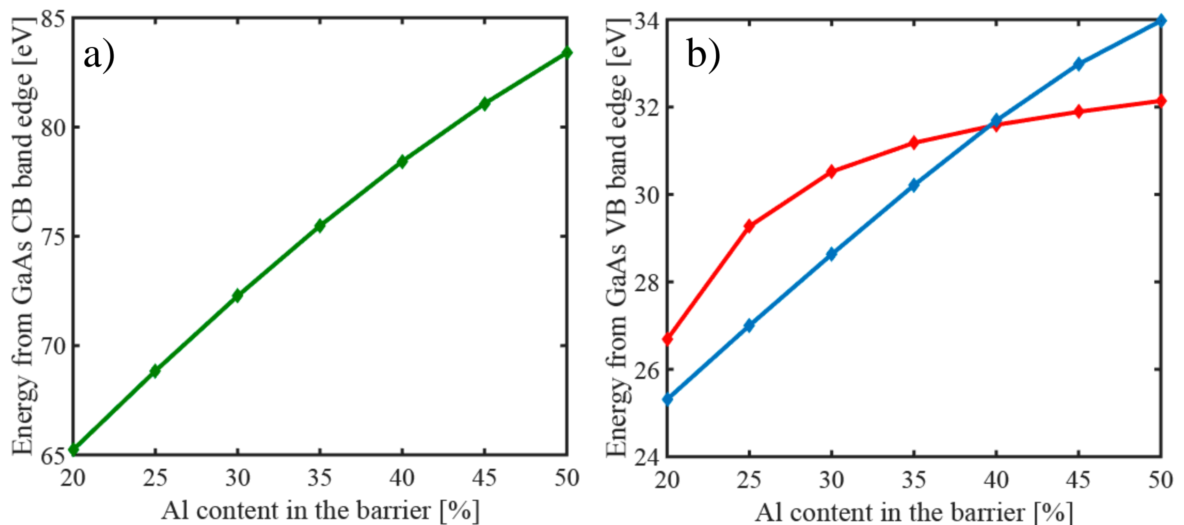

Figure 6.5 (a) Calculated confinement energy dependence of the first CB state versus the QDM barrier composition. Inset is schematic of the QDM core part. (b) Calculated energy position of the first 2 VB state from QD barrier composition. Blue line corresponds to LH transitions, red to HH transition.

Figure 6.6 (a) displays a summary of the calculated optical spectra, taking into account Coulomb interaction as a perturbation and a line broadening of 2 meV. The lowest energy transition is mainly LH-like for low barriers, and becomes degenerate with the HH-like one at ~40% Al. The spectra show the evolution of the HH and LH transition lines, their crossing when Al content becomes ~40%, and at 50% the complete change of the GS to HH one. Figure 6.6 (b) shows the spectral positions of the GS and the first excited transition versus the barrier Al content, indicating the VB character (red color for HH, blue for LH). Figure 6.6 (c) shows the VB mixing dependence on the barrier height. Summarizing, the common trend for all structures is that at certain vertical confinement strength the GS transition changes between LH to HH like, and as a consequence the emission polarization of the GS also changes.

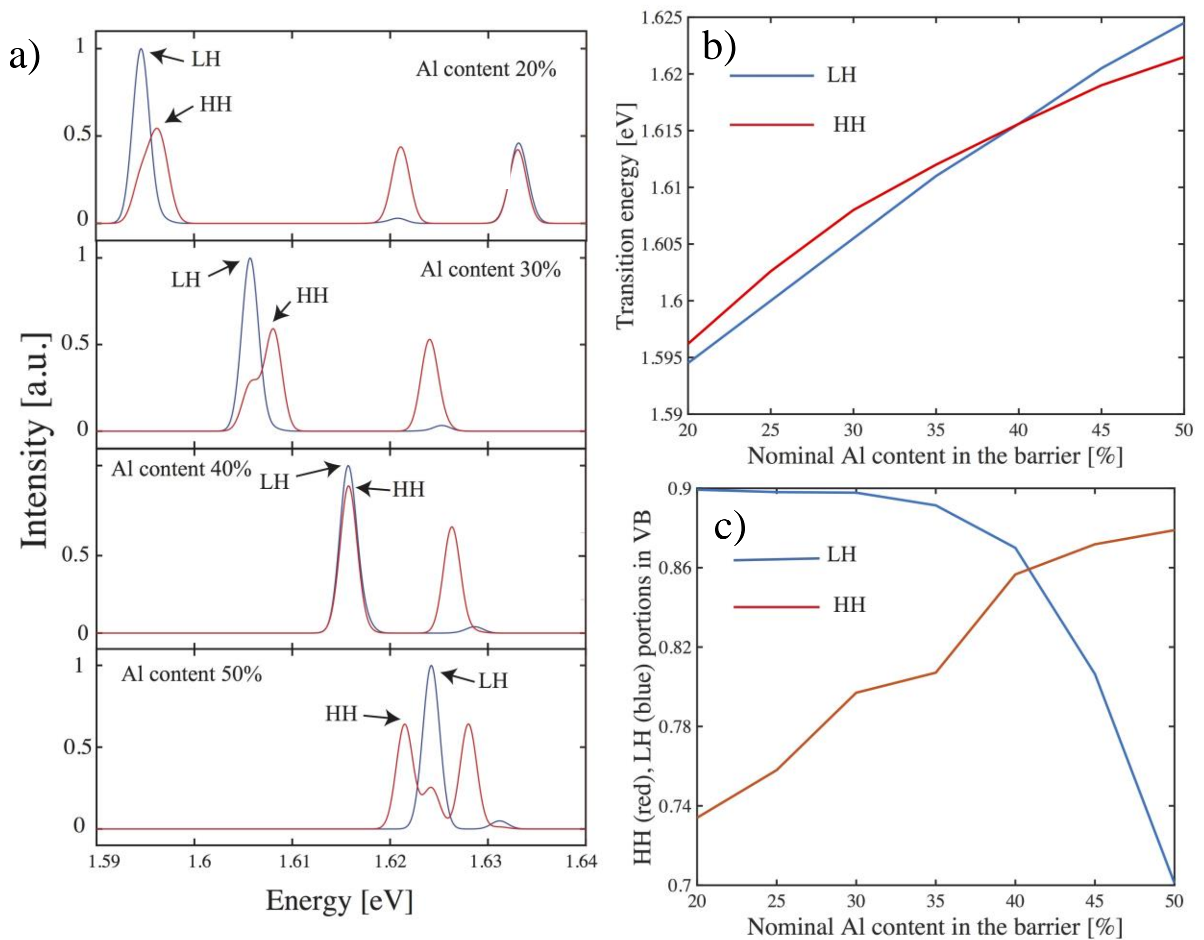

Figure 6.6 (a) Calculated polarization-resolved spectra of the QDM for different heights of the barrier (Al content). Blue and red curves correspond to linear polarization parallel and perpendicular to the growth directions. Coulomb interaction and linewidth broadening accounted for as in Chapter 4. Lines corresponding to HH-like and LH-like transitions are indicated. (b) Calculated energies of the lowest energy transitions in (a) versus QDM thickness barrier height. Different colors correspond to different transition types, the red line between CB and HH transition, blue line between CB and LH transition. (c) HH and LH portions in VB states presented in (b).

This figure illustrates the two regimes of behavior, with two different GS transition types and polarization of emitted light. The QDM system at the intermediate point were the HH and LH states are almost degenerate opens an opportunity to change dynamically the GS emission character by applying an external electric field, due to the sensitivity of such structure.

6.3.3 Polarization control via external electric field

In this section, we consider the effect of an external electric field in a QDM with the following structural parameters: QD cores of 20% Al content and thickness t=7 nm each, QD external barriers of 40% Al content, QD inner barrier thickness d=5 nm and 35% Al content. Figure 6.7 shows the simulation results of the system without external electric field (*E=0*). Figure 6.7 (a) presents the calculated optical spectra and figure 6 (b) the corresponding DOLP spectra. For this configuration. The GS LH and HH transition are almost at the same energy, with more complex structure of the excited states transitions. The right panel of figure 6.7 shows side view of the lowest CB and VB states WFs isosurfaces.

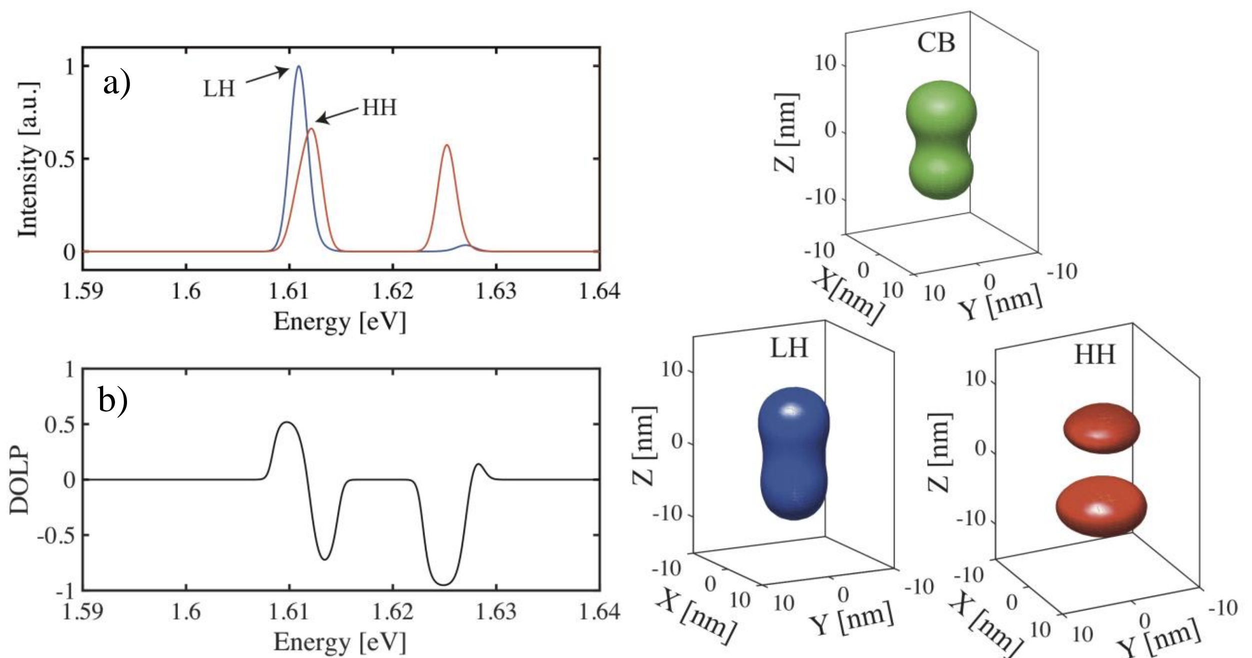

Figure 6.7 QDM structure (see text for parameters) without electric field. Left panel: (a) Calculated optical spectra taking into account Coulomb interaction and 2 meV broadening. (b) DOLP spectra. Right panel: wavefunction iso-surfaces of the lowest energy CB and VB states: green – electron; red – HH; blue - LH.

For the same QDM structure, the additional potential asymmetry induced by an external electric field of E=9000 [V/cm] aligned in the growth direction dramatically changes the optical spectra and WFs shapes (figure 6.8). As in the case of the single QD with the applied electric field, the polarization of the GS transition and its energy change. In contrast to the case E=0, the lowest energy transition has now DOLP=-0.6 as opposed to DOLP=+0.5 to its more important HH character of the VB state involved. Note that the CB and VB WFs are pushed in the opposite direction by the electric field, as usual for a Stark effect. This also leads to a reduction in the transition strength due to the smaller WF overlaps.

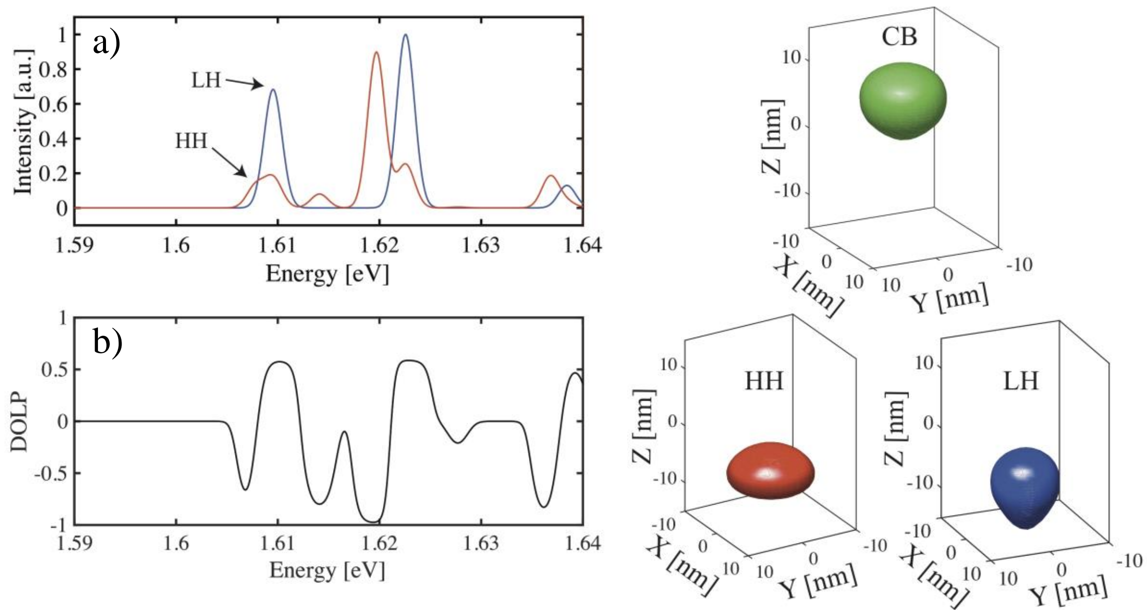

Figure 6.8 QDM structure (see text for parameters) subject to an electric field E=9000 V/cm, applied in the +z direction. Left panel: (a) Calculated optical spectra taking into account Coulomb interaction and 2 meV broadening. (b) DOLP spectra. Right panel: wavefunction iso-surfaces of the lowest energy CB and VB states: green – electron; red – HH; blue – LH.

6.4 QD superlattices in inverted pyramids

A next step to scale up the family of nanostructures discussed is the formation of a QD superlattice (QDSL). QDSLs are useful for achieving entangled QD states and performing quantum manipulations of their WF features. In this section, we will consider QDSL structures formed in inverted pyramids, as shown schematically in figure 6.9. Using numerical simulations, we first demonstrate the formation of QDSL minibands and then introduce the effect of an applied electric field. The impact on the polarization of the emitted light is discussed.

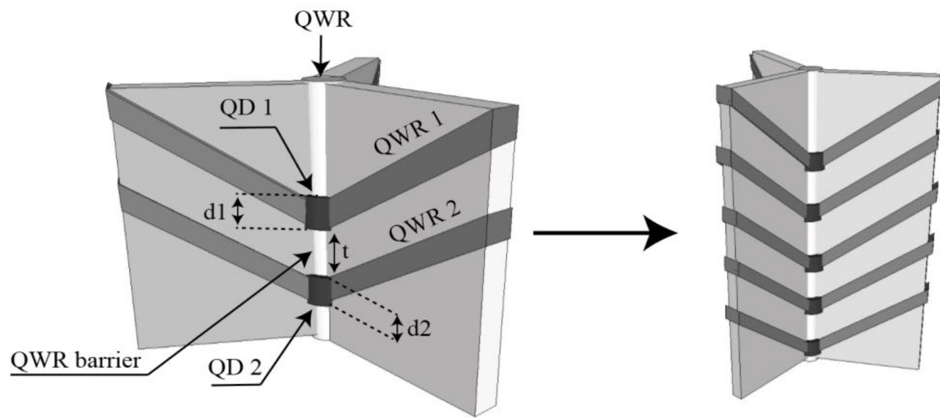

Figure 6.9. Schematic picture of pyramidal QD molecule (left) and pyramidal QD superlattice (right).

6.4.1 Miniband formation in pyramidal QD superlatticces

QDSLs can be realized experimentally in pyramidal systems as a vertically aligned coupled QD array. In such systems, the barrier height and width are crucial parameters that define the coupling strength between the QDs, via the CB and VB WFs overlaps due to tunneling to neighbor QDs. As a result with increasing coupling we see a “forest” of optical transition lines. The case of two-QDs molecule can be extended to N QDs, which leads us to the formation of minibands, as shown for the case of QW superlattices [178]. Depending on coupling strength we can distinguish three types of QDSL: SL with strong QD coupling, which is basically a system close to a QWR; completely decoupled QDs (week coupling); and system with intermediate coupling strength. Applying an electric field to a strongly coupled QDSL can be used to dynamically change the system and tune it among these categories. In particular, an electric filed can remove the degeneracy of the CB and VB states, resulting in the so-called Wannier–Stark ladder effect [179].

We have simulated pyramidal QDSL structures where the coupling strength is significant enough to produce SL minibands. The model is an extension of the QDM system (see figure 6.9). In the first example, the QDs are each 10 nm thick, with 20% nominal Al content, separated by 12 nm thick barriers of 30% nominal Al content. The QDSL is sandwiched between external barriers of 40% nominal Al content. The results for a 5-QDSL structure with these parameters are displayed in figure 6.10. The CB states are presented in figure 6.10 (a), where the confinement energies of the first CB states are shown, with a schematic inset of the structure. The right side displays the calculated WFs isosurfaces. The envelope functions of the CB SL states are not completely delocalized due to the small number of coupled QDs and the strong effects of the external barriers. The VB structure, presented in figure 6.10 (b), is more complex due to VB mixing effects and difference effective masses. The remarkable effect is that the lower energy VB states are delocalized across the entire SL and have dominant LH character. This is in contrast to the HH-like lowest energy VB state for the uncoupled QDs.

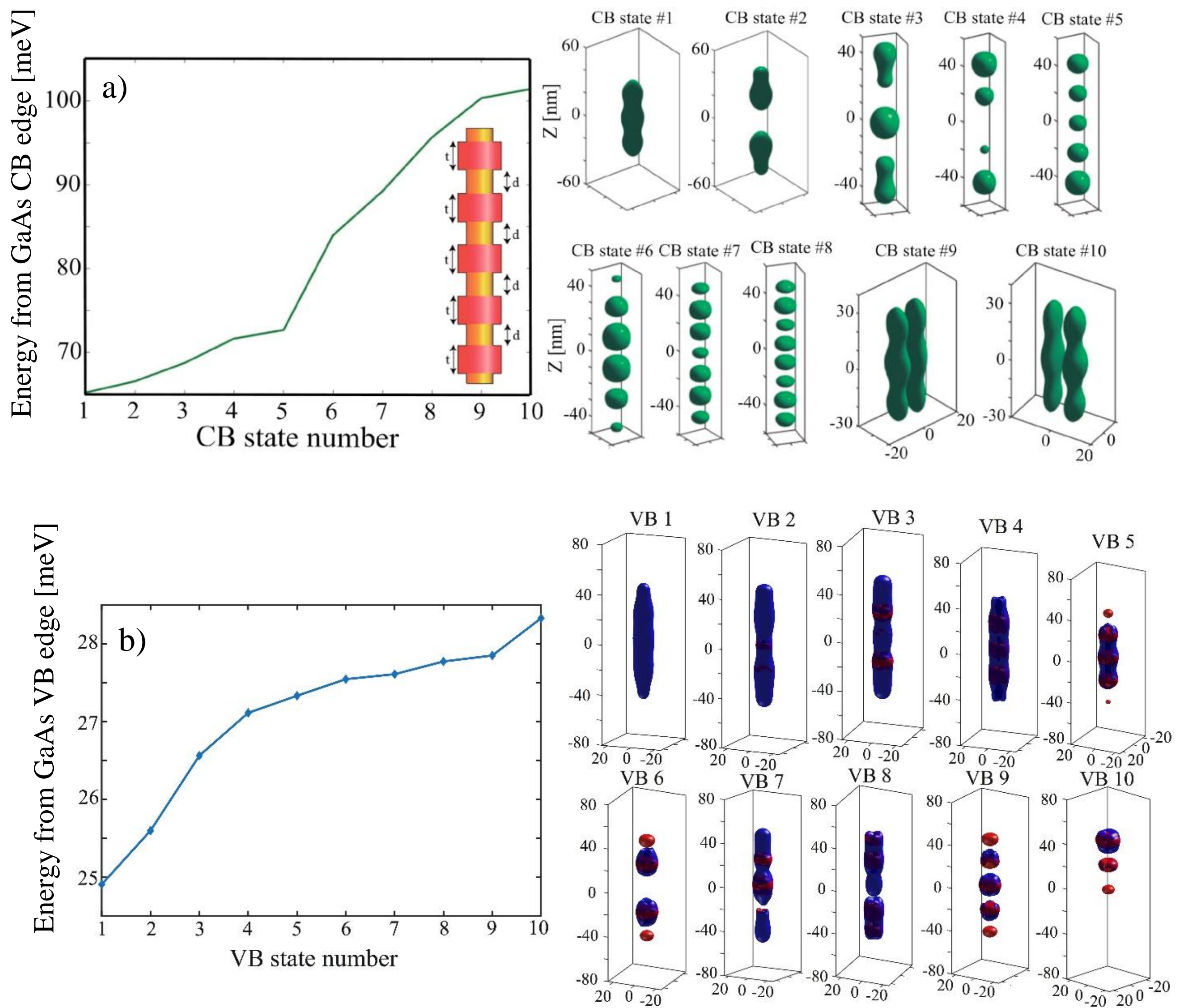

Figure 6.10. 5-QD pyramidal QDSL structure (see text for parameters). (a) Confinement energies of the first CB states. Inset is a schematic picture of the QDSL core part. Right panel: CB WFs (probability density isosurface) of the first 10 CB states. (b) Confinement energies of the first VB states. Right panel: VB WFs of the first 10 VB states; Red and blue colors indicate HH and LH components.

Another case considered here is a weaker coupling QDSL, presented in figure 6.11. In this case, 10 coupled QDs are embedded into a vertical (central) QWR with a following barrier parameters: composition is 50% nominal Al content and barrier thickness is 7 nm. All other parameters are as for the 5QDSL structure discussed above. The coupled CB and VB states are now closely spaced in energy, and start forming a SL quasi-continuous minibands. As in the case of the 5 QDs, the WFs consist of periodic parts (in each QD) modulated by envelope functions. Differently than in the more strongly coupled 5 QDSL, the coupled VB states maintain some HH character. This is because of the weaker QD-QD coupling that is insufficient to obtain crossing of the LH-like states to lower energies (see for example figure 6.5).

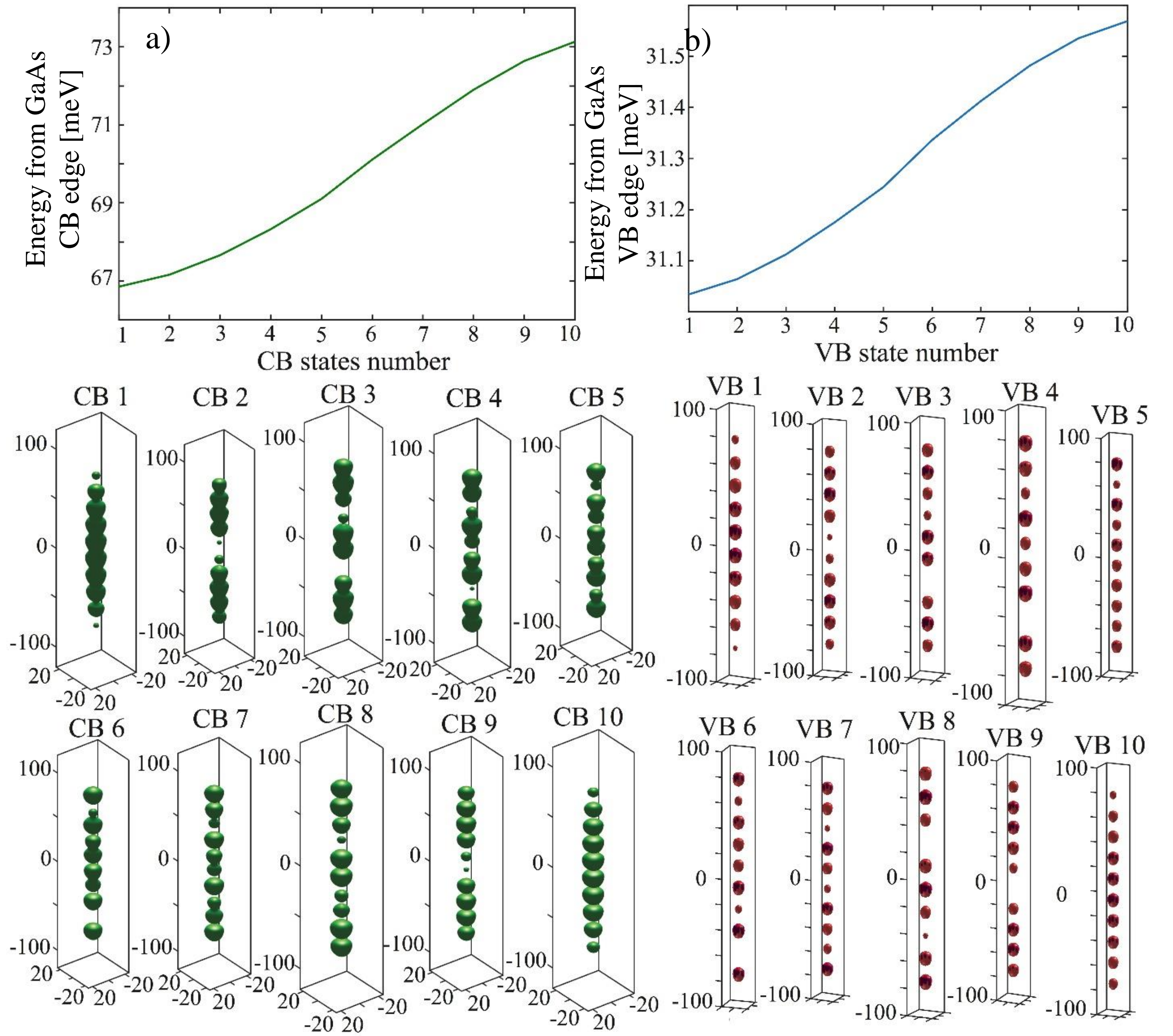

Figure 6.11. 10-QD pyramidal QDSL structure (see text for parameters). (a) Confinement energies and WFs (probability density isosurfaces) of the first 10 CB states. (b) Confinement energies and WFs of the first 10 VB states bellow; Red and blue colors indicate HH and LH components.

Figure 6.12 presents the optical spectra for the two cases of strongly (left part) and weakly (right part) coupled QDs (5 and 10 correspondently) in a QDSL. The 5-QD SL spectra remind QWR spectra (see figure 6.14 a) in the sense that the lowest energy transitions are LH-like, but the diference is the group of adjacent HH-related transitions. Thus, the GS DOLP is 0.6, but due to the presence of the HH transitions, the DOLP of the excited state transitions decreases down to -0.5 and less. The 10-QD SL spectra demonstrate the effect of weak coupling between the QDs, where all transitions are HH-like at slightly different energies. As a result, the DOLP is -1. Little asymmetry in spectra shape comes from asymmetry (mirror reflection) in QDs geometry (bottom part, see Chapter 2).

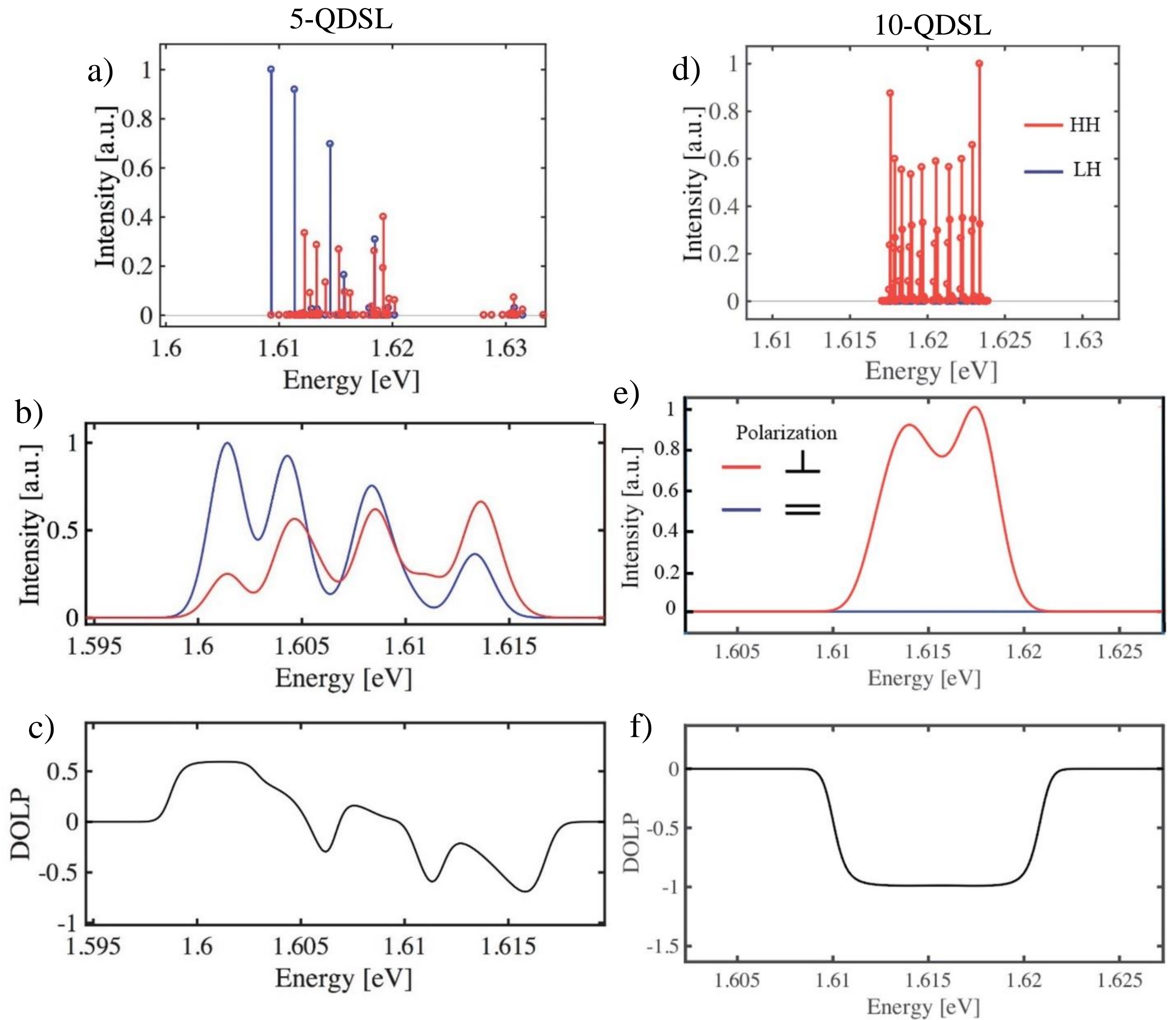

Figure 6.12 Calculated optical spectra of the pyramidal QDSLs (without electric field) of figures 6.13 (a-c) and 6.14 (d-f). (a),(d) optical spectra without broadening and Coulomb interaction. (b),(e) optical spectra with coulomb interaction and 2 meV broadening. (c),(f) DOLP spectra for parts (b) and (e).

6.4.2 Effect of electric field on QD superlattice properties

As it was demonstrated above for the QD and QDM cases, the electric field modifies the confinement potential and leads to modification of optical properties of the nanostructure. The simplest structure representing the limit case of strongly coupled QDSLs is a QWR. As an example, we have simulated the effect of the electric field in an $Al_{0.2}Ga_{0.8}As$ QWR sandwiched in between $Al_{0.4}Ga_{0.6}As$ barriers (nominal parameters) in with length of 160 nm and the standard diameter of d=18 nm. Figure 6.13 presents the simulation results for the 160 nm-QWR under electric field with 3000 V/cm. The CB and VB structure and corresponding WFs are shown in

parts (a) and (b), respectively. The CB WFs have envelope functions resembling Airy functions shapes as in case of simple triangular potential wells. While VB structure has more complex behavior due to the 4x4 Luttinger Hamiltonian structure. There are two important specific features in the VB: localization of the LH and HHWFs in opposite part of the well (different charges), and the fact they keep dominant LH features.

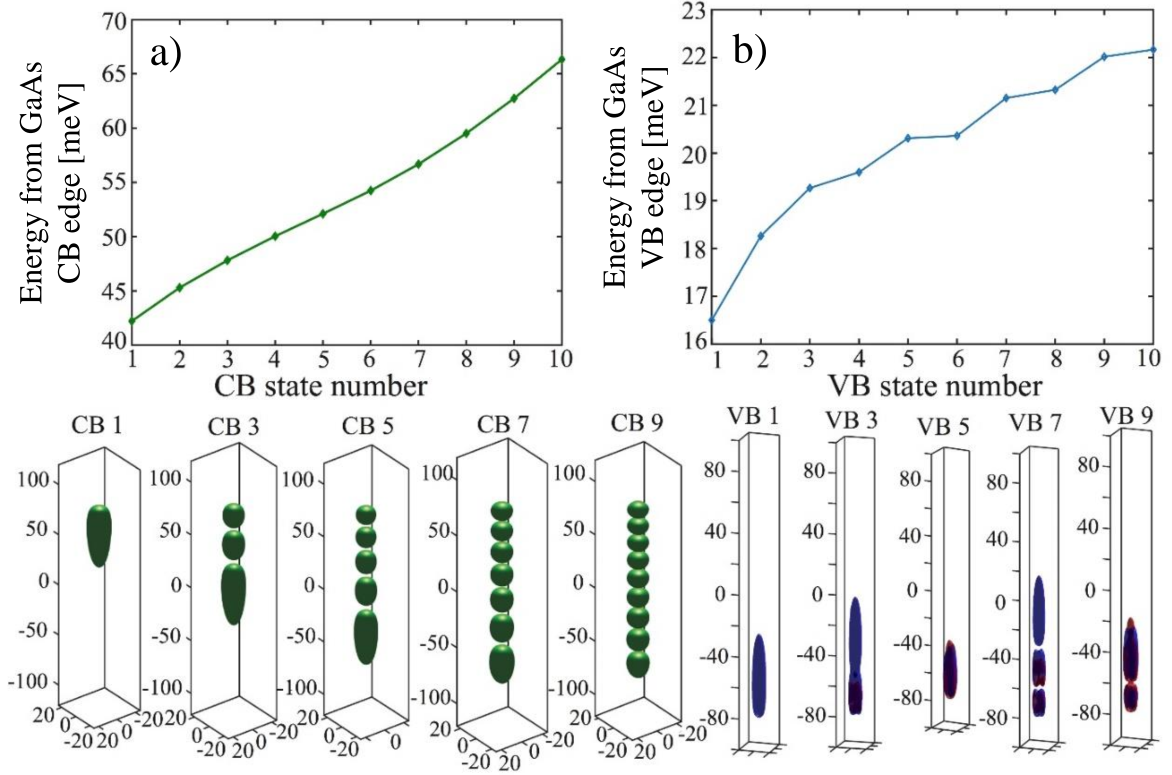

Figure 6.13. 160 nm pyramidal QWR structure (see text for parameters) under electric field E= 3000 [V/cm] (along z direction). (a) Confinement energies of the first CB states and CB WFs (probability density isosurface) of some states (bottom. (b) Confinement energies of the first VB states and VB WFs of some VB states (bottom); red and blue colors indicate HH and LH components.

The effect of the external electric field on optical properties of the 160nm-QWR is presented in figure 6.14. Comparing the spectra without and with electric field, we see the rise of the importance of the HH-like transitions and the decrease of the DOLP under electric field. In such long structures, electrons and holes shift in opposite directions under the electric field, and as a consequence we do not see significant spectral red shifts due to weak overlap between the lowest CB and VB states. Increasing the electric field intensity will lead to further state separation in the CB and VB and decreased WF overlaps, thus leaving only transitions related to highly excited CB and VB states.

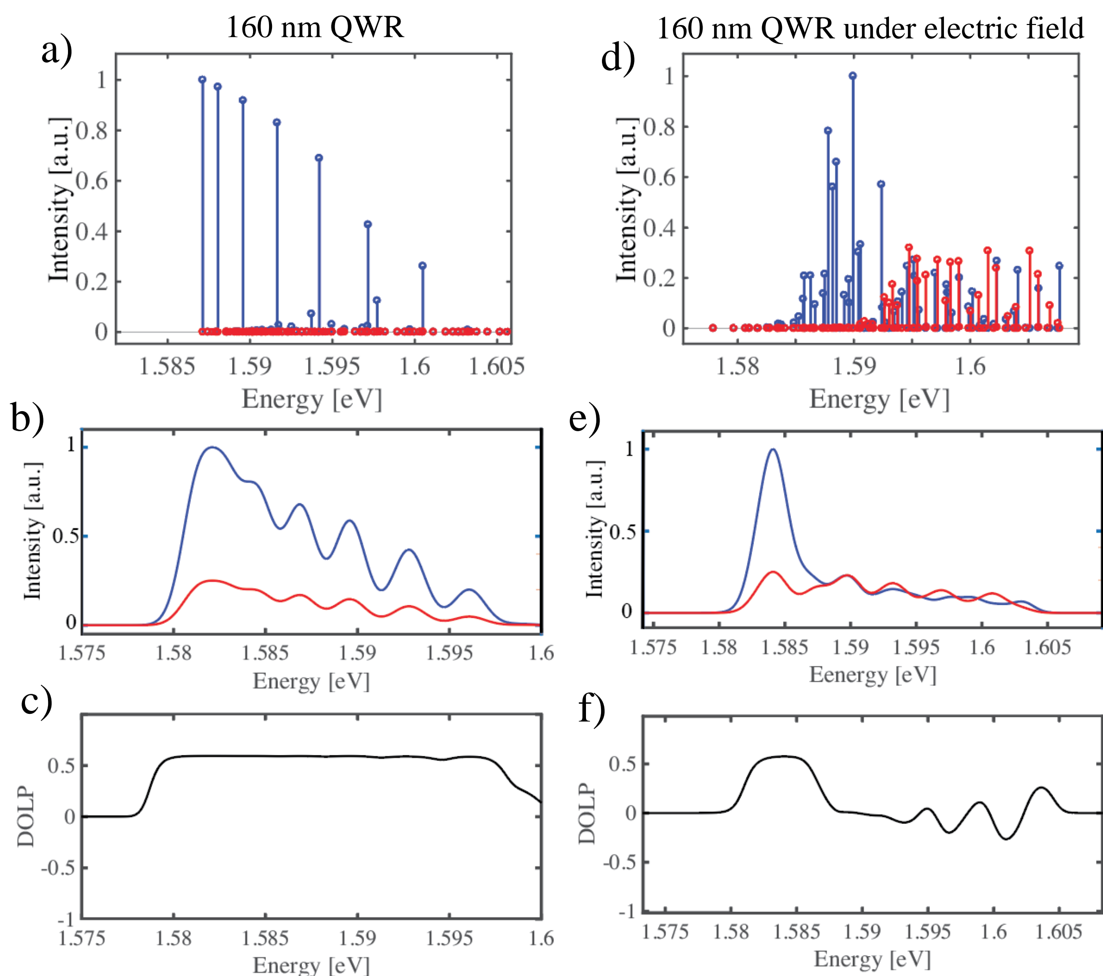

Figure 6.14. Calculated optical spectra and DOLP of the pyramidal 160 nm-QWR. E= 0 [V/cm]: (a) optical spectra without broadening and Coulomb interaction, (b) optical spectra with coulomb interaction and 2 meV broadening, (c) DOLP spectra for part (b). E= 3000 [V/cm]: (d) optical spectra without broadening and Coulomb interaction, (e) optical spectra with coulomb interaction and 2 meV broadening, (f) DOLP spectra for part (e). Note that in (a) and (d) by the red and blue colors shown HH and LH transitions, while in (b) and (e) red color corresponds to light polarization perpendicular to the QD, blue along.

Figure 6.15 shows the result of the 5 QDSL (strong coupled QDs) band structure under electric field with intensity E= 3000 [V/cm]. The applied electric field changes the CB structure and WFs shapes dramatically. The WFs are more localized, with the GS WF localized in 2 side QDs, and the first excited state localized in 3 QDs. The WFs localization is controlled by the confinement potential that is now tilted by the electric field. The envelope of the CB WF remind those of the QWR under electric field; in a sense the QD barriers act on the WFs as a perturbation compared to the QWR case. The electric field also affects many aspects of the VB, obviously the energy spacing and WF tunneling, but it also has an effect on the LH and HH portions of the VB states. The presence of the HH portion is already significant in the first VB state, where it is localized more than the LH portion due to the different effective masses. As in the QWR case, the lowest CB and VB state have low overlap due to the E-field induced localization (see also figure 6.17).

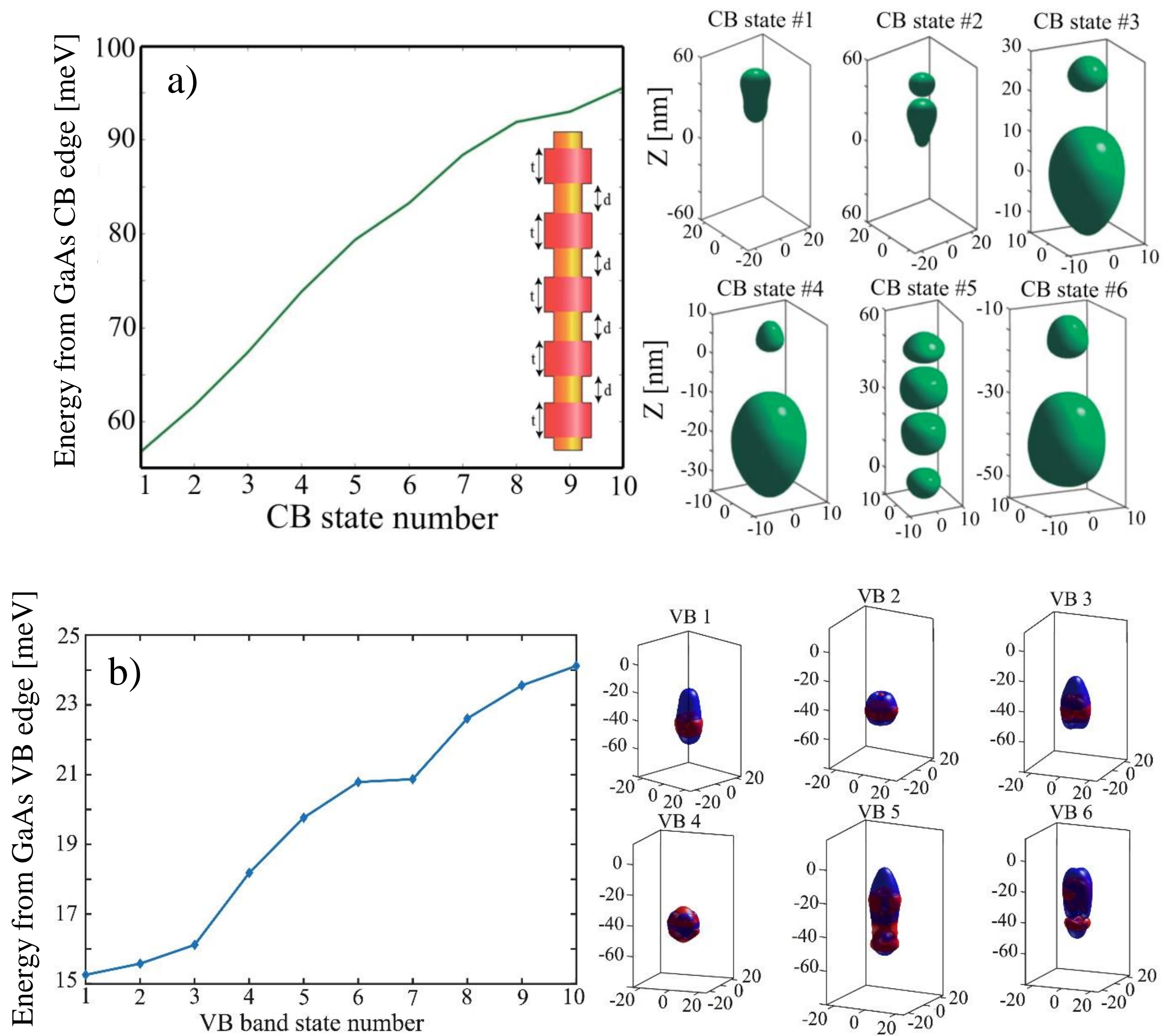

Figure 6.15 5-QD pyramidal QDSL structure (see text for parameters) under electric field E=-3000 [V/nm] (along z direction). (a) Confinement energies of the first CB states. Inset is a schematic picture of the QDSL core part. Right panel: CB WFs (probability density isosurface) of the first 6 CB states. (b) Confinement energies of the first VB states. Right panel: VB WFs of the first 6 VB states; Red and blue colors indicate HH and LH components.

The CB and VB structure of the 10-QDs SL under electric field (1000 V/cm) is presented in figure 6.16. Due to the relatively high barriers between the QDs, the WFs are localized in a few QDs. The center of mass (WF) of each state is shifted on equal distance (QD to QD) from state to state (figure 6.16 (a)). The CB dispersion line demonstrates almost liner behavior with respect to the state number. In the VB, the electric field casues the holes to tunnel through the barriers and thist leads to the formation of LH like states instead of the HH states formed in the absence of electric field (compare with figure 6.11).

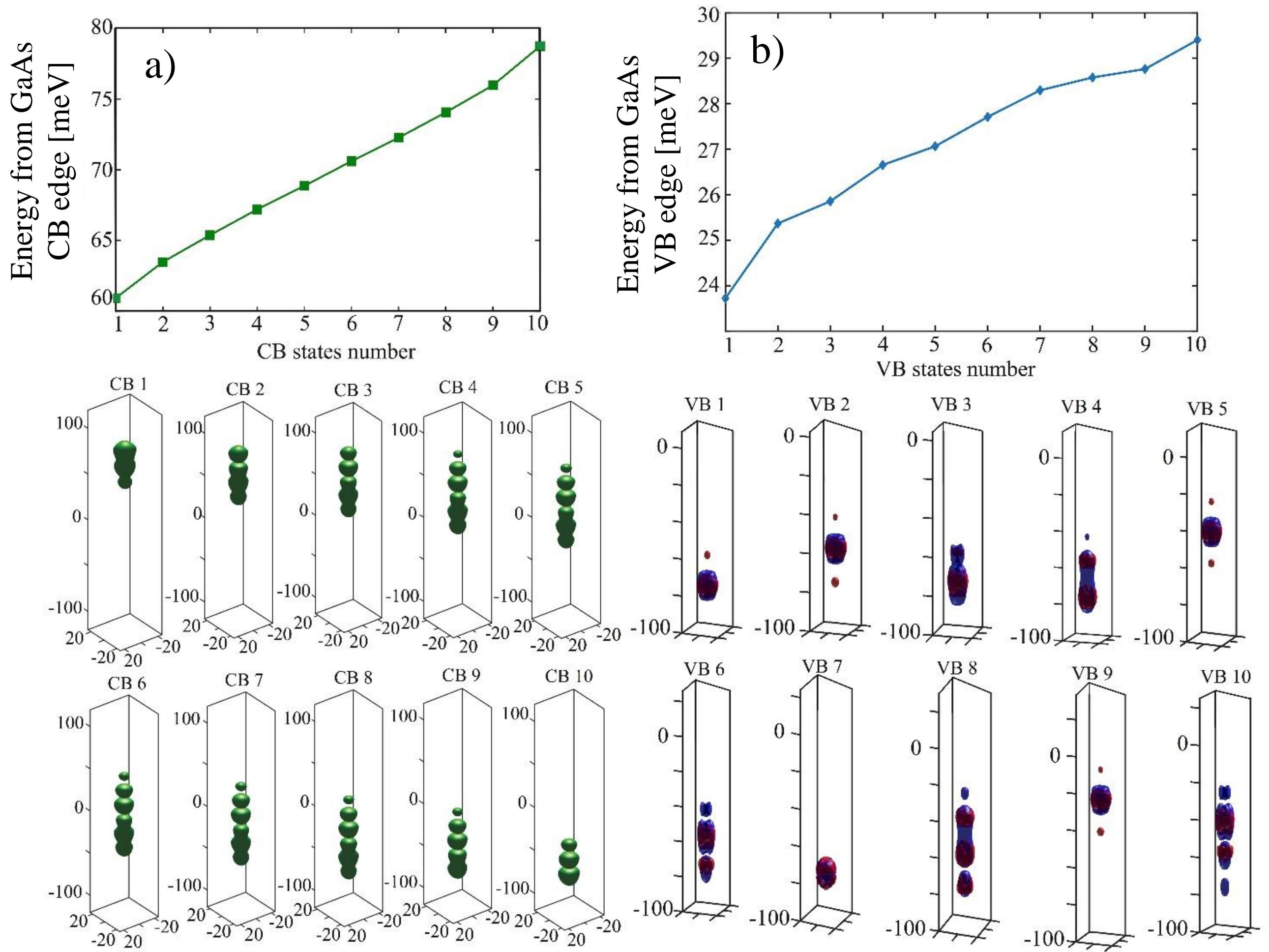

Figure 6.16. 10-QD pyramidal QDSL structure (see text for parameters) under electric field E=1000 [V/cm] (along z direction). (a) Confinement energies of the first CB states and CB WFs (probability density isosurface) of the first 10 CB states bellow. (b) Confinement energies of the first VB states and VB WFs of the first 10 VB states bellow; Red and blue colors indicate HH and LH VB WFs components.

The calculated spectra of the considered QDSLs (5-QDs and 10-QDs), under electric field, are presented in figure 6.17. As in the QWR case, the electric field causes localization of the CB and VB states in different parts of the SL. The result is reduced overlaps between the low energy states of the CB and the VB, and the optical spectra consist predominantly of transitions between exited states. In particular, the effect of the electric field is to qualitatively change the polarization features of the weakly coupled QD SL. Their spectra now show a forest of mixed HH/LH lines as opposed to almost pure HH transitions in the absence of the electric field (compare to figure 6.12 (d)). In the 5-QDSL (strong coupled QDs), LH transitions were dominant already without electric field.

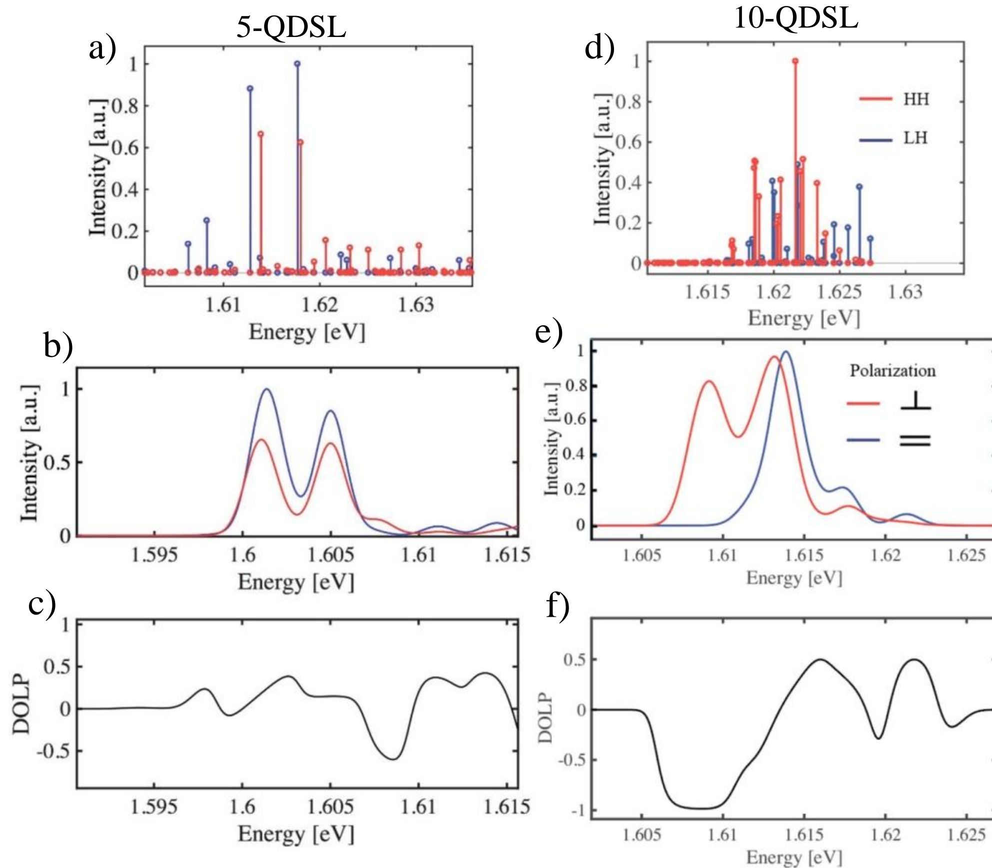

Figure 6.17. (a)-(c) 5 strong coupled QD in SL under electric field with intensity of 3000 V/cm (along z direction) (a)calculated spectra (b) spectra taking into account Coulomb interaction and 2meV line broadening (c) DOLP . (d)-(f) 10 week coupled QD in SL under electric field of 1000 V/cm (along z direction), (d) calculated spectra, (e) spectra taking into account Coulomb interaction and 2meV line broadening, (f) DOLP.

6.5 Summary

The sensitivity of VB state structure to the environment of QD and QDM makes them good candidates for polarization controlled single photon source. To find a good structural parameters for polarization switching a number of QDs was simulated from 8 nm and 23 nm length. The "equilibrium" point where LH and HH are at the same energy positions was found in between 12-14 nm long QD. Application of electric field along the QD change the VB structure in such that GS of VB becomes HH thus DOLP changes. QDM nanostructure is more sensitive to the potential variations in the barrier between the QDs and the physical principle of polarization switching effect relay on coupling strength between the QDs. High sensitivity of QDM VB structure to the coupling strength environmental parameters makes them useful as polarization switching device. External electric field modifies the coupling strength between QDs, thus affects on DOLP. This knowledge will be useful for construction of future polarization switching devices. We went further and increased the number of coupled QD up to 5 strong coupled QDs and 10 weak coupled QDs systems. Effect of optical miniband formation in QD SL and the effect of electric field was discussed.

Chapter 7. Conclusion and future directions

7.1 Conclusion

The target of this thesis was to study the optical properties, especially the polarization state of the optical emission, of nanostructures with different dimensionalities from 1D to 0D. For this purpose, different types of $Al_xGa_{1-x}As$/GaAs nanostructures were realized experimentally and simulated numerically. We used site-controlled MOVPE growth on patterned substrates to engineer novel quantum nanostructures with tailored potential with high reproducibility. Analysis of the relationship between nanostructure parameters and the optical properties yielded understanding of the main factors that determine the polarization state of the emission, and proposals for novel structures in which dynamic control of polarization can be achieved.

As a first step, we have designed and fabricated AlGaAs nanostructures with parabolically shaped potential profile along the growth direction by modulating the Al content during the growth process. Three parabolically shaped samples with 480 nm, 240 nm, and 120 nm length were grown by varying the Al content between 20 and 40 % (nominally), thus tailoring the confinement strength. A 480 nm long QWR structure and a thin QD structure were also fabricated in order to compare the effects of 2D and 3D quantum confinements. In this way we could prepare a whole range of quantum confined structures in the same strain-free GaAs/AlGaAs system and with similar geometrical features.

PL spectroscopy has been used for observation of the confined states. The states energy separation are strongly affected by the quantum confinement strength. For 120 nm, 240 nm and 480 nm long patabolically shped QDs the separation of the observed transitions are ~2, 4 and 6 meV, correspondently. On the other hand, a 5 nm-thick QD sample showed ~20 meV separation, whereas for a 480 nm-long QWR structure states were not resolvable in the PL spectra due to inhomogeneous broadening. Time resolved measurements by streak camera presented the evolution of exciton dynamics versus the confinement strength. The simulation results show agreement with the experimental spectra. Systematic increase in the multi-exciton binding energy with increasing confinement strength was observed. We represented the confinement strength as the energy difference between the CB ground state and first excited state transitions. Using this definition we could plot a map presenting the evolution of the 1D-0D nanostructures as a function of the confinement strength.

Polarization resolved PL spectroscopy has been used to study the effects of VB structure on the degree of linear polarization (DOLP). Quantum confinement affects at the same time the energy states separation, the LH and HH portions of the VB state, the geometry of the wavefunctions and their overlaps, and the state occupation; the sum of these effects determines the DOLP. Pure HH and LH transitions result in distinctly different DOLP (-1 and 0.6, respectively),

but due to the inhomogeneous broadening intermediate DOLP values occur. Moreover, the spectra and DOLP depend on state occupation. We have presented a method for estimating the state occupation, effective Fermi energy and carrier temperature. Studying the DOLP power dependence we have evidenced excited myltiexcitonic states at high excitation powers that lead to under estimation of the DOLP compared to the modeled one.

Dynamic control of the polarization properties of the nanostructure emission is challenging, but an important task for future applications. Several methods of dynamic polarization control have been discussed, particularly the effect of electric fields on the QD VB structure and the optical spectra. To this end, we have considered two types of nanostructures: pyramidal GaAs/AlGaAs QDs of thickness between 8 nm to 23 nm, and pyramidal GaAs/AlGaAs QD molecule with different potential barrier parameters (height and thickness). For each structure we found parameters for which HH-like and LH-like VB states were resonant in energy, and adjusting the confinement parameters we were able to tune the polarization properties. We then showed that adding an electric field on a structure close to switching between two polarization states can serve to achieve dynamic polarization tuning. As an extension of these concepts, formation of minibands in pyramidal QD superlattice systems and its behavior under electric field were analyzed for different QD coupling strengths. It was shown that electric field can modify the number of hybridized states in such a QD-superlattices and thus change its optical and transport properties. Preliminary results on the implementation of electric fields in pyramidal quantum nanostructures were presented.

In general, our study illustrates how the details of quantum confinement in semiconductor QWR and QD structures can be adjusted in real (experimental) structures and thereby employed in controlling the polarization states of light emitted by these nanostructures. By achieving single photon emission from such QDs, it should be possible to design in this way single photon emitters with adjustable polarization state.

7.2 Future directions

In chapter 6, we have analyzed the impact of confinement and electric field on the polarization of the emitted light. The ability to control emission polarization of a single photon source has great importance for future nano optical devices. One of the ways to implement electric field in the nanostructure is to use a Schottky diode structure; the fabrication process for the simplest case of a GaAs/AlGaAs QW is demonstrated in appendix D.

Here we present preliminary results on the application of an electric field using a Schottky diode integrated with a pyramidal 240nm-parabolic-QD. The results are shown in figure 7.1. Figure 7.1 (a) presents top SEM image of a single pyramidal structure with the contact area (circle), and figure 7.1 (b) is an image of a cleaved sample before the measurements. The current-voltage characteristic of the resulting Schottky diode structure is shown in figure 7.1 (c); the useful region for the applied voltage is in between 0 V and -2 V. This voltage should be enough, according to our simulation results, to achieve the desirable intensity of electric field for optical polarization switching.

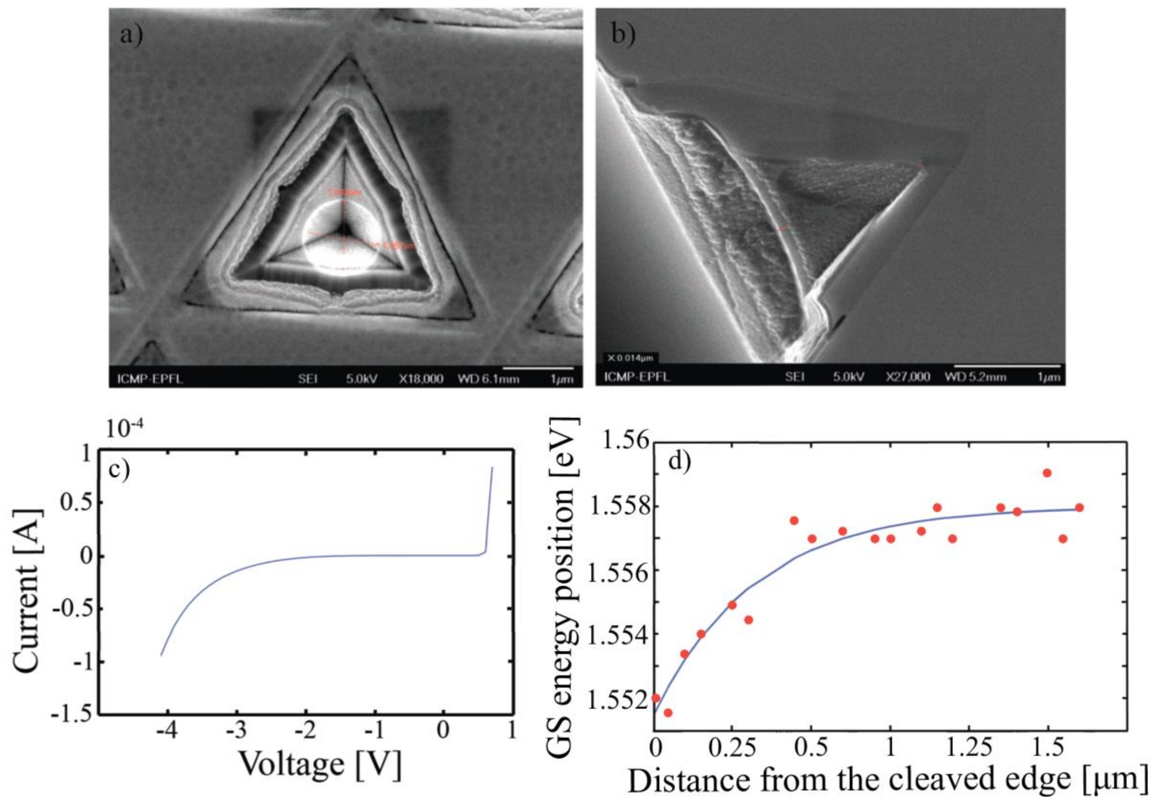

Figure 7.1. (a) Top view SEM image of the 240nm parabolically shaped AlGaAs QD with Schottky diode contact (circle in the center). (b) The same sample, cleaved e for polarization resolved PL measurements. (c) Current-voltage characteristic of a Schottky diode on a 240nm parabolically shaped AlGaAs QD sample. (d) Ground state transition energy versus the position of the QD from the cleaved edge; blue line is an exponential fit to the data.

We have measured the PL spectra of a row of pyramids at fixed temperature and excitation power. The cleaved edge makes a certain angle with respect to the row of QDs, and thus the distance of each QD from the cleaved surface changes in steps of ~50 nm. We observed that the GS transition energy shifts systematically from pyramid to pyramid (see Figure 7.1 (d)). We explain the red shift when the QD approaches the cleaved surface as due to a Stark effect because of a built-in electric field near the surface (charge depletion area). This effect should be taken into account when applying the electric field with the Schottky contact.

Unexpectedly, we have found that for given distance from the cleaved edge and specific voltage values the PL spectral lineshape changed from smooth peaks to multiple sharp lines (see Fig. 7.2). We tentatively attribute this effect to a change in the potential profile along the pyramidal QD leading to exciton localization.

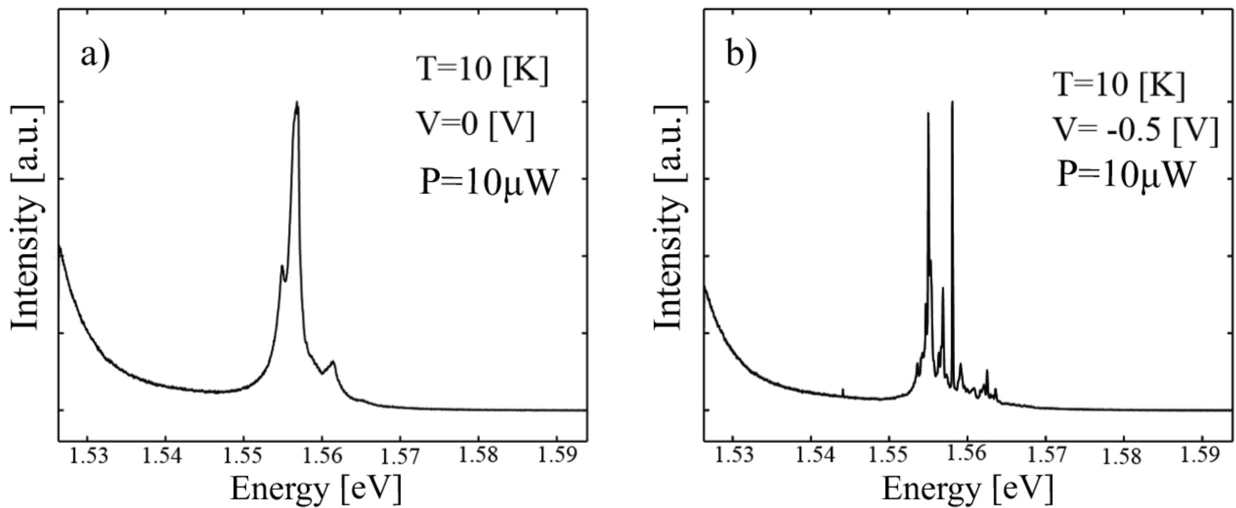

Figure 7.2 PL spectra of a 240nm parabolically shaped AlGaAs QD (a) with and (b) without applied reverse bias.

Contributions to thesis work

The author of this thesis fabricated the patterned substrates and did structural characterization before and after the MOVPE growth. He participated in the design of the grown structure. The MOVPE itself was done by Dr. Alok Rudra. The author performed all continuous wave PL measurements presented in this Thesis. All time-resolved PL experiments using streak camera reported in this Thesis were performed in the laboratory of Prof. N. N. Sibeldin by Dr. V. Tsvetkov and Dr. M. Skorikov at Lebedev Physical Institute of the Russian Academy of Sciences in Moscow. Electron beam lithography for Schottky diode contacting was performed by Dr. Benjamin Dwir. Numerical simulation results were obtained by the author using a Mathlab code written by Prof. K. F. Karlsson.

Appendix A. Fabrication process flow

This appendix summarizes the processing steps involved in the preparation of the patterned substrates for growth of the pyramidal structures, as well as the post-growth steps prior to the photoluminescence (PL) spectroscopy and Schottky diode fabrication.

I. Pre-growth substrate preparation

These steps serve to produce the pyramid patterns on the GaAs substrates and their cleaning prior to MOVPE growth of the quantum nanostructures.

1. Wafer preparation

a) SiO_2 or SiN layer deposition (60nm) using PECVD at T=300 ^{0}C on 2-inch GaAs (111) B oriented wafer.
b) Bake at 160 ºC, t= 5 min, to remove moisture from the substrate surface.
c) HMDS primer spin-coated at 3500 rpm / 3 s^{-2} / 30 s; not needed in case of SiN due to good enough adhesion.
d) Photoresist (negative) spin-coated at 3500 rpm / 3 s^{-2} / 30 s.
e) Bake at 90 ºC, t= 5min.

2. Photolithograpy

a) Exposure in mask aligner through the photolithograpy mask.
b) MF-319 development for 35–37 s + H_2O rinse to stop the reaction + Dry under N_2 flow.
c) Bake at 115 ◦C, t=15 min.
d) O_2-plasma etch, t= 2.5 min, P= 50W, pressure= 300 mTorr (removal of resist residues).

3. Oxide/nitride mask patterning

a) BHF (Buffer HF, 12.5%) SiO_2/SiN etching on a test-piece (remove the photoresist from the test-piece first). End-point (criterion: BHF stops wetting the hydrophobic surface) after ~ t_{test}= 22 s. Repeat with the sample, t_{sample}= 22 s + 6 s.
b) H_2O long rinsing + Dry under N_2 flow.

4. Resist stripping

a) Acetone free rinsing, t= 5 min.
b) Acetone rinsing in ultrasonic bath, t= 3 min.
c) Iso-Propanol rinsing, t= 2 x 5 s.
d) H_2O rinsing + dry under N_2 flow.

5. Br:Methanol etching of pyramids

a) Etch in Br_2: Methanol 1 ml: 100 ml, t= 40 ~ 50 s.

b) Methanol rinsing, t= 10 s.
c) Methanol rinsing in ultrasonic bath, t= 1 min.
d) H_2O rinsing + dry under N_2 flow + put samples in boxes.
e) BHF, t= 75 s, SiO_2 (SiN) removal.
f) H_2O rinsing + dry under N_2 flow. Store samples in box.

6. Cleaning before the MOVPE growth

a) O_2-plasma etching: t= 5 min, P= 50 W, Pressure= 400 m Torr (surface cleaning).
b) HF etching until the surface becomes hydrophobic.
c) H_2O rinsing (short) + dry under N_2 flow + store samples immediately under vacuum or under N_2 atmosphere (to avoid oxidation).

II. Post-growth surface etching

Surface etching step after the MOVPE growth step removes parasitic growth and permits observing inherent spectra in subsequent PL experiments.

a) Photoresist deposition: 5000 rpm /3 s $^{-2}$/30 s.
b) Bake at 90 °C, 5 min.
c) Bake at 115 °C, 15 min.
d) O_2-plasma etch, 25 – 35 min, 75 W, 0.8 Torr. Check sample's surface during the etching process by SEM.
e) Chemical etching in H_2SO_4 :H_2O_2 :H_2O (1:8:160) for 50s+H_2O rinse.
f) Acetone rinse in ultrasonic bath for 3 min (Photoresist removal) + acetone rinse + isopropanol rinse + H_2O rinse, N_2 dry. After this step the sample is ready for first PL quality check.

III. Back etching

The aim of back etching is to increase the PL emission efficiency in top-view geometry (see Chapter 3).

1. Substrate preparation for mechanical polishing
a) Cleave a GaAs (111)B support piece, with slightly larger size compared to sample.

b) Deposition of Ti (20 nm)/Au (200 nm) on top of the sample surface.
c) Heat the sample to ~ 90 °C.
d) Glue the sample (metal side) to the support using black wax.
e) Cool down to room temperature.
f) Heat sample (together with the support) to ~ 45 °C.
g) Glue the sample (together with the support) to a piece of glass using white wax.

2. Mechanical thinning

a) Mechanical etching using polishing powder with 5µm particle size.

b) Thin down the sample's substrate to 200µm (originally 350µm thick substrate)

3. Chemical etching

a) Slow etching in solution flow of $NH_4OH:H_2O_2$ (8 ml : 240 ml) using liquid rotation apparatus for further substrate thinning.

IV. Schottky diode fabrication

Schottky diodes are fabricated on the pyramidal nanostructures in order to apply electric fields (see Chapter 7).

1. Schottky contact deposition

1. Mask definition by E-beam lithography
   a) SiN deposition (120 nm).
   b) PMME spin coating at 2000r/min.
   c) E-beam lithography.
   d) PMMA developing for 1 min.
   e) BHF etching for 1 min, RIE with CF_4 for 4.5 min.

2. Photoresist deposition (for large pads)
   a) Baking at 115 ^{0}C for 5 min.
   b) Photoresist 5214, spin coating at 6000 r/min.
   c) Baking at 90 ^{0}C for 2 min.

3. Photolithography
   a) UV exposure through photomask.
   b) Baking for 1 min at 115 ^{0}C.
   c) UV exposure for 15 s without mask.

4. Metal deposition
   a) O_2 plasma for 30 sec (cleaning).
   b) Deoxidization in HCl for 40 sec.
   c) Metal deposition of 20/200nm Ti/Au.
   d) Lift-off for 5-7 min with acetone in ultrasonic bath.

2. Ohmic back contact deposition

Ohmic contact deposition on the n-type substrate side.

1. Metal multilayer deposition.
   a) Deposition of Ni 10 nm/Ge 20 nm/Au 40 nm/Ni 20 nm/Au 200 nm.
   b) Annealing at 400 ^{0}C for 3 min.

Appendix B. MOVPE growth parameters

General layer structure and growth parameters

All samples grown by MOVPE, presented in this thesis, consist of three parts: (i) buffer layer, graded AlGaAs, etch-stop AlGaAs, and AlGaAs barrier; (ii) core part of the nanostructure (QD/QWR); (iii) upper AlGaAs barrier and GaAs cap. The details are given in Table B1. Nominal thickness corresponds to that obtained on (100) substrates.

Layer	Material	Al content (%)	Nominal thickness (nm)	Susceptor Temperature (°C)
Buffer	GaAs	0	10	735
Ramp	AlGaAs	30-75	10	>770
Etch-stop	AlGaAs	75	45	770
Lower barrier	AlGaAs	40	100	705
QD/QWR core	*	*	*	*
Upper barrier	AlGaAs	40	45	705
Cap	GaAs	0	5	705

Table B1. General table of the growth layers sequence.

Parabolic Quantum Dots

For the AlGaAs parabolic QDs (PQDs), the core consists of an AlGaAs layer of total thickness L in which the (nominal) Al content was parablically graded from 40% (bottom) to 20% (center) and finally to 40% (top) in a symmetric way. Table B2 shows the details of the layers composing one half of the parabolic structure, for the case where the actual PQD thickness is L=120 nm (so called 120 nm-PQD structure). For the 240-nm-PQD and 480-nm-PQD structures a factor of 2 and 4 applies to the thicknesses in Table B2, respectively.

Layer	Material	Al content (%)	Nominal thickness (nm)	Growth rate (nm/s)	Duration (s)	Susceptor T (°C)	V/III pressure ratio
Par. grading	AlGaAs	40-39	0.76	0.065	11.7	705	1259
Par. grading	AlGaAs	39-38	0.78	0.065	12.0	705	1255
Par. grading	AlGaAs	38-37	0.8	0.065	12.3	705	1363
Par. grading	AlGaAs	37-36	0.825	0.065	12.7	705	1399
Par. grading	AlGaAs	36-35	0.85	0.065	13.1	705	1238
Par. grading	AlGaAs	35-34	0.88	0.065	13.5	705	1268
Par. grading	AlGaAs	34-33	0.91	0.065	14.0	705	1302
Par. grading	AlGaAs	33-32	0.95	0.065	14.6	705	1335
Par. grading	AlGaAs	32-31	0.99	0.065	15.2	705	1370
Par. grading	AlGaAs	31-30	1.035	0.065	15.9	705	1353
Par. grading	AlGaAs	30-29	1.085	0.065	16.7	705	1291
Par. grading	AlGaAs	29-28	1.15	0.065	17.7	705	1233
Par. grading	AlGaAs	28-27	1.225	0.065	18.8	705	1179
Par. grading	AlGaAs	27-26	1.315	0.065	20.2	705	1130
Par. grading	AlGaAs	26-25	1.43	0.065	22.0	705	1086
Par. grading	AlGaAs	25-24	1.58	0.065	24.3	705	1109
Par. grading	AlGaAs	24-23	1.8	0.065	27.7	705	1133
Par. grading	AlGaAs	23-22	2.13	0.065	32.8	705	1158
Par. grading	AlGaAs	22-21	2.75	0.065	42.3	705	1186
Par. grading	AlGaAs	21-20	4.2	0.065	64.6	705	1069
Par. grading	AlGaAs	20	1	0.065	15.4	705	1102

Table B2. Layer parameters for the 120 nm parabolic QDs.

"Thin" Quantum Dot

Layer	Material	Al content (%)	Nominal thickness (nm)	Growth rate (nm/s)	Duration (s)	Susceptor T °C	V/III pressure ratio
Buffer	GaAs	0	10	0.091	109.9	735	715
Ramp	AlGaAs	30-75	10	0.13	76.9	>770	882
Etch-stop	AlGaAs	75	45	0.13	346.2	770	882
Barrier	AlGaAs	40	100	0.04	2500.0	705	1326
QD	GaAs	0	1	0.024	41.7	705	2149
Barrier	AlGaAs	40	45	0.04	1125.0	705	1326
Cap	GaAs	0	5	0.024	208.3	705	2149

Table B3. Layer parameters for the thin GaAs QD structure.

480 nm Quantum Wire

Layer	Material	Al content %	Nominal thickness (nm)	Growth rate (nm/s)	Duration (s)	Susceptor T °C	V/III pressure ratio
Buffer	GaAs	0	10	0.091	109.9	735	715
Ramp	AlGaAs	30-75	10	0.13	76.9	>770	882
Etch-stop	AlGaAs	75	45	0.13	346.2	770	882
Barrier	AlGaAs	40	100	0.04	2500.0	705	1326
QWR	AlGaAs	20	240	0.065	41.7	705	1102
Barrier	AlGaAs	40	45	0.04	1125.0	705	1326
Cap	GaAs	0	5	0.024	208.3	705	2149

Table B4. Layer parameters for the 480 nm QWR structure.

Appendix C. Wavefunctions in pyramidal nanostructures

This appendix displays additional simulation results related to the confined states in the 120, 240 and 480 nm parabolic quantum dots (PQDs) that were not presented in Chapter 4 (Section 4.4). See Chapter 4 for the details of the structures.

120 nm parabolic quantum dot

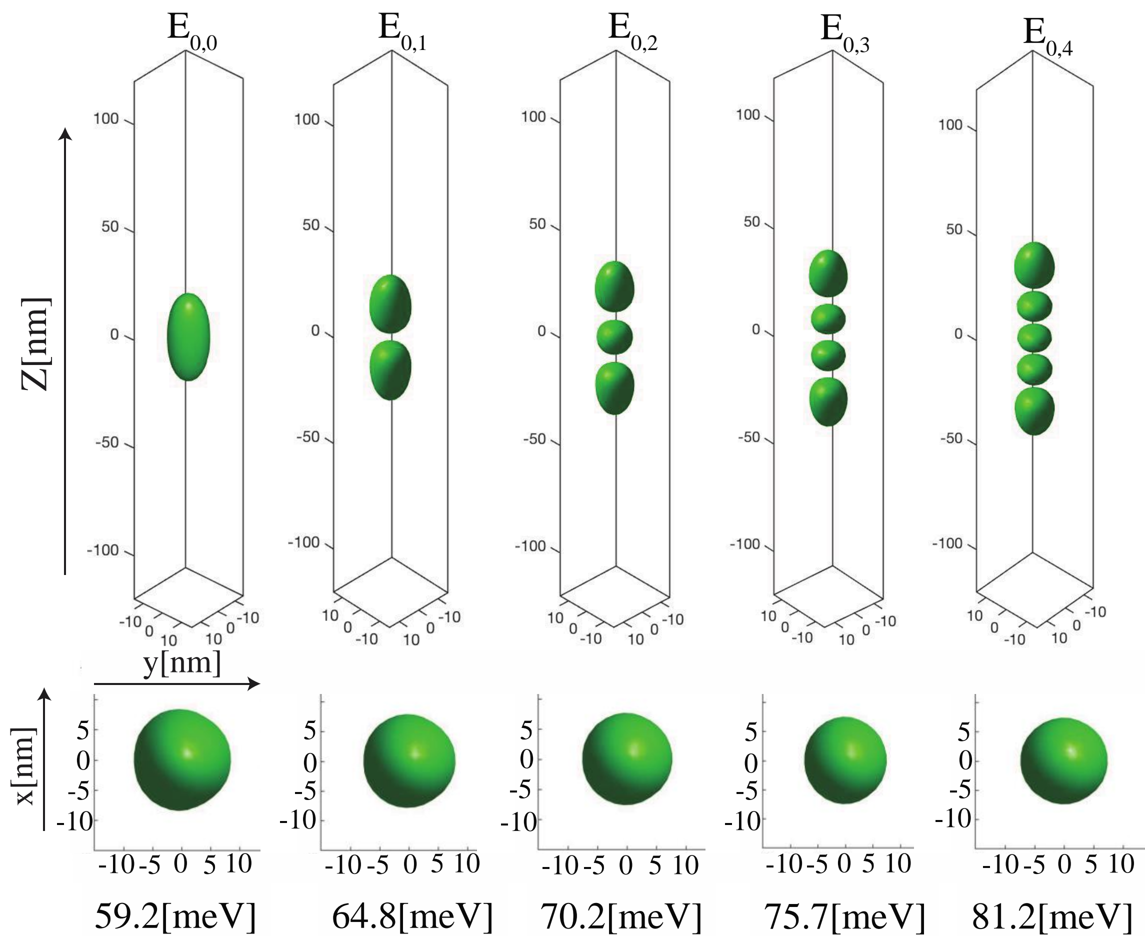

Figure C.1 Calculated electron wavefunctions (isosurfaces of probability density) of the first 5 electronic states for the 120 nm parabolic QD. Upper part: 3D plot (side view); bottom part: top view, with corresponding confinement energy measured from the GaAs band edge.

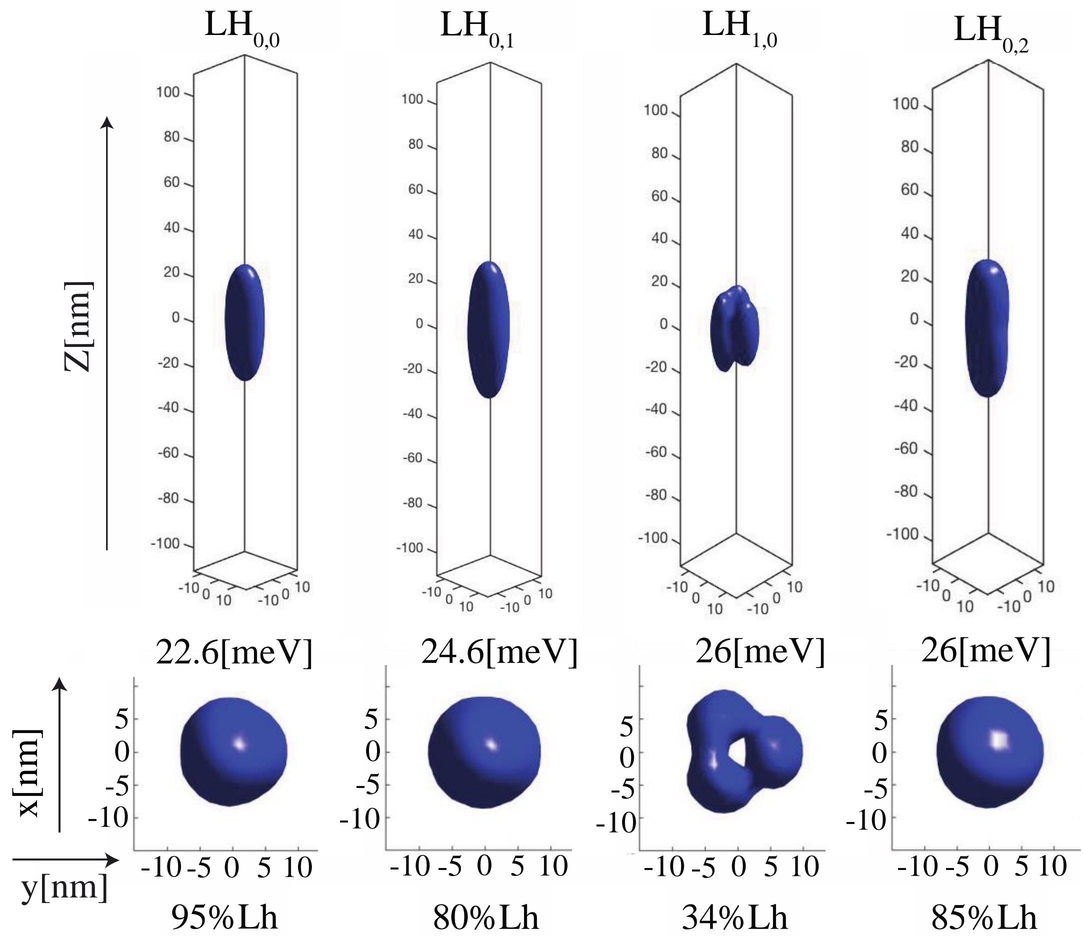

Figure C.2 Calculated light hole components of the wavefunctions (probability density isosurface) of the first 4 valence band states for the 120 nm parabolic QD. Upper part: 3D plot (front view); bottom part: top view, with the corresponding energy from GaAs VB edge and LH portion.

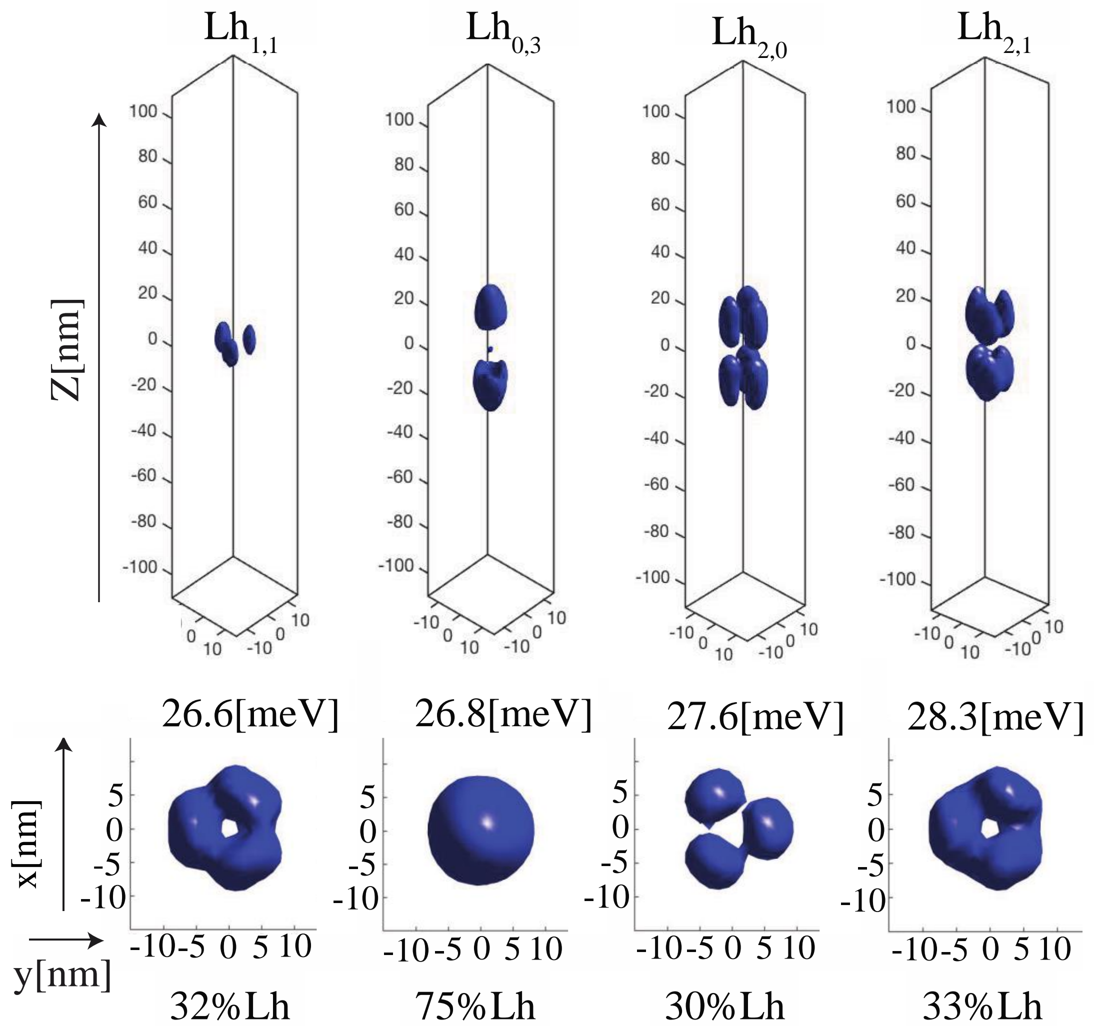

Figure C.3 Same as in Fig. C.2, for VB states 5-8.

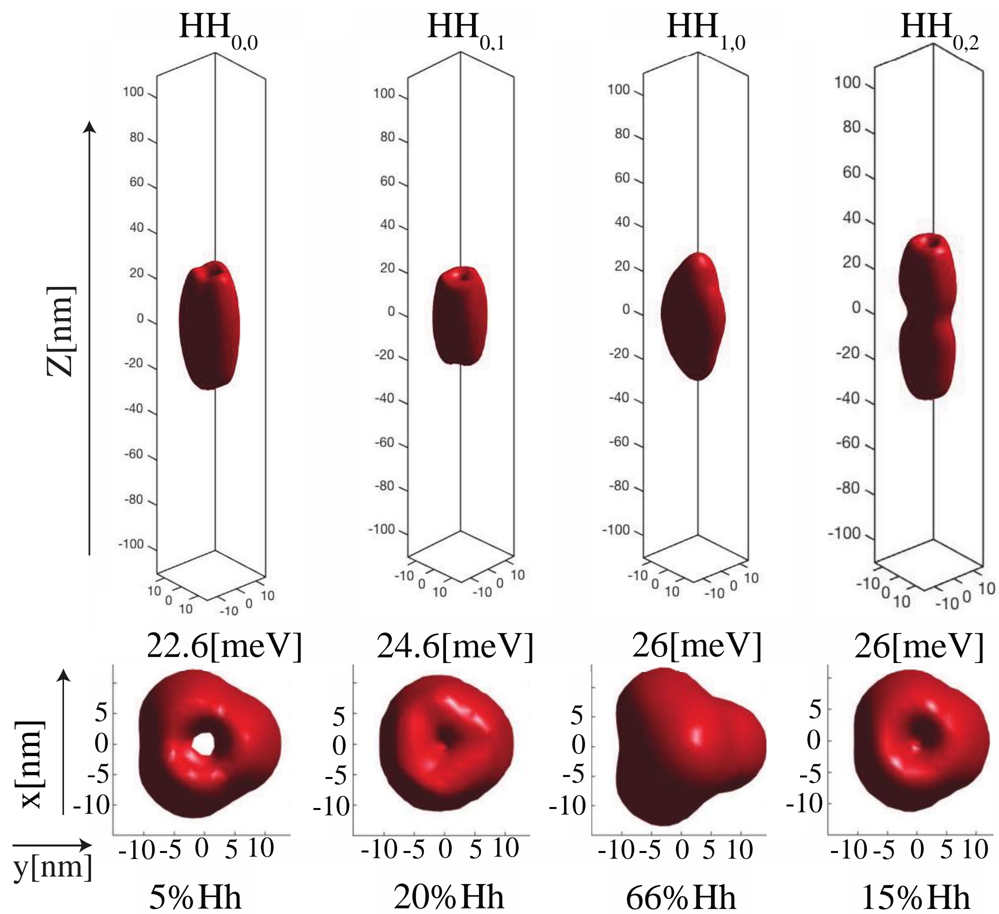

Figure C.4 Calculated heavy hole components of the wavefunctions (probability density isosurface) of the first 4 valence band states for the 120 nm parabolic QD. Upper part: 3D plot (front view); bottom part: top view, with the corresponding energy from GaAs VB edge and HH portion.

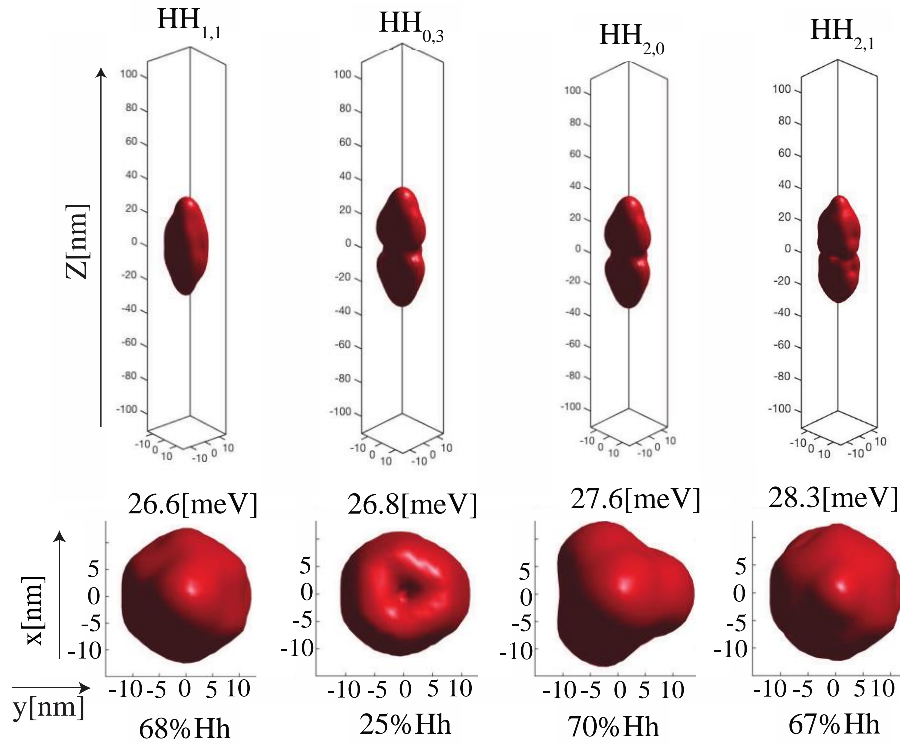

Figure C.5 Same as in Fig. C.4, for VB states 5-8.

240 nm parabolic quantum dot

Figures C.6 presents the modeled transition strength (overlaps between CB and VB wavefunctions) for the 240 nm PQD. Different colors presents different transition types: red for the HH component, blue for the LH component. The same with figure C.7 but for 480nm PQD.

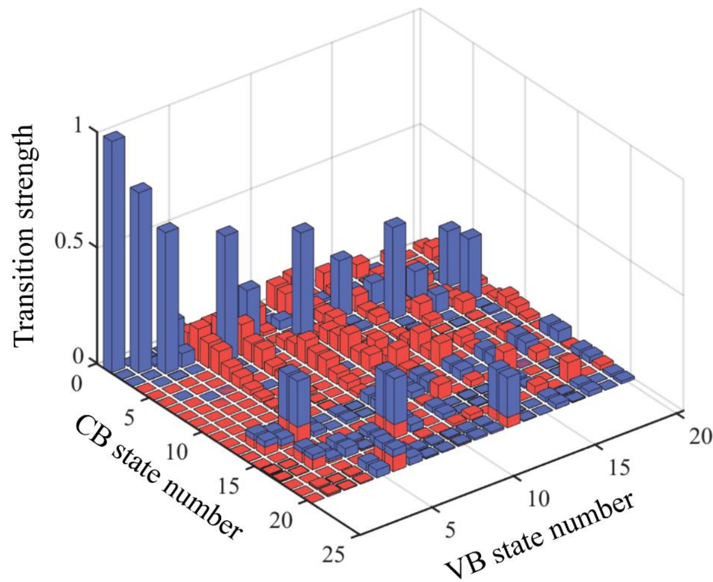

Figure C.6 Transition strength (normalized) of the optical transitions in the 240 nm PQD. Blue and red correspond to the LH and HH components.

480 nm parabolic quantum dot

Calculated wavefunctions and overlaps for the case of the 480nm-PQD are presented in figures C.7 and C.8.

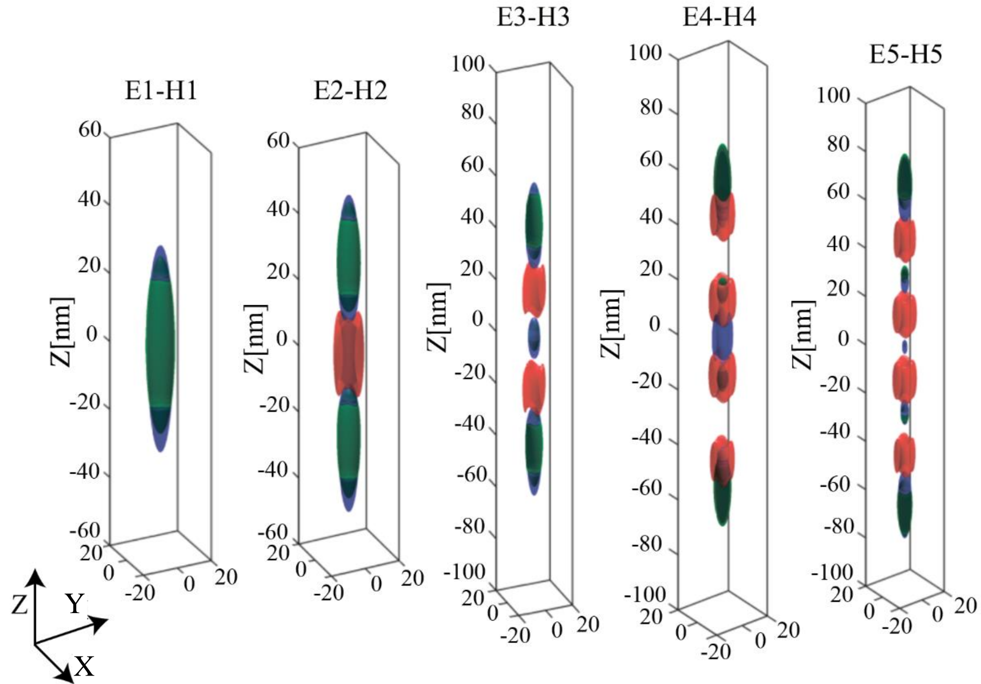

Figure C.7 CB and VB wave functions (Green CB, blue LH, red HH) of the first 5 main transitions in the 480 nm PQD.

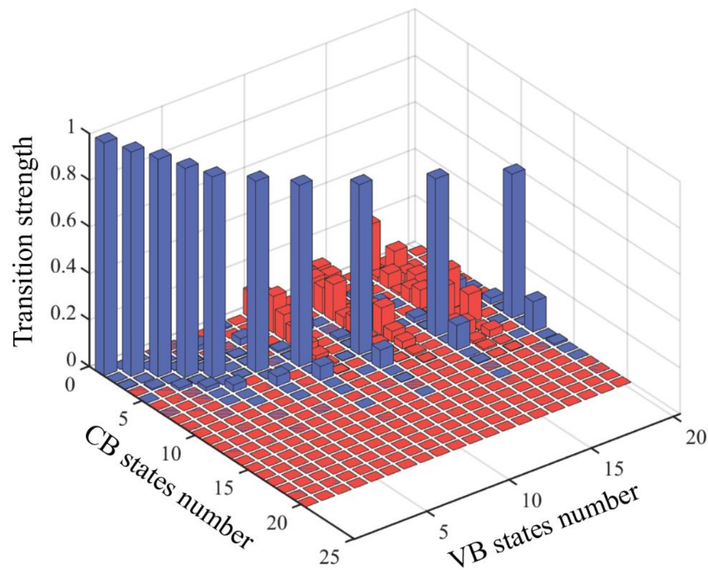

Figure C.8 The same as in figure C.6 for the 480 nm PQD.

References

[1] Louis De Broglie, "The wave nature of the electron," *Nobel Lect.*, 1929.

[2] M. S. I. Freestone, N. Meeks, "The lycurgus cup - a roman nanotechnology.," *Gold Bull. 40(4)270–277,* 2007.

[3] S. N. Gorb, *Functional Surfaces in Biology*, Little Str. University of Kiel, Germany, 2009.

[4] J. P. Vigneron *et al.*, "Optical structure and function of the white filamentary hair covering the edelweiss bracts," *Phys. Rev. E 71, 011906*, 2005.

[5] J. Bardeen, "Semiconductor research leading to the point contact transistor," *Nobel Lect.*, no. December 11, 1956.

[6] J. S. Kilby, "Miniaturized Electronic Circuits," *Pat. issued to Texas Instruments 1964*.

[7] G. E. Moore, "Cramming More Components onto Integrated Circuits," *Electronics*, pp. 114–117, 1965.

[8] M. Grundmann, *The Physics of Semiconductors*, vol. 13, no. 5. 1967.

[9] N. Holonyak, R. M. Kolbas, R. D. Dupuis, and P. D. Dapkus, "Quantum-Well Heterostructure Lasers," *IEEE J. Quantum Electron.*, vol. 16, no. 2, pp. 170–186, 1980.

[10] G. S. K. Knechtli, R.C., R.Y. Loo, "High-efficiency GaAs solar cells," *Electron Devices*, no. 5, 1984.

[11] A. A. Bergh and P. J. Dean, "Light-emitting diodes," *Proc. IEEE*, vol. 60, no. 2, pp. 156–223, 1972.

[12] A. Y. Cho and J. R. Arthur, "Molecular beam epitaxy," *Prog. Solid State Chem.*, vol. 10, no. PART 3, pp. 157–191, 1975.

[13] M. J. Ludowise, "Metalorganic chemical vapor deposition of III-V semiconductors," *J. Appl. Phys.*, vol. 58, no. 8, 1985.

[14] S.-W. Hla, "Scanning tunneling microscopy single atom/molecule manipulation and its application to nanoscience and technology," *J. Vac. Sci. Technol. B Microelectron. Nanom. Struct.*, vol. 23, no. 4, p. 1351, 2005.

[15] K. S. Novoselov *et al.*, "Electric Field Effect in Atomically Thin Carbon Films," *Science (80-.).*, vol. 306, no. 5696, pp. 666–669, 2004.

[16] A. H. C. Neto, F. Guinea, N. M. R. Peres, K. S. Novoselov, and A. K. Geim, "The electronic properties of graphene," *Rev. Mod. Phys.*, vol. 81, no. March, 2007.

[17] W. L. Barnes, A. Dereux, and T. W. Ebbesen, "Surface plasmon subwavelength optics,"

Nature, vol. 424, no. 6950, pp. 824–830, 2003.

[18] S. Kawata, Y. Inouye, and P. Verma, "Plasmonics for near-field nano-imaging and superlensing," *Nat. Photonics*, vol. 3, no. 7, pp. 388–394, 2009.

[19] M. L. Juan, M. Righini, and R. Quidant, "Plasmon nano-optical tweezers," *Nat. Photonics*, vol. 5, no. 6, pp. 349–356, 2011.

[20] X. Li, M. Soler, C. I. Özdemir, A. Belushkin, F. Yesilköy, and H. Altug, "Plasmonic nanohole array biosensor for label-free and real-time analysis of live cell secretion," *Lab Chip*, vol. 17, no. 13, pp. 2208–2217, 2017.

[21] K. J. Freedman, L. M. Otto, A. P. Ivanov, A. Barik, S. H. Oh, and J. B. Edel, "Nanopore sensing at ultra-low concentrations using single-molecule dielectrophoretic trapping," *Nat. Commun.*, vol. 7, pp. 1–9, 2016.

[22] S. J. P. Kress *et al.*, "A customizable class of colloidal-quantum-dot spasers and plasmonic amplifiers," *Sci. Adv.*, vol. 3, no. 9, pp. 1–8, 2017.

[23] P. Berini and I. De Leon, "Surface plasmon-polariton amplifiers and lasers," *Nat. Photonics*, vol. 6, no. 1, pp. 16–24, 2012.

[24] B. Ji *et al.*, "Non-blinking quantum dot with a plasmonic nanoshell resonator," *Nat. Nanotechnol.*, vol. 10, no. 2, pp. 170–175, 2015.

[25] G. M. Akselrod *et al.*, "Probing the mechanisms of large Purcell enhancement in plasmonic nanoantennas," *Nat. Photonics*, vol. 8, no. 11, pp. 835–840, 2014.

[26] T. Schumacher, K. Kratzer, D. Molnar, M. Hentschel, H. Giessen, and M. Lippitz, "Nanoantenna-enhanced ultrafast nonlinear spectroscopy of a single gold nanoparticle," *Nat. Commun.*, vol. 2, no. 1, pp. 333–335, 2011.

[27] D. Yoo *et al.*, "Low-Power Optical Trapping of Nanoparticles and Proteins with Resonant Coaxial Nanoaperture using 10 nm gap Low-Power Optical Trapping of Nanoparticles and Proteins with Resonant Coaxial Nanoaperture using 10 nm gap," *Nano Lett.*, vol. 18 (6), pp. 3637–3642, 2018.

[28] D. Y. Lei, K. Appavoo, F. Ligmajer, Y. Sonnefraud, R. F. Haglund, and S. A. Maier, "Optically-Triggered Nanoscale Memory Effect in a Hybrid Plasmonic-Phase Changing Nanostructure," *ACS Photonics*, vol. 2, no. 9, pp. 1306–1313, 2015.

[29] H. A. Atwater and A. Polman, "Plasmonics for improved photovoltaic devices," *Nat. Mater.*, vol. 9, no. 3, pp. 205–213, 2010.

[30] The Royal Swedish Academy of Sciences, "The Nobel Prize in Physics 2018," *nobelprize.org*, 2018.

[31] T. D. Ladd, F. Jelezko, R. Laflamme, Y. Nakamura, C. Monroe, and J. L. O 'brien, "Quantum computers," *Nature*, vol. 464, 2010.

[32] A. D. Córcoles *et al.*, "Demonstration of a quantum error detection code using a square

lattice of four superconducting qubits," *Nat. Commun.*, vol. 6, 2015.

[33] H. Bernien *et al.*, "Probing many-body dynamics on a 51-atom quantum simulator," *Nature*, vol. 551, no. 7682, pp. 579–584, 2017.

[34] N. Gisin and R. Thew, "Quantum communication," *Nat Phot.*, vol. 1, no. 3, pp. 165–171, 2007.

[35] L. Kim, P. O. Anikeeva, S. A. Coe-sullivan, J. S. Steckel, M. G. Bawendi, and V. Bulovic, "Contact Printing of Quantum Dot Light- Emitting Devices Contact Printing of Quantum Dot Light-Emitting Devices," *Nano Lett.*, vol. 8, no. 12, pp. 4513–4517, 2008.

[36] M. G. B. Yasuhiro Shirasaki, Geoffrey J. Supran and and V. B. Bulović, "Colloidal QDs for light-emitting applications," *Nat. PHOTONICS www.nature.com/naturephotonics*, vol. 7, 2013.

[37] T. H. Kim *et al.*, "Full-colour quantum dot displays fabricated by transfer printing," *Nat. Photonics*, vol. 5, no. 3, pp. 176–182, 2011.

[38] B. Ellis *et al.*, "Ultralow-threshold electrically pumped quantum-dot photonic-crystal nanocavity laser," *Nat. Photonics*, vol. 5, no. 5, pp. 297–300, 2011.

[39] S. Chen *et al.*, "Electrically pumped continuous-wave III-V quantum dot lasers on silicon," *Nat. Photonics*, vol. 10, no. 5, pp. 307–311, 2016.

[40] I. L. Medintz, H. T. Uyeda, E. R. Goldman, and H. Mattoussi, "Quantum dot bioconjugates for imaging, labelling and sensing," *Nat. Mater.*, vol. 4, no. 6, pp. 435–446, 2005.

[41] J. Wu, S. Chen, A. Seeds, and H. Liu, "Quantum dot optoelectronic devices: Lasers, photodetectors and solar cells," *J. Phys. D. Appl. Phys.*, vol. 48, no. 36, 2015.

[42] C. Kitell, *Introduction to Solid State Physics*. 1986.

[43] M. Simone, "Fabrication and characterization of planar Gunn diodes for Monolithic Microwave Integrated Circuits .," *PhG thesis Forschungzentrum Jülich*, p. 62, 2005.

[44] A. R. Degheidy and E. B. Elkenany, "Temperature and hydrostatic pressure dependence of the electronic structure of AlxGa1-xAs alloys," *Mater. Sci. Semicond. Process.*, vol. 15, no. 5, pp. 505–515, 2012.

[45] P. W. Webb, G. T. Wright, S. Brojdo, T. J. Riley, and G. T. Wright, "The silicon-germanium n-p heterojunction," Br. J. Appl. Phys., 1964.

[46] Z. I. Alferov, "Electroluminescence of heavily-doped heterojunctions pAlxGa1-xAs-nGaAs," J. Lumin., vol. 2, pp. 869–884, 1970.

[47] Y. Arakawa and H. Sakaki, "Multidimensional quantum well laser and temperature dependence of its threshold current," *Appl. Phys. Lett.*, vol. 40, no. 11, pp. 939–941, 1982.

[48] S. Nakamura, M. Senoh, N. Iwasa, and S. I. Nagahama, "High-power InGaN single-quantum-well-structure blue and violet light-emitting diodes," *Appl. Phys. Lett.*, vol. 67, no.

1995, p. 1868, 1995.

[49] K. W. J. Barnham *et al.*, "Quantum well solar cells," *Phys. E Low-Dimensional Syst. Nanostructures*, vol. 14, no. 1–2, pp. 27–36, 2002.

[50] Z. I. Alferov, "Nobel lecture: The double heterostructure concept and its applications in physics, electronics, and technology," *Rev. Mod. Phys.*, vol. 73, no. 3, pp. 767–782, 2001.

[51] A. Lyasota, "Interaction between site-controlled quantum dot systems and photonic cavity structures," *PhD thesis, EPFL*, 2017.

[52] B. F. Levine, "Quantum-well infrared photodetectors," *J. Appl. Phys.*, vol. 74, no. 8, 1993.

[53] X.-L. Wang and V. Voliotis, "Epitaxial growth and optical properties of semiconductor quantum wires," *J. Appl. Phys. Appl. Phys. Rev.*, vol. 99, no. 101, 2006.

[54] A. R. Goñi, L. N. Pfeiffer, K. W. West, A. Pinczuk, H. U. Baranger, and H. L. Stormer, "Observation of quantum wire formation at intersecting quantum wells," *Appl. Phys. Lett.*, vol. 61, no. 16, pp. 1956–1958, 1992.

[55] H. Akiyama, "One-dimensional excitons in GaAs quantum wires," *J. Phys. Condens. Matter*, vol. 10, no. 14, pp. 3095–3139, 1998.

[56] J. Szeszko, "Quantum Wire - Quantum Dot Systems Grown in Inverted Pyramids," *PhD thesis, EPFL*, vol. 5760, 2013.

[57] H. J. Joyce *et al.*, "III–V semiconductor nanowires for optoelectronic device applications," *Prog. Quantum Electron.*, vol. 35, pp. 23–75, 2011.

[58] H. J. Fan, P. Werner, and M. Zacharias, "Semiconductor nanowires: From self-organization to patterned growth," *Small*, vol. 2, no. 6, pp. 700–717, 2006.

[59] B. Mandl *et al.*, "Growth mechanism of self-catalyzed group III-V nanowires," *Nano Lett.*, vol. 10, no. 11, pp. 4443–4449, 2010.

[60] P. Mohan, J. Motohisa, and T. Fukui, "Controlled growth of highly uniform, axial/radial direction-defined, individually addressable InP nanowire arrays," *Nanotechnology*, vol. 16, no. 12, pp. 2903–2907, 2005.

[61] L. Schubert *et al.*, "Silicon nanowhiskers grown on 〈111〉 Si substrates by molecular-beam epitaxy," *Appl. Phys. Lett.*, vol. 84, no. 24, pp. 4968–4970, 2004.

[62] C. Zhang, X. Miao, P. K. Mohseni, W. Choi, and X. Li, "Site-controlled VLS growth of planar nanowires: Yield and mechanism," *Nano Lett.*, vol. 14, no. 12, pp. 6836–6841, 2014.

[63] R. S. Wagner and W. C. Ellis, "Vapor-liquid-solid mechanism of single crystal growth," *Appl. Phys. Lett.*, vol. 4, no. 5, pp. 89–90, 1964.

[64] M. S. Gudiksen, J. Wang, and C. M. Lieber, "Size-dependent photoluminescence from single indium phosphide nanowires," *J. Phys. Chem. B*, vol. 106, no. 16, pp. 4036–4039, 2002.

[65] K. Tomioka, J. Motohisa, S. Hara, K. Hiruma, and T. Fukui, “GaAs/AlGaAs core multishell nanowire-based light-emitting diodes on Si,” *Nano Lett.*, vol. 10, no. 5, pp. 1639–1644, 2010.

[66] R. Yan, D. Gargas, and P. Yang, “Nanowire photonics,” *Nat. Photonics*, vol. 3, 2009.

[67] J. Wang, M. S. Gudiksen, X. Duan, Y. Cui, and C. M. Lieber, “Highly polarized photoluminescence and photodetection from single indium phosphide nanowires,” *Science (80-.).*, vol. 293, no. 5534, pp. 1455–1457, 2001.

[68] S. Nadj-Perge, S. M. Frolov, E. P. A. M. Bakkers, and L. P. Kouwenhoven, “Spin-orbit qubit in a semiconductor nanowire,” *Nature*, vol. 468, no. 7327, pp. 1084–1087, 2010.

[69] Z. Yang *et al.*, “Broadly defining lasing wavelengths in single bandgap-graded semiconductor nanowires,” *Nano Lett.*, vol. 14, no. 6, pp. 3153–3159, 2014.

[70] M. Walther, E. Kapon, J. Christen, D. M. Hwang, and R. Bhat, “Carrier capture and quantum confinement in GaAs/AlGaAs quantum wire lasers grown on V-grooved substrates,” *Appl. Phys. Lett.*, vol. 60, no. 5, pp. 521–523, 1992.

[71] R. Nötzel *et al.*, “Micro-photoluminescence study at room temperature of sidewall quantum wires formed on patterned GaAs (311)A substrates by molecular beam epitaxy,” *Japanese J. Appl. Physics, Part 2 Lett.*, vol. 35, no. 3 A, 1996.

[72] T. Muranaka, S. Kasai, C. Jiang, and H. Hasegawa, “Control of morphology and wire width in InGaAs ridge quantum wires grown by atomic hydrogen-assisted selective molecular beam epitaxy,” *Phys. E Low-Dimensional Syst. Nanostructures*, vol. 13, no. 2–4, pp. 1185–1189, 2002.

[73] R. Schirhagl, K. Chang, M. Loretz, and C. L. Degen, “Nitrogen-Vacancy Centers in Diamond: Nanoscale Sensors for Physics and Biology,” *Annu. Rev. Phys. Chem.*, vol. 65, no. 1, pp. 83–105, 2014.

[74] P. V. Kamat, “Quantum dot solar cells. The next big thing in photovoltaics,” *J. Phys. Chem. Lett.*, vol. 4, no. 6, pp. 908–918, 2013.

[75] R. Gill, M. Zayats, and I. Willner, “Semiconductor quantum dots for bioanalysis,” *Angew. Chemie - Int. Ed.*, vol. 47, no. 40, pp. 7602–7625, 2008.

[76] M. J. Holmes, K. Choi, S. Kako, M. Arita, and Y. Arakawa, “Room-Temperature Triggered Single Photon Emission from a III- Nitride Site-Controlled Nanowire Quantum Dot,” *Nano Lett.*, vol. 14 (2), pp. 982–986, 2014.

[77] P. Lodahl, S. Mahmoodian, and S. Stobbe, “Interfacing single photons and single quantum dots with photonic nanostructures,” *Rev. Mod. Phys.*, vol. 87, no. 2, pp. 347–400, 2015.

[78] M. Pelton *et al.*, “Efficient Source of Single Photons: A Single Quantum Dot in a Micropost Microcavity,” *Phys. Rev. Lett.*, no. 233602, 2002.

[79] V. Wood and V. Bulović, “Colloidal quantum dot light-emitting devices,” *Nano Rev.*, vol. 1, no. 1, p. 5202, 2010.

[80] P. Gladyshev, V. Kouznetsov, C. M. Bonilla, and S. Arulmani, “Colloidal quantum dots: synthesis, properties and applications,” *Russ. Chem. Rev. Rev.*, 2016.

[81] X. Brokmann, E. Giacobino, M. Dahan, and J. P. Hermier, “Highly efficient triggered emission of single photons by colloidal CdSe/ZnS nanocrystals,” *Appl. Phys. Lett.*, vol. 85, no. 5, pp. 712–714, 2004.

[82] D. Gammon, E. S. Snow, B. V Shanabrook, D. S. Katzer, and D. Park, “Linewidths in the Gallium Arsenide Homogeneous Optical Spectrum Single Quantum Dot,” *Science (80-.).*, vol. 273, no. July, pp. 87–90, 1996.

[83] A. Huggenberger *et al.*, “Narrow spectral linewidth from single site-controlled In(Ga)As quantum dots with high uniformity,” *Appl. Phys. Lett.*, vol. 98, no. 13, pp. 2009–2012, 2011.

[84] W. Wegscheider, G. Schedelbeck, G. Abstreiter, M. Rother, and M. Bichler, “Atomically Precise GaAs AlGaAs Quantum Dots Fabricated by Twofold Cleaved Edge Overgrowth,” *Phys. Rev. Lett.*, vol. 79, 1997.

[85] M. E. Reimer *et al.*, “Bright single-photon sources in bottom-up tailored nanowires,” *Nat. Commun.*, 2012.

[86] G. B. J.-Y. Marzin, J.-M. Gerard, A. Izrael, and D. Barrier, “Photoluminescence ofSingle InAs Quantum Dots Obtained by Self-Organized Growth on GaAs on GaAs,” *Phys. Rev. Lett.*, vol. 73, 1994.

[87] E. Stock *et al.*, “Single-photon emission from InGaAs quantum dots grown on (111) GaAs,” *Appl. Phys. Lett.*, vol. 96, no. 9, pp. 1–4, 2010.

[88] S. Reitzenstein and A. Forchel, “Quantum dot micropillars,” *J. Phys. D. Appl. Phys.*, vol. 43, no. 3, 2010.

[89] A. Kiraz, C. Reese, B. Gayral, L. Zhang, and W. V Schoenfeld, “Cavity-quantum electrodynamics with quantum dots,” *J. Opt. B*, 2003.

[90] M. T. Rakher, N. G. Stoltz, L. A. Coldren, P. M. Petroff, and D. Bouwmeester, “Polarization-switchable single photon source using the Stark effect,” *Appl. Phys. Lett.*, vol. 93, no. 9, pp. 2008–2010, 2008.

[91] K. Hennessy *et al.*, “Quantum nature of a strongly coupled single quantum dot-cavity system,” *Nature*, vol. 445, no. 7130, pp. 896–899, 2007.

[92] S. Reitzenstein *et al.*, “Quantum dot micropillar lasers,” *2009 Asia Commun. Photonics Conf. Exhib.*, vol. 2009–Suppl, pp. 1–10, 2009.

[93] E. Peter *et al.*, “Exciton-photon strong-coupling regime for a single quantum dot embedded in a microcavity,” *Phys. Rev. Lett.*, vol. 95, no. 6, pp. 1–4, 2005.

[94] A. Schwagmann *et al.*, “On-chip single photon emission from an integrated semiconductor quantum dot into a photonic crystal waveguide,” *Appl. Phys. Lett.*, vol. 99, no. 26, 2011.

[95] A. Javadi *et al.*, “Single-photon non-linear optics with a quantum dot in a waveguide,” *Nat.*

Commun., vol. 6, pp. 6–10, 2015.

[96] Y. H. Huo *et al.*, “A light-hole exciton in a quantum dot,” *Nat. Phys.*, vol. 10, no. 1, pp. 46–51, 2013.

[97] K. D. Jöns *et al.*, “Triggered indistinguishable single photons with narrow line widths from site-controlled quantum dots,” *Nano Lett.*, vol. 13, no. 1, pp. 126–130, 2013.

[98] A. Mohan *et al.*, “Record-low inhomogeneous broadening of site-controlled quantum dots for nanophotonics,” *Small*, vol. 6, no. 12, pp. 1268–1272, 2010.

[99] G. Schedelbeck, W. Wegscheider, M. Bichler, and G. Abstreiter, “Coupled Quantum Dots Fabricated by Cleaved Edge Overgrowth : From Artificial Atoms to Molecules,” *Science (80-.).*, vol. 278, pp. 1792–1796, 1997.

[100] M. T. Björ *et al.*, “One-dimensional Steeplechase for Electrons Realized,” *Nano Lett.*, vol. 2, no. 2, pp. 87–89, 2002.

[101] J. W. Mark S. Gudiksen, Lincoln J. Lauhon and David C. Smith & Charles M. Lieber, “Growth of nanowire superlattice structures for nanoscale photonics and electronics,” *Lett. to Nat.*, 2002.

[102] M. Heiss *et al.*, “Self-assembled quantum dots in a nanowire system for quantum photonics,” *Nat. Mater.*, vol. 12, no. 5, pp. 439–444, 2013.

[103] D. Alonso-Álvarez *et al.*, “Strain balanced quantum posts,” *Cit. Appl. Phys. Lett*, vol. 98, 2011.

[104] B. Dwir, K. Leifer, and E. Kapon, “Mixed dimensionality quantum heterostructures grown in axially modulated V grooves,” *Phys. Rev. B*, vol. 2121, no. 73, 2003.

[105] R. Songmuang, S. Kiravittaya, and O. G. Schmidt, “Formation of lateral quantum dot molecules around self-assembled nanoholes,” *Appl. Phys. Lett.*, vol. 82, no. 10, pp. 2892–113120, 2003.

[106] J. Bao *et al.*, “Optical Properties of Rotationally Twinned Nanowire Superlattices,” *Nano Lett.*, vol. 8, pp. 836–841, 2008.

[107] D. Spirkoska *et al.*, “Structural and optical properties of high quality zinc-blende/wurtzite GaAs nanowire heterostructures,” *Phys. Rev. B - Condens. Matter Mater. Phys.*, vol. 80, no. 24, pp. 1–9, 2009.

[108] K. A. Dick *et al.*, “Control of III-V nanowire crystal structure by growth parameter tuning,” *Semicond. Sci. Technol.*, vol. 25, no. 2, 2010.

[109] G. Biasiol, “Formation Mechanisms of Low-Dimensional Semiconductor Nanostructures Grown by OMCVD on Nonplanar Substrates,” *PhD thesis, EPFL*, vol. 1859, 1998.

[110] Y. Ducommun, “Semiconductor quntum dots grown in inverted pyramids.” PhD thesis, EPFL, 2001.

[111] E. Pelucchi *et al.*, “Mechanisms of quantum dot energy engineering by metalorganic vapor phase epitaxy on patterned nonplanar substrates,” *Nano Lett.*, vol. 7, no. 5, pp. 1282–1285, 2007.

[112] A. Surrente, R. Carron, P. Gallo, A. Rudra, B. Dwir, and E. Kapon, “Self-formation of hexagonal nanotemplates for growth of pyramidal quantum dots by metalorganic vapor phase epitaxy on patterned substrates,” *Nano Res.*, vol. 9, no. 11, pp. 3279–3290, 2016.

[113] Q. Zhu, “Semiconductor vertical quantum structures self-formed in inverted pyramids,” *PhD thesis, EPFL*, vol. 4145, 2008.

[114] Q. Zhu, E. Pelucchi, S. Dalessi, K. Leiter, M. A. Dupertuis, and E. Kapon, “Alloy segregation, quantum confinement, and carrier capture in self-ordered pyramidal quantum wires,” *Nano Lett.*, vol. 6, no. 5, pp. 1036–1041, 2006.

[115] Q. Zhu, K. F. Karlsson, E. Pelucchi, and E. Kapon, “Transition from two-dimensional to three-dimensional quantum confinement in semiconductor quantum wires/quantum dots,” *Nano Lett.*, vol. 7, no. 8, pp. 2227–2233, 2007.

[116] A. Hartmann, Y. Ducommun, L. Loubies, K. Leifer, and E. Kapon, “Structure and photoluminescence of single AlGaAs/GaAs quantum dots grown in inverted tetrahedral pyramids,” *Appl. Phys. Lett.*, vol. 73, no. 16, pp. 2322–2324, 1998.

[117] M. Felici, P. Gallo, A. Mohan, B. Dwir, A. Rudra, and E. Kapon, “Site-controlled InGaAs quantum dots with tunable emission energy,” *Small*, vol. 5, no. 8, pp. 938–943, 2009.

[118] V. Troncale, K. F. Karlsson, E. Pelucchi, A. Rudra, and E. Kapon, “Control of valence band states in pyramidal quantum dot-in-dot semiconductor heterostructures,” *Appl. Phys. Lett.*, vol. 91, no. 24, pp. 45–48, 2007.

[119] V. Troncale, “Tailored-Potential Pyramidal Quantum Dot Heterostructures,” *PhD thesis, EPFL*, vol. 4786, 2010.

[120] Q. Zhu *et al.*, “Hybridization of electron and hole states in semiconductor quantum-dot molecules,” *Small*, vol. 5, no. 3, pp. 329–335, 2009.

[121] J. Szeszko *et al.*, “Exciton confinement and trapping dynamics in double-graded-bandgap quantum nanowires,” *Appl. Phys. Lett.*, vol. 100, no. 21, pp. 0–4, 2012.

[122] J. Szeszko, V. V. Belykh, A. Rudra, N. N. Sibeldin, and E. Kapon, “Exciton localization and drift in tailored-potential quantum nanowires,” *Appl. Phys. Lett.*, vol. 104, no. 26, pp. 1–5, 2014.

[123] I. V. Kulkova *et al.*, “Emission wavelength control of ordered arrays of InGaAs/GaAs quantum dots,” *J. Cryst. Growth*, vol. 464, no. November 2016, pp. 69–74, 2017.

[124] E. Kapon *et al.*, “Site- And energy-controlled pyramidal quantum dot heterostructures,” *Phys. E Low-Dimensional Syst. Nanostructures*, vol. 25, no. 2–3 SPEC.ISS., pp. 288–297, 2004.

[125] Ć. Milan, “Cavity quantum electrodynamics with systems of site-controlled quantum dots

and photonic crystal cavities," *PhD thesis, EPFL*, vol. 5957, 2013.

[126] P. Gallo *et al.*, "Integration of site-controlled pyramidal quantum dots and photonic crystal membrane cavities," *Appl. Phys. Lett.*, vol. 92, no. 263101–1, 2008.

[127] M. Davanco *et al.*, "Heterogeneous integration for on-chip quantum photonic circuits with single quantum dot devices," *Nat. Commun.*, 2017.

[128] C. P. Dietrich, A. Fiore, M. G. Thompson, M. Kamp, and S. Ofling, "GaAs integrated quantum photonics: Towards compact and multi-functional quantum photonic integrated circuits," *Laser Photon. Rev.*, 2016.

[129] J.-H. Kim, S. Aghaeimeibodi, C. J. K. Richardson, R. P. Leavitt, D. Englund, and E. Waks, "Hybrid Integration of Solid-State Quantum Emitters on a Silicon Photonic Chip," *Nano Lett.*, vol. 17, pp. 7394–7400, 2017.

[130] Shun Lien Chuang, "Physics of Optoelectronic Devices," 1995.

[131] P. O. Löwdin, "A note on the quantum-mechanical perturbation theory," *J. Chem. Phys.*, vol. 19, no. 11, pp. 1396–1401, 1951.

[132] J. M. Luttinger, "Quantum Theory of Cyclotron Resonance in Semiconductors : General Theory," *Phys. Rev.*, vol. 102, no. 1030, 1956.

[133] J. M. Luttinger and W. Kohn, "Motion of Electrons and Holes in Perturbed Periodic Fields," *Phys. Rev.*, vol. 97, 1955.

[134] B.K. Ridley, *Quantum processes in semiconductors*, 4th ed. 1999.

[135] E. O. Kane, "Band structure of indium antimonide," *J. Phys. Chem. Solids*, vol. 1, no. 4, pp. 249–261, 1957.

[136] J. H. Davies, "The Physics of Low-Dimensional Semiconductors." Cambridge University Press, 1998.

[137] I. Vurgaftman, J. R. Meyer, and L. R. Ram-Mohan, "Band parameters for III-V compound semiconductors and their alloys," *J. Appl. Phys.*, vol. 89, no. 11 I, pp. 5815–5875, 2001.

[138] Y.-C. Chang and J. N. Schulman, "Interband optical transitions in GaAs-Ga1-xAlxAs and InAs-GaSb superlattices," *Phys. Rev. B*, vol. 31, no. 4, pp. 2069–2079, 1985.

[139] T. B. Bahder, "Eight-band kp model of strained zinc-blende crystals," *Phys. Rev. B*, vol. 41, no. 17, pp. 11992–12001, 1990.

[140] G. Goldoni, F. Rossi, E. Molinari, and A. Fasolino, "Band structure and optical anisotropy in V-shaped and T-shaped semiconductor quantum wires," *Phys. Rev. B*, vol. 55, no. 11, p. 7110, 1997.

[141] G. Fishman, "Hole subbands in strained quantum-well semiconductors in [hhk] directions," *PRB*, vol. 52, 1995.

[142] D. Gershoni, C. H. Henry, and G. A. Baraff, “Calculating the Optical Properties of Multidimensional Heterostructures: Application to the Modeling of Quaternary Quantum Well Lasers,” *IEEE J. Quantum Electron.*, vol. 29, no. 9, pp. 2433–2450, 1993.

[143] L.D. Landau E.M Lifshitz, “Quantum Mechanics Non-Relativistic Theory.” Institute of Physical Problems USSR, Academy of Sciences, 1965.

[144] G. H. Wannier, “The structure of electronic excitation levels in insulating crystals,” *Phys. Rev.*, vol. 52, no. 3, pp. 191–197, 1937.

[145] X. F. He, “Excitons in anisotropic solids: The model of fractional-dimensional space,” *Phys. Rev. B*, vol. 43, no. 3, pp. 2063–2069, 1991.

[146] J. C. Maan, G. Belle, A. Fasolino, M. Altarelli, and K. Ploog, “Magneto-optical determination of exciton binding energy in GaAs-Ga1-xAlxAs quantum wells,” *Phys. Rev. B*, vol. 30, no. 4, pp. 2253–2256, 1984.

[147] B. A. Vojak, N. Holonyak, W. D. Laidig, K. Hess, J. J. Coleman, and P. D. Dapkus, “The exciton in recombination in AlxGa1−xAs-GaAs quantum-well heterostructures,” *Solid State Commun.*, vol. 35, no. 6, pp. 477–481, 1980.

[148] Emil S. Koteles and J. Y. Chi, “Experimental exciton binding energies in GaAs/AlxGa1-x Asquantum wells as a function of well width,” *Phys. Rev. 8*, vol. 37, no. 11, 1988.

[149] K. F. Karlsson, M.-A. Dupertuis, H. Weman, and E. Kapon, “Fractional-dimensional excitonic absorption theory applied to V -groove quantum wires,” *Phys. Rev. B*, vol. 70, no. 15, p. 153306, 2004.

[150] T. Someya, H. Akiyama, and H. Sakaki, “Enhanced binding energy of one-dimensional excitons in quantum wires,” *Phys. Rev. Lett.*, vol. 76, no. 16, pp. 2965–2968, 1996.

[151] R. J. Warburton *et al.*, “Coulomb interactions in small charge-tunable quantum dots: A simple model,” *Phys. Rev. B*, vol. 58, no. 24, pp. 16221–16231, 1998.

[152] A. Hartmann, Y. Ducommun, E. Kapon, U. Hohenester, and E. Molinari, “Few-particle effects in semiconductor quantum dots: observation of multicharged excitons,” *Phys. Rev. Lett.*, vol. 84, no. 24, pp. 5648–5651, 2000.

[153] R. J. Warburton *et al.*, “Optical emission from a charge-tunable quantum ring,” *Nature*, vol. 405, no. 6789, pp. 926–929, 2000.

[154] A. Schliwa, M. Winkelnkemper, and D. Bimberg, “Few-particle energies versus geometry and composition of In(x)Ga(1-x)As/GaAs self-organized quantum dots,” *Phys. Rev. B - Condens. Matter Mater. Phys.*, vol. 79, no. 7, pp. 1–14, 2009.

[155] C. Jarlov, P. Gallo, M. Calic, B. Dwir, A. Rudra, and E. Kapon, “Bound and anti-bound biexciton in site-controlled pyramidal GaInAs/GaAs quantum dots,” *Appl. Phys. Lett.*, vol. 101, no. 19, 2012.

[156] G. Biasiol and E. Kapon, “Mechanisms of self-ordering of quantum nanostructures grown on nonplanar surfaces,” *Phys. Rev. Lett.*, vol. 81, no. 14, pp. 2962–2965, 1998.

[157] Q. Zhu, E. Pelucchi, S. Dalessi, K. Leifer, M.-A. Dupertuis, and E. Kapon, "Alloy Segregation, Quantum Confinement, and Carrier Capture in Self-Ordered Pyramidal Quantum Wires," *Nano Lett.*, vol. 6, no. 5, pp. 1036–1041, 2006.

[158] R. F. Kopf, M. H. Herman, M. L. Schnoes, A. P. Perley, G. Livescu, and M. Ohring, "Band offset determination in analog graded parabolic and triangular quantum wells of GaAs/AlGaAs and GaInAs/AlInAs," *J. Appl. Phys.*, vol. 71, no. 10, pp. 5004–5011, 1992.

[159] W. Langbein, H. Gislason, and J. M. Hvam, "Optimization of the confinement energy of quantum-wire states in T-shaped GaAs/Al(x)Ga(1-x)As structures," *Phys. Rev. B*, vol. 54, no. 20, pp. 14595–14603, 1996.

[160] S. Dalessi and M. A. Dupertuis, "Maximal symmetrization and reduction of fields: Application to wave functions in solid-state nanostructures," *Phys. Rev. B - Condens. Matter Mater. Phys.*, vol. 81, no. 12, pp. 1–33, 2010.

[161] V. Dimastrodonato, E. Pelucchi, and D. D. Vvedensky, "Self-limiting evolution of seeded quantum wires and dots on patterned substrates," *Phys. Rev. Lett.*, vol. 108, no. 25, pp. 1–5, 2012.

[162] M. Lazarev, J. Szeszko, A. Rudra, K. F. Karlsson, and E. Kapon, "Parabolic tailored-potential quantum-wires grown in inverted pyramids," *J. Cryst. Growth*, vol. 414, pp. 196–199, 2015.

[163] K. F. Karlsson *et al.*, "Optical polarization anisotropy and hole states in pyramidal quantum dots," *Appl. Phys. Lett.*, vol. 89, no. 25, 2006.

[164] A. Hartmann, Y. Ducommun, K. Leifer, and E. Kapon, "Structure and optical properties of semiconductor quantum nanostructures self-formed in inverted tetrahedral pyramids," *J. Phys. Condens. Matter*, vol. 11, no. 31, pp. 5901–5915, 1999.

[165] A. A. Dobrovolsky, V. V Lemanov, A. B. Sherman, and V. I. Kozub, "Dielectric constant of semi-insulating gallium arsenide," *Electron. Lett.*, vol. 16, no. 7, pp. 244–245, 1980.

[166] Q. Zhu *et al.*, "Pyramidal GaAs/ Alz Ga1-z As quantum wire/dot systems with controlled heterostructure potential," *Phys. Rev. B - Condens. Matter Mater. Phys.*, vol. 82, no. 16, pp. 1–13, 2010.

[167] J. Szeszko, V. V. Belykh, A. Rudra, B. Dwir, N. N. Sibeldin, and E. Kapon, "Multiexciton dynamics in tailored band-gap quasi-one-dimensional systems," *Phys. Rev. B - Condens. Matter Mater. Phys.*, vol. 91, no. 24, pp. 1–15, 2015.

[168] I. Söllner *et al.*, "Deterministic photon-emitter coupling in chiral photonic circuits," *Nat. Nanotechnol.*, vol. 10, no. 9, pp. 775–778, 2015.

[169] A. Lyasota *et al.*, "Integration of multiple site-controlled pyramidal quantum dot systems with photonic-crystal membrane cavities," *J. Cryst. Growth*, vol. 414, pp. 192–195, 2015.

[170] P. W. Fry *et al.*, "Inverted Electron-Hole Alignment in InAs-GaAs Self-Assembled Quantum Dots," *Phys. Rev. Lett.*, vol. 84, no. 4, pp. 733–736, 2000.

[171] A. J. Bennett *et al.*, "Electric-field-induced coherent coupling of the exciton states in a single quantum dot," *Nat. Phys.*, vol. 6, no. 12, pp. 947–950, 2010.

[172] J. Martín-, "Strain-tuning of the optical properties of semiconductor nanomaterials by integration onto piezoelectric actuators," *Semicond. Sci. Technol*, vol. 33, 2018.

[173] S. G. Carter *et al.*, "Quantum control of a spin qubit coupled to a photonic crystal cavity," *Nat. Photonics*, vol. 7, no. 4, pp. 329–334, 2013.

[174] J. Zhang *et al.*, "Single Photons On-Demand from Light-Hole Excitons in Strain-Engineered Quantum Dots," *Nano Lett.*, 2014.

[175] Q. Zhu, F. Karlsson, A. Rudra, E. Pelucchi, and E. Kapon, "Quantum dot molecules realized with modulated quantum wire heterostructrues," *Phys. E Low-Dimensional Syst. Nanostructures*, vol. 40, no. 6, pp. 1815–1818, 2008.

[176] M. F. Doty *et al.*, "Antibonding ground states in InAs quantum-dot molecules," *Phys. Rev. Lett.*, vol. 102, no. 4, pp. 1–4, 2009.

[177] W. Wegscheider, G. Schedelbeck, M. Bichler, and G. Abstreiter, "Atomically precise quantum dots fabricated by two-fold cleaved edge overgrowth: From artificial atoms to molecules," *Phys. E Low-Dimensional Syst. Nanostructures*, vol. 3, no. 1–3, pp. 103–111, 1998.

[178] R. Dingle and etc., "Direct Observation of Superlattice Formation in a Semiconductor Heterostructure," *Phys. Rev. Lett.*, vol. 34, no. 21, pp. 1327–1330, 1975.

[179] E. E. Mendez and etc., "Stark Localization in GaAs-GaAlAs Superlattices under an Electric Field," *Phys. Rev. Lett.*, vol. 60, no. 23, pp. 2426–2429, 2008.

List of publications

M. Lazarev, J. Szeszko, A. Rudra, K.F. Karlsson and E. Kapon "Parabolic Tailored-Potential Quantum-Wires Grown in Inverted Pyramids" Journal of Crystal Growth" (2014)

M. Lazarev, A. Rudra, K.F. Karlsson, V. Tsvetkov, M. Skorikov, N. N. Sibeldin and E. Kapon "Valence band mixing and light polarization in tailored-potential semiconductor quantum dots" (2019, in preparation)

Conferences

J. Szeszko, V. V. Belykh, A. Rudra1,M.Lazarev, P. Gallo, N. N. Sibeldin and E. Kapon "Site-controlled tailored-potential quantum wires grown by OMVPE on patterned substrates", 17th International Conference on Metalorganic Vapour Phase Epitaxy. Lausanne, Switzerland, July 13-18 2014 (poster).

M.Lazarev. A. Rudra, K.F. Karlsson and E. Kapon "Valence Band Mixing in Tailored Potential quasi-1D nanostructures" International conference of optics of excitons in confined systems OECS 11-16 October 2015 Jerusalem (oral)

Mikhail Lazarev

Citizenship : Russia
Address: Chemin de Champagne 2
CH-1025 Saint-Sulpice, Switzerland
E-mail : Mikhail.lazarev@epfl.ch
Phone number : +41 78 6458626

Education:

2002-2007 High school "Lyceum" Troitsk, Moscow, Russia.

2007-2011 **Bachelor degree in Applied Mathematics and Physics, Moscow Institute of Physics and Technology (MIPT)**, department of Problems of Physics and Energetics. Thesis: "Features of the formation of forbidden bands in one-dimensional photonic crystals of high contrast".
Supervisors: Dr. Alexander Merzlikin

2011-2013 **Master degree in Applied Mathematics and Physics, Moscow Institute of Physics and Technology (MIPT)**, department of Problems of Physics and Energetics. Thesis: "Tunneling of the electron packet in graphene".
Supervisors: Prof. Yury Lozovik

2013-2019 **PhD Student, Ecole Polytechnique Fédérale de Lausanne (EPFL)**, Laboratory of Physics of Nanostructures (LPN). Thesis: "Tailored-Potential Semiconductor Quantum Nanostructures Grown in Inverted Pyramids".
Supervisors: Prof. Eli Kapon

Professional experience:

2013-2019 Laboratory of Physics of Nanostructures, EPFL – PhD student, teaching assistant for general physics.
2010-2013 Laboratory assistant at Institute of Theoretical and Applied Electromagnetics RAS.
2007-2009 Teacher at Physical-Technical school at Moscow Institute of Physics and Technology (State University).
2009-2013 Private tutor.

Technical skills:

Nanofabrication, clean room processing, lithography, microscopy techniques, spectroscopy, optics laboratory, cryogenic experiments.

Computer skills:

Matlab, Python, Fortran, Wolfram Mathematica, Java, Latex, UNIX, Adobe Illustrator CC.

Languages:

Russian	Mother tongue
English	Fluent
German	Beginner
French	Beginner

Ce document a été imprimé au Centre d’impression EPFL,
imprimerie climatiquement neutre, certifiée myClimate.